

Boundary Effects on the Electrical Conductivity of Cerium Oxide Thin Films

Von der Fakultät Chemie der Universität Stuttgart
zur Erlangung der Würde eines

Doktors der Naturwissenschaften

(Dr. rer. nat.) genehmigte Abhandlung

Vorgelegt von
Marcus Göbel
aus Halle (Saale)

Hauptberichter: Prof. Dr. J. Maier

Mitberichter: Prof. Dr. J. Bill

Prüfungsvorsitzender: Prof. Dr. J. van Slageren

Tag der Einreichung: 15. November 2012

Tag der mündlichen Prüfung: 23. Januar 2013

Max-Planck-Institut für Festkörperforschung
Stuttgart
2012

*Gewidmet
meiner Verlobten Mariya*

*“What we know is a drop,
what we don't know is an ocean.”*

Isaac Newton

Erklärung

Die vorliegende Doktorarbeit wurde vom Autor selbst in der Abteilung von Prof. J. Maier am Max-Planck-Institut für Festkörperforschung, im Zeitraum von Oktober 2008 bis November 2012 angefertigt. Der Inhalt ist die eigene Arbeit des Autors, Ausnahmen sind gekennzeichnet, und wurde noch nicht zur Erlangung einer Qualifizierung oder eines Titels an einer akademischen Institution eingereicht.

Stuttgart, 14. November 2012

Marcus Göbel

Declaration

The work described in this thesis was carried out by the author in the Department of Prof. J. Maier at the Max Planck Institute for Solid State Research from October 2008 to November 2012. The contents are the original work of the author except where indicated otherwise and have not been previously submitted for any other degree or qualification at any academic institution.

Stuttgart, November 14, 2012

Marcus Göbel

Table of Contents

Abstract	xv
Zusammenfassung	xix
Chapter 1 Introduction and Motivation	1
1.1 Space Charge Layer Effects	1
1.2 Cerium Oxide in Applications	2
1.3 Cerium Oxide Thin Films.....	3
Chapter 2 Theoretical Background	5
2.1 The Defect Chemistry of Cerium Oxide.....	5
2.1.1 Pure and Acceptor Doped Cerium Oxide.....	5
2.1.2 Donor Doped Cerium Oxide	6
2.1.3 The Bulk Conductivity and its Dependencies	7
2.1.4 The Electrolytic Domain Boundary in the Bulk	12
2.2 Space Charge Effects	12
2.2.1 General Considerations	13
2.2.2 Space Charge Layer Profiles.....	16
2.2.3 Conductivity Effects.....	18
2.2.3.1 Effective Conductivity Values	18

2.2.3.2 Conductivity Pathways in Cerium Oxide 19

2.2.3.3 The Electrolytic Domain Boundary in Polycrystalline Material 21

2.2.3.4 Analytical Solutions 22

2.2.3.5 Local Mean Conductivities 23

Chapter 3 Modeling25

3.1 Numerical Calculation of Space Charge Layer Profiles 25

3.2 Further Characteristics of Space Charge Layer Profiles..... 28

3.3 One Dimensional Overlapping Space Charge Layer Profiles..... 29

Chapter 4 Experimental Setup 31

4.1 Sample Preparation 31

4.1.1 Powder Preparation 31

4.1.2 Sintering..... 31

4.1.3 Pulsed Laser Deposition..... 32

4.1.3.1 General Description 32

4.1.3.2 Used Parameters 32

4.1.3.3 Target Holder 33

4.2 Microstructure Characterization 34

4.2.1 X-Ray Diffraction 34

4.2.2 Scanning Electron Microscopy, Focused Ion Beam and Transmission
Electron Microscopy 35

4.3 Conductivity Measurements 35

4.3.1 Impedance Spectroscopy 35

4.3.1.1 Impedance Spectra Characterized by RC Elements 35

4.3.1.2 Characteristic Device Parameters 36

4.3.2 Measurement Cell 37

4.3.3 Flow Controller Setup and Calibration 38

4.3.4 Temperature Calibration 40

4.3.5 Spurious Conductances of Substrate and Sample Holder 41

Chapter 5 Results and Discussion	43
5.1 Numerical Calculations of Space Charge Layer Effects in Cerium Oxide.....	43
5.1.1 Section Introduction	43
5.1.2 Preliminary Considerations	44
5.1.2.1 Accuracy of the Numerical Approach	44
5.1.2.2 Parameters.....	45
5.1.3 Relationships between the Characteristics of Space Charge Layer Profiles and the Conductivity Effects.....	45
5.1.3.1 Typical Space Charge Layer Profiles in CeO ₂	45
5.1.3.2 Charge Contributions in Space Charge Layers.....	46
5.1.3.3 The Space Charge Layer Extent	49
5.1.3.4 Conductivity Effects	49
5.1.3.5 Influence of a Mobile Dopant.....	52
5.1.4 Accuracy of the Analytical Space Charge Layer Solutions	54
5.1.4.1 Analytical Solutions in the Literature.....	54
5.1.4.1.1 Areas of the Different Analytical Approximation Cases	54
5.1.4.1.2 The Space Charge Layer Extent in the Analytical Solutions	56
5.1.4.1.3 Effective Conductivity and Effective Conductivity Change	56
5.1.4.1.4 Quantitative Impact of the Assumptions Made in the Analytical Solutions on their Accuracy	57
5.1.4.2 Improved Analytical Solutions	60
5.1.4.2.1 Gouy-Chapman Case	60
5.1.4.2.2 Mott-Schottky Case	61
5.1.4.2.2.1 Low Space Charge Potentials.....	61
5.1.4.2.2.2 Moderate and Large Space Charge Potentials	62
5.1.4.2.3 Mixed Case	63
5.1.4.2.4 Accuracy of the Improved Analytical Solutions	66
5.1.4.2.5 Self Consistency Check for the Analytical Relationships	68
5.1.4.2.6 Space Charge Layers Characterized by Unrealistically Large Concentrations	68
5.1.4.3 Examples.....	70
5.1.4.3.1 Low Space Charge Layer Potentials.....	70
5.1.4.3.2 Moderate Space Charge Layer Potentials.....	70
5.1.4.3.3 Mixed Case.....	70
5.1.5 Considerations on the SCL Charge.....	71
5.1.5.1 Maximum Value of the SCL Charge in CeO ₂	71
5.1.5.2 Relationship between SCL Potential and Charge	71
5.1.5.3 Expected Conductivity Effects under Consideration of the SCL Charge	72
5.1.6 Section Conclusions	74
5.2 Impedance Spectra	77
5.2.1 Measured Impedance Spectra	77
5.2.2 Equivalent Circuits	78

5.2.3 Total Effective Resistance and Conductivity	81
5.3 Grain Boundary vs. Film Substrate Interface Effects – Cerium Oxide Thin Films on Al₂O₃ <0001> and SiO₂ <0001>	83
5.3.1 Section Introduction.....	83
5.3.2 Microstructure.....	84
5.3.3 Conductivity Data	86
5.3.3.1 Acceptor Doped Thin Films	86
5.3.3.1.1 Epitaxial Thin Films on Al ₂ O ₃ <0001>	86
5.3.3.1.2 Polycrystalline Thin Films on SiO ₂ <0001>.....	88
5.3.3.2 Nominally Pure Thin Films.....	92
5.3.3.2.1 Oxygen Partial Pressure Dependence.....	92
5.3.3.2.2 Epitaxial Thin Films on Al ₂ O ₃ <0001>	92
5.3.3.2.3 Polycrystalline Thin Films on SiO ₂ <0001>.....	95
5.3.3.2.4 Reduced Reduction Enthalpy	96
5.3.4 Section Conclusions	97
5.4 Reduced Grain Boundary Effects in Cerium Oxide Thin Films on Al₂O₃ <1102> and MgO <100>	98
5.4.1 Section Introduction.....	98
5.4.2 Microstructure.....	98
5.4.3 Conductivity Data	100
5.4.4 Section Conclusions	103
5.5 Strongly Enhanced Electronic Conductivity Domain in Nanocrystalline Cerium Oxide Thin Films	104
5.5.1 Section Introduction.....	104
5.5.2 Microstructure.....	105
5.5.3 Conductivity Data	106
5.5.3.1 Preliminary Considerations	106
5.5.3.1.1 Thermal Stability of the <i>rt-nano</i> Thin Film.....	106
5.5.3.1.2 Expected Conductivity Properties.....	107
5.5.3.1.2.1 Expected Bulk Properties.....	108
5.5.3.1.2.2 Expected Properties of Nanocrystalline Material.....	109
5.5.3.2 Temperature Dependence	111
5.5.3.3 Oxygen Partial Pressure Dependence.....	113
5.5.3.4 Further Considerations on the Activation Energy	115
5.5.3.5 Enhanced Electronic Bulk Conductivity	119
5.5.3.6 Change in the Electronic Activation Energy at 500 °C	122
5.5.3.7 Grain Boundary Effects in the 1 and 0.15 mol% Gd Doped and Nominally Pure Thin Films.....	123
5.5.4 Section Conclusions	125

5.6 Electronically Blocking Grain Boundaries in Donor Doped Cerium Oxide.....	127
5.6.1 Section Introduction.....	127
5.6.2 Microstructure.....	127
5.6.3 Conductivity Data	129
5.6.3.1 Defect Chemistry	129
5.6.3.2 Grain Boundary Effects	131
5.6.4 Section Conclusions	133
Chapter 6 Main Conclusions.....	135
Acknowledgements.....	I
List of Abbreviations.....	III
List of Symbols	V
Index of Equations.....	XVII
Index of Figures.....	XIX
Index of Tables.....	XXIII
References.....	XXV
Curriculum Vitae.....	XXXIV

Abstract

Boundary effects in mixed and ionic conductors and in particular space charge layer (SCL) effects are a major field of research in solid state ionics since they are known to strongly affect the electrical transport properties of the materials. In particular, in this study the boundary effects of cerium oxide were investigated which due to its high ionic conductivity is a material of large relevance for a wide range of applications such as solid oxide fuel cells (SOFCs), oxygen membranes and catalysis. Here the thin film geometry was applied which offers the advantage of a usually well defined microstructure allowing to access effects at both the film-substrate interface (FSI) and the grain boundaries (GBs).

The cerium oxide thin films were grown with pulsed laser deposition (PLD) on various substrates: Al_2O_3 $\langle 0001 \rangle$, Al_2O_3 $\langle 1\bar{1}02 \rangle$, SiO_2 $\langle 0001 \rangle$ and MgO $\langle 100 \rangle$. Depending on target material and growth conditions hereby thin films were prepared of (1) different doping contents (nominally pure, acceptor doped and donor doped), (2) different microstructures (epitaxial and nanocrystalline) and (3) different thicknesses (between 20 and 450 nm). Their microstructure was characterized with X-ray diffraction (XRD), scanning electron microscopy (SEM), transmission electron microscopy (TEM), high resolution TEM (HRTEM) and electron diffraction. The defect chemistry and conductivity properties of the samples were investigated with impedance spectroscopy at various temperatures and oxygen partial pressures ($p\text{O}_2$).

Additionally, a software to numerically compute the SCL profiles and conductivity effects in ceria was developed. Hereby a stepwise calculation of the electric potential, electric field and local concentrations was applied to solve the one-dimensional Poisson equation.

The numerical approach allowed for the determination of all relevant SCL profile characteristics (SCL potential, charge, extent, steepness, etc.) and for the correlation of them with both the material properties (equilibrium constants, doping, etc.) and the resulting conductivity effects. The conductivity effects were observed to be a function of not only the SCL potential and extent

as entirely expected, but also the SCL steepness. Interestingly, in the Gouy-Chapman case the SCL extent was found to depend not only on the doping content but also weakly on the SCL potential, in comparison with the Debye length λ which is potential independent. Also, it could be demonstrated that the maximum value the SCL charge can reach is limited resulting in a restriction of the conductivity effects in certain cases. In particular, for strongly doped samples in the Gouy-Chapman case the relative excess conductivity was found to be limited to small values only.

Notably, the numerical approach was observed to yield precise results without the use of further assumptions also for asymmetric and mixed cases in contrast to the well known analytical solutions which were observed to often produce rather unreliable results in these situations. This allowed for a test of the assumptions made in the analytical solutions which resulted in the development of improved analytical relationships to describe the effects of non-overlapping SCLs. Remarkably, the new analytical approach which is not restricted to CeO₂ but generally applicable was observed to yield very reliable outcomes even for complex situations, such as low potentials, asymmetric and mixed cases.

In most cases the boundary effects were found to dominate the conductivity of the investigated ceria thin films. Effects at both the film-substrate interface and at the grain boundaries were observed.

As expected in the framework of the SCL theory no significant FSI effect was detected in strongly acceptor doped films.

In epitaxial, nominally pure CeO₂ films grown on Al₂O₃ <0001> the conductivity was observed to be reduced at the FSI. Qualitatively and quantitatively the observation was found to be in agreement with the SCL theory.

In nanocrystalline, acceptor doped samples grown on SiO₂ <0001> a significant decrease of the conductivity at the GBs was observed in accordance with a SCL potential of 0.32 ± 0.05 V at 700 °C. For this set of samples furthermore a thickness dependence of the grain size was detected resulting in a considerable change of the conductivity with film thickness that otherwise is the typical fingerprint of an effect at the FSI. Therefore, it could be demonstrated that a thickness dependent conductivity in polycrystalline samples can not always be assigned to FSI effects. This finding is of relevance for a number of similar studies on interface effects.

Nanocrystalline, acceptor doped films grown on Al₂O₃ <1 $\bar{1}$ 02> and MgO <100> substrates were found to exhibit a less significant decrease of the ionic conductivity compared with the films on SiO₂ <0001>. The SCL potential was observed to be decreased to a value of 0.19 ± 0.05 V at

700 °C. Here it is most probably the smaller lattice mismatch between substrate and CeO₂ film which results in an only small misorientation of adjacent grains and, hence, less pronounced GB core charges and SCL effects.

Thin films prepared at room temperature, characterized by a nanocrystalline microstructure with very small grains, were measured to exhibit very pronounced SCL effects. Here for acceptor doped samples the ionic conductivity was found to be decreased by three orders of magnitude corresponding to a SCL potential of 0.30 ± 0.05 V at 300 °C (compared with 0.22 ± 0.05 V at 300 °C for nanocrystalline films fabricated at 720 °C). In addition to the rather high SCL potential most likely here the Mott-Schottky assumption of a flat dopant profile is fulfilled much better resulting in a particularly strong depletion of the oxygen vacancies in the SCLs.

Remarkably, for these samples the oxygen partial pressure of the onset of the electronic conductivity, the electrolytic domain boundary, was found to be shifted by 29 orders of magnitude compared with what is expected from an extrapolation of the literature bulk data to low temperatures. Two superimposing effects were found to be the origin of this drastic shift: (1) The pronounced SCL effects result in a decrease of the ionic conductivity and an increase of the electronic conductivity which contributes to 16 orders of magnitude of the pO_2 shift. This is comparable to a recently discovered shift of the transition pO_2 in nanocrystalline SrTiO₃ between *n*- and *p*-type conduction by 12 orders of magnitude due to SCL effects [Lupetin *et al.*, *Angew. Chem. Int. Edit.* **49**, 10123]. (2) Already in the bulk the electronic conductivity was measured to be strongly increased resulting in a further shift of the pO_2 by 13 orders of magnitude and, hence, in the observed total shift by $16 + 13 = 29$ orders of magnitude. Both effects also affect the activation energies resulting in an increase of the ionic value and a decrease of the electronic value. Notably, in this particular case the electronic activation energy falls even below the ionic value. This resulted in the remarkable observation of an increase of the electronic conductivity contribution for decreasing temperatures in marked contrast to the properties typically observed in ceria.

Unexpectedly, in some of the nanocrystalline, acceptor doped or nominally pure CeO₂ films prepared at high temperatures not only the ionic transport (due to the SCL effects mentioned above) but also the electronic transport was found to be blocked at the GBs. This indicates that - superimposed with SCL effects - also other boundary effects on the electronic conductivity are present, such as changes of the reduction enthalpy and/or mobility effects.

Notably, also in the donor doped CeO₂ samples the electronic conductivity was observed to be decreased at the GBs. The recorded conductivity data indicates that either a negative SCL potential or a change of the electron mobility at the GBs is the cause of this effect. The investigation could also confirm the presence of oxygen interstitial defects in donor doped cerium oxide which was suggested in earlier studies of this barely investigated material.

Zusammenfassung

Die Erforschung von Grenzflächeneffekten und im Speziellen von Raumladungseffekten in gemischten und ionischen Leitern ist ein bedeutendes Teilgebiet der physikalischen Festkörperchemie, insbesondere da in vielen dieser Materialien die elektrische Leitfähigkeit durch diese Effekte dominiert wird. In dieser Studie wurden Grenzflächeneffekte in dünnen Schichten aus Ceroxid untersucht, ein Material welches aufgrund seiner hohen ionischen Leitfähigkeit von großer Bedeutung für eine Reihe von Anwendungen wie Festoxidbrennstoffzellen, Sauerstoffmembranen und die Katalyse ist. Der Vorteil der Dünnschicht-Geometrie ist hierbei in erster Linie die im Allgemeinen besser definierte Mikrostruktur, die es ermöglicht, sowohl die Eigenschaften der Schicht-Substrat-Grenzfläche als auch die der Korngrenzen zu untersuchen.

Hierzu wurden dünne Schichten aus Ceroxid mit gepulster Laserdeposition auf verschiedenen Substraten präpariert: Al_2O_3 $\langle 0001 \rangle$, Al_2O_3 $\langle 1\bar{1}02 \rangle$, SiO_2 $\langle 0001 \rangle$ und MgO $\langle 100 \rangle$. In Abhängigkeit des Targetmaterials und der Wachstumsbedingungen wurden hierbei Schichten hergestellt, welche sich durch (1) verschiedene Dotierungen (nominell rein, akzeptordotiert und donordotiert), (2) verschiedene Mikrostrukturen (epitaktisch und nanokristallin) und (3) verschiedene Dicken (zwischen 20 und 450 nm) auszeichneten. Die Mikrostruktur der Proben wurde mit Röntgenstrukturanalyse, Rasterelektronenmikroskopie, Transmissionselektronenmikroskopie und Elektronenbeugung charakterisiert. Die Leitfähigkeitseffekte in den dünnen Schichten und die Defektchemie des Materials wurden mittels Impedanzspektroskopie bei verschiedenen Temperaturen und Sauerstoffpartialdrücken untersucht.

Zusätzlich wurde auch eine Software zur numerischen Bestimmung der Raumladungsprofile und der entsprechenden Leitfähigkeitseffekte in Ceroxid programmiert. Der hierfür verwendete Algorithmus zur Lösung der eindimensionalen Poisson-Gleichung beruhte auf einer schrittweisen Berechnung des elektrischen Potentials, des elektrischen Felds und der lokalen Defektkonzentrationen.

Der numerische Ansatz ermöglichte es, alle relevanten Eigenschaften der Raumladungsprofile (Raumladungspotential, -ladung, -ausdehnung, -steilheit, etc.) zu untersuchen und sowohl mit den Materialeigenschaften (Defektgleichgewichte, Dotierung, etc.) als auch den resultierenden Leitfähigkeitseffekten zu korrelieren. Hierbei konnte gezeigt werden, dass nicht nur das Potential und die Ausdehnung der Raumladungszonen, sondern auch ihre Steilheit die Leitfähigkeitseffekte beeinflussen. Interessanterweise und im Vergleich mit der Debyelänge λ , welche keine Funktion des Raumladungspotentials ist, ergaben die numerischen Berechnungen, dass sich die Raumladungsausdehnung im Gouy-Chapman-Fall nicht nur mit dem Dotiergehalt, sondern auch leicht mit dem Raumladungspotential ändert. Des Weiteren konnte demonstriert werden, dass der Maximalwert, den die Ladung der Raumladungszone annehmen kann, begrenzt ist und dass dies wiederum in einer starken Asymmetrie der Leitfähigkeitseffekte bezüglich des Dotiergehalts und des Raumladungspotentials resultiert. Beispielsweise ergaben die Berechnungen, dass in stark akzeptordotierten Ceroxid sehr große Leitfähigkeitseffekte auftreten können, wenn das Raumladungspotential einen positiven Wert annimmt (wie experimentell gemessen). Bei negativen Raumladungspotentialen hingegen wird die Leitfähigkeit des gleichen Materials nur wenig beeinflusst.

Vor allen Dingen zeichnete sich der numerische Ansatz dadurch aus, auch in komplexen Fällen, wie asymmetrischen und gemischten Situationen, präzise Ergebnisse zu liefern. Mit Hilfe der numerischen Berechnungen konnten daher die Annahmen und Vereinfachungen der viel verwendeten analytischen Näherungen getestet werden. Der Test ergab, dass sich die Genauigkeit der analytischen Näherungen je nach Fall unterscheidet und dass sie in vielen, auch experimentell relevanten Situationen oft nur gering ist. Insbesondere mündete der Test in der Entwicklung neuer, verbesserter analytischer Lösungen zur Beschreibung nichtüberlappender Raumladungszonen. Der Vergleich mit den numerischen Berechnungen konnten zeigen, dass diese Formeln (welche nicht auf Ceroxid beschränkt sondern allgemein anwendbar sind) sehr zuverlässige Ergebnisse liefern, selbst in komplizierten Situationen wie in asymmetrischen und gemischten Fällen und bei niedrigen Raumladungspotentialen.

Die experimentellen Untersuchungen ergaben, dass in dünnen Ceroxidschichten in den meisten Fällen Grenzflächeneffekte die Leitfähigkeit dominieren. Sowohl Effekte an der Schicht-Substrat-Grenzfläche als auch an den Korngrenzen wurden detektiert.

Wie unter Berücksichtigung der Raumladungstheorie erwartet, wurde keine wesentlich veränderte Leitfähigkeit an der Schicht-Substrat-Grenzfläche in stark akzeptordotierten Schichten beobachtet.

In epitaktischen, nominell reinen, auf Al_2O_3 $\langle 0001 \rangle$ gewachsenen Ceroxidschichten hingegen wurde eine deutliche Verminderung der Leitfähigkeit gemessen. Sowohl qualitativ als auch quantitativ ist dieser Effekt in Übereinstimmung mit der Raumladungstheorie.

In nanokristallinen, akzeptordotierten Schichten, welche auf SiO_2 $\langle 0001 \rangle$ präpariert wurden, konnte ein deutlicher Abfall der Leitfähigkeit an den Korngrenzen nachgewiesen werden. Dieser Leitfähigkeitseffekt ließ sich auf ein Raumladungspotential an den Korngrenzen von 0.32 ± 0.05 V bei 700 °C zurückführen. Bei jener Probenreihe wurde außerdem beobachtet, dass die Leitfähigkeit mit abnehmender Schichtdicke stark sank, da die laterale Korngröße in diesem Fall zunahm. Normalerweise ist solch ein Leitfähigkeitstrend ein typischer Nachweis für einen Effekt an der Schicht-Substrat-Grenzfläche. Somit konnte gezeigt werden, dass eine schichtdickenabhängige Leitfähigkeit nicht in jedem Fall einem Effekt an der Schicht-Substrat-Grenzfläche zugeordnet werden kann. Dieses Ergebnis ist von großer Relevanz für eine Reihe ähnlicher Studien von Grenzflächeneffekten.

Auf Al_2O_3 $\langle 1\bar{1}02 \rangle$ und MgO $\langle 100 \rangle$ gewachsene, nanokristalline, akzeptordotierte Schichten zeigten eine weniger stark ausgeprägte Abnahme der ionischen Leitfähigkeit im Vergleich mit den oben beschriebenen Schichten auf SiO_2 $\langle 0001 \rangle$. Die relativ betrachtete höhere Leitfähigkeit dieser Proben entspricht einem kleineren Raumladungspotential von 0.19 ± 0.05 V bei 700 °C. Die wahrscheinlichste Ursache für diesen Effekt ist die kleinere Gitterfehlpassung zwischen dem Substrat und der Ceroxidschicht. Diese führt zu einer nur relativ kleinen Fehlorientierung benachbarter Körner und somit zu niedrigeren Korngrenzenkernladungen und schwächeren Raumladungseffekten.

Dünne Schichten, welche bei Raumtemperatur hergestellt wurden und daher eine nanokristalline Mikrostruktur mit äußerst kleinen Körnern aufwiesen, zeigten besonders stark ausgeprägte Raumladungseffekte. In den so präparierten, akzeptordotierten Proben wurde ein Abfall der ionischen Leitfähigkeit um drei Größenordnungen beobachtet. Dies entspricht einem Raumladungspotential von 0.30 ± 0.05 V bei 300 °C (im Vergleich mit 0.22 ± 0.05 V bei 300 °C für nanokristalline Proben, welche bei 720 °C hergestellt wurden). Zusätzlich zu dem recht hohen Raumladungspotential ist in diesem Fall höchstwahrscheinlich die Mott-Schottky-Näherung eines konstanten Dotierprofils besser erfüllt. Dies resultiert in einer besonders starken Verarmung der Sauerstoffleerstellen in den Raumladungszonen.

Bemerkenswerterweise ergaben die Messungen, dass in diesen Proben der Sauerstoffpartialdruck, bei dem die elektronische Leitfähigkeit einsetzt, um 29 Größenordnungen erhöht ist (im Vergleich mit dem durch Extrapolation der Literaturdaten erwarteten Wert). Weitere Untersuchungen konnten zeigen, dass diese drastische Verschiebung auf zwei Ursachen beruht: (1) Die oben beschriebenen, besonders deutlich ausgeprägten Raumladungseffekte resultierten in einem Abfall der ionischen und einem Anstieg der

elektronischen Leitfähigkeit. Dieser Effekt trug 16 Größenordnungen zu der Verschiebung des Sauerstoffpartialdrucks bei. Damit ist er vergleichbar mit einer unlängst beobachteten Verschiebung des Sauerstoffpartialdrucks (am Übergang zwischen *n*- und *p*-Leitung) in nanokristallinem SrTiO₃ um 12 Größenordnungen, welche auf ähnlichen Raumladungseffekten basiert [Lupetin *et al.*, *Angew. Chem. Int. Edit.* **49**, 10123]. (2) Bereits im Volumenanteil der CeO₂-Schichten konnte eine stark erhöhte elektronische Leitfähigkeit nachgewiesen werden, die in einer Verschiebung des Sauerstoffpartialdrucks um weitere 13 Größenordnungen resultierte (insgesamt daher eine Verschiebung um 16 + 13 = 29 Größenordnungen). Beide Effekte beeinflussten auch die Aktivierungsenergien und führten zu einem Anstieg der ionischen und zu einem Abfall der elektronischen Aktivierungsenergie. Insbesondere konnte gezeigt werden, dass in diesen speziellen Proben die elektronische Aktivierungsenergie sogar die ionische unterschritt. Dies spiegelte sich in der außergewöhnlichen Beobachtung wieder, dass die elektronische Überföhrungszahl mit sinkender Temperatur stieg, im Gegensatz zu dem üblicherweise in anderen Ceroxidproben gemessenen Verhalten.

In einigen der nanokristallinen und akzeptordotierten (oder nominell reinen) Schichten aus Ceroxid, die bei hohen Temperaturen hergestellt wurden, wurde beobachtet, dass nicht nur die ionische Leitfähigkeit, sondern unerwarteterweise auch die elektronische Leitfähigkeit an den Korngrenzen abfällt. Damit konnte gezeigt werden, dass – in Überlagerung mit den Raumladungseffekten – auch andere Grenzflächeneffekte wie eine Änderung der Reduktionenthalpie und/oder der Mobilität an den Korngrenzen die elektronische Leitfähigkeit beeinflussen.

Auch in donordotierten Ceroxid wurde ein Abfall der elektronischen Leitfähigkeit an den Korngrenzen beobachtet. Die Untersuchungen ergaben, dass in diesem Material zwei mögliche Ursachen einen solchen Leitfähigkeitsabfall bewirken konnten: (1) ein negatives Raumladungspotential und (2) eine Minderung der Elektronenmobilität. Ebenso wurde die Anwesenheit von Sauerstoffzwischengitterdefekten, wie sie schon in früheren Studien dieses bisher kaum untersuchten Materials beobachtet wurde, bestätigt.

Chapter 1

Introduction and Motivation

In this thesis space charge layer (SCL) effects in thin films of CeO_2 are investigated. Hereby, the motivation of the project bases on two foundations. (1) From the basic research point of view studies of SCL effects in ionic and mixed conductors are of large significance and (2) the investigated material, cerium oxide, is particularly relevant for applications, such as fuel cells, catalysis and oxygen membranes.

1.1 Space Charge Layer Effects

Space charge layers are of major importance in both basic research and applications. A prominent example is the wide range of modern electronics and information technology that completely rests upon transistors and diodes, which base on SCLs effects. Also in ionic conductors SCLs were found to be crucial, since they are able to change their material properties (conductivity, storage capacity, etc.) considerably. The model of heterogeneous doping by Maier^[1, 2] provides the general description of SCLs in ionic conductors. There are a number of causes inducing SCLs. Examples are charged boundary cores (as e.g. in CeO_2)^[3-17] and redistribution phenomena at interfaces between differently doped areas (as e.g. in diodes) or between different conductors.^[18, 19] SCLs can be formed at both grain boundaries (GBs)^[6-17, 20, 21] and heterojunctions.^[19] They were found to drastically vary the electrical transport properties for a wide range of materials and are able to induce conductivity changes by many orders of magnitude.^[10, 16, 17]

A material that exhibits strong boundary effects is cerium oxide. It was Chiang *et al.* who firstly found a strong increase of the electronic conductivity of nanocrystalline ceria.^[3, 4] Maier and coworkers^[10, 11, 22] and Tschöpe and coworkers^[6-8, 12] could show that the origin of this enrichment of electrons at the GBs and of the corresponding depletion of oxygen vacancies are SCLs with a positive electric potential. Also other boundary effects, such as structural strain, are reported to influence the conductivity in CeO_2 .^[23-29]

1.2 Cerium Oxide in Applications

Ionic conductors play a key role in the worldwide challenge to develop renewable energy sources and more efficient energy storages. This comprises not only novel batteries but also a number of different fuel cell technologies. Solid oxide fuel cells^[30-32] (SOFCs) are of special interest since in comparison with other fuel cell techniques they can be fueled not only with hydrogen but also with hydrocarbons.^[33-35] This gives the advantage to avoid the problems inherent in a hydrogen infrastructure such as H₂ production, storage and transport, which at least partially remain unsolved even today.

SOFCs combine the advantage of the high energy density of hydrocarbons (in contrast to batteries) with a much higher efficiency in comparison with internal combustion engines. Therefore, they have the potential to be applied in many fields such as (1) more efficient central power production, (2) distributed power production, (3) balancing of power fluctuations of renewable energy sources (in combination with gas turbines) and (4) very efficient and fuel flexible range extenders in cars.^[35] They are even significant in (5) the production of liquid fuels from excess electricity (using reversible SOFCs (RSOFCs)).^[35] Furthermore, (6) thanks to their emission of pure CO₂ and easily separable H₂O SOFCs are promising for inexpensive carbon sequestration techniques.^[35]

A major problem of the SOFC technology is the very high process temperature making it necessary to use expensive ceramic interconnect plates instead of readily available stainless steel parts.^[31] Hence, one of the main goals in SOFC development is the reduction of the process temperature to intermediate temperatures (500 - 750°C)^[36-38] and even below (300 - 500 °C).^[39] However, the nowadays most often used electrolyte material yttria stabilized zirconia (YSZ) lacks sufficient conductivity in these temperature ranges. A promising material with a high oxygen vacancy conductivity at intermediate and low temperatures is acceptor doped cerium oxide, due to its low ionic activation energy value of only about 0.7 eV.^[40, 41] As far as solid electrolytes are concerned the ionic conductivity of ceria is only surpassed by Bi₂O₃ based materials (Fig. 1), which, however, are not stable in the reducing atmosphere at the anode.¹ In addition to its relevance as SOFC electrolyte CeO₂ is significant for a number of other applications such as catalysis^[42-44] and oxygen membranes.^[45-49]

However, in polycrystalline CeO₂ the ionic conductivity is strongly reduced due to a positive SCL potential at the GBS^[6-8, 10-14, 16, 17, 22] while the electronic conductivity is enhanced.^[3, 4] Therefore,

¹ As shown in ref. ^[39] Bi₂O₃ based materials can only be used in bilayer electrolytes with a sufficiently thick acceptor doped cerium oxide layer at the anode side of the bilayer.

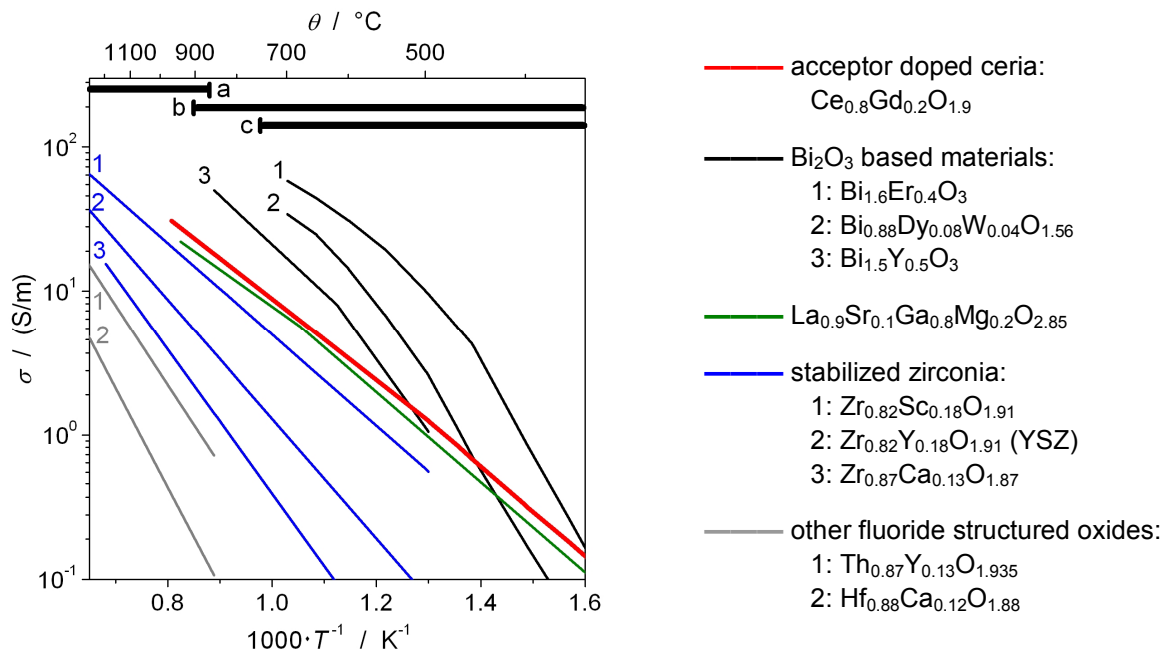


Fig. 1: Ionic Conductivities of Selected SOFC Electrolytes

Data taken from ref. [31, 39, 41]. The bars at the top of the graph indicate the thermal stability of selected interconnect plate materials:

(a) La (Ca) CrO₃ (b) Cr-Fe (Y₂O₃) / Inconel - Al₂O₃ (c) stainless steel

σ : conductivity, T : temperature in K, θ : temperature in °C

the positive SCL potential limits the applicability of cerium oxide considerably. It is worth noting that several approaches have been studied to modify the SCL properties in order to increase the conductivity at the GBs (not only in CeO₂), such as segregation of aliovalent cations at the interfaces,^[50] decoration of the GBs^[51, 52] and preference doping of GBs via GB diffusion.^[53]

With none of the above modifications the decrease in ionic conductivity at the GBs could be sufficiently suspended. This shows that further research on the origin and characteristics of the SCL effects is necessary since only a full understanding of them might allow for the development of highly conductive, polycrystalline ceria.

1.3 Cerium Oxide Thin Films

In addition to the investigation of new, highly conductive materials a second approach to lower the process temperature in SOFCs is the development of novel fuel cells on a sub-mm scale (μ SOFCs) by using thin film electrolytes. In future μ SOFCs may even be capable of replacing batteries in portable devices in view of the larger energy densities of hydrocarbons.^[54-71]

Therefore, further research on the conductivity properties of thin film electrolytes is particularly attractive.

Moreover, in contrast to pellets where the boundaries are more or less randomly distributed, thin films are characterized by a better determined geometry. This allows for an easier experimental accessibility of the boundary effects:

- (A) Thin films offer the advantage of a well defined film-substrate interface (FSI) (Fig. 2, left panel), whose properties are accessible by investigating thin films of various thicknesses (as shown in section 5.3).
- (B) The microstructure of thin films can be tailored by choosing different substrate materials and deposition conditions. This allows for the preparation of nanocrystalline thin films (Fig. 2, right panel) of different grain sizes (sections 5.3, 5.5 and 5.6) and also differently oriented grains (section 5.4). In particular, the preparation of extremely small grains with strongly enhanced GB effects is possible (section 5.5). The polycrystalline samples can then be compared with epitaxially grown thin films (i.e. single crystalline films without GBs) allowing for the separation of bulk properties and SCL effects at the GBs.

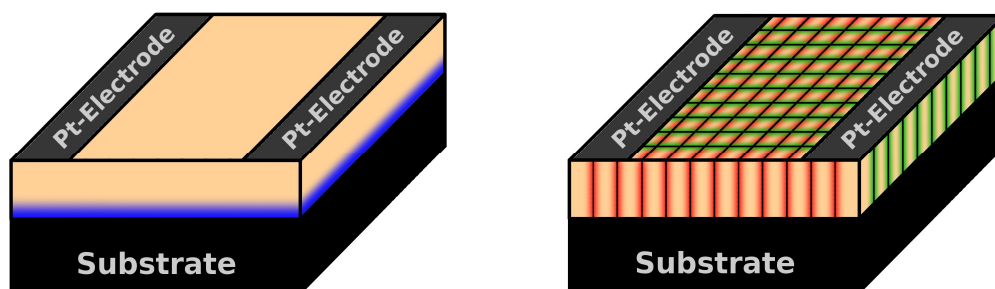


Fig. 2: Idealized Geometries of Epitaxial and Polycrystalline Thin Films

Thin films offer a well defined geometry to study FSI effects (left) and GB effects (right).

Legend: **blue**: effect at the film substrate interface, **green**: increased (electron) conductivity along parallel grain boundaries, **red**: decreased (ionic) conductivity across perpendicular grain boundaries (see also section 2.2.3.2)

Reproduced from Gregori, Göbel and Maier^[17] with permission from ECS Transactions, The Electrochemical Society (Copyright 2012).

Hence, in conclusion the study presented in this thesis combines the highly relevant basic research of SCL effects with the investigation of cerium oxide, a crucial material for applications. Furthermore, the thin film geometry is not only significant for novel, microscopic fuel cell devices but also an ideal sample geometry to distinguish various boundary effects. For all these reasons here SCL effects in cerium oxide thin films are studied.

Chapter 2

Theoretical Background

2.1 The Defect Chemistry of Cerium Oxide

2.1.1 Pure and Acceptor Doped Cerium Oxide

CeO₂ crystallizes in the fluorite (CaF₂) structure.^[72] Here the cerium cations are arranged in a face-centered cubic structure with the oxide ions occupying the tetrahedral holes. This leaves the larger octahedral holes unoccupied and results in a considerable anion mobility that is typical for fluorite structured materials. As a second consequence the creation of anti-Frenkel pairs of oxygen vacancies V₀^{••} and oxygen interstitials O_i['] is favored:^[73]



$$K_F = c_{V_0^{\bullet\bullet}, \infty} c_{O_i', \infty} \quad \{2\}^{3, 4}$$

In contrast to most other elements which form fluorite structured oxides, such as zirconium, Ce^{IV} can be easily reduced to Ce^{III}. Hereby, in the Kröger-Vink notation the Ce^{III} cations (i.e. the Ce_{Ce}['] defects) are denoted as (excess) electrons e'. The comparatively high mass action constant K_R of the reduction reaction under oxygen excorporation (eq. {3} and {4}) is also a consequence of the high tolerance of the material towards oxygen vacancies. In this reaction the bulk electron concentration n_∞ ⁵ is in equilibrium with the outer oxygen partial pressure pO_2 :^[72, 74]



$$K_R = pO_2^{1/2} c_{V_0^{\bullet\bullet}, \infty} c_{e', \infty}^2 \equiv pO_2^{1/2} c_{V_0^{\bullet\bullet}, \infty} n_\infty^2 \quad \{4\}^5$$

² O_0^x : oxide ions on oxygen sublattice sites, V_i^x : unoccupied interstitial positions

³ K_F : equilibrium constant of the anti-Frenkel pair formation, $c_{V_0^{\bullet\bullet}, \infty}$ ($c_{O_i', \infty}$): bulk concentration of oxygen vacancies (doubly charged oxygen interstitials)

⁴ In the following the index ∞ refers to the bulk.

⁵ For simplicity for the bulk electron concentration in the following the symbol n_∞ is used instead of $c_{e', \infty}$.

As a consequence, ceria is a mixed ionic electronic conductor (MIEC) with electrons and oxygen vacancies being the only two charge carriers (CCs) that significantly contribute to the total electric conductivity.

Finally, the excess electrons are in equilibrium with electron holes h^\bullet . However, for the oxygen partial pressures considered here (≤ 1 bar) their concentration is only negligibly small due to the rather high electron concentration and the large band gap of 6 eV.^[75-77]



$$K_H = n_\infty c_{h^\bullet, \infty} \quad \{6\}^{6, 7}$$

2.1.2 Donor Doped Cerium Oxide

In contrast to acceptor doped and pure ceria which are important materials for a number of applications the defect chemistry of donor doped CeO₂ has been barely investigated. Hence, it is instructive to consider another more extensively studied, fluoride structured oxide in which the cation can easily be oxidized to an oxidation state of +5 or even +6: UO₂. Similarly to the donor doping in CeO₂ the oxidation of uranium in UO₂ favors the formation of oxygen interstitials for charge compensation.^[78-82] This can be described in the oxygen insertion reaction which will be of relevance in section 5.6.3.1:



$$K_I = \frac{K_F}{K_R} = \frac{c_{\text{O}_i'', \infty}}{p\text{O}_2^{1/2} \cdot n_\infty^2} \quad \{8\}^8$$

In addition to doubly charged oxygen interstitials O_i' UO₂ is also known to accommodate singly charged oxygen interstitials O_i' which are in equilibrium with the O_i' defects according to:^[78]



$$K_S = \frac{n_\infty c_{\text{O}_i', \infty}}{c_{\text{O}_i'', \infty}} \quad \{10\}^9$$

⁶ K_H : equilibrium constant of the electron-hole formation, $c_{h^\bullet, \infty}$: bulk concentration of the electron holes

⁷ Note that in semiconductors physics the bulk concentration of the electron holes is usually designated with the symbol p_∞ (in analogy to n_∞ for the electron bulk concentration). However, as described above for the oxygen partial pressures regarded here the electron holes are not relevant in CeO₂. Indeed in this thesis their bulk concentration appears in eq. {6} only. Therefore, $c_{h^\bullet, \infty}$ is used to designate the bulk concentration of the h^\bullet defects in eq. {6} whereas conveniently the common symbol $p\text{O}_2$ is applied to designate the oxygen partial pressure, a quantity which is of large significance in many sections of this thesis.

⁸ K_I : equilibrium constant of the oxygen insertion

In view of the fact that CeO₂ and UO₂ have the same structure and show only a slight difference in the cation radius for donor doped ceria a similar defect chemistry as in UO₂ is expected.^[73, 83] As a matter of fact, the few previous studies on U, Nb and Ta doped CeO₂ indicate that also these materials are characterized by the presence of electrons, singly and doubly charged oxygen interstitials.^[73, 83-89] The O_i' defects in CeO₂ are probably stabilized by favorable elastic interactions.^[15]

The conductivity of donor doped CeO₂ is dominated by electrons (*n*-type conductivity) since not only their mobility but also their bulk concentration is larger compared with the oxygen vacancies.^[74, 90-92]

2.1.3 The Bulk Conductivity and its Dependencies

In general, for each arbitrary type of defect *i* the bulk concentration $c_{i,\infty}$ corresponds to a bulk conductivity $\sigma_{i,\infty}$ (depending on the defect's charge number z_i and mobility u_i):

$$\sigma_{i,\infty} = |z_i| e u_i c_{i,\infty} \quad \{11\}^{10}$$

The bulk concentrations are determined by the above defect equilibria and the charge neutrality condition, which in CeO₂ is:

$$2c_{V_O^{\bullet\bullet},\infty} + c_{h^{\bullet},\infty} + |z_D| c_D = n_\infty + 2c_{O_i^{\bullet\bullet},\infty} + c_{O_i^{\bullet},\infty} + |z_A| c_A \quad \{12\}^{11}$$

In the most cases the individual defect concentrations are different by orders of magnitude. Therefore, the relationship can be simplified by setting all concentrations zero, with the exception of the largest one on each side of the equation. For each case this yields typical dependencies of the total effective conductivity σ_m ¹² on the temperature *T*, oxygen partial pressure pO_2 and acceptor and donor dopant levels c_A and c_D as shown in Table 1. These are the activation energy E_a , pO_2 dependence M_{pO_2} and dopant dependencies M_A and M_D , respectively:

⁹ K_S : equilibrium constant of the formation of singly charged oxygen interstitials,
 $c_{O_i^{\bullet},\infty}$: bulk concentration of singly charged oxygen interstitials

¹⁰ e : electron charge

¹¹ z_D (c_D): charge number (bulk concentration) of the donor dopant, z_A (c_A): charge number (bulk concentration) of the acceptor dopant

¹² At the moment it is sufficient to define the total effective conductivity σ_m as the sum over all bulk conductivity contributions $\sigma_{i,\infty}$. Furthermore, in Table 1, Fig. 3, Fig. 4 and Fig. 5 the smaller contributions are neglected resulting in $\sigma_m \approx \sigma_{V_O^{\bullet\bullet},\infty}$ or $\sigma_m \approx \sigma_{e^{\bullet},\infty}$ depending on the actual defect chemistry regime. However, as shown in more detail in section 2.2.3 this definition is not valid if boundary effects become significant since then σ_m (and its dependencies) can vary strongly from the bulk values.

Doping Content	Regime Number	Charge Neutrality Condition	Conductivity Type	Majority Charge Carrier	Dependencies of the Bulk Conductivity		
					pO_2 Dependence M_{pO_2}	Dopant Dependence M_A, M_D	Activation Energy E_a
nominally pure	(I)	$2c_{V_O^{\bullet\bullet}, \infty} = n_\infty$	electronic	$n_\infty = (2K_R)^{1/3} pO_2^{-1/6}$	$-1/6$	0	$\frac{1}{3}\Delta H_R + h_e$
	(II-a)	$2c_{V_O^{\bullet\bullet}, \infty} = z_A c_A$		$n_\infty = (2K_R)^{1/2} (z_A c_A)^{-1/2} pO_2^{-1/4}$	$-1/4$	$-1/2$	$\frac{1}{2}\Delta H_R + h_e$
acceptor doping	(II-b)			ionic ($V_O^{\bullet\bullet}$)	$c_{V_O^{\bullet\bullet}, \infty} = \frac{1}{2} z_A c_A$	0	1
	(III)			$n_\infty = z_D c_D$	0	1	h_e
donor doping	(IV)	$ z_D c_D = 2c_{O_i^{\bullet}, \infty}$	electronic	$n_\infty = \left(\frac{K_R}{2K_F}\right)^{1/2} (z_D c_D)^{1/2} pO_2^{-1/4}$	$-1/4$	$1/2$	$\frac{1}{2}(\Delta H_R - \Delta H_F) + h_e$
	(V)	$ z_D c_D = c_{O_i^{\bullet}, \infty}$		$n_\infty = \frac{K_R}{K_F K_S} \cdot z_D c_D \cdot pO_2^{-1/2}$	$-1/2$	1	$\Delta H_R - \Delta H_F - \Delta H_S + h_e$

Table 1: Defect Chemistry Regimes in CeO_2

ΔH_F : enthalpy of anti-Frenkel pair formation, ΔH_S : enthalpy of the formation of singly charged oxygen interstitials

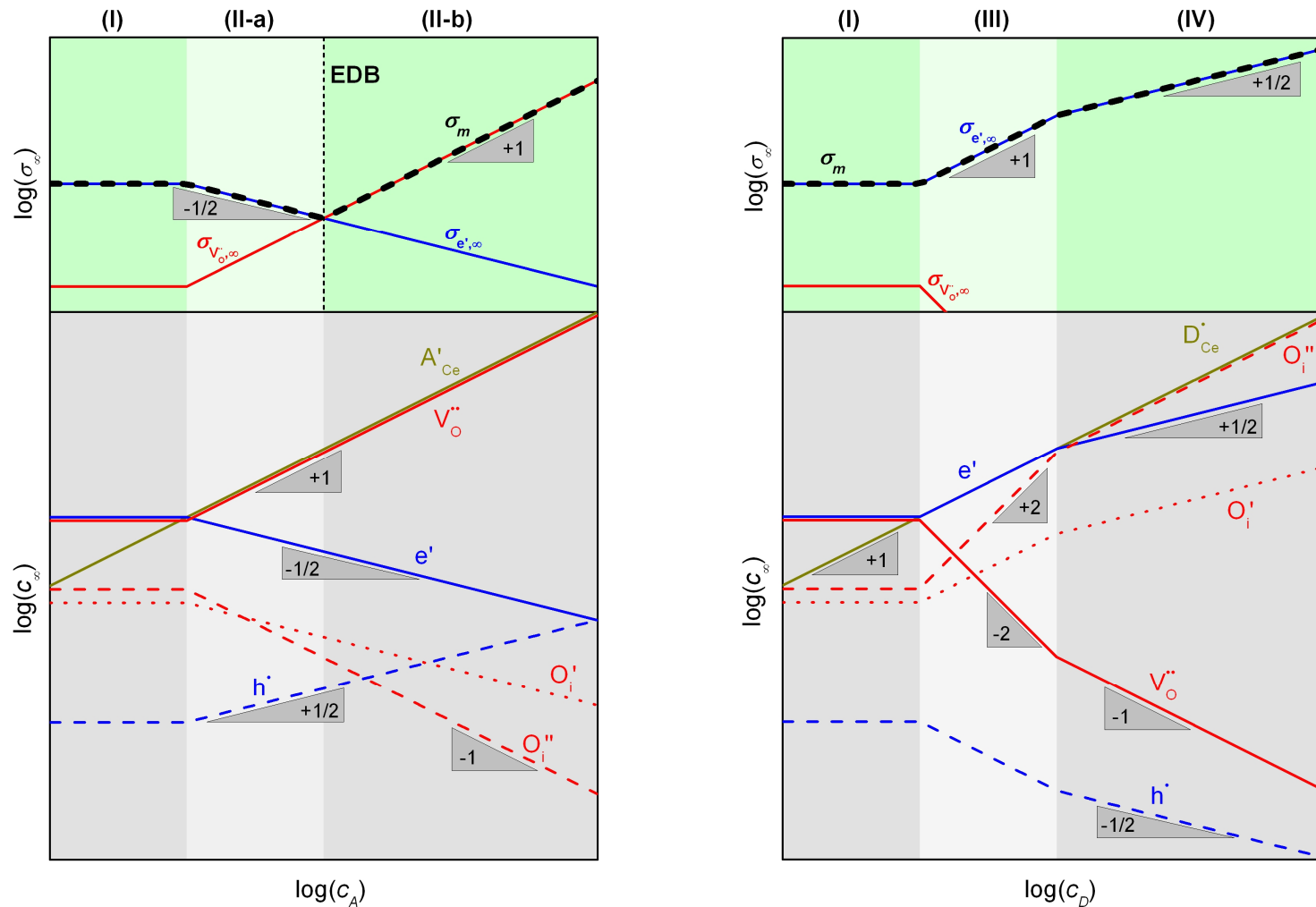


Fig. 3: Dopant Dependence Kröger-Vink Diagrams of Acceptor Doped (Left Panel) and Donor Doped CeO_2 (Right Panel)

Each panel consists of two charts. While the below (grey) chart is a classical Kröger-Vink diagram (e.g. a defect concentration plot), the above (green) chart is a qualitative plot of the corresponding conductivities of the electrons $\sigma_{e^{\bullet}, \infty}$ (red line) and the oxygen vacancies $\sigma_{V_{O}^{\bullet\bullet}, \infty}$ (blue line). The dashed black line shows the total effective conductivity σ_m .¹² A'_{Ce} : singly charged acceptor dopant on cerium site, D'_{Ce} : singly charged donor dopant on cerium site

Right Panel: Reprinted from Göbel et al.^[15] (Copyright 2012) with permission from Elsevier.

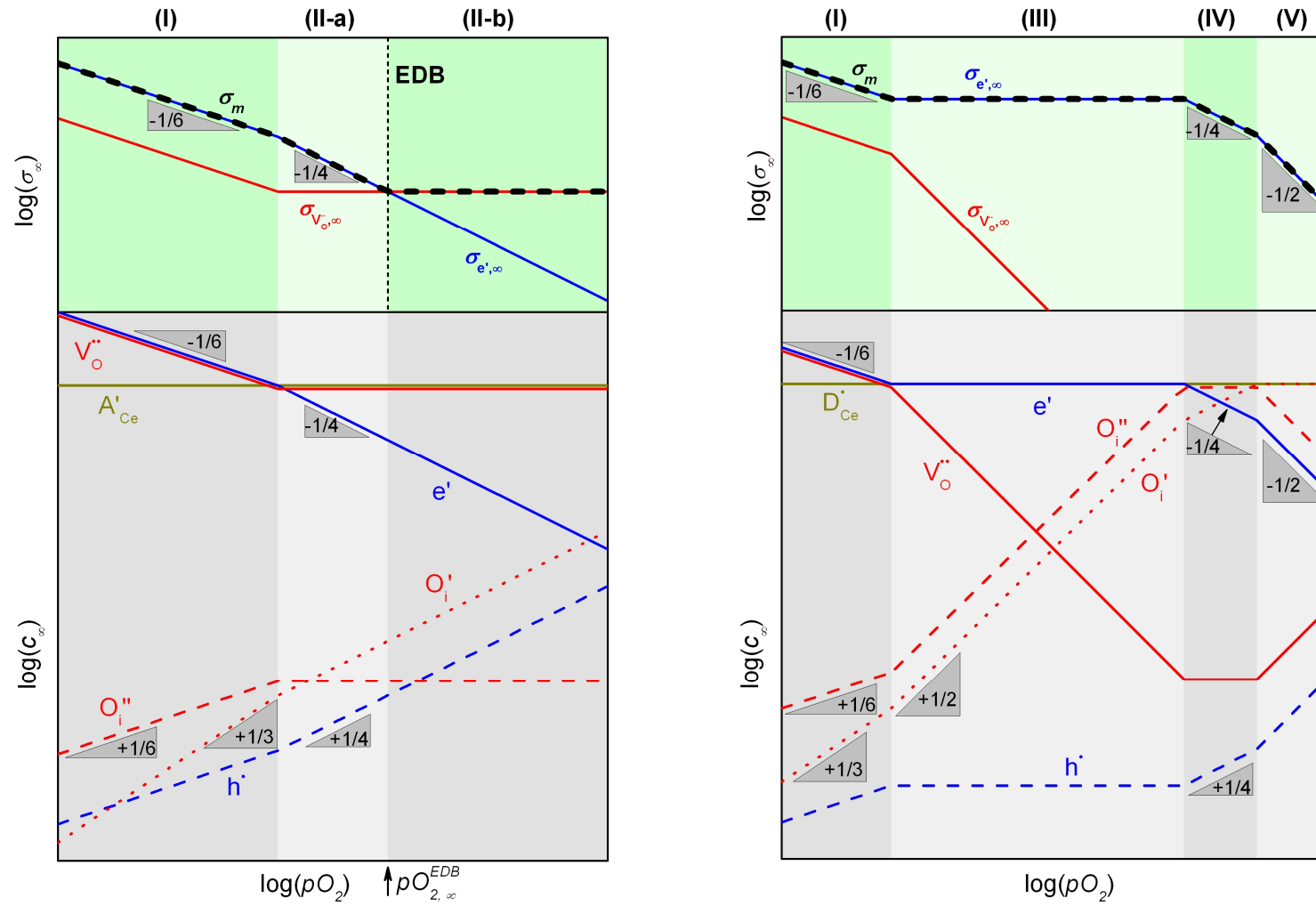


Fig. 4: pO_2 Dependence Kröger-Vink Diagrams of Acceptor Doped (Left Panel) and Donor Doped CeO_2 (Right Panel)

Each panel consists of two charts. While the below (grey) chart is a classical Kröger-Vink diagram (e.g. a defect concentration plot), the above (green) chart is a qualitative plot of the corresponding conductivities of the electrons $\sigma_{e',\infty}$ (red line) and the oxygen vacancies $\sigma_{V_{O}^{\bullet\bullet},\infty}$ (blue line). The dashed black line shows the total effective conductivity σ_m .¹² Right Panel: Reprinted from Göbel et al.^[15] (Copyright 2012) with permission from Elsevier.

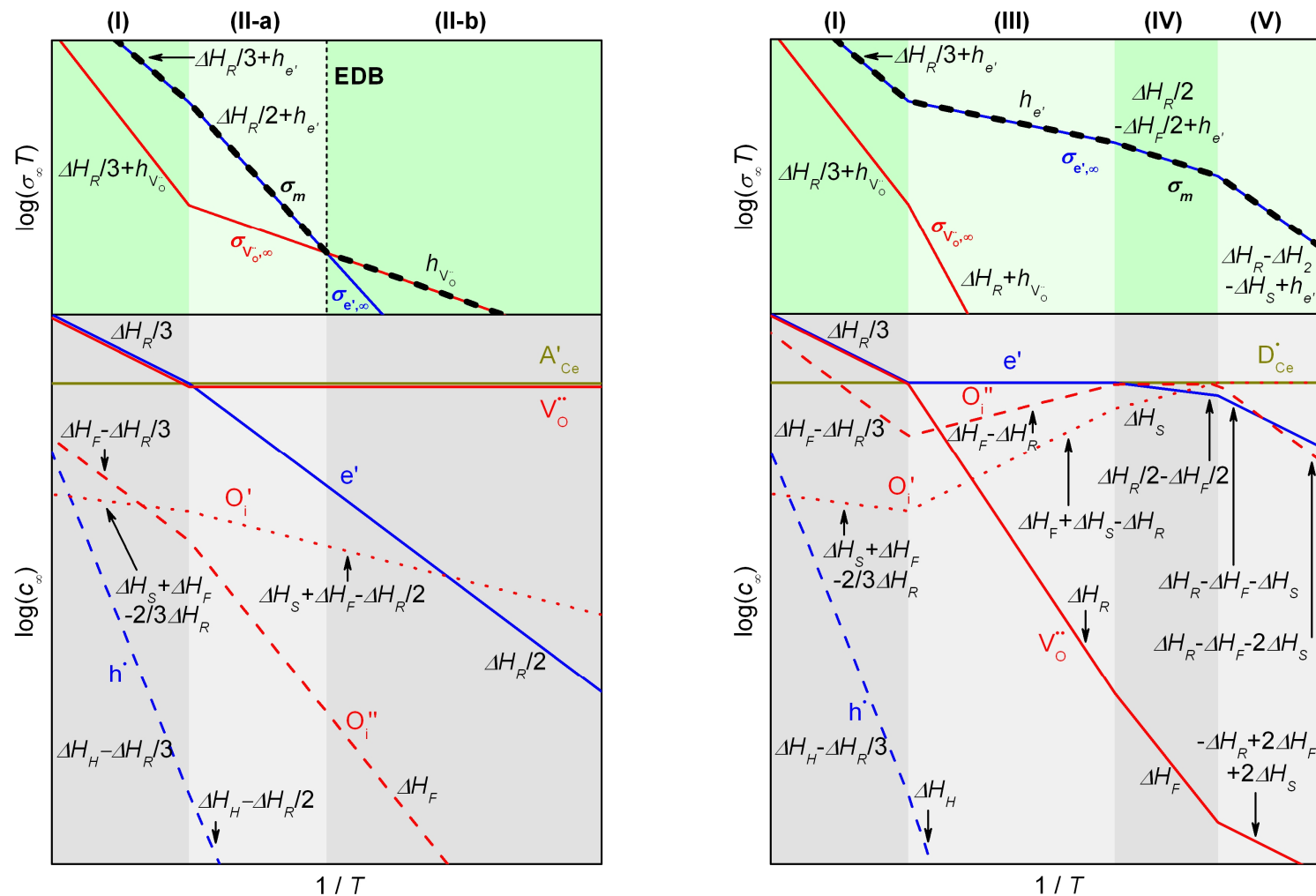


Fig. 5: Temperature Dependence Kröger-Vink Diagrams of Acceptor Doped (Left Panel) and Donor Doped CeO_2 (Right Panel)

Each panel consists of two charts. While the below (grey) chart is a classical Kröger-Vink diagram (e.g. a defect concentration plot), the above (green) chart is a qualitative plot of the corresponding conductivities of the electrons $\sigma_{e', \infty}$ (red line) and the oxygen vacancies $\sigma_{V_{\text{O}}^{\bullet\bullet}, \infty}$ (blue line). The dashed black line shows the total effective conductivity σ_m .¹² ΔH_H : enthalpy of the electron-hole formation

$$E_a = -k_B \frac{d \ln(\sigma_m T)}{d(T^{-1})} \quad \{13\}^{13}$$

$$M_{pO_2} = \frac{d \log(\sigma_m)}{d \log(pO_2)} \quad \{14\}^{13}$$

$$M_A = \frac{d \log(\sigma_m)}{d \log([Z_A]c_A)}, \quad M_D = \frac{d \log(\sigma_m)}{d \log([Z_D]c_D)} \quad \{15\}^{13}$$

In the experiment the given dependencies allow for the identification of the actual defect chemistry regime as shown later. For the temperature dependence of the equilibrium constants K and the defect mobilities u_i the following relations are relevant:

$$K = K_0 \cdot e^{-\frac{\Delta H}{k_B T}} \quad \{16\}^{14}$$

$$u_i = \frac{U_{i,0}}{T} e^{-\frac{h_i}{k_B T}} \quad \{17\}^{15}$$

Depending on the conditions either electrons or oxygen vacancies dominate the conductivity in ceria. Thereby the electrons are transported according to a small polaron hopping mechanism with an electron hopping energy h_e , between 0.2 and 0.6 eV.^[90, 91] The activation energy of the oxygen vacancy motion $h_{V_O^{\bullet\bullet}}$ is 0.7 eV for Gd doped ceria and changes slightly for other dopants.^[72, 92]

A good way to qualitatively illustrate the defect chemistry is the use of Kröger-Vink diagrams, such as Fig. 3 to Fig. 5. Here the concentrations are logarithmically plotted against dopant level, oxygen partial pressure and temperature using the relationships in Table 1. Note, however, that in reality at the borders of the defect chemistry regimes a smooth transition between the different dependencies is present.

2.1.4 The Electrolytic Domain Boundary in the Bulk

The electron mobility is orders of magnitudes larger than the ionic one. Therefore, pure ceria (regime (I) in Table 1) and even slightly acceptor doped ceria at high temperatures and low pO_2 (regime (II-a)) exhibits a mainly electronic conductivity. Only strongly acceptor doped ceria at low temperatures and high pO_2 (regime (II-b)) is a predominantly ionic conductor.

¹³ Instead of the effective conductivity σ_m also the effective conductance G_m can be used to determine E_a , M_{pO_2} , M_A and M_D since both quantities differ from each other only by a constant geometrical factor.

¹⁴ K_0 : pre exponential factor (K for $T \rightarrow \infty$), ΔH : reaction enthalpy, k_B : Boltzmann constant

¹⁵ $U_{i,0}$ (h_i): pre exponential factor (activation energy) of the mobility of an arbitrary CC i

Since only under the last mentioned conditions ceria can be used as a fuel cell electrolyte the border between defect chemistry regimes (II-a) and (II-b) is designated as the electrolytic domain boundary (EDB) and in this thesis the corresponding pO_2 value as $pO_{2,\infty}^{EDB}$. Here $pO_{2,\infty}^{EDB}$ in particular concerns the bulk properties of ceria; i.e. it is specifically the pO_2 where $\sigma_{e^{\bullet},\infty} = \sigma_{V_O^{\bullet\bullet},\infty}$ (see also sections 2.2.3.3 and 5.5).

2.2 Space Charge Effects

2.2.1 General Considerations

Whereas in the bulk the charge neutrality condition (e.g. eq. {12}) is strictly fulfilled, locally at the boundaries this is not necessarily the case. As an example, we can take the GBs in pure and acceptor doped CeO_2 which are known to consist of a positively charged GB core.^[10] The reason for this is an imbalance in the cation/anion stoichiometry (mostly a reduced oxide ion occupancy), which could directly be observed with high-resolution transmission electron microscopy (HRTEM) in other oxide materials (e.g. $BaTiO_3$ ^[93]). In the adjacent material the positive charge of the GB core Σ_{Core} is compensated by an enrichment of oppositely charged and a depletion and equally charged defects. The resulting local charge density ρ integrates to the total SCL charge Σ_{SCL} (see Fig. 6):

$$\Sigma_{SCL} = -\frac{1}{2} \Sigma_{Core} \quad \{18\}$$

$$\Sigma_{SCL} = \int_0^{\infty} \rho \cdot dx \quad \{19\}^{16}$$

This zone, in which the local charge neutrality condition is not valid, is the space charge layer. Of course not only charged GB cores are known to induce SCLs. They can also be formed on other interfaces such as heterojunctions and surfaces (see section 1.2).¹⁷

In any case the concentration profiles in the SCL follow the profile of the electric potential Φ . For clarity, here the bulk potential is defined as zero: $\Phi_{\infty} \equiv 0$. Generally, for an arbitrary defect i the electrochemical potential $\bar{\mu}_i$ is:

$$\bar{\mu}_i = \mu_i + z_i e \Phi = \mu_i^0 + k_B T \ln(a_i) + z_i e \Phi \quad \{20\}^{18}$$

¹⁶ x : distance to the interface

¹⁷ A prominent example of a strong SCL effect originating at heterojunctions is given in ref. ^[19].

¹⁸ μ_i (μ_i^0): chemical potential (chemical potential at standard conditions) of an arbitrary CC i

For small concentrations (i.e. no defect associations) the activities a_i can be replaced by concentrations. From the constancy of the electrochemical potential it follows for the local concentration c_i that:^[1, 94]

$$0 = k_B T \ln \frac{c_i}{c_{i,\infty}} + z_i e \Phi \quad \{21\}$$

$$\frac{c_i}{c_{i,\infty}} = e^{-\frac{z_i e}{k_B T} \Phi} \quad \text{and in particular} \quad \frac{c_{i,0}}{c_{i,\infty}} = e^{-\frac{z_i e}{k_B T} \Phi_0} \quad \{22\}$$

Here Φ_0 is the electric potential at the interface, which in the following is simply designated as SCL potential. $c_{i,0}$ is the concentration of CC i at the interface.

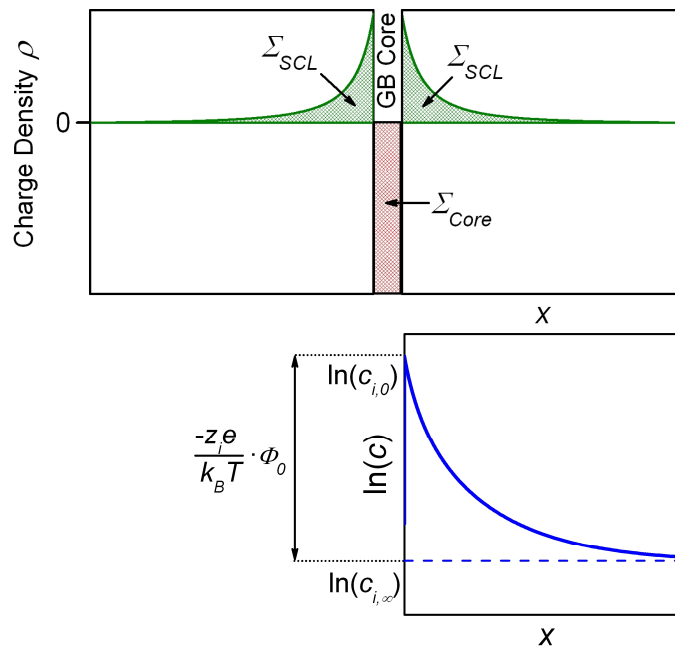


Fig. 6: Basic Characteristics of a Space Charge Layer at a Grain Boundary: the GB Core Charge Σ_{Core} , the SCL Charge Σ_{SCL} and the SCL Potential Φ_0

From eq. {22} it follows for two different kinds of mobile charge carriers h and i :^[1]

$$\frac{c_h}{c_{h,\infty}} = \left(\frac{c_i}{c_{i,\infty}} \right)^{z_h/z_i} \quad \{23\}$$

The enrichment or depletion of CCs changes the local charge density which again is linked to the electric potential via the Poisson equation (here given for one dimension):

$$\frac{d^2\Phi}{dx^2} = -\frac{\rho}{\varepsilon_r \varepsilon_0} \quad \{24\}^{19}$$

ρ can be divided in two contributions ρ_M and ρ_{IM} originating from mobile and immobile CCs, respectively:

$$\rho = \rho_M + \rho_{IM} \quad \text{with} \quad \rho_M = e \cdot \sum_{i=1}^{N_{Mobile}} (z_i c_i) \quad \text{and} \quad \rho_{IM} = e \cdot \sum_{j=1}^{N_{Immobile}} (z_{IM,j} c_{IM,j}) \quad \{25\}^{20}$$

Before solving the profile function let us focus on a useful rearrangement of eq. {24} concerning the electric field E :^[95]

$$\frac{d(E^2)}{dx} = \frac{d\left(\left(\frac{d\Phi}{dx}\right)^2\right)}{dx} = 2 \frac{d\Phi}{dx} \frac{d^2\Phi}{dx^2} = -\frac{2\rho}{\varepsilon_r \varepsilon_0} \frac{d\Phi}{dx} = -\frac{2}{\varepsilon_r \varepsilon_0} \left(\sum_{i=1}^{N_{Mobile}} \left(z_i e c_{i,\infty} e^{-\frac{z_i e}{k_B T} \Phi} \right) + \rho_{IM} \right) \frac{d\Phi}{dx} \quad \{26\}$$

The integration of eq. {26} from an arbitrary coordinate x_k to $+\infty$ with the conditions $\lim_{x \rightarrow +\infty} (E^2) = 0$ and $\lim_{x \rightarrow +\infty} (\Phi) = \Phi_\infty \equiv 0$ yields the relationship between the electric field at x_k , E_{x_k} , and the potential there Φ_{x_k} :^[95]

$$E_{x_k} = \text{sgn}(\Phi_{x_k}) \cdot \sqrt{\frac{2k_B T}{\varepsilon_r \varepsilon_0} \left(\sum_{i=1}^{N_{Mobile}} \left(c_{i,\infty} \left(e^{-\frac{z_i e}{k_B T} \Phi_{x_k}} - 1 \right) \right) - \frac{\rho_{IM}}{k_B T} \Phi_{x_k} \right)} \quad \{27\}$$

Here $\text{sgn}(\Phi_{x_k})$ is the signum function, which is +1 for $\Phi_{x_k} > 0$, 0 for $\Phi_{x_k} = 0$ and -1 for $\Phi_{x_k} < 0$. For $x_k = 0$ eq. {27} allows for the calculation of the electric field at the interface E_0 and, hence, for the determination of the SCL charge Σ_{SCL} :^[95]

$$\Sigma_{SCL} = -\varepsilon_r \varepsilon_0 E_0 = -\text{sgn}(\Phi_0) \cdot \sqrt{2\varepsilon_r \varepsilon_0 k_B T \left(\sum_{i=1}^{N_{Mobile}} \left(c_{i,\infty} \left(e^{-\frac{z_i e}{k_B T} \Phi_0} - 1 \right) \right) - \frac{\rho_{IM}}{k_B T} \Phi_0 \right)} \quad \{28\}$$

Eq. {28} is of major significance. It is not only the relationship between the two most relevant SCL characteristics Σ_{SCL} and Φ_0 , but also valid without further approximations for any case in which the CC profiles are either equilibrium profiles or constant, even if the profiles themselves are unknown. Additionally, it allows for the precise calculation of the conductivity effects in the Gouy-Chapman case (as explained in section 5.1.4.2.1).

¹⁹ ε_r : relative permittivity, ε_0 : vacuum permittivity

²⁰ N_{Mobile} ($N_{Immobile}$): number of mobile (immobile) defects, j : denominates an arbitrary immobile CC, $z_{IM,j}$ ($c_{IM,j}$): charge number (bulk concentration) of an arbitrary immobile CC j

2.2.2 Space Charge Layer Profiles

Eq. {22}, {24} and {25} result in the following differential equation:

$$\frac{d^2\Phi}{dx^2} = -\frac{e}{\varepsilon_r\varepsilon_0} \left(\sum_{i=1}^{N_{Mobile}} \left(z_i c_{i,\infty} e^{-\frac{z_i e}{k_B T} \Phi} \right) + \rho_{IM} \right) \quad \{29\}$$

Eq. {29} can analytically be solved for two ideal cases only.^[1] The defect chemistry of the first case, the Mott-Schottky (MS) case, is characterized by an immobile dopant CC and a mobile CC which is depleted at the SCL. Hence, here the charge density in the SCL is given by the dopant level: $\rho \approx \rho_{IM} = z_{Dop} e c_{Dop}$.^{21, 22}

$$\text{MS case:} \quad \frac{d^2\Phi}{dx^2} = -\frac{z_{Dop} e c_{Dop}}{\varepsilon_r \varepsilon_0} \quad \{30\}$$

In the second case, the Gouy-Chapman (GC) case, all the CCs follow the potential and the SCL defect chemistry is dominated by an enrichment of one CC: $\rho \approx z_{maj} e c_{maj}$.

$$\text{GC case:} \quad \frac{d^2\Phi}{dx^2} = -\frac{z_{maj} e c_{maj,\infty}}{\varepsilon_r \varepsilon_0} e^{-\frac{z_{maj} e}{k_B T} \Phi} \quad \{31\}$$

Here the index *maj* designates the enriched (majority) CC. The index *depl* will be used to designate the depleted CC. Note that both cases are merely approximations for strong depletion and enrichment effects since only then the neglect of the further CCs is realistic. There is only one exception for which eq. {29} can be analytically solved for two CCs. This is the so called symmetrical GC case which is valid for two intrinsic charge carriers with $z_{depl} = -z_{maj}$ and $c_{depl,\infty} = c_{maj,\infty}$:

$$\text{symmetrical GC case:} \quad \frac{d^2\Phi}{dx^2} = -\frac{e}{\varepsilon_r \varepsilon_0} \left(z_{maj} c_{maj,\infty} e^{-\frac{z_{maj} e}{k_B T} \Phi} - z_{maj} c_{maj,\infty} e^{\frac{z_{maj} e}{k_B T} \Phi} \right) \quad \{32\}$$

The solutions of eq. {30} to {32} are:^{23 [1, 94]}

$$\text{MS case:} \quad \Phi = -\frac{z_{Dop} e c_{Dop}}{2\varepsilon_r \varepsilon_0} (x - \lambda^*)^2, \quad \lambda^* = \sqrt{-\frac{2\varepsilon_r \varepsilon_0 \Phi_0}{z_{Dop} e c_{Dop}}}, \quad x < \lambda^* \quad \{33\}$$

²¹ z_{Dop} (c_{Dop}): charge number (bulk concentration) of the either acceptor or donor dopant,
 $z_{Dop} c_{Dop} \equiv z_{ACA} + z_{DCD}$

²² Note that not for all experimental conditions the dopant may be considered as immobile. This ($\rho_{IM} = z_{Dop} e c_{Dop}$) is an assumption specifically made in the MS case.

²³ under the boundary conditions $\Phi_{x=\lambda^*} = 0$ for the MS case, $\lim_{x \rightarrow +\infty} (\Phi) = \Phi_\infty = 0$ for the symmetrical GC case and $\Phi_{x=0} = \Phi_0$ for all cases

$$\text{GC case:} \quad \Phi = \Phi_0 + \frac{2k_B T}{z_{maj} e} \ln \left(1 + \frac{x}{2\lambda} e^{-\frac{z_{maj} e}{2k_B T} \Phi_0} \right), \quad \lambda = \sqrt{\frac{\epsilon_r \epsilon_0 k_B T}{2z_{maj}^2 e^2 c_{maj, \infty}}}, \quad x < 2\lambda \quad \{34\}$$

$$\text{symmetrical GC case:} \quad \Phi = -\frac{2k_B T}{z_i e} \ln \left(\frac{1 + \mathcal{G}_i \cdot e^{-\frac{x}{\lambda}}}{1 - \mathcal{G}_i \cdot e^{-\frac{x}{\lambda}}} \right), \quad \mathcal{G}_i = \frac{e^{-\frac{z_i e}{2k_B T} \Phi_0} - 1}{e^{-\frac{z_i e}{2k_B T} \Phi_0} + 1} \quad \{35\}^{24}$$

The concentration profiles are obtained by inserting eq. {33}-{35} in eq. {22}. While the SCL profiles are continuous and have no fixed length, the quantities λ^* (screening length in the MS case) and 2λ (λ : Debye length) roughly correspond to the extent of the SCL. That means specifically that at $x = \lambda^*$ or $x = 2\lambda$ the potential becomes zero or at least very small. Both cases (MS and GC) have in common that the extent of the SCL decreases with increasing bulk concentrations. However, the shape of the SCL varies considerably between the MS and GC case.

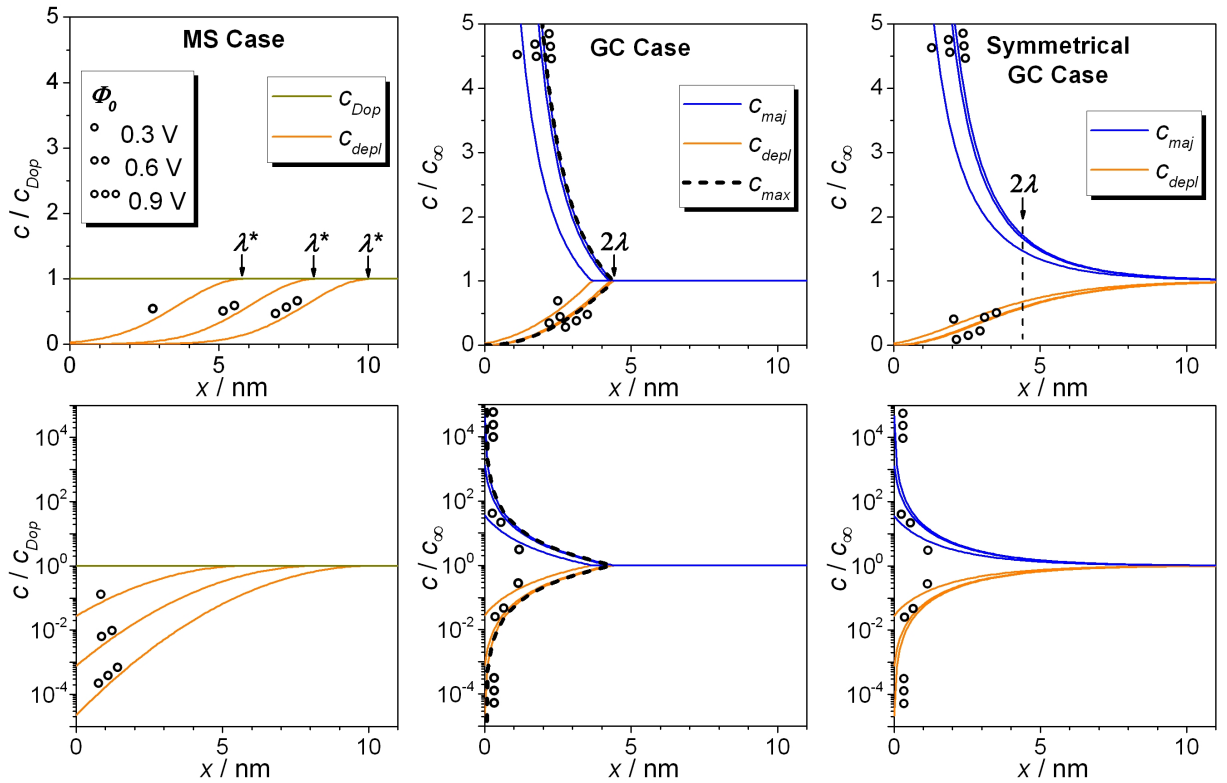


Fig. 7: Example SCL Concentration Profiles Calculated Using the Analytical Approach

The SCL profiles are plotted for three potential values (0.3, 0.6 and 0.9 V) in a linear (above) and logarithmic plot (below).

Parameters: general: $\epsilon_r = 26$, $\theta = 700$ °C, $z_{maj} = z_{Dop} = -z_{depl} = -1$ / GC case: $c_{maj, \infty} = c_{depl, \infty} = 1.25 \cdot 10^{19}$ cm⁻³, $c_{Dop} = 0$ / MS case: $c_{depl, \infty} = c_{Dop} = 1.25 \cdot 10^{19}$ cm⁻³

²⁴ \mathcal{G}_i : degree of influence of an arbitrary CC i (symmetrical GC case)

This can be easily explained under consideration of how the GB core charge is shielded by the SCLs. In the MS case even for a large depletion effect the charge density cannot surpass $z_{Dop}eC_{Dop}$. Therefore, an increasing GB core charge (corresponding to an increase in Φ_0) can only be shielded by increasing the SCL extent λ^* . In the GC case, however, large GB core charges can easily be shielded by enriching the mobile defect close to the interface. As a matter of fact, a rearrangement of eq. {34} shows that for each coordinate x the concentration cannot surpass a certain value c_{max} :

$$c_{maj} < c_{max} = c_{maj,\infty} \cdot \left(\frac{2\lambda}{x}\right)^2, \text{ for } x < 2\lambda \quad \{36\}$$

The limit of eq. {36} as x approaches 0 is infinity. Hence, for strong enrichments nearly the whole SCL charge will be accumulated very close to the interface. As a result, in contrast to the MS case in the GC case the SCL profiles are very steep and the SCL extent 2λ is independent of Φ_0 .

2.2.3 Conductivity Effects

2.2.3.1 Effective Conductivity Values

In polycrystalline samples with SCLs the overall effective resistance R_m often varies considerably from what is expected from the bulk values. Generally, to R_m a corresponding total effective conductivity value σ_m can be assigned:

$$\sigma_m = J \cdot \frac{1}{R_m} \quad \{37\}^{25}$$

Usually, more than one CC contributes to σ_m and for each individual CC an effective conductivity contribution $\sigma_{i,m}$ can be defined:

$$\sigma_m = \sum_{i=1}^{N_{Mobile}} \sigma_{i,m} \quad \{38\}$$

To conveniently quantify the relative effect of the SCLs on the conductivity it is practical to use conductivity values s , which are normalized with regard to the bulk value:

$$s = \frac{\sigma}{\sigma_\infty} \quad \text{and specifically} \quad s_{i,m} = \frac{\sigma_{i,m}}{\sigma_{i,\infty}} \quad \{39\}$$

The SCL alignment with respect to the direction of electrical transport is crucial. For the case discussed here, namely non-overlapping SCLs and sufficiently large grains, in good

²⁵ J : geometrical factor depending on the sample dimensions (for the thin films $J = l_1/(l_2 \cdot L)$, see Fig. 15)

approximation only the parallelly aligned SCLs contribute to a conductivity increase in a polycrystalline material ($\sigma_{i,m} \approx \sigma_{i,m}^{\parallel}$ {40},²⁶ if CC i is enriched in the SCLs), whereas only the perpendicularly aligned SCLs contribute to a decrease in conductivity ($\sigma_{i,m} \approx \sigma_{i,m}^{\perp}$ {41},²⁶ if CC i is depleted in the SCLs).

Hereby the $\sigma_{i,m}^{\parallel}$ ($\sigma_{i,m}^{\perp}$) value contains two contributions: (1) the bulk conductivity $\sigma_{i,\infty}$ and (2) the effective conductivity change due to SCL effects at the parallel (perpendicular) GBs $\Delta\sigma_{i,m}^{\parallel}$ ($\Delta\sigma_{i,m}^{\perp}$):

$$\sigma_{i,m}^{\parallel} = \sigma_{i,\infty} + \Delta\sigma_{i,m}^{\parallel}, \quad s_{i,m}^{\parallel} = 1 + \Delta s_{i,m}^{\parallel} \quad \left(\text{with } s_{i,m}^{\parallel} = \sigma_{i,m}^{\parallel} / \sigma_{i,\infty} \text{ and } \Delta s_{i,m}^{\parallel} = \Delta\sigma_{i,m}^{\parallel} / \sigma_{i,\infty} \right) \{42\}$$

In contrast to the parallel GBs the perpendicular GBs are electrically connected in series with the bulk (see also Fig. 8). Therefore, here the resistivities σ^{-1} have to be added up:

$$(\sigma_{i,m}^{\perp})^{-1} = \sigma_{i,\infty}^{-1} + (\Delta\sigma_{i,m}^{\perp})^{-1}, \quad (s_{i,m}^{\perp})^{-1} = 1 + (\Delta s_{i,m}^{\perp})^{-1} \quad \left(\text{with } s_{i,m}^{\perp} = \sigma_{i,m}^{\perp} / \sigma_{i,\infty} \text{ and } \Delta s_{i,m}^{\perp} = \Delta\sigma_{i,m}^{\perp} / \sigma_{i,\infty} \right) \{43\}$$

2.2.3.2 Conductivity Pathways in Cerium Oxide

Let us now consider how these general definitions apply to the specific case of CeO₂ thin films. Here oxygen vacancies $V_{\text{O}}^{\bullet\bullet}$ and electrons e' contribute to the total effective conductivity:

$$\sigma_m = \sigma_{V_{\text{O}}^{\bullet\bullet},m} + \sigma_{e',m} \quad \{44\}$$

The effective oxygen vacancy and electron conductivities $\sigma_{V_{\text{O}}^{\bullet\bullet},m}$ and $\sigma_{e',m}$ again consist (1) of bulk contributions $\sigma_{V_{\text{O}}^{\bullet\bullet},\infty}$ and $\sigma_{e',\infty}$ and (2) of conductivity changes at the parallel (perpendicular) GBs $\Delta\sigma_{V_{\text{O}}^{\bullet\bullet},m}^{\parallel}$ and $\Delta\sigma_{e',m}^{\parallel}$ ($\Delta\sigma_{V_{\text{O}}^{\bullet\bullet},m}^{\perp}$ and $\Delta\sigma_{e',m}^{\perp}$). However, depending on defect chemistry regime (Table 1), microstructure and SCL potential usually only one or a few of the above quantities significantly contribute to σ_m . Specifically, for CeO₂ thin films seven cases can be distinguished:

- (i) For epitaxial, strongly acceptor doped films the conductivity is given by the ionic bulk value:

$$\sigma_m = \sigma_{V_{\text{O}}^{\bullet\bullet},\infty} \quad \{45\}$$

- (ii) In a polycrystalline, acceptor doped sample with low and moderate positive SCL potentials the oxygen vacancies are depleted at the GBs. Hence, the perpendicular GBs block the ionic transport and $\Delta\sigma_{V_{\text{O}}^{\bullet\bullet},m}^{\perp}$ becomes significant.

²⁶ $\sigma_{i,m}^{\parallel}$ ($\sigma_{i,m}^{\perp}$): effective conductivity of an arbitrary CC i comprising its bulk conductivity and the conductivity change at the parallel (perpendicular) GBs

$$\sigma_m = \sigma_{V_o^{\bullet\bullet},m}^{\perp} = \frac{\sigma_{V_o^{\bullet\bullet},\infty} \cdot \Delta\sigma_{V_o^{\bullet\bullet},m}^{\perp}}{\sigma_{V_o^{\bullet\bullet},\infty} + \Delta\sigma_{V_o^{\bullet\bullet},m}^{\perp}} \quad \{46\}$$

By comparing epitaxial and polycrystalline films the values of $\Delta\sigma_{V_o^{\bullet\bullet},m}^{\perp}$ and $sv_{V_o^{\bullet\bullet},m}^{\perp} = \sigma_{V_o^{\bullet\bullet},m}^{\perp} / \sigma_{V_o^{\bullet\bullet},\infty}$ can be determined. The $sv_{V_o^{\bullet\bullet},m}^{\perp}$ values allow for the calculation of the SCL potential (as explained below, Table 7).

- (iii) For a positive SCL potential the electrons are enriched at the GBs. Therefore, if the SCL potential increases compared with case (ii) (or the acceptor doping content decreases) the increase of electronic conductivity at the parallel GBs becomes perceptible:

$$\sigma_m = \sigma_{V_o^{\bullet\bullet},m}^{\perp} + \sigma_{e',m}^{\parallel} = \frac{\sigma_{V_o^{\bullet\bullet},\infty} \cdot \Delta\sigma_{V_o^{\bullet\bullet},m}^{\perp}}{\sigma_{V_o^{\bullet\bullet},\infty} + \Delta\sigma_{V_o^{\bullet\bullet},m}^{\perp}} + \Delta\sigma_{e',m}^{\parallel} + \sigma_{e',\infty} \quad \{47\}$$

Under the assumption of a constant SCL potential as experimentally observed in ceria^[10] only the electronic contribution is pO_2 dependent (see Table 1, defect chemistry regimes (II-a) and (II-b)). This allows for the determination of $\sigma_{e',m}^{\parallel}$ by measuring the pO_2 dependence of the conductivity and separating constant and varying contributions. The ionic and electronic conductivity pathways in acceptor doped ceria are illustrated in Fig. 8.

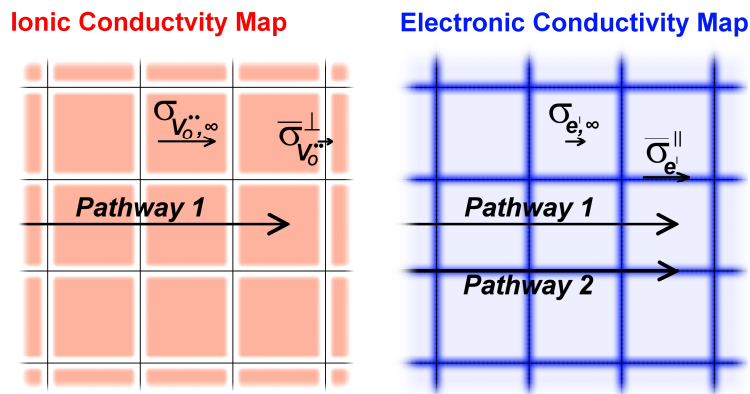


Fig. 8: Idealized Conductivity Maps of Polycrystalline, Acceptor Doped CeO₂

The ionic conductivity is blocked at the GBs, whereas the electronic one is increased there. As a consequence, the bulk pathway (pathway 1) is dominated by the GB conductivity for the oxygen vacancies and by the bulk conductivity for the electrons. Additionally, for the electrons a second, even more efficient transport pathway is available via the conductive parallel GBs (see eq. {47}).

$\bar{\sigma}_{V_o^{\bullet\bullet}}^{\perp}$ and $\bar{\sigma}_{e'}^{\parallel}$ are the local mean oxygen vacancy and electron conductivities in the SCLs as explained below in section 0.

Reproduced from Göbel et al.^[16] by permission of the PCCP Owner Societies.

- (iv) An even higher SCL potential or lower acceptor dopant level (or pure or donor doped material) may result in a conductivity dominated by the electronically shortcutting SCLs:

$$\sigma_m = \sigma_{e',m}^{\parallel} = \sigma_{e',\infty} + \Delta\sigma_{e',m}^{\parallel} \quad \{48\}$$

- (v) Epitaxial, slightly acceptor doped films are characterized by a mixed ionic, electronic bulk conductivity:

$$\sigma_m = \sigma_{V_0^{\bullet\bullet},\infty} + \sigma_{e',\infty} \quad \{49\}$$

As in case (iii) the ionic and electronic contributions can be separated by measuring the pO_2 dependence of the conductivity.

- (vi) Epitaxial, pure and donor doped films exhibit the electronic bulk conductivity:

$$\sigma_m = \sigma_{e',\infty} \quad \{50\}$$

- (vii) For donor doped CeO_2 electronically blocking GBs were found to be decisive which can be described with eq. {51} (see section 5.6):

$$\sigma_m = \sigma_{e',m}^{\perp} = \frac{\sigma_{e',\infty} \cdot \Delta\sigma_{e',m}^{\perp}}{\sigma_{e',\infty} + \Delta\sigma_{e',m}^{\perp}} \quad \{51\}$$

2.2.3.3 The Electrolytic Domain Boundary in Polycrystalline Material

Since due to SCL effects at GBs the effective ionic and electronic conductivity contributions are changed in polycrystalline material also the pO_2 value of the electrolytic domain boundary (EDB) is shifted. Therefore, in analogy to $pO_{2,\infty}^{EDB}$ (which is the pO_2 where $\sigma_{e',\infty} = \sigma_{V_0^{\bullet\bullet},\infty}$, see section 2.1.4) it is useful to define an EDB value $pO_{2,m}^{EDB}$ which describes the pO_2 where the effective conductivity contributions are equal: $\sigma_{e',m} = \sigma_{V_0^{\bullet\bullet},m}$.

In defect chemistry regimes (II-a) and (II-b) the pO_2 dependence M_{pO_2} of the electronic conductivity is $-1/4$ while the ionic conductivity is pO_2 independent (left panel of Fig. 4). Therefore, an increase in the ratio $s_{e',m}/s_{V_0^{\bullet\bullet},m}$ by *one* order of magnitude will result in an increase of $pO_{2,m}^{EDB}$ by *four* orders of magnitude compared with the bulk value $pO_{2,\infty}^{EDB}$:

$$pO_{2,m}^{EDB} = \left(\frac{s_{e',m}}{s_{V_0^{\bullet\bullet},m}} \right)^4 \cdot pO_{2,\infty}^{EDB} \quad \{52\}$$

Hence, even a small change of $s_{e',m}/s_{V_0^{\bullet\bullet},m}$ results in a large change of $pO_{2,m}^{EDB}$. Moreover, in a nanocrystalline material $s_{e',m}/s_{V_0^{\bullet\bullet},m}$ strongly increases with intensifying GB effects (often by many orders of magnitude) since (1) the electronic conductivity is increased at the GBs while (2) the ionic conductivity is decreased there. The resulting considerable shift of the EDB makes it an ideal quantity to detect SCL effects as it will be demonstrated in section 5.5.

2.2.3.4 Analytical Solutions

Let us now consider how to quantify the SCL effects. The conductivity change of an arbitrary CC i at the parallel SCLs can be expressed as a function of its contribution Σ_i on the total SCL charge:

$$\Sigma_i = z_i e \int_0^{\infty} (c_i - c_{i,\infty}) \cdot dx \quad \{53\}$$

$$\Sigma_{SCL} = \sum_{i=1}^{N_{Mobile}} (\Sigma_i) \quad \{54\}$$

Concerning the blocking effect of the perpendicular SCLs a similar quantity Ω_i , which represents a normalized resistance, can be defined:

$$\Omega_i \equiv \frac{1}{|z_i| e} \int_0^{\infty} (c_i^{-1} - c_{i,\infty}^{-1}) \cdot dx \quad \{55\}$$

In approximation the arrangement of grains can be described using the brick layer model. Here the grains are shaped cubically with a uniform grain size d .²⁷ In a single grain the enrichment of CC i incorporates an absolute excess charge of $d^2 \Sigma_i$ for each SCL. This corresponds to a change in the absolute number of CC i by $d^2 \Sigma_i / (z_i e)$ and to a variation of its average concentration by $(d^2 \Sigma_i / (z_i e)) / d^3 = \Sigma_i / (z_i e d)$. Hence, for each parallel SCL the effective conductivity change $\Delta \sigma_{i,m}^{\parallel}$ is $z_i / |z_i| \cdot u_i \Sigma_i / d$ (see eq. {11}). For the same reasoning, $(\Delta \sigma_{i,m}^{\perp})^{-1}$ is equal to $u_i^{-1} \cdot \Omega_i / d$ for each perpendicular SCL. Therefore, if the density of the parallel (perpendicular) SCLs is expressed as a geometry factor Γ^{\parallel} (Γ^{\perp}), it follows:

$$\Delta \sigma_{i,m}^{\parallel} = \Gamma^{\parallel} \cdot \frac{z_i}{|z_i|} u_i \Sigma_i \quad \text{and} \quad \Delta \sigma_{i,m}^{\perp} = \left(\Gamma^{\perp} \cdot \frac{\Omega_i}{u_i} \right)^{-1} \quad \{56\}$$

$$s_{i,m}^{\parallel} = \Gamma^{\parallel} \cdot \frac{\Sigma_i}{z_i e c_{i,\infty}} + 1 \quad \text{and} \quad s_{i,m}^{\perp} = \left(\Gamma^{\perp} \cdot |z_i| e c_{i,\infty} \cdot \Omega_i + 1 \right)^{-1} \quad \{57\}$$

The geometry factors of a polycrystalline pellet (cubic grains with 4 parallel and 2 perpendicular SCLs) and also for other geometries (as they are usually found in thin films) are listed in Table 2.

Consequently, the quantification of the conductivity effects coincides to the determination of Σ_i and Ω_i . For this the appropriate potential profile (e.g. eq. {33}-{35}) needs to be inserted in eq. {22} and then integrated (eq. {53} and {55}). The so obtained analytical solutions in the literature (e.g. ref. [22]) are given in Table 6 (page 55). Note, however, that the relationships for the conductivity effects as they are given in the literature in many cases base on more or less strong simplifications which have been found to result in a limited preciseness and, hence, a reduced reliability of them (see also section 5.1.4). Therefore, new, improved and much more

²⁷ See also Fig. 8, which illustrates the brick layer model in acceptor doped ceria. In this figure, however, for clarity the third dimension is not depicted.

precise analytical solutions have been developed in the framework of this PhD project which are listed in Table 7 (page 65). Further information on how these relationships are derived is given in section 5.1.4.2.

Geometry	Density of Parallel SCLs Γ^{\parallel}		Density of Perpendicular SCLs Γ^{\perp}	
pellet	$\frac{4}{d}$	{58}	$\frac{2}{d}$	{59}
thin film with polycrystalline, columnar microstructure, in-plane measurement	$\frac{2}{d}$	{60}	$\frac{2}{d}$	{61}
thin film with polycrystalline, columnar microstructure, perpendicular measurement	$\frac{4}{d}$	{62}	0	{63}
thin film with epitaxial multilayers, in-plane measurement	$\frac{2}{d_{ML}}$	{64}	0	{65}
thin film with epitaxial multilayers, perpendicular measurement	0	{66}	$\frac{2}{d_{ML}}$	{67}
epitaxial thin film with SCL at the FSI (or at the film surface), in-plane measurement	$\frac{1}{L}$	{68}	0	{69}

Table 2: The Brick Layer Model Applied to Several Sample Geometries

d_{ML} : thickness of an individual multilayer, L : thickness of the thin film

In-plane and perpendicular measurement configurations:

For an in-plane measurement of a thin film the two electrodes are positioned on the same surface of the film as shown in Fig. 15. On the contrary, in a perpendicular configuration the electrodes are applied on the two opposite sides of the film. The distance between the electrodes is then the thin film thickness L . In this study the in-plane configuration was applied.

2.2.3.5 Local Mean Conductivities

Last but not least, beside the effective conductivities also the local mean conductivities in the parallel (perpendicular) SCLs $\bar{\sigma}_i^{\parallel}$ ($\bar{\sigma}_i^{\perp}$) can be used to quantify the conductivity effects. They are connected with the effective values via the following relationship:^[1, 2]

$$\Delta\sigma_{i,m}^{\parallel} = \beta_L^{\parallel} \varphi_L \bar{\sigma}_i^{\parallel} \quad \text{and} \quad (\Delta\sigma_{i,m}^{\perp})^{-1} = \beta_L^{\perp} \varphi_L (\bar{\sigma}_i^{\perp})^{-1} \quad \{70\}^{28}$$

²⁸ φ_L : volume fraction of all SCLs, β_L^{\parallel} (β_L^{\perp}): fraction of the parallelly (perpendicularly) aligned SCLs on all SCLs, in the brick layer model $\beta_L^{\parallel} = 2/3$ and $\beta_L^{\perp} = 1/3$

However, for the practical interpretation of measurement data the effective conductivity values are more useful than the local mean values since (1) they can be derived from the measured resistances easily and since (2) in contrast to $\bar{\sigma}_i^{\parallel}$ and $\bar{\sigma}_i^{\perp}$ their calculation does not incorporate the somewhat ambiguous value of the extent of the (more or less diffuse) SCLs. Therefore, in the following the effective quantities are applied.

Chapter 3

Modeling

3.1 Numerical Calculation of Space Charge Layer Profiles

While the analytical solutions are well able to describe SCL effects for the ideal MS and GC cases, for other more intricate situations, such as mixed cases, they are of limited accuracy only. It is, however, possible to model these cases numerically. This section deals with the basics of the numerical approach.²⁹

In the numerical approach the SCL profiles are determined by a stepwise calculation of the potential Φ . Let us here use the subscripts k and x_k to designate an arbitrary calculation step and the x coordinate at this step, respectively.

At the beginning of each calculation step the local potential there Φ_{x_k} is known (for the very first step at $x=0$ the potential is set equal to the given value of Φ_0). Using the Φ_{x_k} value the concentrations c_{i,x_k} , charge density ρ_{x_k} and electric field E_{x_k} are calculated with eq. {22}, {25} and {27}, respectively. To initialize the next step $k+1$ the x coordinate is increased by an increment Δx_k :

$$x_{k+1} = x_k + \Delta x_k \quad \{71\}$$

The potential at x_{k+1} is then determined with a Taylor expansion of degree three:

$$\Phi_{x_{k+1}} \approx \Phi_{x_k} - \Delta x_k \cdot E_{x_k} - \frac{\Delta x_k^2}{2\epsilon_r \epsilon_0} \left(\rho_{x_k} + \frac{\Delta \rho_{x_{k-1}}}{3} \right) \quad \{72\}^{30}$$

$$\Delta \rho_{x_{k-1}} \equiv \rho_{x_k} - \rho_{x_{k-1}} \quad \{73\}^{30}$$

Subsequently, using the value of $\Phi_{x_{k+1}}$ the calculation of $c_{i,x_{k+1}}$, $\rho_{x_{k+1}}$ and $E_{x_{k+1}}$ follows, et cetera. This cycle is repeated until the potential becomes insignificantly close to zero.

²⁹ Note, that a more detailed description is given in ref.^[96] and the supplementary information therein.

³⁰ $\Delta \rho_{x_{k-1}}$: difference in charge density between the current calculation step k and the previous one $k-1$ (for the first step $\Delta \rho_{x_{k-1}}$ is set equal to zero)

Special care has to be taken for choosing appropriate increment values Δx . Due to the often very steep profile functions k an independent Δx value is inappropriate and leads to a rather large uncertainty. A much better approach is the definition of a fixed number of calculation steps N_{Steps} and the selection of local Δx_k values which fulfill the condition of a constant charge contribution $\Delta \Sigma_{Step}$ (on the total SCL charge Σ_{SCL}) between x_k and $x_k + \Delta x_k$:

$$\Delta x_k = \left| \frac{\Delta \Sigma_{Step}}{\rho_{x_{k-1}}} \right| \quad \text{with} \quad \Delta \Sigma_{Step} \equiv \frac{\Sigma_{SCL}}{N_{Steps}} \quad \{74\}$$

Especially close to the interface the use of eq. {74} leads to a very low calculation uncertainty.

The preciseness can be improved even further by switching to a different selection algorithm of Δx for the second half of the calculation (e.g. after about $N_{Steps}/2$ calculation steps). Hereby, it is useful to define a final potential Φ_{End} close to zero after which the calculation shall stop using the criterion that the local concentration there c_{End} differs only insignificantly from the bulk value (here by a factor of $|(c_{End} - c_\infty)/c_\infty| = 10^{-7}$):

$$\Phi_{End} \equiv \text{sgn}(\Phi_0) \cdot \left| \frac{k_B T}{z_{max} e} \ln \left(\frac{c_{End}}{c_\infty} \right) \right| \quad \{75\}^{31}$$

This allows for the calculation of a coefficient b' which is then used to decrease Φ until it reaches Φ_{End} .

$$b' \equiv \left(\frac{\Phi_{End}}{\Phi_{x_{k-1}}} \right)^{\frac{1}{N_{Steps} - k}} \quad \{76\}$$

$$\Phi_{k+1} = b' \cdot \Phi_k \quad \{77\}$$

The corresponding increments Δx_k can be calculated using a rearrangement of eq. {72}:

$$\Delta x_k = \frac{\varepsilon_r \varepsilon_0}{\rho_{x_k} + \frac{\Delta \rho_{x_{k-1}}}{3}} \cdot \left(-E_{x_k} \pm \sqrt{E_{x_k}^2 - \frac{2}{\varepsilon_r \varepsilon_0} (\Phi_{x_{k+1}} - \Phi_{x_k}) \left(\rho_{x_k} + \frac{\Delta \rho_{x_{k-1}}}{3} \right)} \right) \quad \{78\}^{32}$$

Fig. 9 shows SCL profiles obtained with the numerical calculations. The comparison with the analytical solutions (Fig. 7) indicates that the numerical GC profile is identical with the analytical symmetrical GC case. Since there are no simplifications involved in the symmetrical GC case, this is expected and shows the good quality of the numerical approach (see also section 5.1.2.1). For the MS case the numerical computations show a much larger SCL extent than the analytical approximation. Also this is explicable given that the numerical calculations include the realistic decrease of charge density ρ with increasing x coordinate (and thus the smaller change in

³¹ $|z_{max}|$: largest absolute charge number of all mobile CCs (i.e. largest of all $|z_i|$)

³² The formula gives two Δx values. Here the smallest non-negative solution is the physically rational value.

potential, see eq. {24}) whereas in the analytical approach the charge density is, unrealistically, kept constant over the whole profile range (eq. {30}). A more detailed comparison between the analytical and numerical approaches is given in section 5.1.4.

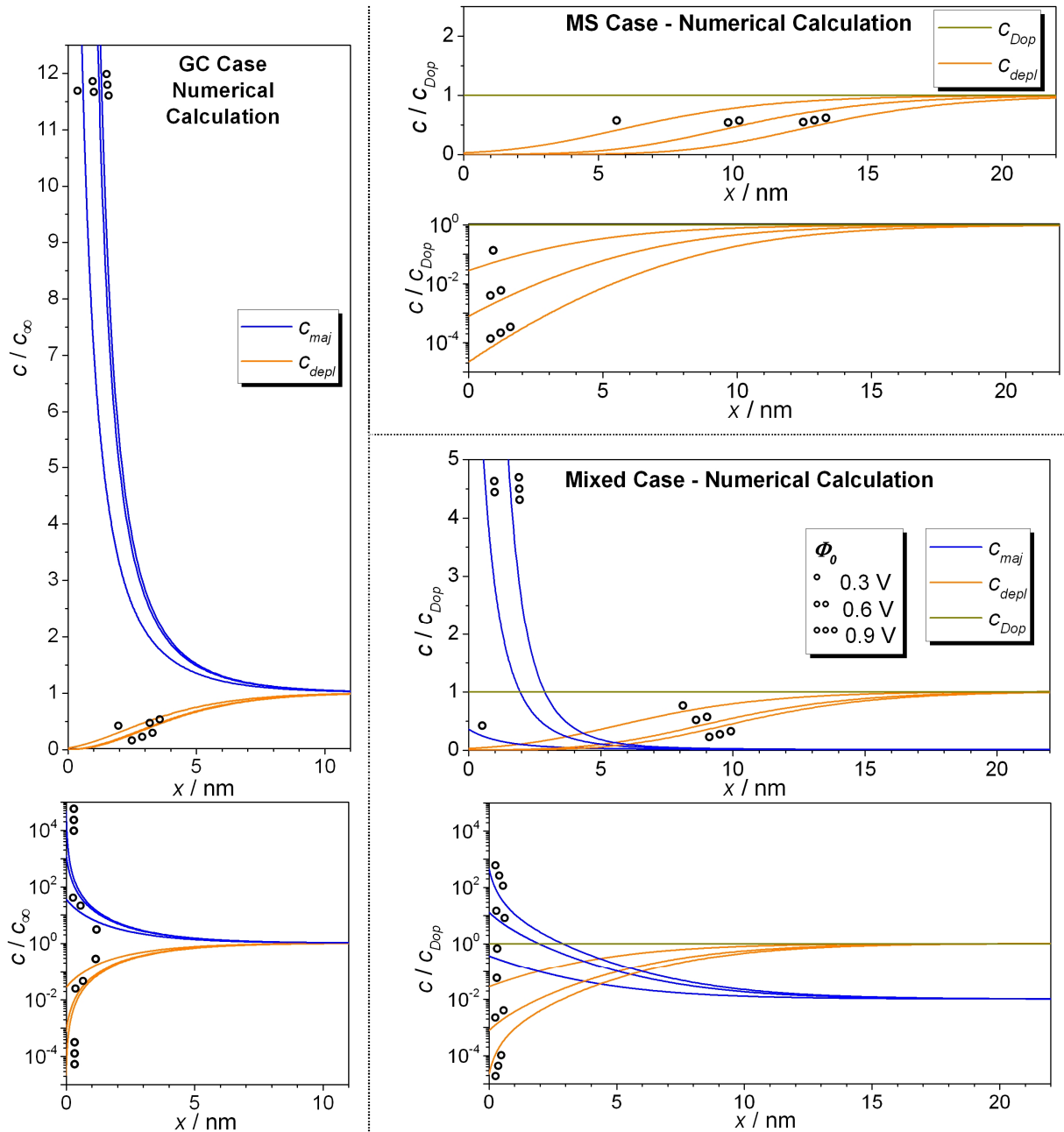


Fig. 9: Example SCL Concentration Profiles Calculated using the Numerical Approach

The SCL profiles are given for three potential values (0.3, 0.6 and 0.9 V) in a linear (above) and logarithmic plot (below).

Parameters: general: $\epsilon_r = 26$, $\theta = 700^\circ\text{C}$, $z_{maj} = z_{Dop} = -z_{depl} = -1$ / GC case: $c_{maj,\infty} = c_{depl,\infty} = 1.25 \cdot 10^{19} \text{ cm}^{-3}$, $c_{Dop} = 0$ / MS case: $c_{depl,\infty} = c_{Dop} = 1.25 \cdot 10^{19} \text{ cm}^{-3}$ / mixed case: $c_{Dop} = 1.25 \cdot 10^{19} \text{ cm}^{-3}$, $c_{maj,\infty} = 0.01 \cdot c_{Dop}$, $c_{depl,\infty} = 1.01 \cdot c_{Dop}$

In contrast to the analytical solutions the numerical approach allows for a precise treatment of the mixed case. In this case, both, an immobile dopant and an enriched CC, contribute significantly to the charge density. Here, the assumptions made in the MS and GC case (eq. {30} and {31}) are not valid anymore. Also example profiles of the mixed case are shown in Fig. 9.

3.2 Further Characteristics of Space Charge Layer Profiles

In the numerical approach the SCL extent l_{SCL} can be quantified as the smallest coordinate for which the relationships {79} and {80} are valid. This means that for all CCs the integration over c_i and c_i^{-1} from 0 to l_{SCL} reaches a certain contribution $q \cdot \Sigma_i$ and $q \cdot \Omega_i$ on the values of Σ_i and Ω_i , respectively (with $0 < q < 1$). In this study a q value of 0.99 was used.

$$q \cdot \Sigma_i \leq z_i e \cdot \int_0^{l_{SCL}} (c_i - c_{i,\infty}) dx \quad \{79\}^{33}$$

$$q \cdot \Omega_i \leq \frac{1}{|z_i| e} \cdot \int_0^{l_{SCL}} (c_i^{-1} - c_{i,\infty}^{-1}) dx \quad \{80\}^{33}$$

Another interesting feature of the SCL profiles is their steepness α . It can be expressed as the ratio of the SCL extent and the charge balance point x_ρ ³⁴ (see Fig. 10):

$$x_\rho = \left(\int_0^{+\infty} x \rho \cdot dx \right) / \left(\int_0^{+\infty} \rho \cdot dx \right) \quad \{81\}$$

$$\alpha = l_{SCL} / x_\rho \quad \{82\}$$

Finally, the SCL conductivity changes can be easily calculated by numerical integration with eq. {53}, {55} and {57}. In order to consider also the less important perpendicular contributions for a CC enrichment and the parallel contributions for a CC depletion the total effective conductivity is here calculated including both, parallel and perpendicular, effects:

$$s_{i,m} = s_{i,m}^{\parallel} s_{i,m}^{\perp} \quad \{83\}$$

³³ Compare with eq. {53} and {55}.

³⁴ x_ρ is the analogue to the “center of mass” concerning the distribution of charge density ρ in the SCL.

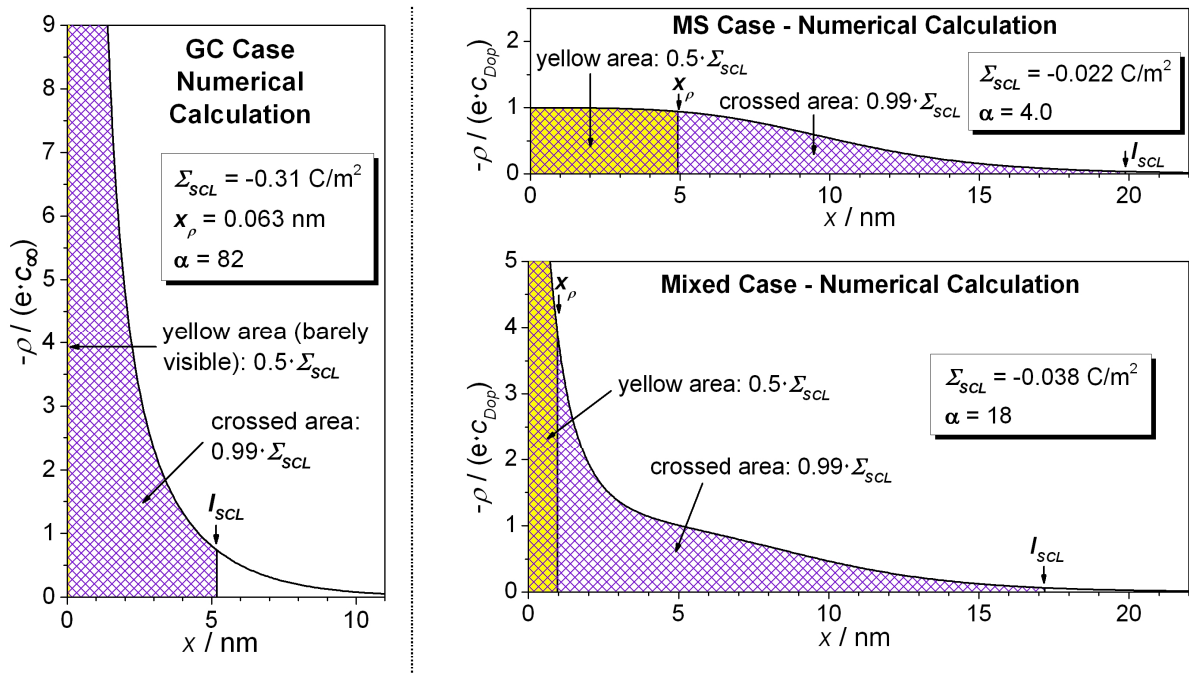


Fig. 10: Illustration of the SCL Extent I_{SCL} , Charge Balance Point x_ρ and Steepness α for Three Example Profiles

In contrast to Fig. 7, Fig. 9 and Fig. 11 here the charge density ρ and not the local concentration is plotted. The corresponding concentration profiles are given in Fig. 9 ($\Phi_0 = 0.6$ V).

At the charge balance point x_ρ the area below the curve of ρ is divided in two equal parts of $0.5 \cdot \Sigma_{SCL}$.

Here for the calculation of I_{SCL} a slightly simplified approach compared with eq. {79} and {80} was used: $q \cdot \Sigma_{SCL} = \int_0^{I_{SCL}} \rho \cdot dx$, with $q = 0.99$.

As already qualitatively expected in section 2.2.2, in contrast to the MS case in the GC case the majority of the charge is located very close to the interface. This corresponds to a charge balance point extremely close to zero and results in a large steepness value α .

3.3 One Dimensional Overlapping Space Charge Layer Profiles

Also overlapping SCL profiles can be computed numerically.^[97] For one dimensional overlapping SCL profiles which are important for instance for very thin multilayer structures the same approach given above with only slight modifications can be applied. As the main difference eq. {84} needs to be applied instead of eq. {27} which bases on an integration with semi infinite boundary conditions (from x_k to $+\infty$). In general, let us define the position where the electric field becomes zero as x_B (in most cases $x_B = d_{ML}/2$ ³⁵). The integration of eq. {26} from an arbitrary coordinate x_k to x_B yields eq. {84}:

³⁵ In the most cases the SCL potential will be identical at both considered interfaces resulting in an axis symmetric profile and, hence, $x_B = d_{ML}/2$ (as shown in Fig. 11). Nonetheless, also asymmetric situations
... footnote continued on next page

$$E_{x_k} = \text{sgn}(\Phi_{x_k}) \cdot \sqrt{\frac{2k_B T}{\epsilon_r \epsilon_0} \left(\sum_{i=1}^{N_{\text{Mobile}}} (c_{i,x_k} - c_{i,x_B}) + \frac{\rho_{\text{Dop}}}{k_B T} (\Phi_{x_B} - \Phi_{x_k}) \right)} \quad \{84\}$$

The additional, initially unknown parameter Φ_{x_B} (the potential in the centre of the layer or grain) is determined by repeatedly computing the SCL profile with more and more refined values of Φ_{x_B} until the corresponding output value of x_B fits with the sample geometry. Example profiles are given in Fig. 11.

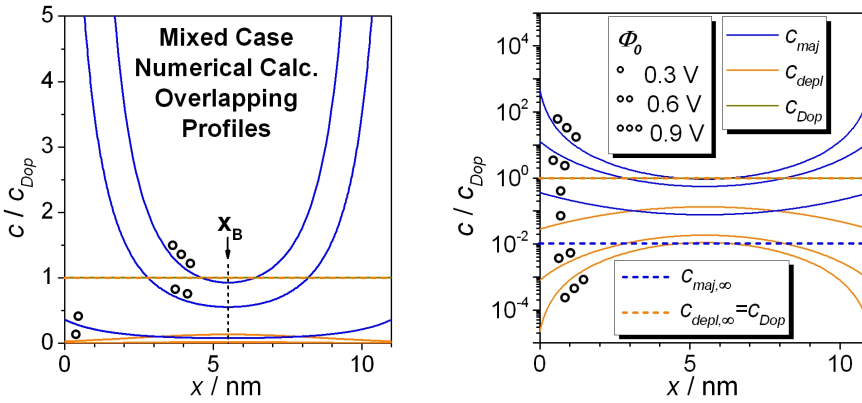


Fig. 11: Example Concentration Profiles of Overlapping SCLs, Calculated using the Numerical Approach

The SCL profiles are given for three potential values (0.3, 0.6 and 0.9 V) in a linear (left) and logarithmic plot (right). The corresponding non-overlapping profiles are shown in Fig. 9 (mixed case).

In contrast to Fig. 9, where there is only one interface at $x = 0$, here two interfaces at $x = 0$ and $x = 11$ nm are present. Since the double SCL extent is considerably larger than $x = 11$ nm (e.g. $2l_{\text{SCL}} = 34$ nm for $\Phi_0 = 0.6$ V, see Fig. 10) both SCLs overlap.

Depending on the value of Φ_{x_B} even in the centre of the grain the local concentrations can vary significantly from the bulk value. Here Φ_{x_B} was found to be 0.17 V, 0.34 V and 0.38 V for Φ_0 values of 0.3 V, 0.6 V and 0.9 V, respectively.

Parameters: $\epsilon_r = 26$, $\theta = 700^\circ\text{C}$, $z_{\text{maj}} = z_{\text{Dop}} = -z_{\text{depl}} = -1$, $c_{\text{Dop}} = 1.25 \cdot 10^{19} \text{ cm}^{-3}$, $c_{\text{maj},\infty} = 0.01 \cdot c_{\text{Dop}}$, $c_{\text{depl},\infty} = 1.01 \cdot c_{\text{Dop}}$

with different Φ_0 values for each interface are possible. In this case, which can be treated with the given numerical approach as well, x_B will differ from $d_{\text{ML}}/2$.

Chapter 4

Experimental Setup

4.1 Sample Preparation

4.1.1 Powder Preparation

For the preparation of the nominally pure and acceptor doped CeO₂ powders Ce(NO₃)₃·6H₂O (Aldrich, 99.99%) and the nitrate of the dopant (e.g. Gd(NO₃)₃·6H₂O or Y(NO₃)₃·6H₂O, Aldrich, 99.99%) were dissolved in doubly distilled water and the solutions subsequently poured in a diluted ammonia solution:



Solution and precipitate were separated by centrifugation. The precipitate was washed firstly with doubly distilled water and secondly with ethanol. The powder was dried under air at 220 °C for 12 hours. Subsequently, it was grinded and calcinated for 5 hours at 450 °C in air.

As an exception, the 10 mol% Gd-doped ceria powder was purchased from Sigma Aldrich (99.9 %).

The 2 mol% Nb doped ceria powders were prepared using a conventional solid state route with CeO₂ and Nb₂O₅ as starting materials. After mixing the two oxides they were heated for 18 hours at 1400 °C.

4.1.2 Sintering

In order to prepare the targets for pulsed laser deposition (PLD) the powders were isostatically cold-pressing at 350 MPa and sintered for 8 hours at 1400 °C in air. The targets were polished to a diameter of 13.5 mm to fit in the PLD target holder (see section 4.1.3.3).

4.1.3 Pulsed Laser Deposition

4.1.3.1 General Description

Pulsed laser deposition is a thin film preparation technique. Hereby the target material is hit by highly energetic laser pulses. Since the majority of the energy of the laser pulses is absorbed by the target its surface temperature temporally becomes extremely elevated (up to several thousand °C) and a plasma plume is created (see Fig. 12). Atoms and ions of the target material are evaporated perpendicularly to the surface and deposit on the substrate at the opposite side of the chamber. In most cases the substrate is heated allowing for a sufficient diffusion of the deposited ions and, thus, for the formation of crystalline material. The main advantage of PLD is the ideally identical cation composition of target and thin film.

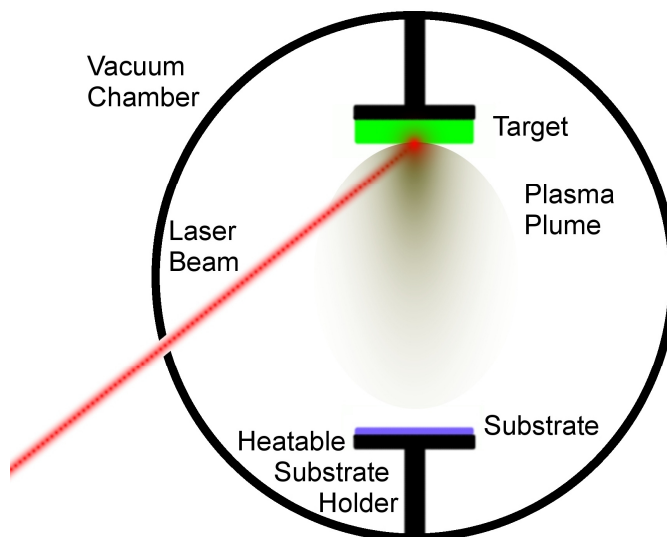


Fig. 12: Pulsed Laser Deposition

4.1.3.2 Used Parameters

The quality and properties of the thin films depend on the deposition conditions (temperature, pO_2 , pulse frequency, etc.). The following parameters in Table 3 were found to be optimal for the growth of the films investigated here and used for their preparation (if not specifically stated differently in the later sections).

In the usual routine of the preparation in the first step the chamber was evacuated. Then with the vacuum pump still open pure oxygen was inserted with the flow corresponding to a pressure of 0.01 mbar. After heating the substrate³⁶ the deposition was started. Upon deposition

³⁶ The temperature of the substrate was monitored using a pyrometer.

the pump valve was closed and the pressure was increased until it reached the ambient pressure. Under these conditions the film was annealed. In the last step the chamber was cooled down to room temperature.

Parameter	Value	Parameter	Value
<i>general</i>		<i>deposition</i>	
PLD chamber	PLD 6	deposition pressure	0.01 mbar
substrate materials	several, e.g.: SiO ₂ <0001>, Al ₂ O ₃ <0001>, Al ₂ O ₃ <1 $\bar{1}$ 02>, MgO <100>, MgO <110>, LaSrAlO ₄ <001>	deposition temperature (at substrate)	720 °C
substrate size	10x10x0.5 mm	laser frequency	5 Hz
substrate polish	one side	laser energy (at lens)	90 mJ
distance between target and substrate	44 mm	energy density at target	1.5 J/cm ²
process gas	O ₂	laser pulses with closed shutter	1200
evacuation pressure	<1 · 10 ⁻⁵ bar	growth rate for CeO₂	≈ 0.82 Å/pulse (from transmission electron microscopy measurements)
heating rate	80 K/min from room temperature to 630 °C, 40 K/min for $\theta > 630$ °C	<i>annealing</i>	
cooling rate	80 K/min	annealing pressure	1 bar
		annealing temperature (at substrate)	720 °C

Table 3: Used PLD Parameters

4.1.3.3 Target Holder

In the beginning of this project the target was fixed with silver epoxy glue. However, at high temperatures the glue occasionally failed to hold the target. Therefore, a new target holder working without glue was designed (Fig. 13).

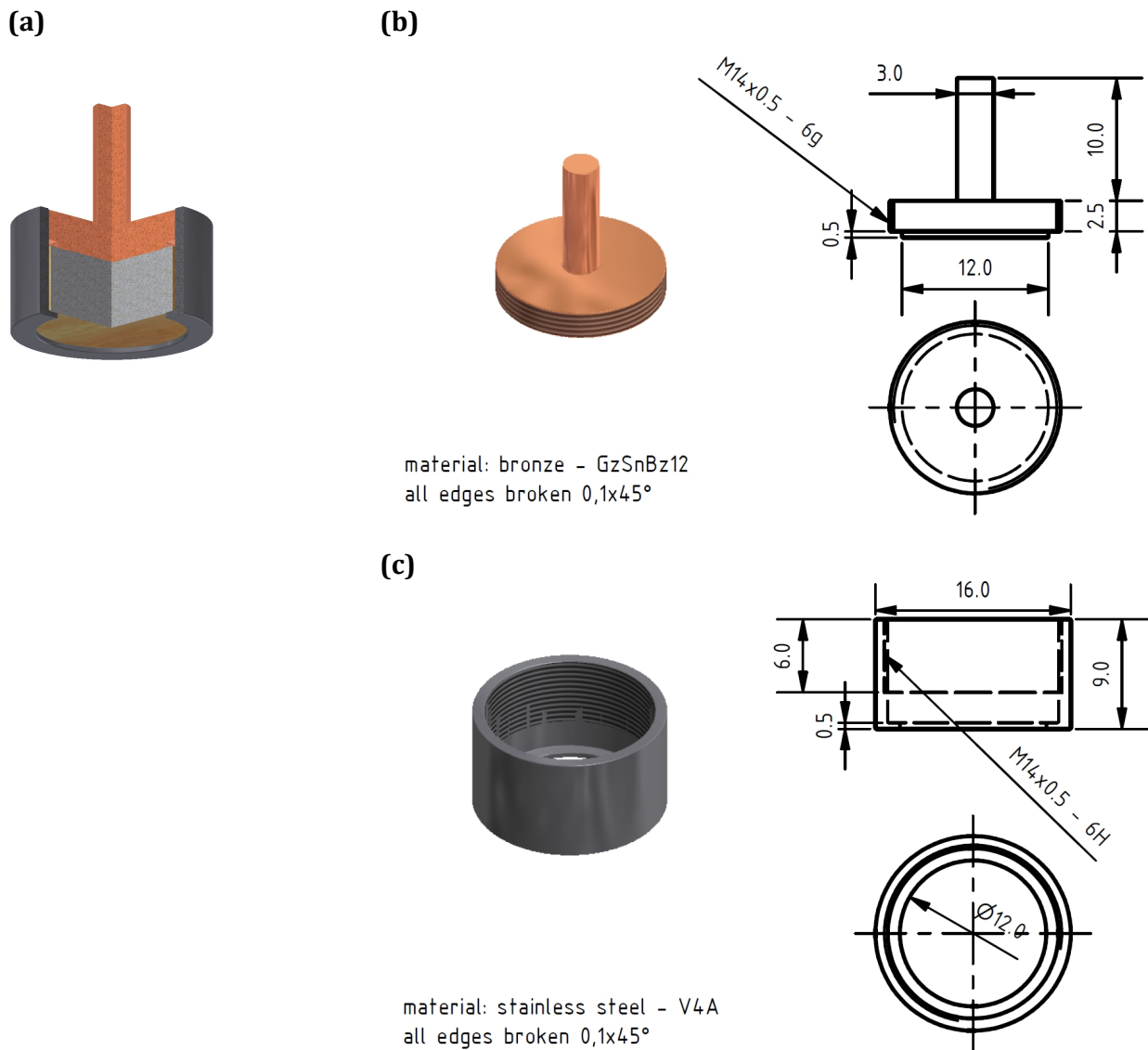


Fig. 13: Design of the PLD Target Holder

(a): Model of the Assembled Target Holder with Target Material (Grey)

(b): Design of the Piston

(c): Design of the Body

All measures in mm. Figures created using the Autodesk software (educational license).

4.2 Microstructure Characterization

4.2.1 X-Ray Diffraction

The samples (powders, pellets (targets) and films) were analyzed using X-Ray diffraction (XRD). The diffractograms were recorded on a Philips Xpert 3710 HTK XRD diffractometer with copper K_{α} radiation (1.54056 Å).

4.2.2 Scanning Electron Microscopy, Focused Ion Beam and Transmission Electron Microscopy

In order to prepare the thin films for transmission electron microscopy (TEM) and high-resolution transmission electron microscopy (HRTEM) lamellae were cut using a focused ion beam (FIB) cross section lift-out technique. Here a Zeiss Crossbeam 1540 ESB scanning electron microscope (SEM) with a gallium ion beam was employed. An acceleration voltage of 30 kV was used and an ion current of 10 pA for the final cut. Using the same electron microscope also SEM micrographs of the samples were recorded.

The donor doped CeO₂ thin films did not undergo the FIB procedure but were prepared for TEM using a tripod polisher.

For the TEM analyses a Zeiss 912 Omega TEM microscope and a JEOL 4000FX TEM microscope were used. The acceleration voltages of the two devices are 120 kV and 400 kV, respectively.

4.3 Conductivity Measurements

4.3.1 Impedance Spectroscopy

4.3.1.1 Impedance Spectra Characterized by RC Elements

Impedance spectroscopy is a measurement technique that in some cases allows for a separation between the several resistive contributions of a sample (e.g. bulk, boundaries, electrode, etc.). Thereby an alternating voltage is applied at the sample and both amplitude and phase shift of the resulting current are recorded in order to determine the impedance Z (the complex resistance). The impedance itself is frequency dependent and can be presented in an impedance spectrum, where normally the negative imaginary part of the impedance $-Z''$ is plotted versus the real part Z' (Nyquist plot). A recorded impedance spectrum is usually analyzed using corresponding equivalent circuits. For the type of samples investigated here these are serially and parallelly connected circuits of resistances and capacitors.

For a single ideal capacitor with the capacitance C the impedance is $Z = (i\omega C)^{-1}$ ³⁷ while, obviously, for a single resistance R the impedance becomes $Z = R$. In a typical sample both polarization (represented by the capacitor) and conduction (represented by the resistor) occur in parallel. The resulting RC elements (one resistor and one capacitor connected in parallel)

³⁷ ω : angular frequency, i : here: imaginary unit

have an impedance of $Z = 1/(R^{-1} + i\omega C) = (R^{-1} - i \cdot \omega C)/(R^{-2} + \omega^2 C^2)$. As it can be checked easily in this case for all frequencies Z'' is negative and the relationship $\sqrt{(Z' - R/2)^2 + (Z'')^2} = R/2$ is fulfilled. Therefore, one RC element creates a typical impedance spectrum with all data points lying on a semicircle of the diameter R which is centered on $R/2$. The maximum of the circle (in $-Z''$ direction, the point $R/2 - i \cdot R/2$) is reached when the angular frequency ω becomes the reciprocal of the relaxation time τ (see Fig. 14): $\omega = 2\pi \cdot f = \tau^{-1} = (RC)^{-1}$.³⁸

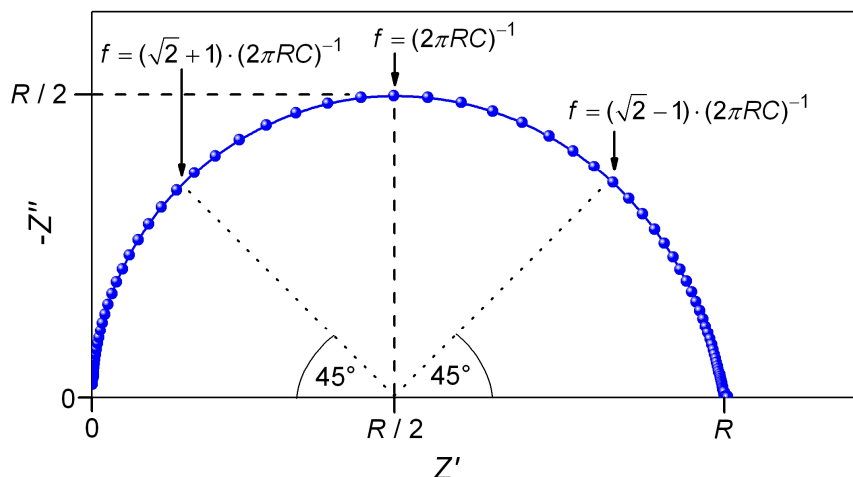


Fig. 14: Typically Measured Impedance Spectrum of a Thin Film Characterized by One RC Element in the Equivalent Circuit

In case of two or more RC elements connected in series the impedance spectra consist of multiple contributions. Depending on how strongly the time constants of the individual contributions vary their corresponding semicircles can be resolved either well or only weakly.

4.3.1.2 Characteristic Device Parameters

For the conductivity measurements two platinum electrodes of a thickness of about 400 nm and a distance of 1 mm between each other were sputtered onto the thin film using an Edwards Auto 306 Turbo device (in-plane configuration, see Fig. 15).

For measuring the impedance spectra a Novocontrol Alpha-A High Performance Frequency Analyzer was utilized. Typically used parameters are given in Table 4.

³⁸ f : frequency

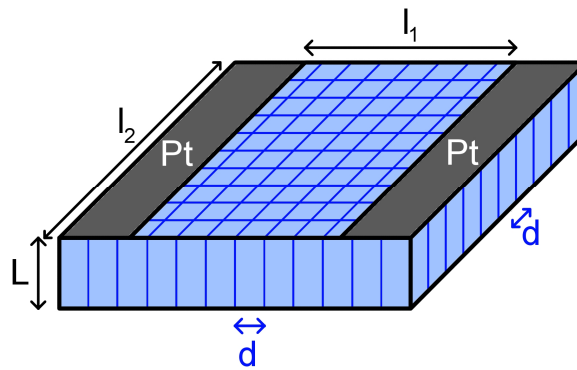


Fig. 15: Geometry of the Investigated Thin Films with Pt Electrodes

As an example a polycrystalline thin film with an ideal columnar grain structure and a uniform lateral grain size d is shown.

l_1 : distance between the electrodes (here 1 mm), l_2 : edge length of the square substrate (here 10 mm)

Reproduced from Göbel et al.^[14] by permission of the PCCP Owner Societies.

Parameter	Value
frequency range	0.2 Hz – 2 MHz
data points per decade	10
integration time	2 s
delay time	0.5 s
output voltage	0.1 V
use low impedance calibration	yes

Table 4: Typically Used Parameters for Impedance Spectroscopy

The impedance spectra were analyzed by fitting the recorded data points with simulated spectra of appropriate equivalent circuits (see also section 5.2.2). For this purpose the software *ZView 2* (Scibner Associates Inc.) was used.

4.3.2 Measurement Cell

For the conductivity measurements a special cell being able to carry 4 samples was designed (Fig. 16). The advantage of such a system is the possibility to expose all 4 samples to the same conditions (temperature and pO_2) allowing a much better comparability between them. The 4 samples were connected with the impedance spectrometer via a home built multiplexer.

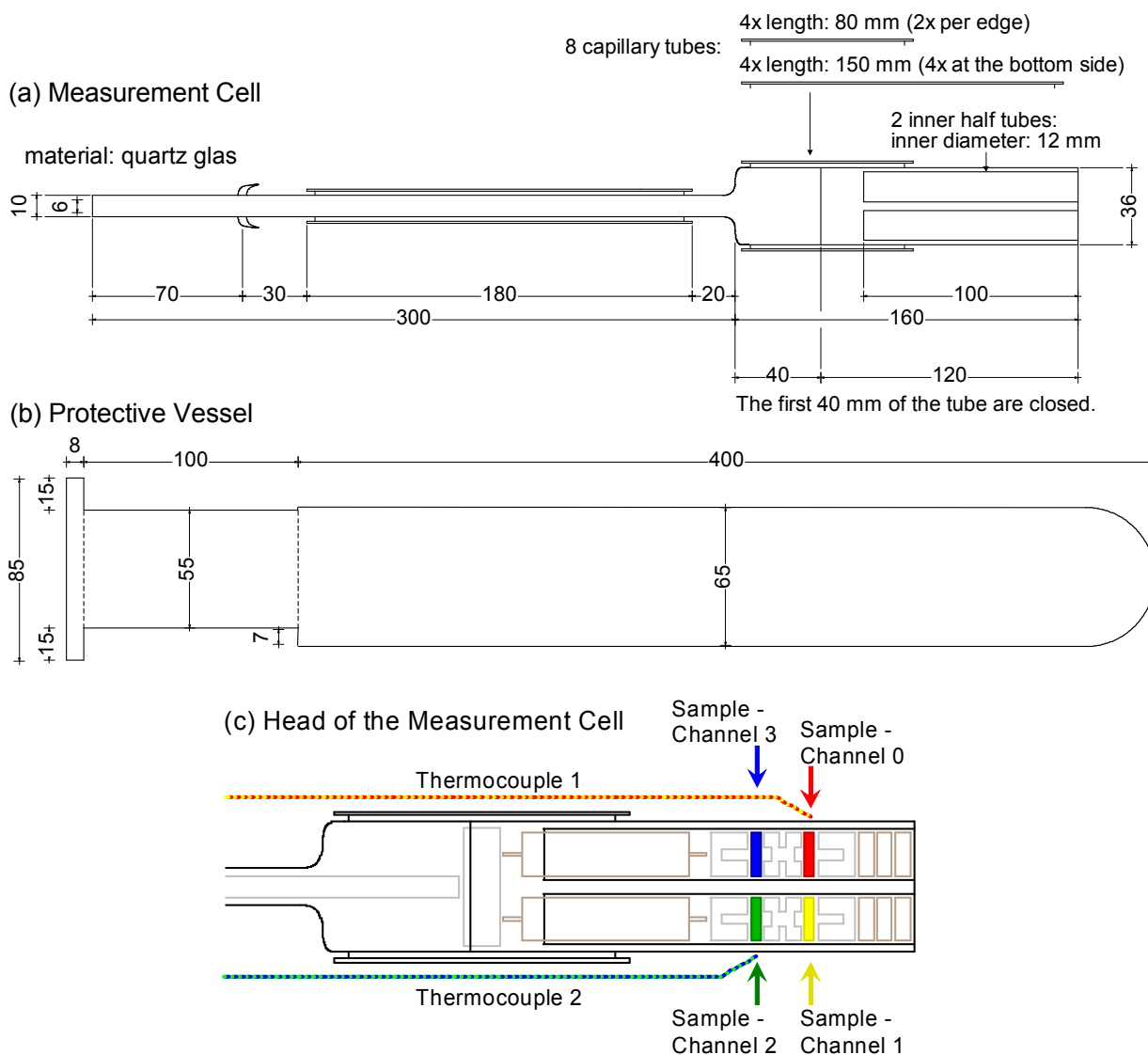


Fig. 16: Design of the Measurement Cell for Simultaneous Measurement of 4 Samples

The positions of the 4 thin films (with corresponding multiplexer channel) and the 2 thermocouples are given in panel (c).

The protective vessel separates the sample holder from the surrounding atmosphere.

All measures in mm. Figures created using the Thouvis software.

4.3.3 Flow Controller Setup and Calibration

4 flow controllers (FCs) were applied to prepare oxygen nitrogen gas mixtures with the desired pO_2 . This way nearly all pO_2 values in the range between 10^{-5} and 1 bar could be mixed continuously. Fig. 17 illustrates the calibration curves of the flow controller system; e.g. for each accessible pO_2 value the corresponding flow controller settings (flow values) are shown. The flow controllers were connected with external valves in order to allow a complete seal of the gas flow. This made it possible to control the flow controller system (and thus the pO_2) with an

automated software (via a Vacom FCU-4 unit) allowing for complex pO_2 and temperature sequences. The pO_2 was monitored with either a Cambridge Sensotech Rapidox 2100 oxygen sensor or a Gen'Air Setnag oxygen pump.

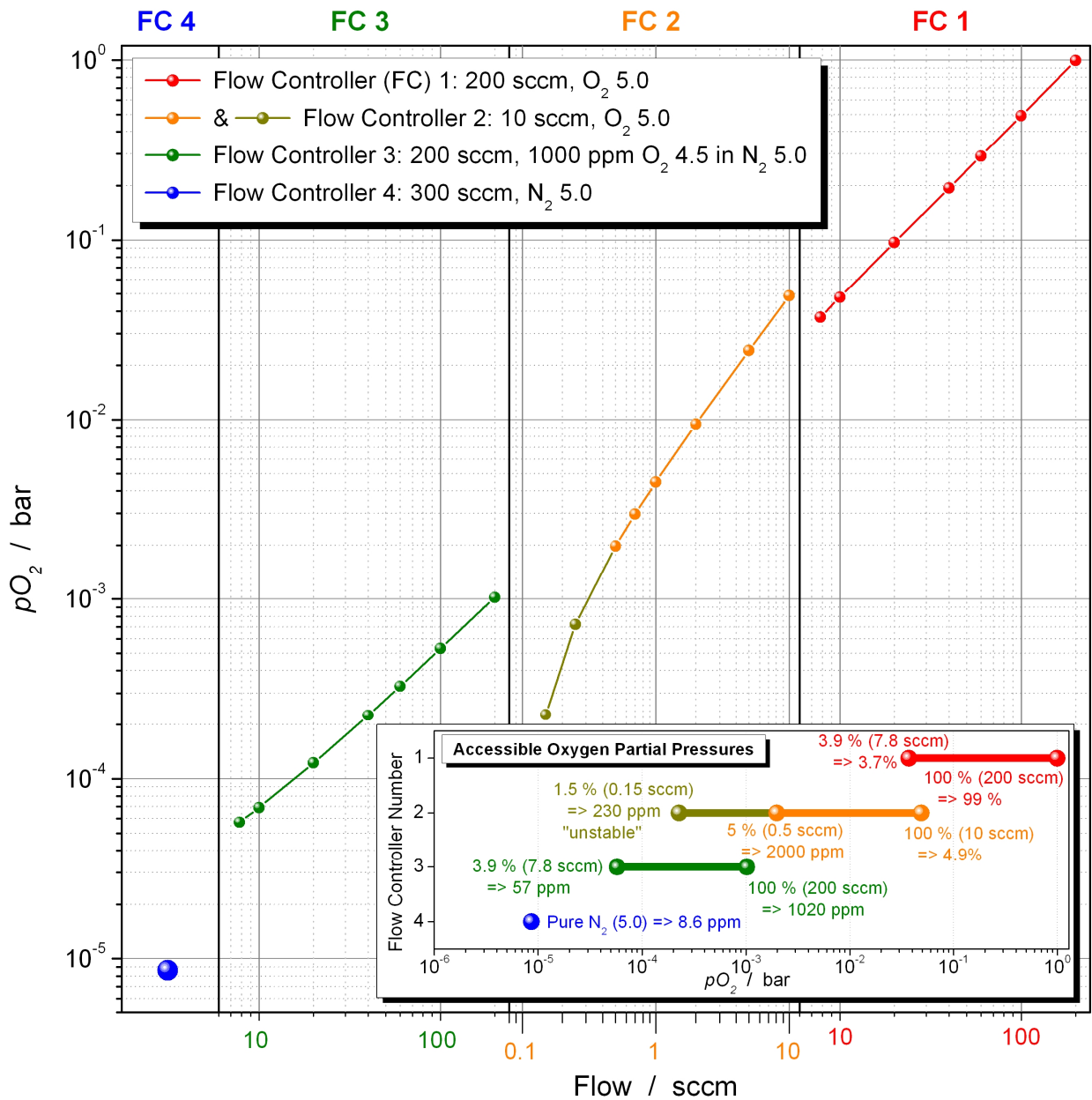


Fig. 17: Calibration of the Mass Flow Controller System

The 4 used flow controllers allow for a nearly continuously accessible pO_2 range between 10^{-5} to 1 bar. For this purpose mixtures of oxygen (FC 1, 2 or 3) and nitrogen (FC 4) were used. Specifically, depending on the desired pO_2 the oxygen flow of FC 1, 2 or 3 was set according to the above plot while the nitrogen flow was set to a value corresponding with a total flow of the mixture of 200 sccm. (E.g. for a pO_2 of 0.1 bar FC 2 and FC 3 were closed, FC 1 was set to a flow of 20 sccm of pure O_2 and FC 4 was set to a flow of 180 sccm of pure N_2 .)

4.3.4 Temperature Calibration

2 pairs of the 4 samples are located on different positions along the axis of the oven and, therefore, perceive different temperatures (depending on the temperature gradient in the oven). Both temperatures $\theta_{Sample,1}$ and $\theta_{Sample,2}$ (in °C, or $T_{Sample,1}$ and $T_{Sample,2}$ in K) were recorded with separate thermocouples (see Fig. 16c). In order to minimize the temperature difference between the two sample pairs the position of the measurement cell in the oven was carefully calibrated. At 30 cm the optimal position with a temperature gradient close to zero was

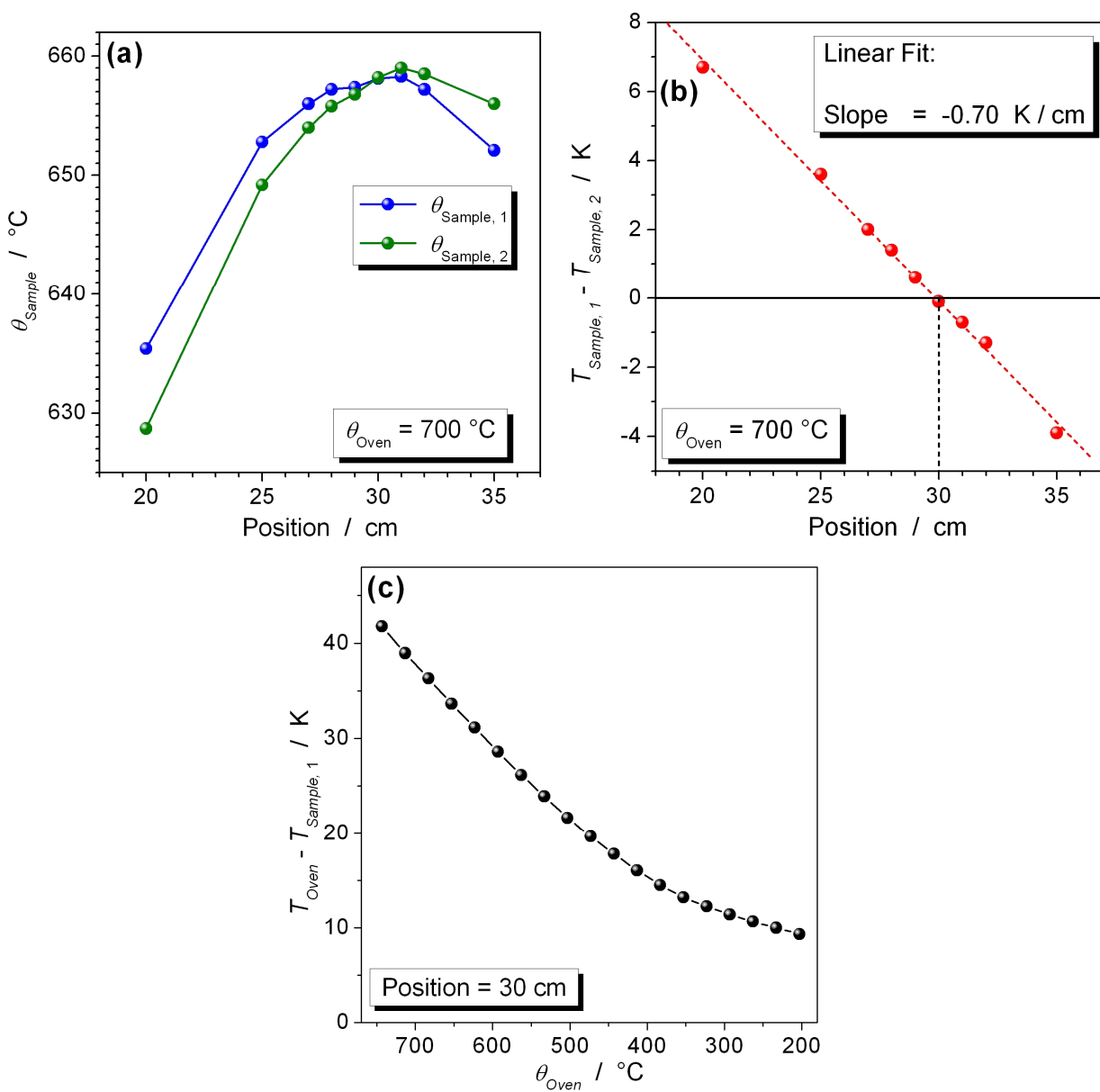


Fig. 18: Temperature Calibration of the Measurement Cell

- (a) The Two Sample Temperatures as a Function of the Position of the Cell in the Oven
- (b) Difference between the Sample Temperatures as a Function the Position of the Cell in the Oven
- (c) Difference between Sample and Oven Temperatures upon Cooling Down

found ($\theta_{Sample,1} \approx \theta_{Sample,2}$, Fig. 18a and Fig. 18b). For clarity, in the later sections the indices “Sample, 1” and “Sample, 2” are omitted and the sample temperature is simply designated as θ (or T).

Additionally, the sample temperature θ is different from the one of the third thermocouple at the heater coil of the oven θ_{Oven} (in °C, or T_{Oven} in K). Due to its fast response θ_{Oven} was used to regulate the temperature using a Eurotherm 2416 controller. Therefore, also the relationship between θ_{Oven} and θ was recorded (Fig. 18c).

4.3.5 Spurious Conductances of Substrate and Sample Holder

In the beginning of the project it was found that the sample holders (e.g. the ceramic pieces that are in direct contact with the thin films) have a rather low resistance at high temperatures leading to large conductances $G = R^{-1}$ connected in parallel with the sample. Obviously, this strongly disturbed the measurement and resulted in a large uncertainty of the results. Therefore, a set of new sample holders was designed. The spurious conductances could be minimized by two measures. (1) The material was changed from quartz to sapphire. (2) The shape of the sample holders was designed to maximize the transport pathway in the sapphire

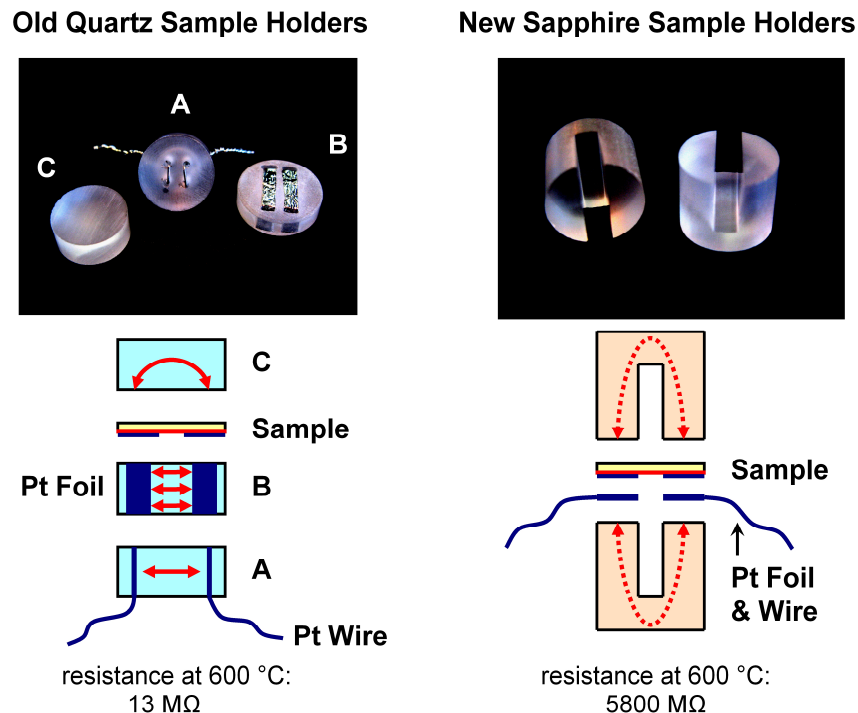


Fig. 19: Comparison between the Old and Newly Designed Sample Holders

The red arrows indicate spurious electric transport pathways.

Reproduced from Göbel et al.^[14] by permission of the PCCP Owner Societies.

parts (Fig. 19). Notably, the sample holder’s conductance could be reduced by more than two orders of magnitude.

Also the conductance of the substrate leads to a similar yet unavoidable measurement uncertainty. Fig. 20 shows the measured conductances of both the new sample holders and the here used substrate materials.

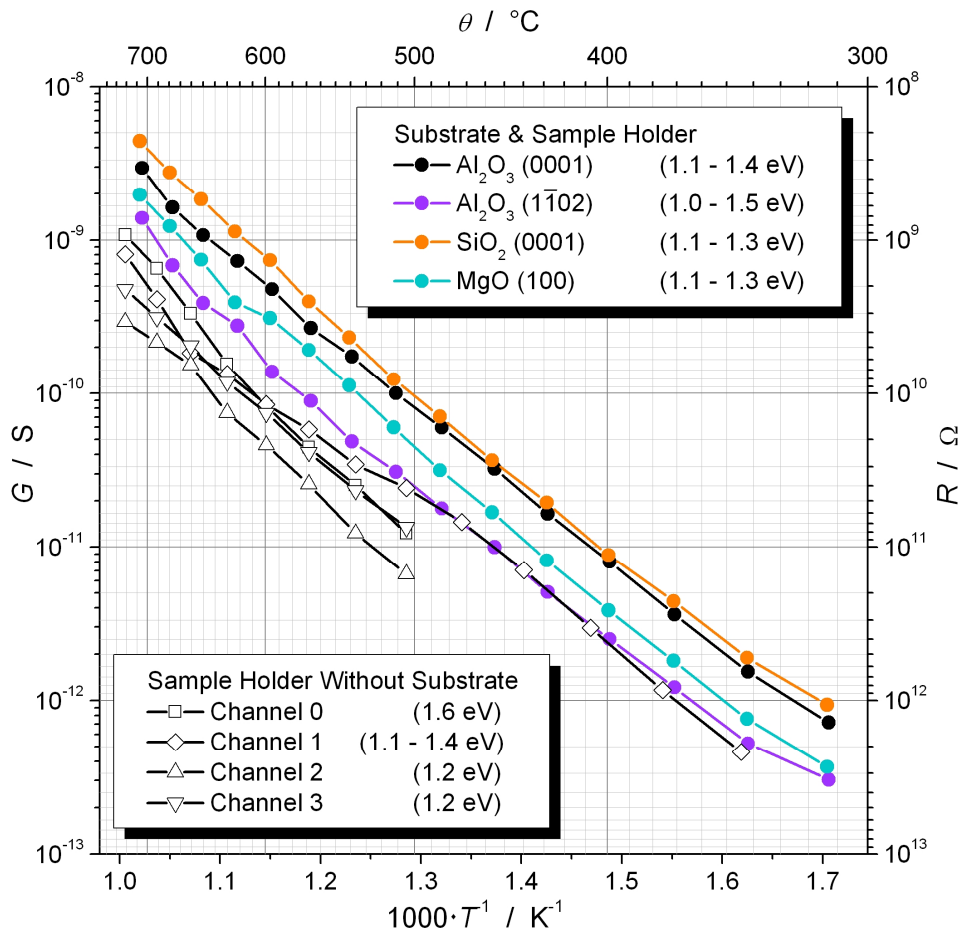


Fig. 20: Spurious Conductances of the Sample Holder and Various Substrates

Depending on the position of the sample in the cell (4 possibilities, channel 0 to 3, see Fig. 16c) the background conductance varies slightly. However, for all 4 positions the conductances were found to be negligibly small compared with the unavoidable substrate contributions.

The observed activation energies are given in brackets.

Chapter 5

Results and Discussion

5.1 Numerical Calculations of Space Charge Layer Effects in Cerium Oxide

5.1.1 Section Introduction

The analytical description of SCL effects in ionic and mixed conductors (see section 0) is a comprehensive theory applied in a large number of studies in the field of solid state ionics. Nevertheless, not every case can be treated analytically without the use of further assumptions:

(A) *Gouy-Chapman Case*

The only case that can be solved analytically without further assumptions is the symmetrical GC case, i.e. two mobile CCs with $z_{depl} = -z_{maj}$ (eq. {32} and {35}). However, for CeO₂ with $z_{V_O^{\bullet\bullet}} = -2 \cdot z_e$, this case does not apply. The initial assumption of the regular GC case, namely the neglect of the non-enriched CCs (eq. {31}), is only valid for strong enrichments and only close to the interface.^[1, 94]

(B) *Mott-Schottky Case*

Similarly, the basic assumption of the MS case that only the dopant contributes to the charge density ρ (eq. {30}) is only valid for pronounced depletion effects and only close to the interface.^[1, 94]

(C) *Mixed Case*

Furthermore, in reality not only the ideal GC and MS cases are of importance. As shown below, in a number of situations both an immobile dopant (as in the MS case) and an enriched CC (as in the GC case) significantly contribute to ρ . For such a mixed case the Poisson equation (eq. {24}) cannot be solved analytically.^[1, 94] The analytical solutions in the literature used in this case base on the rather crude assumption that the charge density profile is not too different from the GC case and that, hence, the GC case can be applied instead.^[22]

Therefore, for CeO₂ the analytical solutions in the literature (Table 6, page 55) for all cases base on certain simplifications. In marked contrast, the numerical approach (Chapter 3) allows for the calculation of the SCL effects in ceria without the use of further assumptions.

To which extent the outcomes of the analytical solutions are affected by the above given assumptions cannot be determined by taking into account the analytical solutions of the literature only. Rather, the numerical calculations can be used as a reference to address this aspect as shown in section 5.1.4.

Furthermore, the numerical approach allows for an accurate determination of the SCL profiles over their whole extent (and not only close to the interface as for the analytical solutions, e.g. compare Fig. 7 and Fig. 9). This makes it possible (1) to determine all the relevant profile characteristics (such as their extent l_{SCL} , steepness α and significant charge contributions Σ_i/Σ_{SCL}) as a function of the material parameters (e.g. the doping content) and (2) to investigate how these characteristics influence the conductivity effects in CeO₂. The results of this analysis are given in section 5.1.3.

Finally, in section 5.1.5 also the total charge of the SCLs Σ_{SCL} and its limiting impact on the conductivity effects is taken into consideration.

5.1.2 Preliminary Considerations

5.1.2.1 Accuracy of the Numerical Approach

As the first step it is instructive to check the accuracy of the numerical approach introduced in Chapter 3. We can take as a reference the analytical solution of the symmetrical GC case (eq. {35}), which is valid without further assumptions. Here the integrated profiles, i.e. the conductivity effects represented by the Σ_i and Ω_i values, were compared. For the analytical solution of the symmetrical GC case they are:^[1, 94]

$$\Sigma_i = 4\lambda \cdot z_i e c_{i,\infty} \frac{\mathcal{G}_i}{1 - \mathcal{G}_i} \quad \text{and} \quad s_{i,m}^{\parallel} = 4\Gamma^{\parallel} \lambda \frac{\mathcal{G}_i}{1 - \mathcal{G}_i} + 1 \quad \{86\}$$

$$\Omega_i = \frac{4\lambda}{|z_i| e c_{i,\infty}} \frac{-\mathcal{G}_i}{1 + \mathcal{G}_i} \quad \text{and} \quad s_{i,m}^{\perp} = \left(4\Gamma^{\perp} \lambda \frac{-\mathcal{G}_i}{1 + \mathcal{G}_i} + 1 \right)^{-1} \quad \{87\}$$

For the definition of \mathcal{G}_i and λ see eq. {34} and {35}.

The comparison of the numerical and analytical approach showed that the calculation uncertainty of the numerical algorithm is very small. The differences are merely in the range between 10⁻¹⁰ % and 10⁻³ %. Even for very steep profiles such as profiles with unrealistically

high potentials of 5 V which are difficult to calculate precisely the uncertainty is smaller than 0.1 %.³⁹

Due to its high accuracy the numerical approach is an ideal tool to check the assumptions made in the other analytical solutions (asymmetric GC case, MS case, mixed case) as shown in detail in section 5.1.4.

5.1.2.2 Parameters

For the discussion of the conductivity effects in nanocrystalline ceria the following parameters are used. The temperature, pO_2 , relative permittivity and grain size were set 700 °C, 10^{-10} bar, 26 and 40 nm, respectively. At this low pO_2 also for donor doped ceria (section 5.6) only electrons and oxygen vacancies have to be considered and oxygen interstitial defects can be neglected.^[89] For the bulk concentrations here experimental data from a set of nominally pure, epitaxial ceria films (see section 5.3.3.2.2) was used: $n_{\infty} = 2 \cdot 10^{18} \text{ cm}^{-3}$ at 700 °C and $pO_2 = 1$ bar, corresponding to $n_{\infty} = 9 \cdot 10^{19} \text{ cm}^{-3}$ ⁴⁰ at a pO_2 of 10^{-10} bar. For different doping contents the bulk concentrations were numerically calculated starting from this value of n_{∞} using eq. {4} and {12} (Fig. 21). The dopant charge numbers were set $z_A = 1$ and $z_D = -1$. Furthermore, the SCL densities I^{\parallel} and I^{\perp} were calculated using eq. {58} and {59}.

5.1.3 Relationships between the Characteristics of Space Charge Layer Profiles and the Conductivity Effects

5.1.3.1 Typical Space Charge Layer Profiles in CeO₂

Table 5 shows a series of exemplary profiles calculated for different doping contents and constant SCL potential values of 0.3 V and -0.3 V. Note that the shape of the profiles crucially depends on the potential and doping value.

In principle, a large part of the information discussed below is already contained in the profiles in Table 5. However, a more practical representation of the data is given in the following charts Fig. 22 to Fig. 34. In each of these graphs one attribute of the SCLs is plotted in a color-coded contour diagram vs. the potential (or SCL charge) and doping content.

³⁹ for one million calculation steps (calculation time ≈ 1 s at a contemporary desktop PC)

⁴⁰ calculated using the pO_2 dependence of the electronic conductivity of $-1/6$ (see Table 1, defect chemistry regime (I))

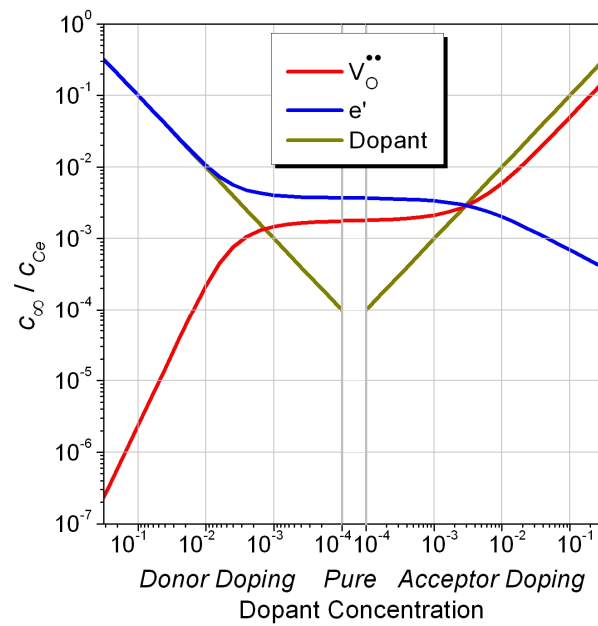


Fig. 21: Expected Bulk Concentrations in CeO₂ at 700 °C and $pO_2 = 10^{-10}$ bar for Different Doping Contents

The plot is divided in three parts. (1) In the left part the donor doping content c_D logarithmically decreases from 30 % to 0.01 %. (2) In the narrow middle part the doping content is set zero (pure ceria). (3) In the right part the acceptor dopant concentration c_A increases from 0.01 % to 30 %.

c_{Ce} : concentration of cerium cations in pure CeO₂ ($c_{Ce} = 2.526 \cdot 10^{22} \text{ cm}^{-3}$)

5.1.3.2 Charge Contributions in Space Charge Layers

Let us start the discussion of the contour diagrams with Fig. 22a which displays the charge contribution of the oxygen vacancies. The positions of the profiles in Table 5 (and Table 8, page 75) are indicated by the circles with white (and black) filling. Although the experimental potential values range from 0.20 V to 0.34 V^[10, 14, 16, 17, 98, 99] here a larger potential range between -0.6 V and 0.6 V is considered in order to regard which conductivity effects can be expected if it would be possible to modify Φ_0 as experimentally under investigation^[50-53, 100] (see also the last two paragraphs in section 1.2).

The oxygen vacancy and electron concentration changes in a SCL integrate to corresponding charge contributions $\Sigma_{V_O^{..}}$ and $\Sigma_{e'}$ (eq. {53}) on the total SCL charge $\Sigma_{SCL} = \Sigma_{V_O^{..}} + \Sigma_{e'}$ (eq. {54}). Hence, the here plotted ratio $\Sigma_{V_O^{..}} / \Sigma_{SCL}$ indicates whether the SCLs are dominated by a change of the oxygen vacancy concentration ($\Sigma_{V_O^{..}} / \Sigma_{SCL} \approx 1$, white color in Fig. 22a) or by an enrichment/depletion of the electrons $\Sigma_{V_O^{..}} / \Sigma_{SCL} \approx 0$ (black color in Fig. 22a). As a result, using this representation it is possible to distinguish between the well-known cases of Gouy-Chapman (SCLs characterized by the enrichment of the majority CC) and Mott-Schottky (SCLs characterized by the depletion of the majority CC) which were already introduced in chapter 2.2.2. In Fig. 22a five regions can be identified using the following definitions:

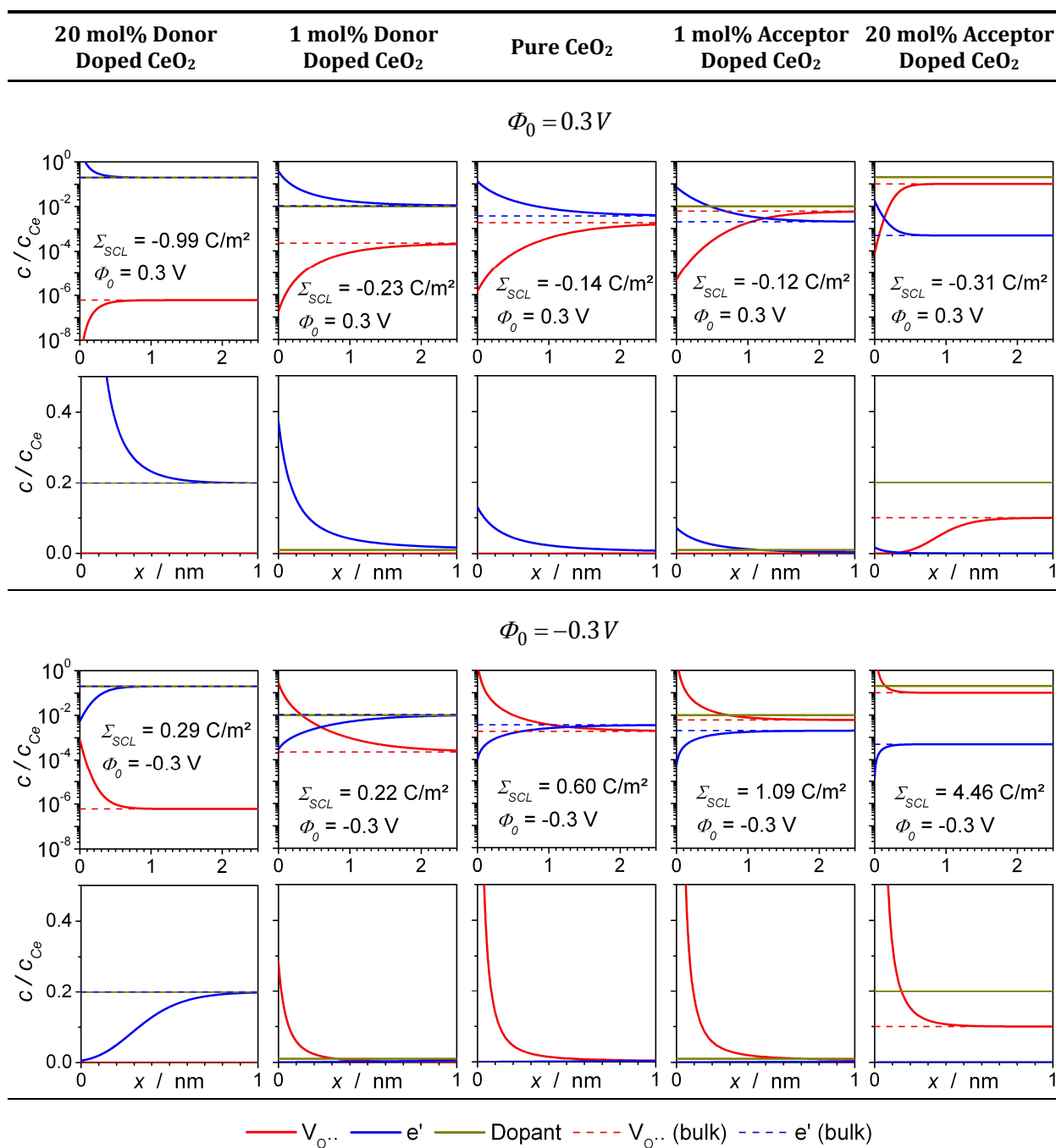


Table 5: Expected SCL Concentration Profiles in CeO₂ Calculated for Constant Potential Values of 0.3 V and -0.3 V Using the Numerical Approach

For each potential value the above graphs are scaled logarithmically and the below graphs linearly.⁴¹

The positions of the profiles are given by the white filled circles in Fig. 22, Fig. 23, Fig. 24, Fig. 33 and Fig. 34.

⁴¹ The scale on the x-axis is different between the logarithmic ($0 \leq x \leq 2.5$ nm) and linear plots ($0 \leq x \leq 1.0$ nm).

Note that in this table the presentation of the concentration profiles is slightly different from the one used in Fig. 7, Fig. 9 and Fig. 11 since not c/c_∞ or c/c_{Dop} are plotted on the y-axis but c/c_{Ce} . Here the (for each column different) bulk concentrations are given as dashed lines.

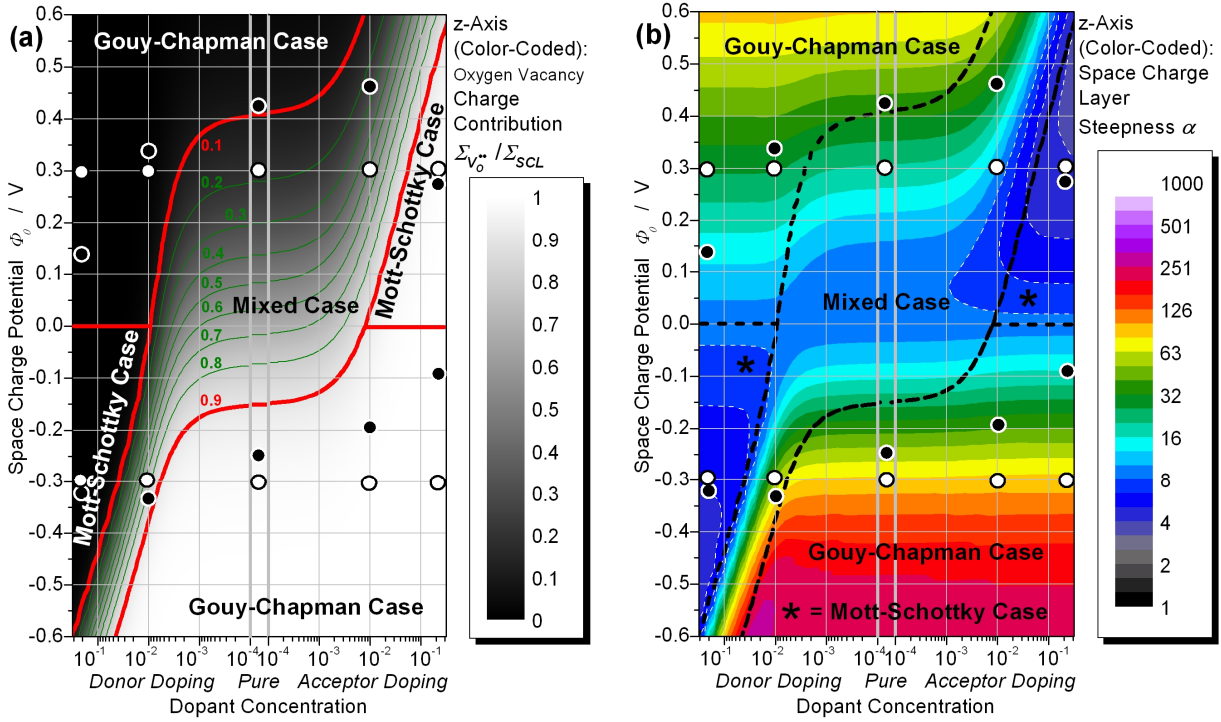


Fig. 22: (a) Charge Contribution of the Oxygen Vacancies and (b) SCL Steepness as a Function of Dopant Concentration and SCL Potential

In the graphs the $\Sigma_{V_0^{**}} / \Sigma_{SCL}$ and α values are plotted in a color-coded contour diagram versus the SCL potential (y-axis) and the dopant concentration (x-axis). Concerning the dopant concentration the diagrams are divided in three divisions (donor doped, pure, acceptor doped) as shown in Fig. 21.

The circles describe the positions of the SCL profiles given in Table 5 (constant Φ_0 values, circles with white filling) and Table 8 (constant Σ_{SCL} values, circles with black filling).

For panel (a), where the $\Sigma_{V_0^{**}} / \Sigma_{SCL}$ values only span from 0 to 1 a linear scaling and a simple grayscale color-code is employed. Here values around 1 (white color) indicate that the SCLs are dominated by an enrichment or depletion of oxygen vacancies, while values of $\Sigma_{V_0^{**}} / \Sigma_{SCL} \approx 0$ (black color) correspond to SCLs dominated by a change of the electron concentration. For intermediate values (grey color) both CCs contribute significantly to the total SCL charge. Using these relationships the diagram can be divided in five cases (two GC cases, two MS cases and the mixed case) as explained in the main text.

The borders between the cases were taken from panel (a) and adopted for panel (b) as well as for Fig. 23, Fig. 24 and Fig. 33.

The steepness values in panel (b) span over a much larger range of several orders of magnitude. Therefore, a logarithmic scale and a more complicated color-code including a larger numbers of colors are used (see legend). Notably, the SCL steepness differs strongly between the cases. The MS profiles are characterized by a rather smooth charge distribution (low α values), whereas the GC type profiles are very steep since here the majority of the SCL charge is located very close to the interface (Fig. 10). Furthermore, the steepness of the GC type profiles increases limitless with increasing $|\Phi_0|$ value. For the MS type profiles, however, the steepness decreases with increasing $|\Phi_0|$ but cannot fall below the limit of 2 (the α value of an ideal flat, rectangle like profile). Hence, for larger absolute potential values the difference between the GC and MS cases in terms of steepness becomes more and more pronounced.

- ✦ $\Phi_0 > 0$ and $\Sigma_{V_0^{**}} / \Sigma_{SCL} < 0.1$: GC case (profiles dominated by the enrichment of e^-)
- ✦ $\Phi_0 > 0$ and $\Sigma_{V_0^{**}} / \Sigma_{SCL} > 0.9$: MS case (profiles dominated by the depletion of V_0^{**})

- ✦ $\Phi_0 < 0$ and $\Sigma_{V_0^{\bullet\bullet}} / \Sigma_{SCL} < 0.1$: MS case (profiles dominated by the depletion of e')
- ✦ $\Phi_0 < 0$ and $\Sigma_{V_0^{\bullet\bullet}} / \Sigma_{SCL} > 0.9$: GC case (profiles dominated by the enrichment of $V_0^{\bullet\bullet}$)
- ✦ $0.1 < \Sigma_{V_0^{\bullet\bullet}} / \Sigma_{SCL} < 0.9$: mixed case (both $V_0^{\bullet\bullet}$ and e' contribute significantly to Σ_{SCL})

As expected, the MS case occurs for strongly acceptor doped samples and positive potentials as well as for strongly donor doped samples and negative potentials. The GC case is located at opposite areas in Fig. 22a. Note that the intermediate mixed case which is only accessible using the numerical approach and not using analytical solutions is fairly large.

Depending on the respective case the shapes of the profiles differ. This can be well observed in Fig. 22b which shows the steepness α of the SCL (eq. {82}). As elucidated in chapter 2.2.2 the GC type SCLs are characterized by very steep profiles (high α values) whereas in the MS case the charge density is distributed more uniformly (low α values) (see also Fig. 10).

5.1.3.3 The Space Charge Layer Extent

Another important SCL attribute is its extent l_{SCL} (eq. {79} and {80}), which is plotted in Fig. 23a. Note that the initial assumption of non-overlapping SCLs is fulfilled over the whole dopant and potential range (since the grain size is 40 nm and l_{SCL} is only between 0.5 nm and 4 nm). As anticipated from eq. {33} and {34} the size of the SCLs crucially depends on the bulk concentrations (and, hence, on the dopant content) and decreases strongly for higher c_A and c_D values (compare with Fig. 21).

Notably, the numerical calculations expose that not only in the MS case (λ^* , eq. {33}) but also in the mixed case and even in the GC case the SCL size l_{SCL} slightly becomes larger with increasing absolute potential value (in comparison with 2λ , eq. {34}) (see also section 5.1.4.1.2).

5.1.3.4 Conductivity Effects

Using the above relationships on the features of the SCL profiles it is now possible to understand the effects of the SCLs on the conductivity as a function of doping content and potential. In the following a brick layer model (here eq. {58} and {59}) was employed to determine the conductivity of a nanocrystalline ceria sample with a grain size of 40 nm. The result is shown in Fig. 24. Here the normalized effective conductivity $s_{i,m} = \sigma_{i,m} / \sigma_{i,\infty}$ is plotted. Let us firstly focus on the oxygen vacancy conductivity in panel (a). As expected, $s_{V_0^{\bullet\bullet},m}$ decisively depends on the SCL potential. For values around 0 V the SCL effects are minimal and the conductivity remains unaffected ($s_{V_0^{\bullet\bullet},m} \approx 1$, color-coded black in Fig. 24a) whereas for increasing $|\Phi_0|$ values the conductivity changes strongly; for the given potential range up to 3 orders of magnitude.

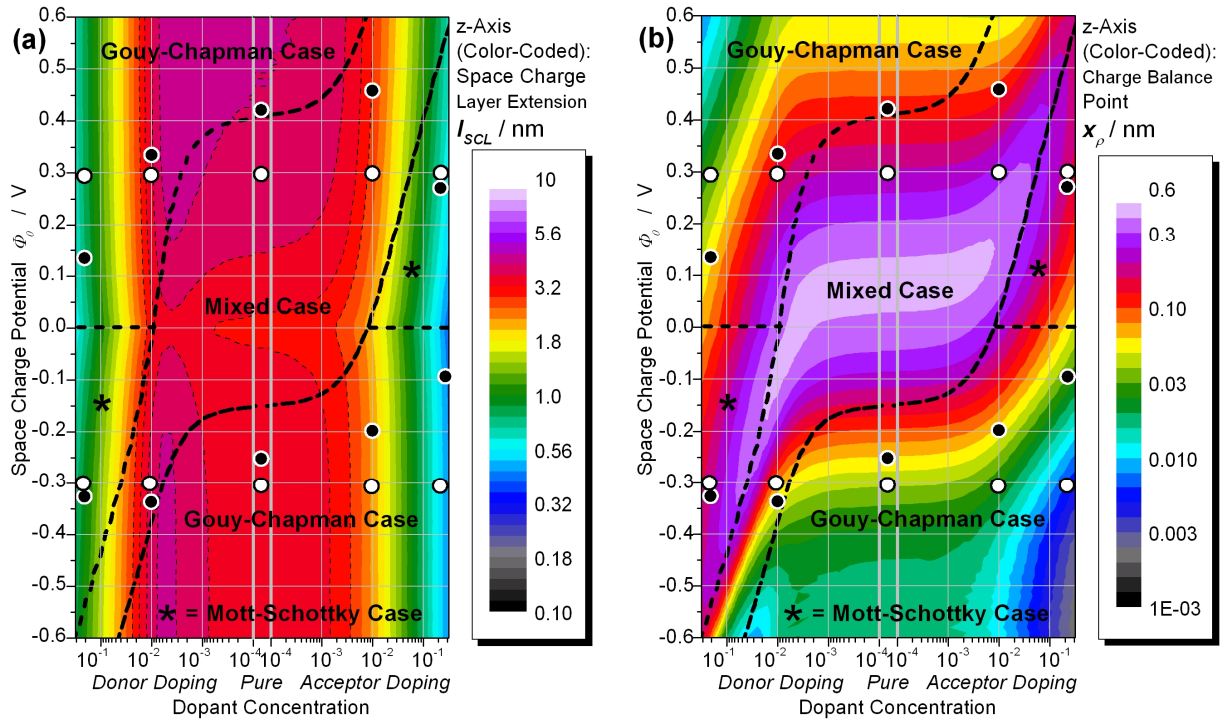


Fig. 23: (a) SCL Extent and (b) Charge Balance Point as a Function of Dopant Concentration and SCL Potential

Similarly to Fig. 22b here the l_{SCL} and x_{ρ} values span a large range of more than one order of magnitude. Therefore, a similar color-code based on a large number of colors and a logarithmic scale are used here too.

The interpretation of the charge balance point x_{ρ} is given in section 5.1.3.4.

The borders between the different cases are taken from Fig. 23a. The circles describe the positions of the SCL profiles given in Table 5 (constant Φ_0 values, circles with white filling) and Table 8 (constant Σ_{SCL} values, circles with black filling).

This is not the only dependency. For constant potentials $s_{V_0^{**},m}$ additionally varies with the doping content. In Fig. 24a it is most evident, that for pure and slightly doped ceria the conductivity stays more or less constant while for high doping contents the SCL effects on the conductivity decrease significantly; an effect that is also observed experimentally.^[12, 101] The origin of this finding is the dopant dependence of the SCL extent (Fig. 23a). Clearly, in the most cases a small SCL of the same potential will influence the total conductivity less strongly compared with a larger one.

The least apparent feature of Fig. 24a is the asymmetric shape. As an example, we can take the maximum of oxygen vacancy enrichment ($s_{V_0^{**},m} > 1000$, green color-code). It is (for potential values between -0.5 V and -0.6 V) around a donor doping content of 10 %. For all other dopant concentrations $s_{V_0^{**},m}$ is much smaller. Similarly on the opposite side of the plot the largest decrease in oxygen vacancy conductivity is observed at an acceptor content of about 5 %.⁴² To

⁴² Here at positive Φ_0 , however, the reduced symmetry is less distinct.

understand this effect it has to be considered that inside the SCL the part of it that mostly affects the total conductivity is the region close to the interface where the enrichment and depletion of CCs is most severe. For very steep SCLs the concentrations quickly approach the bulk values with increasing distance from the boundary. Otherwise, for less steep profiles the large depletion and enrichment which is present close to the interface extends well into the material. Hence, profiles characterized by low steepness values have a larger impact on the conductivity.

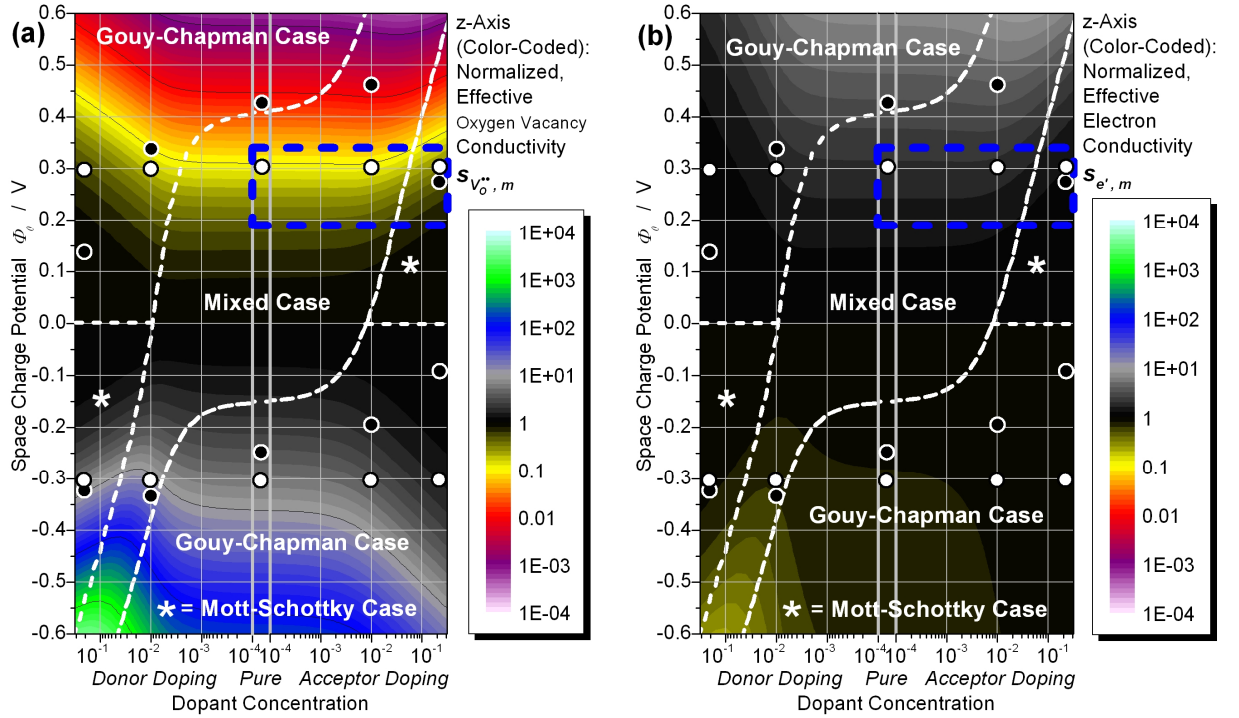


Fig. 24: Normalized Effective Conductivity of the (a) Oxygen Vacancies and (b) Electrons as a Function of Dopant Concentration and SCL Potential, Calculated Using the Numerical Approach

The $s_{i,m} = \sigma_{i,m} / \sigma_{i,\infty}$ values cover more than 6 orders of magnitude and are, hence, plotted logarithmically. Compared with the previous figures a different color-code is used. The region around a potential of 0 V (no or only small SCL effects) corresponds to $s_{i,m} \approx 1$ and a black color-code. For increasing $|\Phi_0|$ values the conductivity effects become significant. This is indicated by the following colors: yellow, red and purple for a conductivity decrease (corresponding to $\sigma_{i,m} \approx 0.1\sigma_{i,\infty}$, $\sigma_{i,m} \approx 0.01\sigma_{i,\infty}$ and $\sigma_{i,m} \approx 0.001\sigma_{i,\infty}$, respectively) and for an increase in conductivity grey, blue and green (corresponding to $\sigma_{i,m} \approx 10\sigma_{i,\infty}$, $\sigma_{i,m} \approx 100\sigma_{i,\infty}$ and $\sigma_{i,m} \approx 1000\sigma_{i,\infty}$, respectively).

The blue rectangle indicates the SCL potential range between 0.20 V and 0.34 V which was observed experimentally in nominally pure and acceptor doped ceria. [10, 14, 16, 17, 98, 99] The borders between the different cases are taken from Fig. 23a. The circles describe the positions of the SCL profiles given in Table 5 (constant Φ_0 values, circles with white filling) and Table 8 (constant Σ_{SCL} values, circles with black filling).

As a result, for a given potential the largest conductivity changes are observed for a steepness value as low as possible in combination with a SCL extent as large as possible. By comparing Fig. 22b with Fig. 23a it becomes clear that this condition is best fulfilled for the region of the

mixed case where indeed for a given potential the highest conductivity changes are found in Fig. 24. The compromise of a large l_{SCL} and a low α value may be roughly quantified as l_{SCL}/α which coincides with the charge balance point x_ρ (eq. {81} and {82}). In Fig. 23b x_ρ is plotted and by comparing with Fig. 24 it can well be observed how, at least qualitatively, the effective conductivity follows this quantity for a given potential value.

In panel (b) of Fig. 24 the effective electron conductivity is shown. Obviously, the electrons are enriched where the oxygen vacancies are depleted. The impact on the effective conductivity is less here due to the lower absolute electron charge number resulting in a smaller concentration change ($n/n_\infty = 1/\sqrt{c_{V_o^{2\bullet}}/c_{V_o^{2\bullet},\infty}}$, see eq. {23}).⁴³

Last but not least, it is useful to check the range of SCL potentials between 0.20 V and 0.34 V, that was found experimentally in pure and acceptor doped ceria (blue rectangle in Fig. 24). [10, 14, 16, 17, 98, 99] Here for the given parameters (temperature and grain size) the oxygen vacancy conductivity is reduced by a factor between 2 and 12 compared with the bulk value (depending on dopant level and potential). This is in agreement with the experimental findings of this study (e.g. see sections 5.3.3.1.2 and 5.4.3).

5.1.3.5 Influence of a Mobile Dopant

Fig. 25 shows how the SCL effects change if the dopant cations are considered to be mobile enough to follow the concentration changes at the SCLs (eq. {22}). In this situation the MS case cannot be realized anymore since the dopant is enriched in the corresponding profiles. Indeed a comparison of Fig. 22a with Fig. 25a shows that exactly the regions of the MS case for immobile dopants are - when the dopant is mobile - characterized by SCLs dominated by the enrichment of the dopant. Therefore, the SCL steepness values in Fig. 25b do not exhibit the low values typical for the MS case. This fact results in much more symmetrical conductivity maps Fig. 25c and Fig. 25d compared with Fig. 24. Only for negative potentials the steepness decreases for strong donor doping which results in a maximum in the conductivity increase of the oxygen vacancies at about 3 % donor doping (which, however, is less pronounced in Fig. 25c than in Fig. 24a). The origin of the steepness decrease here is not a MS case but the difference between the charge numbers of oxygen vacancies (+2) and donor dopant (+1). For negative potentials the oxygen vacancies are particularly strongly enriched (see eq. {22}) leading to very large steepness values for the SCLs dominated by an enrichment of oxygen vacancies. Hence, for an increasing donor dopant level the steepness values get smaller as soon as the charge contribution of the donor dopant becomes significant (compare Fig. 25a and Fig. 25b).

⁴³ n and $c_{V_o^{2\bullet}}$: local electron and oxygen vacancy concentration, respectively

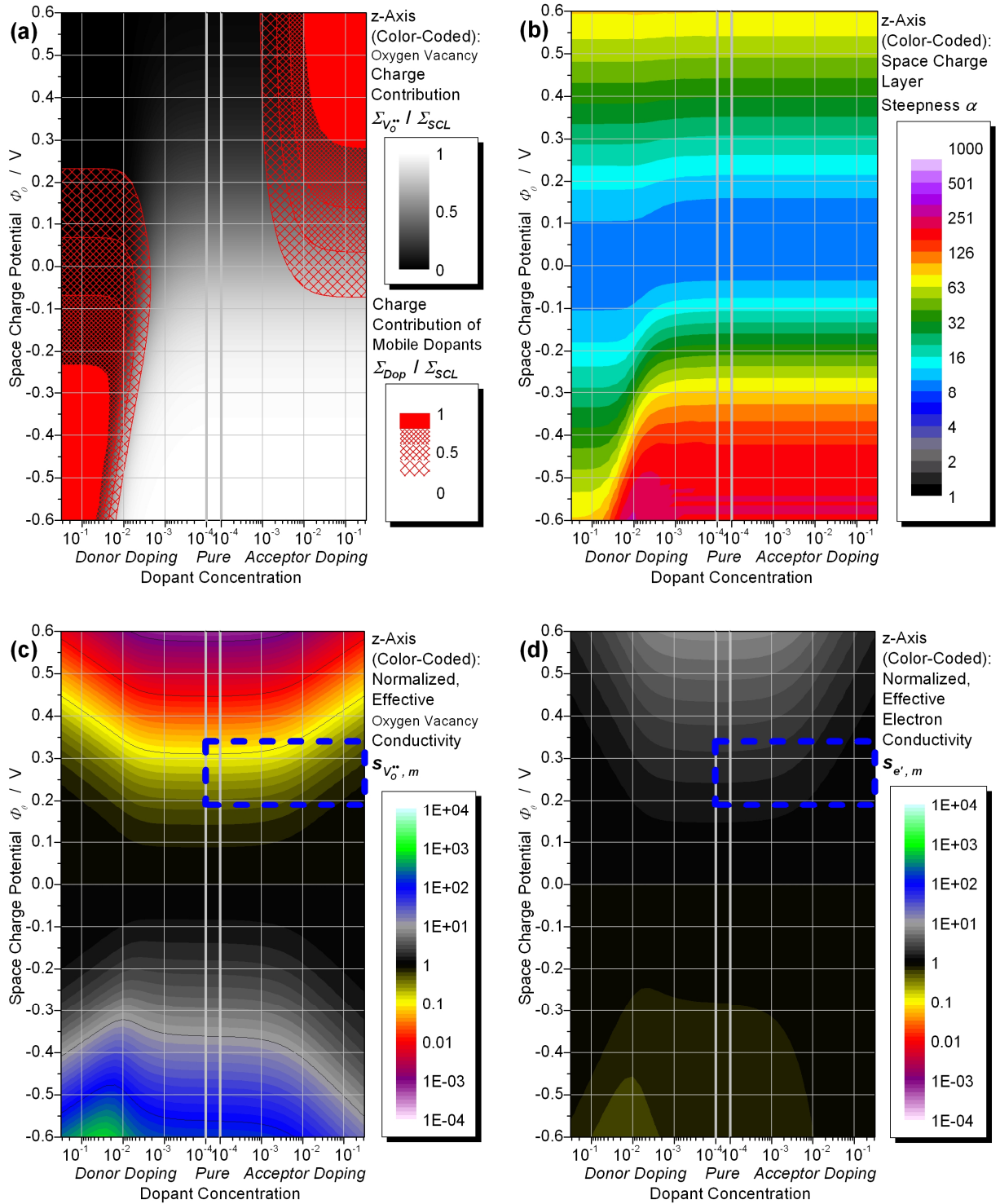


Fig. 25: SCL Characteristics as a Function of Dopant Concentration and SCL Potential, Calculated under the Assumption of a Sufficiently Mobile Dopant Using the Numerical Approach

(a) Oxygen Vacancy and Dopant Charge Contributions

(b) SCL Steepness

(c) Effective Oxygen Vacancy Conductivity

(d) Effective Electron Conductivity

Note that additionally to the charge contribution of the oxygen vacancies panel (a) also shows the charge contribution of the dopant in red color.

The blue rectangle in panels (c) and (d) indicates the SCL potential range between 0.20 V and 0.34 V which was observed experimentally in nominally pure and acceptor doped ceria. [10, 14, 16, 17, 98, 99]

5.1.4 Accuracy of the Analytical Space Charge Layer Solutions

5.1.4.1 Analytical Solutions in the Literature

5.1.4.1.1 Areas of the Different Analytical Approximation Cases

Let us come back to the originally discussed situation of an immobile dopant and examine whether and how strongly the outcomes of the analytical solutions which are derived under further assumptions (see section 5.1.1) deviate from the ones of the numerical approach valid without these assumption. Here firstly the relationships most commonly used in the literature shall be tested. They are given in ref. [22] (see Table 6).

Fig. 26a shows the positions of the different cases in the dopant concentration / SCL potential map. Note that the mixed case cannot be described analytically. Therefore, in comparison with Fig. 22a the area of the GC case is expanded and fills the whole plot. In Fig. 26a the border between the GC case o and the MS case m_2 is given by the line where $n_0 = c_A$. Here $n_0 = n_{\infty} e^{e\Phi_0/k_B T}$ is the local electron concentration at the interface (see eq. {22}). Correspondingly, the condition $c_{V_{O}^{\bullet\bullet},0} = c_D$ (with $c_{V_{O}^{\bullet\bullet},0}$ as the local oxygen vacancy concentration at the interface) separates the cases p and m_1 .

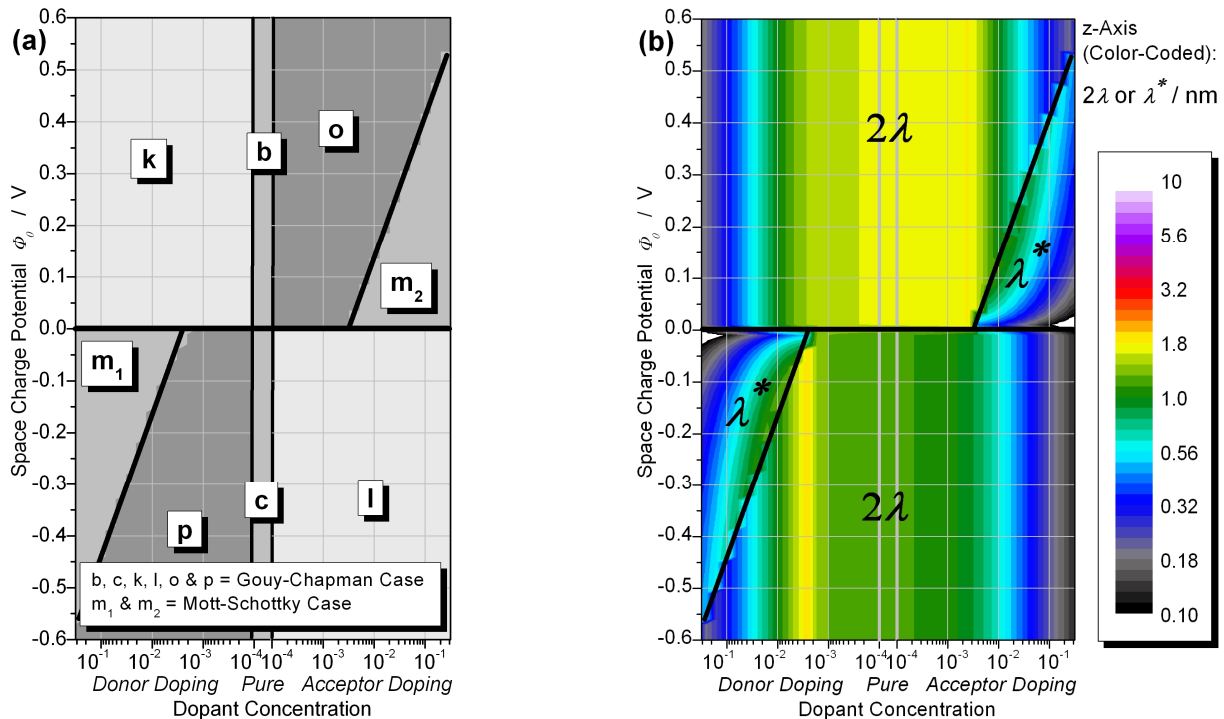


Fig. 26: (a) Areas of the Different Analytical Approximation Cases and (b) Screening Lengths 2λ and λ^* as a Function of Dopant Concentration and SCL Potential

The case designations are in accordance with ref. [22].

Type	Case	Example Profile	Normalized, Effective Oxygen Vacancy Conductivity $s_{V_{O}^{\bullet\bullet},m}$	Normalized, Effective Electron Conductivity $s_{e',m}$
Gouy-Chapman	b		$\frac{1}{2\Gamma^{\perp}\lambda_{V_{O}^{\bullet\bullet}}} \cdot e^{-\frac{3/2 e\Phi_0}{k_B T}}$ {88}	$2\Gamma^{\parallel}\lambda_{e'} \cdot e^{\frac{1/2 e\Phi_0}{k_B T}}$ {89}
	c		$2\Gamma^{\parallel}\lambda_{V_{O}^{\bullet\bullet}} \cdot e^{-\frac{e\Phi_0}{k_B T}}$ {90}	$\frac{1}{2\Gamma^{\perp}\lambda_{e'}} \cdot \frac{k_B T}{-e\Phi_0}$ {91}
	k & o		$\frac{1}{2\Gamma^{\perp}\lambda_{V_{O}^{\bullet\bullet}}} \cdot \frac{n_{\infty}}{c_{V_{O}^{\bullet\bullet},\infty}} e^{-\frac{3/2 e\Phi_0}{k_B T}}$ {92}	$2\Gamma^{\parallel}\lambda_{e'} \cdot e^{\frac{1/2 e\Phi_0}{k_B T}}$ {93}
	l & p		$2\Gamma^{\parallel}\lambda_{V_{O}^{\bullet\bullet}} \cdot e^{-\frac{e\Phi_0}{k_B T}}$ {94}	$\frac{1}{2\Gamma^{\perp}\lambda_{e'}} \cdot \sqrt{\frac{c_{V_{O}^{\bullet\bullet},\infty}}{n_{\infty}}} \cdot \frac{k_B T}{-e\Phi_0}$ {95}
Mott-Schottky	m ₁		$\frac{\Gamma^{\parallel}\lambda_{e'}}{2} \cdot e^{-\frac{2e\Phi_0}{k_B T}}$ {96}	$\frac{1}{\Gamma^{\perp}\lambda_{e'}} \cdot \sqrt{\frac{-e\Phi_0}{k_B T}}$ {97}
	m ₂		$\frac{1}{\Gamma^{\perp}\lambda_{V_{O}^{\bullet\bullet}}} \cdot \sqrt{\frac{2e\Phi_0}{k_B T}}$ {98}	$\Gamma^{\parallel}\lambda_{V_{O}^{\bullet\bullet}} \cdot \frac{e\Phi_0}{e^{\frac{k_B T}{k_B T}}}$ {99}
with $\lambda_{V_{O}^{\bullet\bullet}} = \sqrt{\frac{\epsilon_r \epsilon_0 k_B T}{8e^2 c_{V_{O}^{\bullet\bullet},\infty}}}$ and $\lambda_{e'} = \sqrt{\frac{\epsilon_r \epsilon_0 k_B T}{2e^2 n_{\infty}}}$ {100} ⁴⁴				
— $V_{O}^{\bullet\bullet}$ — e' — Dopant — $V_{O}^{\bullet\bullet}$ (bulk) — e' (bulk)				

Table 6: Analytical Approximations of Non-Overlapping SCL Conductivity Effects in CeO₂ taken from ref. [22]

The case designations are in accordance with ref. [22]. Note that more accurate relationships are given in Table 7. For all cases in Table 6 the dopant is considered to be immobile.

⁴⁴ $\lambda_{V_{O}^{\bullet\bullet}}$ ($\lambda_{e'}$): Debye length with regard to the oxygen vacancies (electrons)

Note that only the quantity λ (Debye length) has a direct physical meaning. Specifically, 2λ is the approximate extent of the SCL in the GC case. The quantities $\lambda_{V_{O}^{\bullet\bullet}}$ and $\lambda_{e'}$ are only defined in order to simplify the equations in Table 6 by summarizing a number of other variables.

5.1.4.1.2 The Space Charge Layer Extent in the Analytical Solutions

In the literature^[1, 22, 94] the quantities plotted in Fig. 26b 2λ (for the GC case, eq. {34}) and λ^* (for the MS case, eq. {33}) are referred to as “effective thickness” of the SCL and in practice they are sometimes used to estimate the extent of the SCL. As an example they are applied to distinguish between non-overlapping and overlapping SCLs (e.g. in ref. ^[21, 51]).

Hence, as a first step it is instructive to check how well 2λ and λ^* correspond to the calculated SCL extent l_{SCL} given in Fig. 23a. Hereby the l_{SCL} value represents the distance from the interface where the integration of the (reciprocal) concentrations yield 99 % of the charge contributions Σ_i (reduced resistances Ω_i) as defined in eq. {79} and {80}. The comparison of Fig. 26b with Fig. 23a yields the following results:

(1) As l_{SCL} also 2λ and λ^* strongly decrease with increasing doping content. (2) Interestingly, for positive SCL potentials 2λ is maximal for small acceptor doping while l_{SCL} is maximal for small donor doping. (3) The slight SCL potential dependence of l_{SCL} in the GC (and mixed) case can not be described with the analytical solutions (i.e. 2λ is potential independent, see eq. {34}). (4) In the MS case the λ^* value reproduces the SCL potential dependence of l_{SCL} . Nonetheless, at low $|\Phi_0|$ values λ^* changes too strongly with the potential in comparison with l_{SCL} . (5) The 2λ and λ^* values are generally smaller than l_{SCL} . Hence, between $x=0$ and $x=2\lambda$ (or $x=\lambda^*$) less than 99 % of the integrated SCLs are regarded.

5.1.4.1.3 Effective Conductivity and Effective Conductivity Change

The effective conductivity values calculated using the equations in Table 6 are displayed in Fig. 27. Qualitatively, the results are similar with the ones in Fig. 24. However, quantitatively there are significant differences. If the equations in Table 6 are strictly applied over a wide potential range a depletion of CCs is predicted where they are enriched and vice versa (crossed area in Fig. 27). This discrepancy originates from the assumption made in the formulae in ref. ^[22] that the effective conductivity is equal to the conductivity change: $\sigma_{i,m}^{\parallel} \approx \Delta\sigma_{i,m}^{\parallel}$ and $\sigma_{i,m}^{\perp} \approx \Delta\sigma_{i,m}^{\perp}$ (compare with eq. {42} and {43}). Clearly, this assumption is valid for strong SCL effects only. Hence, for low $|\Phi_0|$ values a large discrepancy is expected. However, what is apparently unexpected in ref. ^[22] is that this area of low potentials is rather large and in particular extends well into the potential range experimentally observed in CeO₂ (blue rectangle in Fig. 27). Especially, for the electrons nearly for the whole area in Fig. 27b (i.e. even for much larger potentials up to ± 0.6 V) the above assumption cannot be applied. However, it is uncomplicated to avoid this simplification. Hereby the terms {89}, {90}, {93}, {94}, {96} and {99} have to be set equal to $s_{i,m} - 1$ instead of $s_{i,m}$. Terms {88}, {91}, {92}, {95}, {97} and {98} characterizing the depleted CC have to be set equal to $((s_{i,m})^{-1} - 1)^{-1}$.

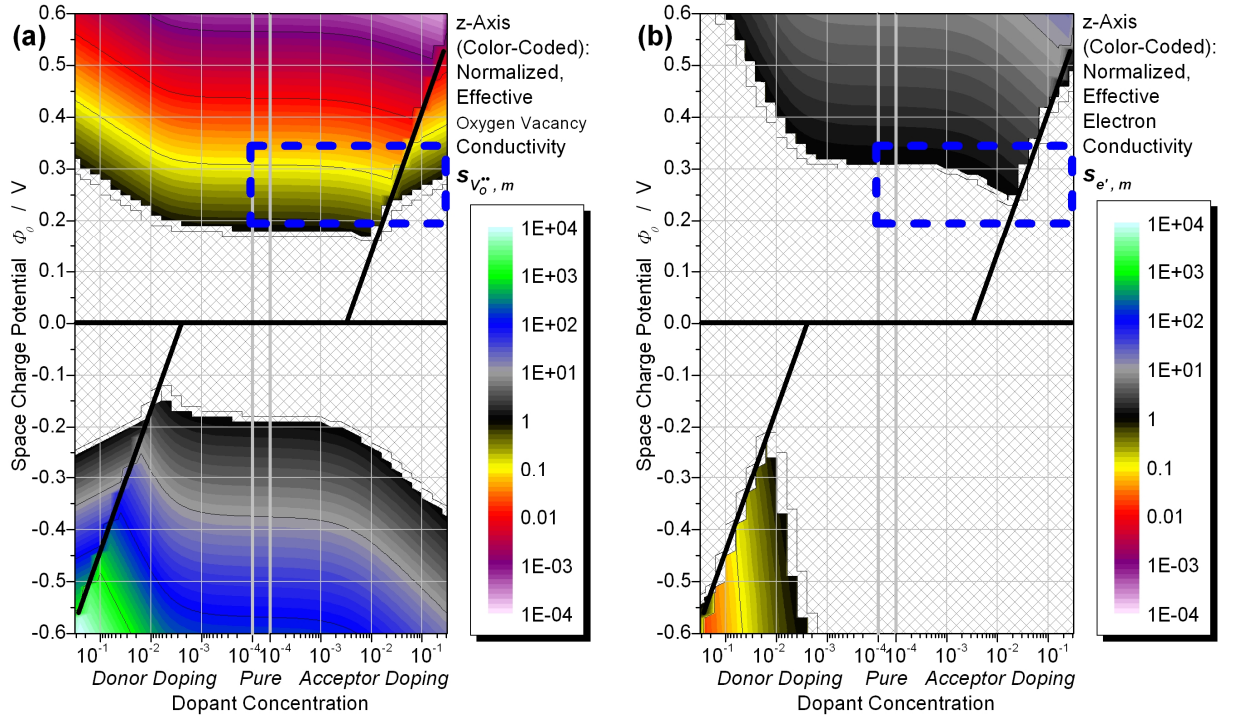


Fig. 27: Normalized Effective Conductivity of the (a) Oxygen Vacancies and (b) Electrons as a Function of Dopant Concentration and SCL Potential, Calculated Using the Analytical Solutions in ref. [22] (Table 6)

The crossed area shows the positions where, if the formulae in ref. [22] (Table 6) are strictly applied, the $s_{i,m}$ values are < 1 although the CC is enriched in the SCLs or where $s_{i,m} > 1$ despite the depletion of the CC (see main text).

The blue rectangle indicates the SCL potential range between 0.20 V and 0.34 V which was observed experimentally in nominally pure and acceptor doped ceria. [10, 14, 16, 17, 98, 99]

5.1.4.1.4 Quantitative Impact of the Assumptions Made in the Analytical Solutions on their Accuracy

After this simple modification of the relationships in Table 6 the conductivity values were calculated once again (Fig. 28). The above discussed uncertainty is clearly not present in Fig. 28 anymore. At first glance, the largest difference between Fig. 24 and Fig. 28 is the distinct border between the GC and MS case in Fig. 28.

A more quantitative view on the accuracy of the analytical approximations is given in Fig. 29a and Fig. 29b, where the deviation values δ are plotted:

$$\text{if CC } i \text{ is enriched: } \delta_i = \frac{s_{i,m}^{Approx} - 1}{s_{i,m}^{Num} - 1} \quad \{101\}$$

$$\text{if CC } i \text{ is depleted: } \delta_i = \frac{(s_{i,m}^{Approx})^{-1} - 1}{(s_{i,m}^{Num})^{-1} - 1} \quad \{102\}$$

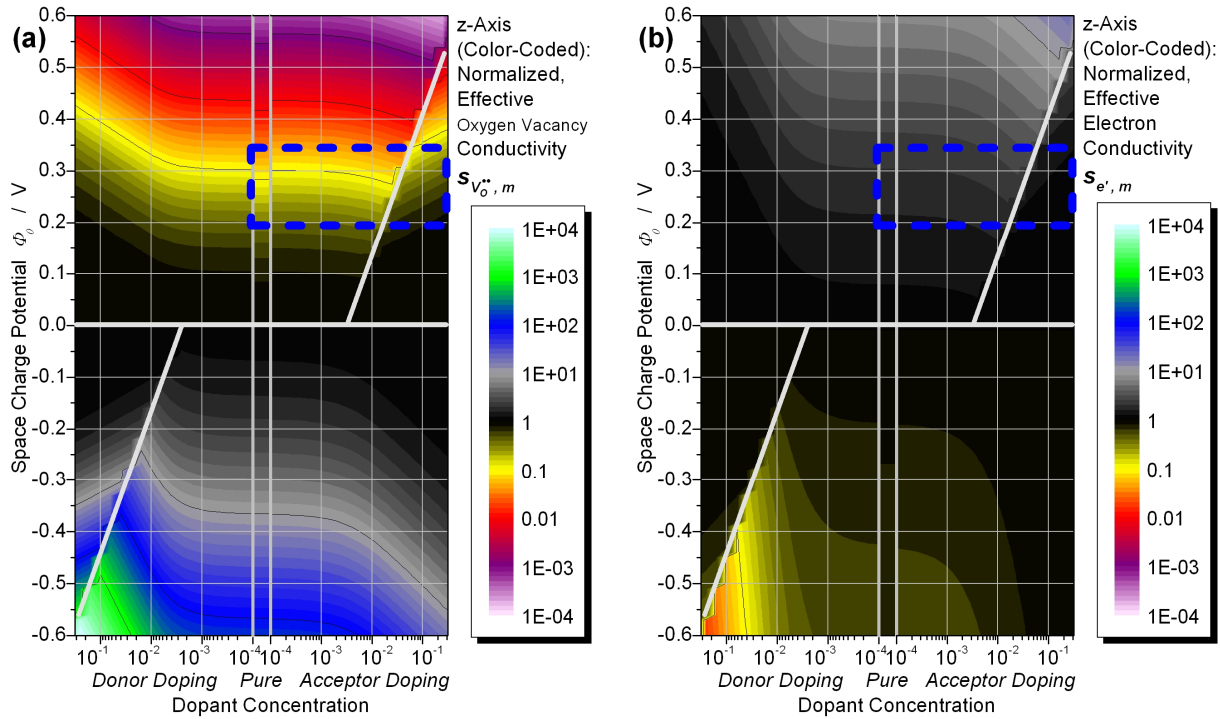


Fig. 28: Normalized Effective Conductivity of the (a) Oxygen Vacancies and (b) Electrons as a Function of Dopant Concentration and SCL Potential, Calculated Using the Analytical Solutions in ref. [22] (Table 6) under Consideration of the Bulk Conductivity Contribution

The blue rectangle indicates the SCL potential range between 0.20 V and 0.34 V which was observed experimentally in nominally pure and acceptor doped ceria.^[10, 14, 16, 17, 98, 99]

Here $s_{i,m}^{Approx}$ are the results of the analytical and $s_{i,m}^{Num}$ the results of the numerical approach. Values of $\delta_i = 1$, $\delta_i < 1$ or $\delta_i > 1$ indicate that the analytical approximations correctly estimate, underestimate or overestimate the effective conductivity change, respectively.⁴⁵

For clarity it is helpful to summarize the deviation values in three regions of different accuracy:

- ✦ In region (1) (green area in Fig. 29c and Fig. 29d) the analytical approximations are very precise and differ by less than 10 % from the numerical approach ($0.9 < \delta_i < 1.1$).
- ✦ In region (2) (yellow area in Fig. 29c and Fig. 29d) the analytically approximations deviate by up to a factor of 2 ($0.5 < \delta_i < 2.0$). Such discrepancies may still be acceptable given that other assumptions like the brick layer model contribute to a systematic error of similar significance.
- ✦ In region (3) the uncertainty exceeds a factor of 2 ($\delta_i < 0.5$ or $\delta_i > 2.0$, red region in Fig. 29c and Fig. 29d). Here the analytically approach does not yield reliable conductivity values.

⁴⁵ As an example, a slight conductivity increase of 5% in the numerical approach and an increase of 10% in the analytical approximations results in a deviance value of $(1.10 - 1)/(1.05 - 1) = 2$.

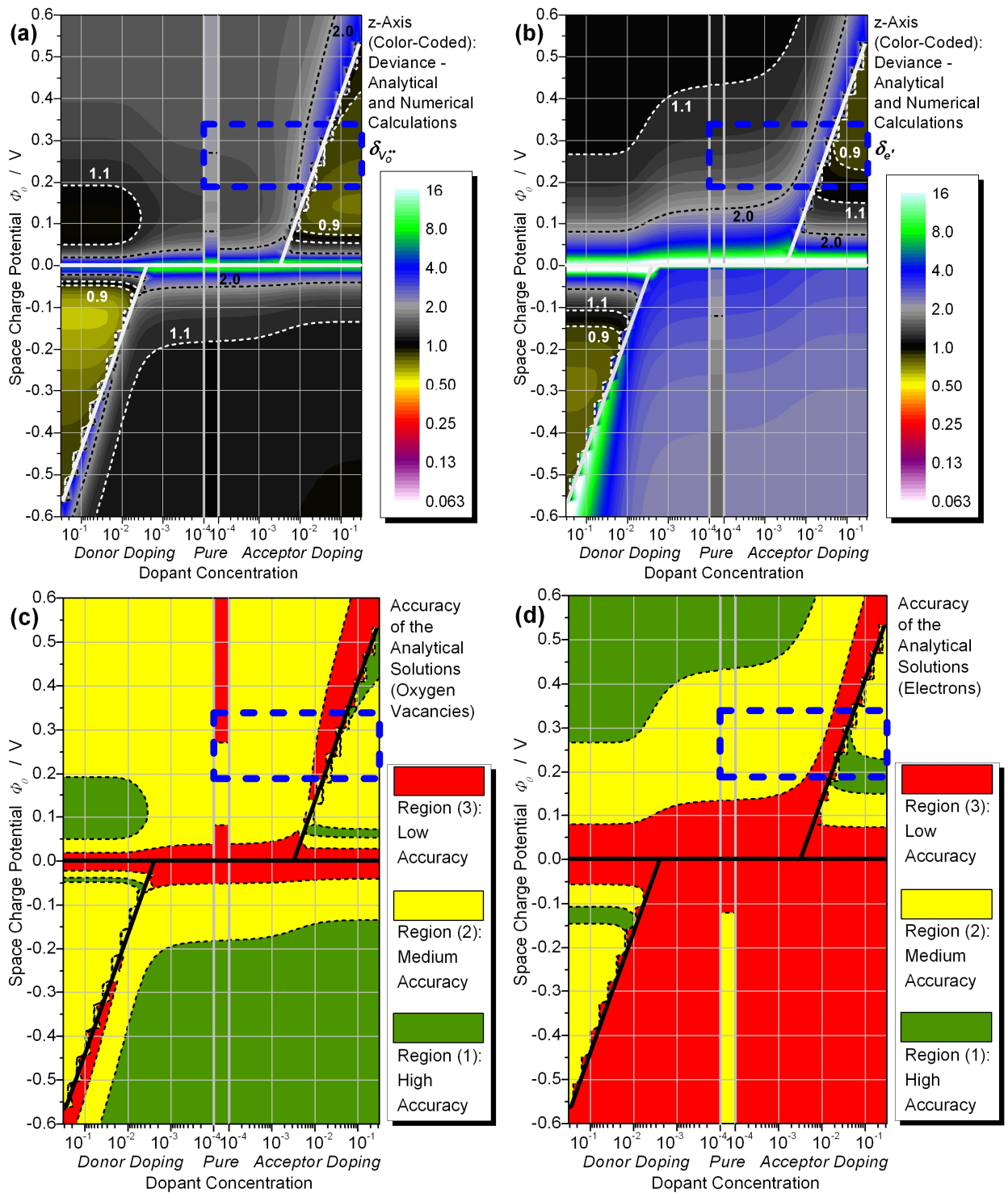


Fig. 29: Deviance δ_i between the Analytical^[221] (Table 6, under Consideration of the Bulk Conductivity) and the Numerical Approach as a Function of Dopant Concentration and SCL Potential

(a) Deviance: Oxygen Vacancies

(b) Deviance: Electrons

(c) Simplified Accuracy Map of the Oxygen Vacancies

(d) Simplified Accuracy Map of the Electrons

In panels (a) and (b) a similar color code compared with Fig. 24, Fig. 27 and Fig. 31 is used. Values of $\delta_i = 1$ (black color) indicate that both approaches yield identical results. If $\delta_i < 1$ ($\delta_i > 1$), the analytical approach underestimates (overestimates) the effective conductivity change as indicated by yellow, red and purple (grey, blue and green) colors.

In panels (c) and (d) the results are summarized in regions of accuracy (1) to (3) (see main text).

There are two main causes, why for several situations the analytical approach in the literature yields uncertain results (see also section 5.1.4.2).

As the first cause the relationships in Table 6 are derived under the assumption of a strong enrichment or depletion effect. Hence, the accuracy of the analytical solutions is particularly low for small exponents $|z_i|e\Phi_0/k_B T$ (see eq. {22}). Therefore, at low potentials their accuracy is limited (see Fig. 29). Additionally, for the electrons with $|z_e|=1$ region (1) of high accuracy is smaller and region (3) of low accuracy is larger in comparison with the oxygen vacancies with $|z_{V_O^{\bullet\bullet}}|=2$. As it will be elucidated in section 5.1.4.2.1 the neglect of the further constant (potential independent) terms in the derivation of the formulae in Table 6 results in a particularly large error in case of eq. {91} and {95} since here the term $z_i e\Phi_0/k_B T$ is not even in the exponent (Fig. 29d, extended red area at negative potentials).

As the second cause the rather crude assumption that the mixed case can be treated identically to the GC case produces a large uncertainty in the region around the border between the MS and GC case in Fig. 29.

In conclusion, while Fig. 29c and Fig. 29d show that the equations in Table 6 for some cases yield precise outcomes they also indicate that for a broad dopant and potential range including the experimentally interesting Φ_0 values the accuracy of the analytical approach is significantly limited. This made it particularly attractive to develop new, improved analytical relationships to model the SCL effects as discussed in section 5.1.4.2.

5.1.4.2 Improved Analytical Solutions

5.1.4.2.1 Gouy-Chapman Case

The analytical solutions of the GC case in Table 6 base on potential function {35} which in principle is only valid for symmetrical situations (i.e. two CCs with $z_{depl} = -z_{maj}$).^[22] Here it was found that two modifications strongly increase the preciseness of this approach.

The resulting terms of the integration (eq. {53} and {55}) of the so obtained concentration profiles contain both Φ_0 dependent and Φ_0 independent contributions. Since the formulae in Table 6 are derived under the assumption of strong SCL effects the constant contributions have been neglected here (e.g. $e^{|e\Phi_0/k_B T|} + const$ is set equal to $e^{|e\Phi_0/k_B T|}$).^[22] Hence, as a first measure to increase the preciseness of the solutions such simplifications should be avoided. This of particular relevance for eq. {91} and {95} since here Φ_0 is not even in the exponent resulting in large deviance values (see the extended red area in Fig. 29d at negative Φ_0).

As a second much more significant modification it is useful to regard the so obtained Σ'_i and \mathcal{Q}'_i values (eq. {113} and {115}-{120} in Table 7, page 65) as preliminary only. The fact that the

potential profile {35} is strictly speaking not valid for asymmetric situations results in an under- or overestimation of the Σ'_i and Ω'_i parameters. It is, nevertheless, possible to substantially correct this error. Here is instructive to consider a special property of the SCL profiles in the GC case. Let us define the sum of all Σ'_i values as preliminary SCL charge Σ'_{SCL} (see eq. {54}). If the SCL effects are under- or overestimated all $|\Sigma'_i|$ and $|\Omega'_i|$ values and, hence, also the Σ'_{SCL} value are expected to be under- or overestimated by approximately the same degree. Since the total SCL charge Σ_{SCL} can be calculated without the use of further assumptions (eq. {28}) it is easy to estimate the degree of under- or overestimation by comparing Σ'_{SCL} with Σ_{SCL} . The Σ'_i and Ω'_i values can then simply be corrected by the factor $\Sigma_{SCL}/\Sigma'_{SCL}$ (see eq. {112}). This correction was found to considerably increase the preciseness of the analytical approach resulting in very accurate conductivity values even for low potentials.

If only the enriched majority CC significantly contributes to Σ'_{SCL} for this CC the equations simplify to the easily understandable relationship $\Sigma_{maj} = \Sigma_{SCL}$ (eq. {114}).

5.1.4.2.2 Mott-Schottky Case

5.1.4.2.2.1 Low Space Charge Potentials

The fact that the so modified formulae of the GC case yield accurate results also for low potentials is significant for the MS case too. Let us here in a thought experiment consider a material with one enriched CC 1 and one immobile CC 2. For simplicity $z_1 = -z_2$ and $c_{1,\infty} = c_{2,\infty}$. If CC 1 is enriched a typical GC case is present. In this case the charge density is given by $\rho = z_1 e c_{1,\infty} \cdot e^{-z_1 e \Phi_0 / k_B T} + z_2 e c_{2,\infty} = z_1 e c_{1,\infty} \cdot (e^{-z_1 e \Phi_0 / k_B T} - 1)$. For low potentials the power $e^{-z_1 e \Phi_0 / k_B T}$ becomes $\approx 1 - z_1 e \Phi_0 / k_B T$ and, thus, the charge density $\rho \approx z_1 e c_{1,\infty} \cdot (-z_1 e \Phi_0 / k_B T)$.

In a reverse situation where CC 1 is immobile and CC 2 is mobile CC 2 will be depleted and the MS case applies. In this case $\rho = z_1 e c_{1,\infty} + z_2 e c_{2,\infty} e^{-z_2 e \Phi_0 / k_B T} = z_1 e c_{1,\infty} \cdot (1 - e^{z_1 e \Phi_0 / k_B T})$. For low SCL potentials it follows that $\rho \approx z_1 e c_{1,\infty} \cdot (1 - (1 + z_1 e \Phi_0 / k_B T)) = z_1 e c_{1,\infty} \cdot (-z_1 e \Phi_0 / k_B T)$. However, this is exactly the same relationship as derived for the GC case above. Therefore, as long as only low $|\Phi_0|$ values are concerned the conductivity effects in the MS case can be treated in good approximation using the same relationships as for the GC case (i.e. eq. {115}-{120}) including the above described correction eq. {112}, see Table 7 for further details). Here with the numerical approach as a reference it was found that this approach yields very precise conductivity values for $e^{|\Phi_0| / k_B T} < 4$.

5.1.4.2.2.2 Moderate and Large Space Charge Potentials

The formulae for the MS case in Table 6 base on the linearization of the potential profile {33}:

$$\Phi = \Phi_0(1 - x/\lambda^*) \quad \{103\}$$

This is a very strong simplification and, hence, more precise relationships are expected if the more realistic parabola profile {33} is used instead. The integration of the resulting e^{-x^2} terms from 0 to λ^* results in the non-elementary inverse error function erfi which is closely related to the error function erf.⁴⁶

Interestingly, the so obtained relationships⁴⁷ were found to produce less precise conductivity values compared with the equations that base on the linear potential profile. The reason for this is given in Fig. 30. On the one hand, eq. {33} results in a too steep potential profile and, hence, in an underestimation of the conductivity change.⁴⁸ On the other hand, close to the interface the linearization of the profile leads to an overestimation of the potential. Apparently, both effects partly compensate each other resulting in more or less precise outcomes.

From a calculus point of view eq. {33} does not well describe the profile function obtained with the numerical approach because it has a different slope at the interface (Fig. 30). In particular, for eq. {33} the slope at $x=0$, which is the electric field $-E_0$, is not equal to the applicable value given in the eq. {28}. Note again that eq. {28} yields a precise value for E_0 without the use of further assumptions. Hence, it is possible to modify the parabola profile in such a way that now at $x=0$ not only $\Phi = \Phi_0$ and $d^2\Phi/dx^2 = -\rho_0/\varepsilon_r\varepsilon_0$ ^{49, 50} but also $d\Phi/dx = -E_0$ under consideration of eq. {28}:

$$\Phi = -\frac{\rho_0}{2\varepsilon_r\varepsilon_0}x^2 - E_0x + \Phi_0, \quad \text{with } E_0 \text{ being determined using eq. {28}, page 15} \quad \{108\}$$

Clearly, eq. {108} reproduces the potential profile of the numerical approach much better than eq. {33} and eq. {103} (Fig. 30). The integration of eq. {108} inserted in eq. {22} from $x=0$ to the minimum of the parabola at $x_{MS} = \Sigma_{SCL}/\rho_0$ yields eq. {121} and {122} in Table 7. Using the numerical approach as a reference these formulas were found to produce much more precise effective conductivity values in comparison with the equations given in the literature (Table 6).

⁴⁶ $\text{erfi}(x) = -i \cdot \text{erf}(i \cdot x)$ (i = imaginary unit) and $\text{erf}(x) = 2/\pi \int_0^x e^{-t^2} dt$

⁴⁷ For CeO₂ they are:

$$\text{case m}_1: s_{V_o^{\bullet\bullet},m} = \Gamma^{\parallel} \lambda_e \sqrt{\pi/2} \cdot \text{erfi}(-2e\Phi_0/k_B T) + 1 \quad \{104\}, s_{e',m} = (\Gamma^{\perp} \lambda_e \sqrt{\pi} \cdot \text{erfi}(-e\Phi_0/k_B T) + 1)^{-1} \quad \{105\}$$

$$\text{case m}_2: s_{V_o^{\bullet\bullet},m} = (\Gamma^{\perp} \lambda_{V_o^{\bullet\bullet}} \sqrt{\pi/2} \cdot \text{erfi}(2e\Phi_0/k_B T) + 1)^{-1} \quad \{106\}, s_{e',m} = \Gamma^{\parallel} \lambda_{V_o^{\bullet\bullet}} \sqrt{\pi} \cdot \text{erfi}(e\Phi_0/k_B T) + 1 \quad \{107\}$$

⁴⁸ In addition to Fig. 30 it is instructive to compare the MS type profiles in Fig. 7 with the ones in Fig. 9. These plots show clearly that eq. {33} results in an increased SCL steepness and a decreased SCL extent.

⁴⁹ Compare with eq. {24}.

⁵⁰ Hereby ρ_0 is the charge density at the interface (see eq. {25} in Table 7 - Parameters).

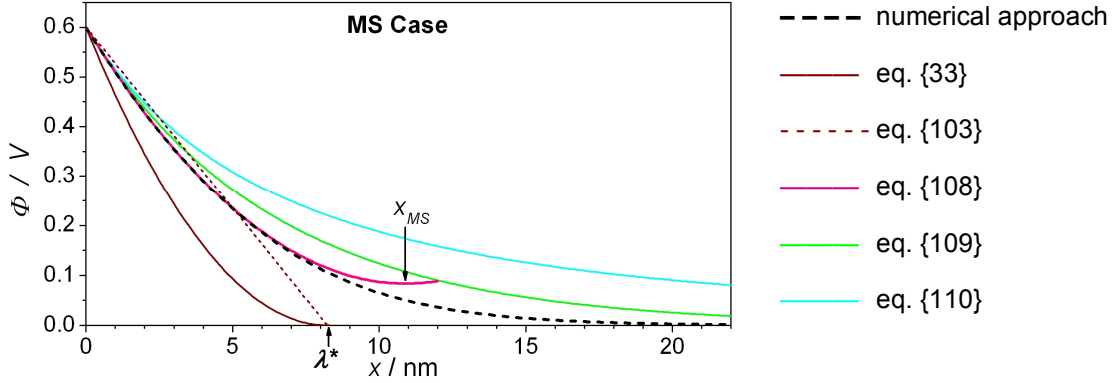


Fig. 30: Example SCL Potential Profiles of the MS Case

Clearly, eq. {33} underestimates the potential profile obtained using the numerical approach whereas eq. {108} deviates much less strongly from this curve.

Additionally to eq. {108} also two other model profile functions with $d\Phi/dx = -E_0$ at $x=0$ were tested which are analytically integrable after inserting them in eq. {22}: $\Phi = \Phi_0 \cdot e^{-x \cdot E_0 / \Phi_0}$ {109} and $\Phi = 4\Phi_0^3 E_0^{-2} / (x + 2\Phi_0 E_0^{-1})^2$ {110}. Nonetheless, they were found to describe the potential profile less accurate compared with eq. {108}.

Parameters: $\Phi_0 = 0.6 \text{ V}$, $\varepsilon_r = 26$, $\theta = 700 \text{ }^\circ\text{C}$, $Z_{Dop} = -Z_{depl} = -1$ and $C_{depl,\infty} = C_{Dop} = 1.25 \cdot 10^{19} \text{ cm}^{-3}$

5.1.4.2.3 Mixed Case

In the literature the border region between the GC and MS case, i.e. the mixed case, is simply described using the GC approach instead.^[22] However, Fig. 29 shows that this method results in highly unreliable results. Therefore, here a better approach to analytically treat the mixed case is suggested. As illustrated in Fig. 10 (page 29) in the mixed case the charge density profile is divided in two regions. Close to the interface (in Fig. 10 for $x < 2.5 \text{ nm}$) the enriched CC dominates the charge density similarly to the GC case whereas for larger x values the charge density profile becomes rather flat and is dominated by the doping content as in the MS case.

Hence, we can define a transition potential Φ_T at which the charge density contribution of the enriched CC just reaches the charge density contribution ρ_{IM} of the immobile (dopant) CCs:

$$\Phi_T = \frac{k_B T}{-z_{maj} e} \cdot \ln \left[\frac{\rho_{IM}}{z_{maj} e c_{maj,\infty}} \right] \quad \{111\}$$

The total Σ_i and Ω_i values can then be expressed as the sum of the GC like contribution (where $|\Phi|$ is larger than $|\Phi_T|$) and the MS like contribution (where $|\Phi|$ is smaller than $|\Phi_T|$): $\Sigma_i = \Delta\Sigma_{i,GC} + \Delta\Sigma_{i,MS}$ and $\Omega_i = \Delta\Omega_{i,GC} + \Delta\Omega_{i,MS}$.

To calculate the MS contribution the same equations as for the real MS case (eq. {121}, {122}) can be used. Here only Φ_0 needs to be replaced by the value of Φ_T .

Effective Conductivities $s_{i,m} = \sigma_{i,m} / \sigma_{i,\infty}$

Enriched Charge Carriers: $s_{i,m} = s_{i,m}^{\parallel}$ with $s_{i,m}^{\parallel} = \Gamma^{\parallel} \cdot \frac{\Sigma_i}{z_i e c_{i,\infty}} + 1$ {40},{57}*

Depleted Charge Carriers: $s_{i,m} = s_{i,m}^{\perp}$ with $s_{i,m}^{\perp} = \left(\Gamma^{\perp} |z_i| e c_{i,\infty} \Omega_i + 1 \right)^{-1}$ {41},{57}*

The geometrical factors Γ^{\parallel} and Γ^{\perp} are given in Table 2.

Gouy-Chapman Case

Correction

$$\Sigma_i = \frac{\Sigma_{SCL}}{\Sigma'_{SCL}} \Sigma'_i \quad \text{and} \quad \Omega_i = \frac{\Sigma_{SCL}}{\Sigma'_{SCL}} \Omega'_i \quad \text{with} \quad \Sigma'_{SCL} = \sum_{i=1}^{N_{Mobile}} \Sigma'_i \quad \{112\}$$

Enriched Majority Charge Carrier

in general: $\Sigma'_{maj} = z_{maj} e c_{maj,\infty} \cdot 2\lambda(A-1)$, $\Omega'_{maj} = \left(|z_{maj}| e c_{maj,\infty} \right)^{-1} \cdot 2\lambda(A^{-1}-1)$ {113}

if all Σ'_i except Σ'_{maj} are very small: $\Sigma_{maj} = \Sigma_{SCL}$ {114}

Depleted Charge Carriers

if $\frac{z_{depl}}{z_{maj}} = -\frac{1}{2}$: $\Sigma'_{depl} = z_{depl} e c_{depl,\infty} 2\lambda \ln \left[\frac{1}{2}(A^{-1}+1) \right]$, $\Omega'_{depl} = \left(|z_{depl}| e c_{depl,\infty} \right)^{-1} 2\lambda \ln \left[\frac{1}{2}(A+1) \right]$ {115}

if $\frac{z_{depl}}{z_{maj}} = -1$: $\Sigma'_{depl} = z_{depl} e c_{depl,\infty} \cdot 2\lambda(A^{-1}-1)$, $\Omega'_{depl} = \left(|z_{depl}| e c_{depl,\infty} \right)^{-1} \cdot 2\lambda(A-1)$ {116}

if $\frac{z_{depl}}{z_{maj}} = -2$: $\Sigma'_{depl} = z_{depl} e c_{depl,\infty} 2\lambda \left(\frac{A^{-3}}{3} + A^{-1} - \frac{4}{3} \right)$, $\Omega'_{depl} = \left(|z_{depl}| e c_{depl,\infty} \right)^{-1} 2\lambda \left(\frac{A^3}{3} + A - \frac{4}{3} \right)$ {117}

Further Enriched Minority Charge Carriers

if $\frac{z_{enr}}{z_{maj}} = \frac{1}{2}$: $\Sigma'_{enr} = z_{enr} e c_{enr,\infty} \cdot 2\lambda \cdot \ln \left[\frac{1}{2}(A+1) \right]$, $\Omega'_{enr} = \left(|z_{enr}| e c_{enr,\infty} \right)^{-1} \cdot 2\lambda \ln \left[\frac{1}{2}(A^{-1}+1) \right]$ {118}

if $z_{enr} = z_{maj}$: $\Sigma'_{enr} = z_{enr} e c_{enr,\infty} \cdot 2\lambda(A-1)$, $\Omega'_{enr} = \left(|z_{enr}| e c_{enr,\infty} \right)^{-1} \cdot 2\lambda(A^{-1}-1)$ {119}

if $\frac{z_{enr}}{z_{maj}} = 2$: $\Sigma'_{enr} = z_{enr} e c_{enr,\infty} \cdot 2\lambda \left(\frac{A^3}{3} + A - \frac{4}{3} \right)$, $\Omega'_{enr} = \left(|z_{enr}| e c_{enr,\infty} \right)^{-1} \cdot 2\lambda \left(\frac{A^{-3}}{3} + A^{-1} - \frac{4}{3} \right)$ {120}

Mott-Schottky Case

Moderate and High Potentials (i.e. $e^{|\phi_0/k_B T|} > 4$)

$$\Sigma_i = z_i e c_{i,\infty} \cdot \left(-x_{MS} - \frac{1}{\rho_0} \cdot \frac{\sqrt{\rho_0}}{\sqrt{z_i}} \cdot \sqrt{\frac{\pi \epsilon_r \epsilon_0 k_B T}{2e}} \cdot e^{\frac{-z_i e}{k_B T} \left(\phi_0 - \frac{x_{MS} E_0}{2} \right)} \cdot \operatorname{erfi} \left[E_0 \frac{\sqrt{z_i}}{\sqrt{\rho_0}} \sqrt{\frac{e \epsilon_r \epsilon_0}{2 k_B T}} \right] \right) \quad \{121\}^{**,*}$$

$$\Omega_i = \frac{1}{|z_i| e c_{i,\infty}} \cdot \left(-x_{MS} + \frac{1}{\rho_0} \cdot \frac{\sqrt{\rho_0}}{\sqrt{z_i}} \cdot \sqrt{\frac{-\pi \epsilon_r \epsilon_0 k_B T}{2e}} \cdot e^{\frac{z_i e}{k_B T} \left(\phi_0 - \frac{x_{MS} E_0}{2} \right)} \cdot \operatorname{erfi} \left[E_0 \frac{\sqrt{z_i}}{\sqrt{\rho_0}} \sqrt{\frac{-e \epsilon_r \epsilon_0}{2 k_B T}} \right] \right) \quad \{122\}^{**,*}$$

Low Potentials (i.e. $e^{|\Phi_0/k_B T|} < 4$)

→ Use the formulae of the Gouy-Chapman case {115}-{120} including the correction, eq. {112}. To calculate λ and A with eq. {34} and {124} set $z_{maj} = -\text{sgn}[\Phi_0]$ and $z_{maj} e c_{maj,\infty} = \rho_{IM}$.

Mixed Case

(1) Determine Φ_T :

$$\Phi_T = \frac{k_B T}{-z_{maj} e} \cdot \ln \left[\frac{\rho_{IM}}{z_{maj} e c_{maj,\infty}} \right] \quad \{111\}$$

(2a) Calculate all values $\Delta \Sigma'_{i,GC} = \Sigma'_{i,\Phi_0} - \Sigma'_{i,\Phi_T}$ and $\Delta \Omega'_{i,GC} = \Omega'_{i,\Phi_0} - \Omega'_{i,\Phi_T}$. Hereby Σ'_{i,Φ_0} and Ω'_{i,Φ_0} are the results of the unchanged equations of the Gouy-Chapman case whereas for Σ'_{i,Φ_T} and Ω'_{i,Φ_T} the Φ_0 values need to be replaced by Φ_T in the respective formulae.

(2b) In analogy determine the $\Delta \Sigma_{SCL,GC} = \Sigma_{SCL,\Phi_0} - \Sigma_{SCL,\Phi_T}$ value.

(2c) Perform the Gouy-Chapman case correction with

$$\Delta \Sigma_{i,GC} = \frac{\Delta \Sigma_{SCL,GC}}{\Delta \Sigma'_{SCL,GC}} \Delta \Sigma'_{i,GC}, \quad \Delta \Omega_{i,GC} = \frac{\Delta \Omega_{SCL,GC}}{\Delta \Omega'_{SCL,GC}} \Delta \Omega'_{i,GC} \quad \text{and} \quad \Delta \Sigma'_{SCL,GC} = \sum_{i=1}^{N_{Mobile}} \Delta \Sigma'_{i,GC} \quad \{123\}.$$

(3) Calculate the quantities $\Delta \Sigma_{i,MS}$ and $\Delta \Omega_{i,MS}$ with the equations of the Mott-Schottky case. Hereby Φ_0 needs to be replaced by Φ_T in the respective formulae.

(4) Add the GC and MS contributions: $\Sigma_i = \Delta \Sigma_{i,GC} + \Delta \Sigma_{i,MS}$ and $\Omega_i = \Delta \Omega_{i,GC} + \Delta \Omega_{i,MS}$.

Parameters

General:

$$\Sigma_{SCL} = -\varepsilon_r \varepsilon_0 E_0, \quad E_0 = \text{sgn}[\Phi_0] \cdot \sqrt{\frac{2k_B T}{\varepsilon_r \varepsilon_0} \left(\sum_{i=1}^{N_{Mobile}} (c_{i,0} - c_{i,\infty}) - \frac{\rho_{IM}}{k_B T} \Phi_0 \right)} \quad \{28\}$$

$$\rho_0 = \rho_{IM} + e \cdot \sum_{i=1}^{N_{Mobile}} (z_i c_{i,0}), \quad \rho_{IM} = e \cdot \sum_{j=1}^{N_{Immobile}} (z_{IM,j} c_{IM,j}), \quad c_{i,0} = c_{i,\infty} \cdot e^{-\frac{z_i e}{k_B T} \Phi_0} \quad \{25\}, \{22\}$$

Gouy-Chapman Case:

$$\lambda = \sqrt{\frac{\varepsilon_r \varepsilon_0 k_B T}{2z_{maj}^2 e^2 c_{maj,\infty}}}, \quad A = e^{-\frac{1/2 z_{maj} e \Phi_0}{k_B T}} \quad \{34\}, \{124\}$$

Mott-Schottky Case:

$$x_{MS} = \frac{\Sigma_{SCL}}{\rho_0} \quad \{125\}$$

Table 7: Improved Analytical Approximations of Non-Overlapping SCL Conductivity Effects

In marked contrast to the analytical solutions in the literature (Table 6, ref. [22]) these relationships were found to be not only very precise for large but also for moderate and small SCL effects. Furthermore they allow for an accurate description of the mixed case.

Hereby *i*, *enr* and *depl* denote an arbitrary, an arbitrary enriched and an arbitrary depleted charge carrier, respectively. *maj* denotes the enriched majority charge carrier in the Gouy-Chapman case.

* The assumptions $s_{i,m} = s_{i,m}^{\parallel}$ and $s_{i,m} = s_{i,m}^{\perp}$ are valid for the usual situation where the grain size *d* is much larger than the extent of the SCLs l_{SCL} . However, if *d* becomes comparable with l_{SCL} (but the SCLs do not yet significantly overlap) both parallel and perpendicular contributions become relevant: $s_{i,m} \approx s_{i,m}^{\parallel} \cdot s_{i,m}^{\perp}$.

** Note that depending on what is the sign of ρ_0 and z_i the term $\sqrt{\rho_0}/\sqrt{z_i}$ is not always equal to $\sqrt{\rho_0/z_i}$.

*** In the less common case that $z_i \cdot \rho_0$ is negative (e.g. for Σ_i of the depleted CC) the argument of the erfi function becomes imaginary and eq. {121} and {122} can be rearranged according to $\text{erfi}(x) = -i \cdot \text{erf}(i \cdot x)$.

For the GC contribution values Σ'_{i,Φ_0} and Ω'_{i,Φ_0} (with Φ_0 inserted as the SCL potential) and Σ'_{i,Φ_T} and Ω'_{i,Φ_T} (with Φ_T inserted as the SCL potential) need to be computed using the relationships of the regular GC case in Table 7. The differences of both quantities $\Sigma'_{i,\Phi_0} - \Sigma'_{i,\Phi_T}$ and $\Omega'_{i,\Phi_0} - \Omega'_{i,\Phi_T}$ then yield (after the correction, eq. {123}) the above mentioned GC contributions $\Delta\Sigma_{i,GC}$ and $\Delta\Omega_{i,GC}$. For further details see Table 7.

Notably, despite the complex nature of the mixed case this approach was found to yield very precise results.

5.1.4.2.4 Accuracy of the Improved Analytical Solutions

The improved analytical relationships are given in Table 7. Fig. 31 shows the conductivities obtained with these formulae. Notably, the improved relationships are able to describe the smooth transition between the GC and MS case (compare Fig. 31 with Fig. 24 and Fig. 28).

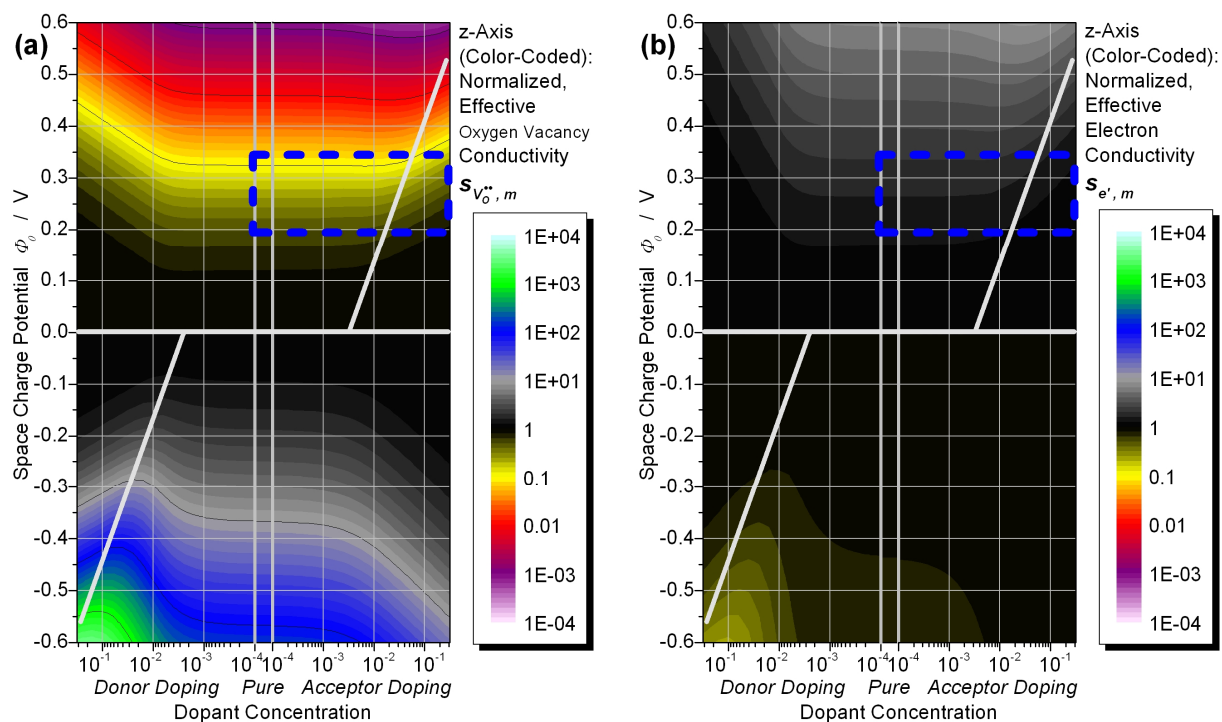


Fig. 31: Normalized Effective Conductivity of the (a) Oxygen Vacancies and (b) Electrons as a Function of Dopant Concentration and SCL Potential, Calculated Using the Improved Analytical Solutions in Table 7

The blue rectangle indicates the SCL potential range between 0.20 V and 0.34 V which was observed experimentally in nominally pure and acceptor doped ceria.^[10, 14, 16, 17, 98, 99]

Fig. 32 displays the divergence between the numerical and the improved analytical approach. It is stunning to observe how strongly the preciseness of the improved analytical approach is

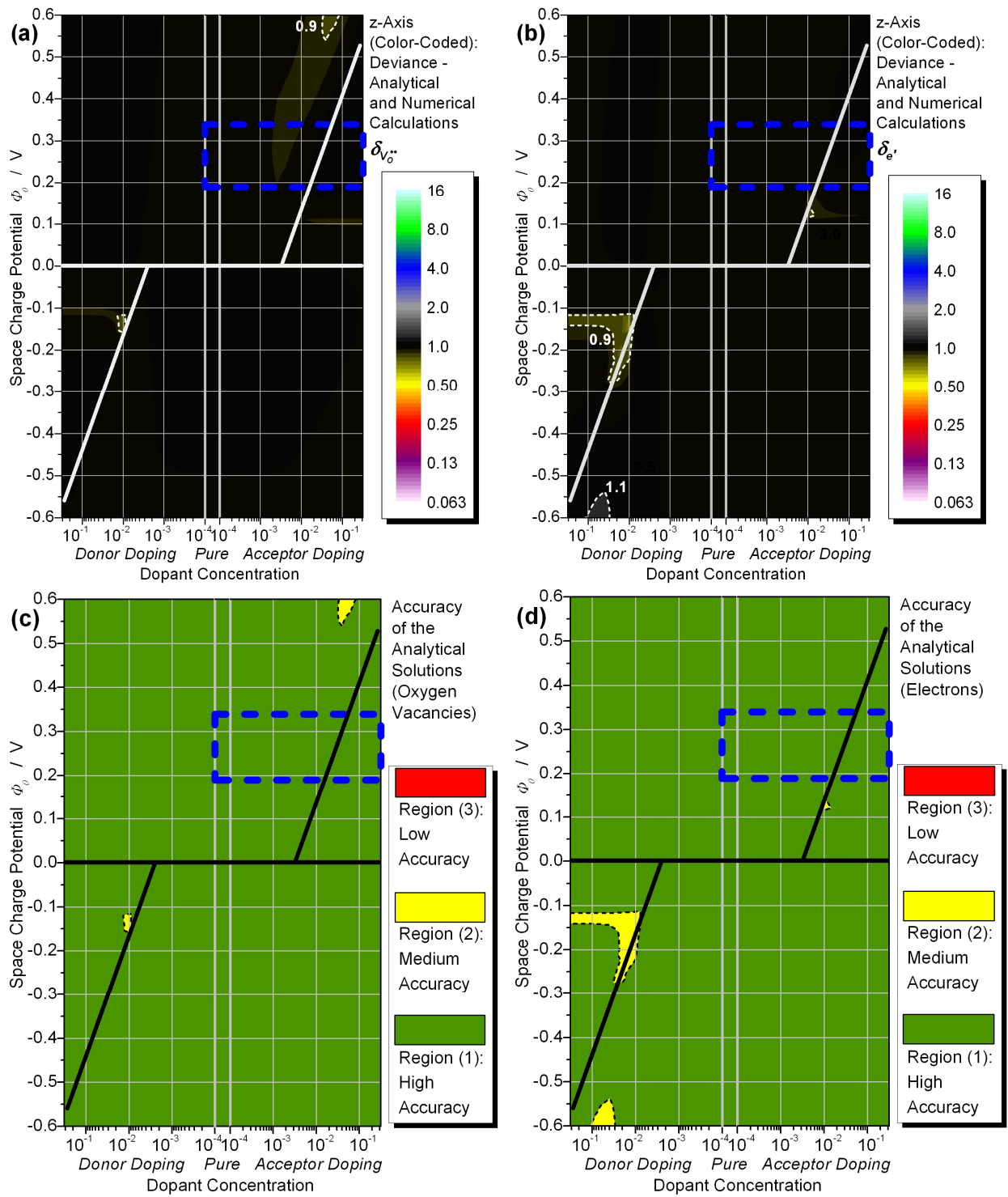


Fig. 32: Deviance δ_i between the Improved Analytical (Table 7) and the Numerical Approach as a Function of Dopant Concentration and SCL Potential

(a) Deviance: Oxygen Vacancies

(b) Deviance: Electrons

(c) Simplified Accuracy Map of the Oxygen Vacancies

(d) Simplified Accuracy Map of the Electrons

In panels (c) and (d) the results are summarized in regions of accuracy (1) to (3) (see main text in section 5.1.4.1.4).

increased in comparison with the formulae in the literature (Fig. 29). Notably, for the improved analytical relationships and the given parameters region (3) of low accuracy vanished completely while region (2) of medium accuracy is strongly diminished and, hence, region (1) of high accuracy (uncertainty < 10 %) covers nearly all cases. Even for very intricate situations which are not describable using the approach in the literature, such as low potentials and the mixed case, the improved formulae yield astonishingly precise results.

5.1.4.2.5 Self Consistency Check for the Analytical Relationships

In the present study the numerical calculations could be used as a reference to check whether the results of the analytical approaches are reliable. For the case that the numerical approach is not available here a self consistency check is suggested.

In analogy to the mixed case it is possible to separate the potential profile function in two or more parts also for the regular GC and MS cases (e.g. to separate it in a part where $|\Phi_0| > |\Phi| > |\Phi_0/2|$ and a second subdivision where $|\Phi_0/2| > |\Phi| > 0$). The separation can result in a larger preciseness of the resulting conductivity value only. Hence, if the values calculated with undivided and divided profiles differ significantly they must be unreliable.

5.1.4.2.6 Space Charge Layers Characterized by Unrealistically Large Concentrations

Using a similar approach as for the mixed case also an approach how to deal with another complex SCL situation which has not been regarded so far shall be proposed here. In the GC (or the mixed) case the enrichment of the majority CC can be so severe that its concentration exceeds the physically realistic maximum value.⁵¹ In order to treat this case analytically we can again separate the potential profile in two parts where firstly $|\Phi_0| > |\Phi| > |\Phi_E|$ and secondly $|\Phi_E| > |\Phi| > 0$: $\Sigma_i = \Delta\Sigma_{i,E} + \Delta\Sigma_{i,GC}$ and $\Omega_i = \Delta\Omega_{i,E} + \Delta\Omega_{i,GC}$. Hereby Φ_E , E_E , ρ_E and x_E are the potential, electric field, charge density and coordinate, respectively, where the concentration of the enriched CC reaches its maximum value $c_{maj,max}$:

$$\Phi_E = \frac{k_B T}{-z_{maj} e} \cdot \ln \left[\frac{c_{maj,max}}{c_{maj,\infty}} \right] \quad \{126\}$$

For the calculation of $\Delta\Sigma_{i,GC}$ and $\Delta\Omega_{i,GC}$ (i.e. the part of the profile where $|\Phi_E| > |\Phi| > 0$) the same relationships given in Table 7 for the GC (or the mixed) case can be used with Φ_0 being replaced by Φ_E .

⁵¹ E.g. in CeO₂ the e' concentration can not surpass the concentration of the cerium cations.

For the contributions $\Delta\Sigma_{i,E}$ and $\Delta\Omega_{i,E}$ (i.e. the profile subdivision close to the interface where $|\Phi_0| > |\Phi| > |\Phi_E|$) the concentration of the enriched CC can be set equal to $c_{maj,max}$. This results in a nearly constant charge density and, thus, in a MS like situation which in good approximation can be described with a similar potential profile as eq. {108}:

$$\Phi = -\frac{\rho_E}{2\varepsilon_r\varepsilon_0}(x - x_E)^2 - E_E(x - x_E) + \Phi_E \quad \{127\}$$

$$x_E = \frac{1}{\rho_E} \left(\varepsilon_r\varepsilon_0 E_E \pm \sqrt{\varepsilon_r\varepsilon_0 (\varepsilon_r\varepsilon_0 E_E^2 - 2\rho_E(\Phi_0 - \Phi_E))} \right) \quad \{128\}$$

Hereby $\Phi = \Phi_0$ at $x = 0$ and $d\Phi/dx = -E_E$, $d^2\Phi/dx^2 = -\rho_E/\varepsilon_r\varepsilon_0$ at $x = x_E$. The enriched majority CC $\Delta\Sigma_{maj,E}$ is then given by eq. {129}:

$$\Delta\Sigma_{maj,E} = z_i e x_E (c_{maj,max} - c_{maj,\infty}) \quad \{129\}$$

For the calculation of the $\Delta\Sigma_{i,E}$ and $\Delta\Omega_{i,E}$ values of the depleted and further enriched minority CCs the integration of eq. {127} inserted in eq. {22} results in similar relationships as eq. {121} and {122} in Table 7:⁵²

$$\Delta\Sigma_{i,E} = z_i e c_{i,\infty} \left(-x_E + \frac{1}{\sqrt{\rho_E} \sqrt{z_i}} \sqrt{\frac{\pi \varepsilon_r \varepsilon_0 k_B T}{2e}} e^{\frac{-z_i e}{k_B T} \left(\Phi_E + \frac{\varepsilon_r \varepsilon_0 E_E^2}{2\rho_E} \right)} \cdot A_{\Delta\Sigma} \right) \quad \{133\}$$

with
$$A_{\Delta\Sigma} = \operatorname{erfi} \left[\frac{\sqrt{z_i}}{\sqrt{\rho_E}} \sqrt{\frac{e}{2\varepsilon_r \varepsilon_0 k_B T}} \varepsilon_r \varepsilon_0 E_E \right] - \operatorname{erfi} \left[\frac{\sqrt{z_i}}{\sqrt{\rho_E}} \sqrt{\frac{e}{2\varepsilon_r \varepsilon_0 k_B T}} (\varepsilon_r \varepsilon_0 E_E - x_E \rho_E) \right] \quad \{134\}$$

$$\Delta\Omega_{i,E} = \frac{1}{|z_i| e c_{i,\infty}} \left(-x_E + \frac{1}{\sqrt{\rho_E} \sqrt{-z_i}} \sqrt{\frac{\pi \varepsilon_r \varepsilon_0 k_B T}{2e}} e^{\frac{z_i e}{k_B T} \left(\Phi_E + \frac{\varepsilon_r \varepsilon_0 E_E^2}{2\rho_E} \right)} \cdot A_{\Delta\Omega} \right) \quad \{135\}$$

with
$$A_{\Delta\Omega} = \left(\operatorname{erfi} \left[\frac{\sqrt{-z_i}}{\sqrt{\rho_E}} \sqrt{\frac{e}{2\varepsilon_r \varepsilon_0 k_B T}} \varepsilon_r \varepsilon_0 E_E \right] - \operatorname{erfi} \left[\frac{\sqrt{-z_i}}{\sqrt{\rho_E}} \sqrt{\frac{e}{2\varepsilon_r \varepsilon_0 k_B T}} (\varepsilon_r \varepsilon_0 E_E - x_E \rho_E) \right] \right) \quad \{136\}$$

⁵² Since constant charge density profiles are likely to occur also in other SCL situations it is instructive to give the general solution of an arbitrary parabola potential profile. For arbitrary coefficients $\gamma_1, \gamma_2, \gamma_3, \xi_1, \xi_2, \xi_3, \nu$ and ψ it is:

$$\Phi = \gamma_1 (x - \xi_1)^2 + \gamma_2 (x - \xi_1) + \gamma_3 \quad \{130\}$$

$$Int = \int_{\xi_2}^{\xi_3} (e^{\psi\nu\Phi} - 1) dx \quad \{131\}$$

$$Int = \xi_2 - \xi_3 + \frac{\sqrt{\pi}}{2\sqrt{\gamma_1} \sqrt{\psi} \sqrt{\nu}} e^{-(\psi\nu) \left(\frac{\gamma_2^2}{4\gamma_1} - \gamma_3 \right)} \left(\operatorname{erfi} \left[\frac{\sqrt{\psi} \sqrt{\nu}}{2\sqrt{\gamma_1}} (\gamma_2 + 2\gamma_1 (\xi_3 - \xi_1)) \right] - \operatorname{erfi} \left[\frac{\sqrt{\psi} \sqrt{\nu}}{2\sqrt{\gamma_1}} (\gamma_2 + 2\gamma_1 (\xi_2 - \xi_1)) \right] \right) \quad \{132\}$$

Hereby $\psi \in \{1, -1\}$ and usually $\nu = -z_i e / k_B T$ (eq. {22}), $\Sigma_i = z_i e c_{i,\infty} \cdot Int$ with $\psi = 1$ (eq. {53}) and $\Omega_i = Int / |z_i| e c_{i,\infty}$ with $\psi = -1$ (eq. {55}).

5.1.4.3 Examples

5.1.4.3.1 Low Space Charge Layer Potentials

The samples discussed in section 5.4 (parameters: $d = 16$ nm, $c_A = 10\%$, $\theta = 700^\circ\text{C}$) show an only rather small conductivity change: $s_{V_0^{**},m} \approx 0.5$. Here the numerical approach yields a potential of 0.19 V. With 0.20 V the improved analytical formulae (Table 7) differ only slightly from this outcome, while with 0.25 V the non-improved equations in Table 6 are much more inaccurate.

5.1.4.3.2 Moderate Space Charge Layer Potentials

The films analyzed in section 5.3.3.1.2 (parameters: $d = 16$ nm, $c_A = 10\%$, $\theta = 700^\circ\text{C}$) exhibit a larger SCL potential of 0.32 V. Let us now check what conductivity values are expected using the different approaches. The numerical solution yields $s_{V_0^{**},m} = 0.077$. Here with values of 0.077 and 0.098 the improved and the non-improved analytical solutions are in very good and acceptable agreement, respectively.

However, for the electrons the conductivity values of the strictly applied, non-improved analytical solutions in Table 6 differ strongly, since due to their lower absolute charge number the assumption of a strong SCL effect (i.e. a large $|z_i|e\Phi_0/k_B T$ term) is less precisely fulfilled than for the oxygen vacancies (see section 5.1.4.1.4). Here the numerical, improved analytical and non-improved analytical approaches yield results of $s_{e^-,m} = 2.06$, 2.06 and 0.90, respectively.

5.1.4.3.3 Mixed Case

Also samples in the mixed case were investigated in this study (section 5.5). For comparability with the two above examples, let us take the same parameters ($d = 16$ nm, $c_A = 10\%$, $\theta = 700^\circ\text{C}$, $\Phi_0 = 0.32$ V) and in a thought experiment decrease the pO_2 until n_∞ increases to $6 \cdot 10^{19}$ cm⁻³. Here n_0 is just above the dopant concentration (for $\Phi_0 = 0.32$ V) and, hence, the SCLs are in the mixed case between the ideal GC and MS cases. Here the numerical approach yields a $s_{V_0^{**},m}$ value of 0.083. With 0.076 the improved analytical solutions are in agreement while the non-improved solutions are imprecise and yield a value of 0.0262.

For the electrons the numerical calculation yields $s_{e^-,m} = 1.98$. Again the improved and non-improved analytical relationships yield precise and imprecise values of 1.96 and 3.38, respectively. For the mixed case the boundary conditions of the non-improved analytical approximations are evidently inadequate while, notably, the improved equations can be used to determine the effective conductivity values. The failure of the non-improved equations is clear in this case as they rely on oversimplified assumptions.

5.1.5 Considerations on the SCL Charge

5.1.5.1 Maximum Value of the SCL Charge in CeO₂

In the literature it is nearly exclusively the SCL potential that is used to characterize SCL effects found experimentally. The reason for this is probably the wide use of analytical solutions (such as the ones in ref. [22]) which allow for a rather simple and direct calculation of the Φ_0 values. However, other parameters such as the SCL charge Σ_{SCL} are also important since in some cases they limit the expected conductivity effects significantly.

Let us firstly consider the maximum value of Σ_{SCL} . If we assume that not more than half of the oxide ions are expected to be missing in the GB core in one (100) plane, this results in an upper limit of $2 \cdot 2e / (5.41 \cdot 10^{-10} \text{ m})^2 \approx 2 \text{ C/m}^2$ for $|\Sigma_{Core}|$ and of 1 C/m^2 for $|\Sigma_{SCL}|$ (with a lattice constant of 5.41 \AA)^[102] (see eq. {18}).

5.1.5.2 Relationship between SCL Potential and Charge

Fig. 33a shows the SCL charge as a function of SCL potential and doping content. Note that for positive potentials the SCL charge becomes negative and vice versa. As expected, $|\Sigma_{SCL}|$ increases with increasing $|\Phi_0|$.

In the MS case the local charge density cannot surpass the dopant value $\rho_{Dop} = z_{Dop} e c_{Dop}$, whereas in the GC case the charge density contribution of the enriched CC usually exceeds ρ_{Dop} . Therefore, the largest $|\Sigma_{SCL}|$ values were observed in the GC case in Fig. 33a. Furthermore, since in the GC case the oxygen vacancies are enriched ($\Phi_0 < 0$) more strongly than the electrons (enriched for $\Phi_0 > 0$),⁵³ for a given $|\Phi_0|$ value the SCL charge is larger for $\Phi_0 < 0$ than for $\Phi_0 > 0$ (Fig. 33a).

For a given potential in Fig. 33a $|\Sigma_{SCL}|$ increases with increasing doping content. At first glance this might be counterintuitive given that the SCL extent decreases with increasing doping content. However, while l_{SCL} is proportional to $(c_{Dop})^{-1/2}$ (compare with λ^* and λ in eq. {33} and {34}) for constant l_{SCL} values Σ_{SCL} is expected to be proportional to c_{Dop} . Hence, for an increasing dopant concentration the decrease of l_{SCL} is overcompensated and $|\Sigma_{SCL}|$ increases. The numerical calculations show that for large doping contents this increase of $|\Sigma_{SCL}|$ can even result in a value that exceeds the maximum value of 1 C/m^2 (indicated by the crossed area in Fig. 33a).

⁵³ due to their charge number of $|z_{V\bullet\bullet}| = 2$ in comparison with $|z_{e'}| = 1$

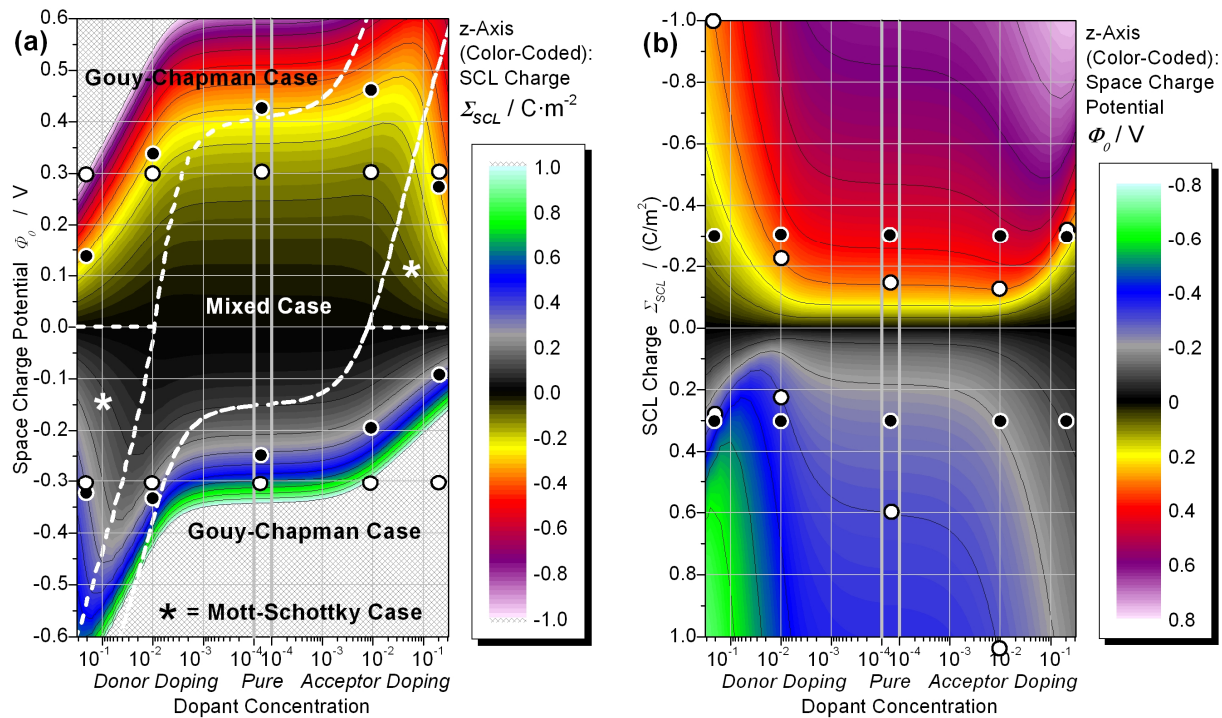


Fig. 33: Relationship between the SCL Potential and the SCL Charge as a Function of Dopant Concentration, Calculated Using the Numerical Approach

(a) SCL Charge Σ_{SCL} as a Function of SCL Potential ϕ_0 (b) SCL Potential ϕ_0 as a Function of SCL Charge Σ_{SCL}
 The crossed area in panel (a) corresponds with $|\Sigma_{SCL}|$ values which exceed the theoretical maximum of $1 C/m^2$ (see main text).

Note that for positive SCL potentials the SCL charge is negative and vice versa.

The color code used here shares some similarities with the one applied in Fig. 24, Fig. 27 and Fig. 31. For both quantities, SCL potential and charge, values around zero indicate very small SCL effects and are color coded black.

The borders between the different cases are taken from Fig. 23a (for plot (a)). The circles describe the positions of the SCL profiles given in Table 5 (constant ϕ_0 values, circles with white filling) and Table 8 (constant Σ_{SCL} values, circles with black filling).

5.1.5.3 Expected Conductivity Effects under Consideration of the SCL Charge

In the MS case due to the upper limit of the charge density of $z_{Dop}eC_{Dop}$, for a given potential the SCL charge becomes minimal for the lowest dopant concentration for which the MS case is still valid. In other words, for a given potential the minimum of Σ_{SCL} is approximately at the border between the mixed and the MS case in Fig. 33a.

Due to this, for a given potential the minimum of Σ_{SCL} nearly exactly falls together with the maximum of the conductivity effect (compare Fig. 33a with Fig. 24). As a consequence, when the effective conductivity is plotted as function of the SCL charge in Fig. 34 the axis asymmetry is even pronounced (compared with Fig. 24). Thus the plots in Fig. 34 exhibit two distinct extrema where the conductivity is changed by more than 4 orders of magnitude.

This asymmetry (e.g. the fact that for constant Σ_{SCL} values the effective conductivity change is strongly dopant dependent) is of large relevance for the way in which SCL effects are able to affect the conductivity. Since for many applications, such as SOFCs, the high ionic conductivity of CeO₂ is crucial, a number of attempts were carried out to modify the GBs in order to improve the conductivity of the polycrystalline material. This includes segregation of aliovalent cations at the GBs,^[50] inhomogeneous doping by GB diffusion,^[53] decoration of the GBs of nanocrystalline ceria,^[51, 52] and use of substrates on which CeO₂ films with only small positive potentials can be grown (section 5.4).

Fig. 34a clearly shows that for strongly acceptor doped ceria the ionic conductivity is drastically reduced for to a positive SCL potential (corresponding with a negative SCL charge) as experimentally observed.^[10, 14, 16, 17, 98, 99] Therefore, a change in the potential (and, hence, in the

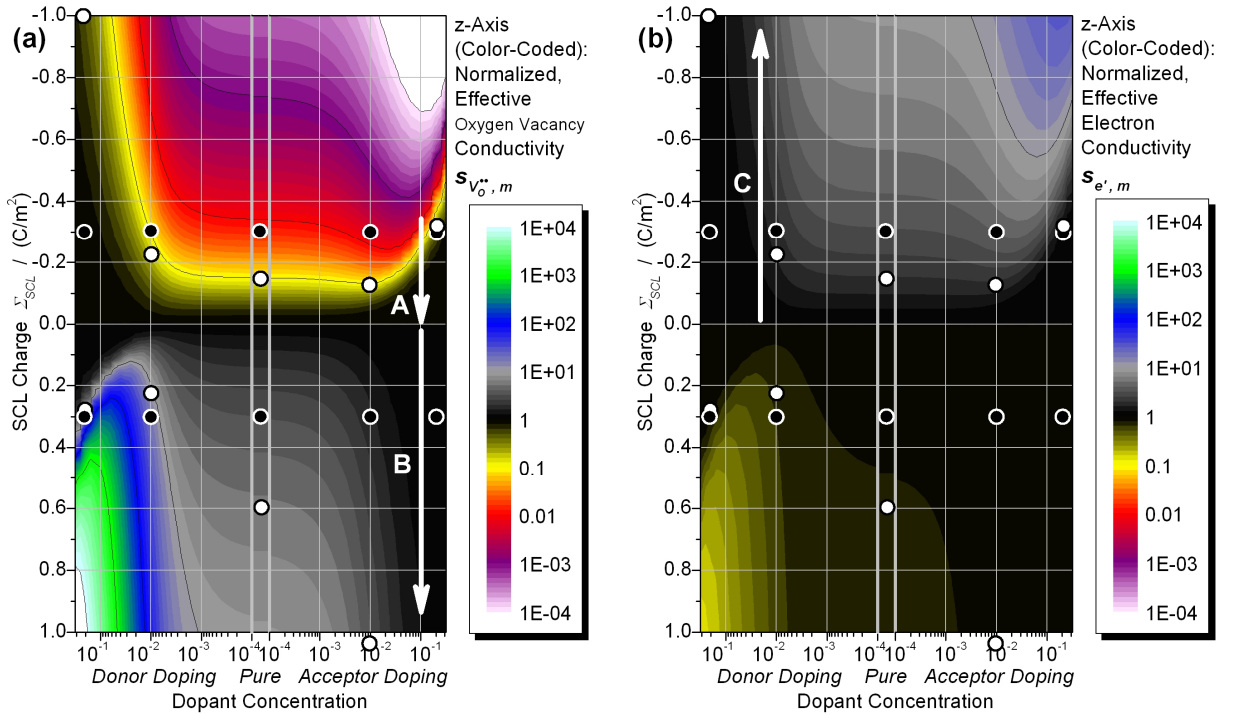


Fig. 34: Normalized Effective Conductivity of the (a) Oxygen Vacancies and (b) Electrons as a Function of Dopant Concentration and SCL Charge, Calculated Using the Numerical Approach

The same color code as in Fig. 24, Fig. 27 and Fig. 31 is used.

A reduction of the positive SCL potential (corresponding with negative Σ_{SCL} values) in strongly acceptor doped CeO₂ is related to a large increase of the oxygen vacancy conductivity (arrow A in panel (a)) until the bulk conductivity is reached ($s_{V_{O^{2-}}, m}^{*} \approx 1$, black color-code). However, for a further decrease of Φ_0 to negative values (positive Σ_{SCL} values) within the realistic charge range, $|\Sigma_{SCL}| < 1 \text{ C/m}^2$, the expected conductivity increase is negligible (arrow B in panel (a)). Correspondingly, in strongly donor doped ceria SCLs with a positive potential (negative Σ_{SCL} values) correlate with a negligibly small increase of the electronic conductivity for $|\Sigma_{SCL}| < 1 \text{ C/m}^2$ (arrow C in panel (b)).

The circles describe the positions of the SCL profiles given in Table 5 (constant Φ_0 values, circles with white filling) and Table 8 (constant Σ_{SCL} values, circles with black filling).

SCL charge) towards a value of zero can indeed strongly increase the ionic conductivity as indicated by arrow A in Fig. 34a. However, after the bulk conductivity is reached even a strong increase in Σ_{SCL} to the limit of 1 C/m^2 (arrow B in Fig. 34a) will not lead to a further significant conductivity increase.

The origin of this consequence is the already high bulk oxygen vacancy concentration. As an example, for a pellet of 20 mol% acceptor doped ceria ($c_A = 5 \cdot 10^{21}\text{ cm}^{-3}$, $c_{V_O^{\bullet\bullet}, \infty} = 2.5 \cdot 10^{21}\text{ cm}^{-3}$) with a grain size of 40 nm the number of oxygen vacancies will not be increased by more than $3 \cdot 10^{20}\text{ cm}^{-3}$ even if the SCLs have the theoretical, maximum charge of 1 C/m^2 . The same effective conductivity can be obtained by just using 22 mol% doped material instead.

To understand this we can also check Fig. 24a again. Here it is indicated that for strongly acceptor doped ceria (e.g. 10 mol% doping content) the ionic conductivity can be increased by one order of magnitude for potential values $\leq -0.5\text{ V}$. However, Fig. 33a shows for such large potentials and for this doping content the resulting SCL charge becomes much larger than 1 C/m^2 . As a matter of fact, as shown in Fig. 33b even for the maximum SCL charge of 1 C/m^2 the corresponding potential value is only -0.2 V and according to Fig. 24a for a potential of -0.2 V no significant conductivity increase is expected in strongly acceptor doped CeO_2 .

Finally, it is worth to consider once more the SCL profiles. The calculated SCL profiles characterized by a constant SCL charge are plotted in Table 8. The comparison with Table 5 (constant SCL potential) shows that the profiles share many similar features but are different in one crucial aspect. The profiles in Table 8 all feature the same area between the curves of the local and the bulk concentrations (under consideration of the defect's charge number). Therefore, here the linear plots of the same case (GC and MS) are all very similar. As a consequence, the logarithmic plots which feature the relative concentration changes are very different. As one example we can take the profile at $+0.3\text{ C/m}^2$ and 20 mol% acceptor doping in Table 8. Here the relative concentration increase of the oxygen vacancies is only minute. Hence, already the profile function itself indicates that for strongly doped samples the SCL effects cannot result in conductivities much larger than the bulk value.

5.1.6 Section Conclusions

Numerical calculations are a powerful and very accurate tool to investigate SCL effects without the necessity to use further simplifications, even for asymmetric and mixed cases.

The dependencies between material parameters, SCL profile characteristics and conductivity effects were investigated over a broad doping content and SCL potential range. Hereby, the SCL steepness α was found to depend on the actual case (GC, MS or mixed) and on the potential, as

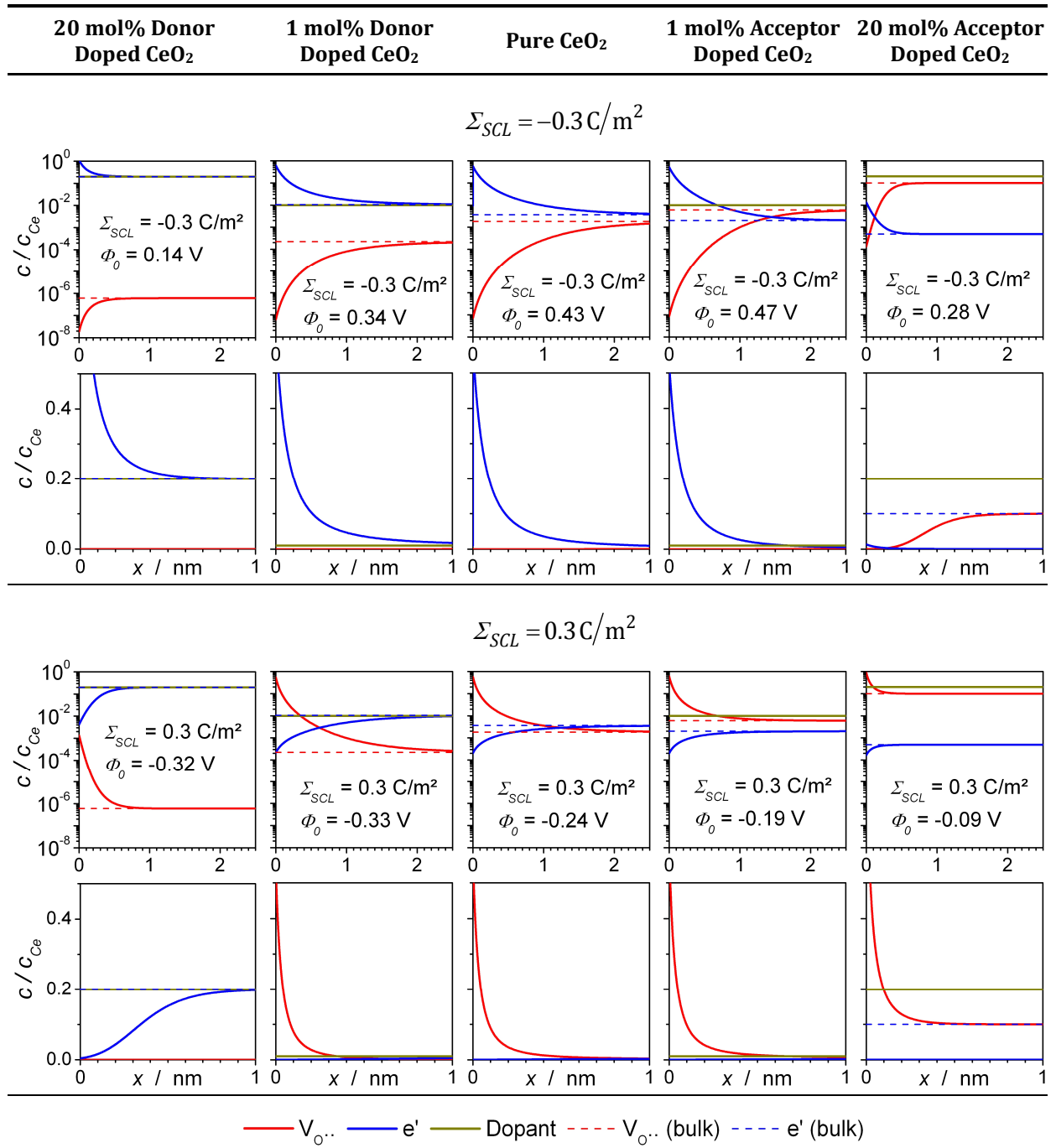


Table 8: Expected SCL Concentration Profiles in CeO₂ Calculated for Constant SCL Charge Values of -0.3 C/m² and 0.3 C/m² Using the Numerical Approach

For each potential value the above graphs are scaled logarithmically and the below graphs linearly.⁴¹

The positions of the profiles are given by the black filled circles in Fig. 22, Fig. 23, Fig. 24, Fig. 33 and Fig. 34.

qualitatively anticipated. For the SCL extent l_{SCL} the clear dependence on the doping content, as expected from the analytical solutions, could be confirmed. However, in comparison with the double Debye length 2λ which in the literature^[1, 22, 94] is regarded as the “effective thickness” of the SCL also in the GC case the SCL extent was observed to be slightly dependent on Φ_0 .

The SCL profile characteristics were found to influence the conductivity effects considerably. As expected, the conductivity effect increases with increasing SCL extent. Furthermore, the calculations indicate that also the steepness α crucially affects the effective conductivity effect which was found to be particularly large for SCLs with low α values. For a given potential the maximum conductivity effects were found in the mixed case since here α is low while l_{SCL} is large.

Interestingly, if the dopant (here with a charge number of ± 1) was considered to be mobile for negative potentials, a similar conductivity trend as above for an immobile dopant was observed, without being in the MS mode. This effect can be explained if one takes into consideration that the oxygen vacancies are enriched particularly strongly due to their higher absolute charge number of +2.

The numerical approach was found to be an ideal instrument to analyze the accuracy of the well known analytical solutions. The preciseness of the analytical approach in the literature was observed to be strongly dependent on the actual case and on the potential. On the one hand, it is most accurate for the enriched CC in the GC case, while, on the other hand, for low potentials and for the mixed case (which is also present in the experimentally observed Φ_0 range) the preciseness was found to be poor.

The comparison between analytical and numerical approach allowed for a test which of the individual aspects of the assumptions made in the analytical approach cause significant uncertainties. Once these aspects were identified more accurate analytical equations could be developed. Remarkably, these improved analytical formulae were observed to be very precise over the whole investigated dopant and potential range, even for complex situations such as low potentials and the mixed case. While the improved analytical solutions were tested for CeO₂ they rest upon fundamental relations and are, hence, expected to work as a general approach also for other materials in which non-overlapping SCL effects are significant.

The impact of the SCL charge was investigated quantitatively. It could be shown that for some cases the limits of the SCL charge restricts the expected excess conductivity strongly resulting in a pronounced asymmetry of them concerning SCL potential and doping content. As an example in strongly acceptor doped CeO₂ for, positive SCL potentials a drastic decrease of the ionic conductivity $s_{V_O^{\bullet\bullet},m}$ compared with the bulk value is expected (as also experimentally observed). However, for the same material and a negative SCL potential $s_{V_O^{\bullet\bullet},m}$ is not anticipated to be significantly increased above the bulk conductivity. This shows that the current attempts to fabricate highly conductive materials by manipulating the SCLs are promising, but only as long as merely the reduction of the conductivity drop at the boundaries is concerned. Using such a “SCL engineering” approach in strongly doped materials, even theoretically, the conductivity is expected to never crucially surpass the bulk value.

5.2 Impedance Spectra

5.2.1 Measured Impedance Spectra

Let us now come to the experimental results of this study. Before analyzing the individual samples and the actual conductivity data in the following four sections 5.3 to 5.6 it is useful to discuss the impedance spectra characteristics which are identical in all experiments of this PhD study. All observed impedance spectra consisted of one semicircle at high frequencies while some of them additionally exhibited a very small low frequency contribution (Fig. 35).

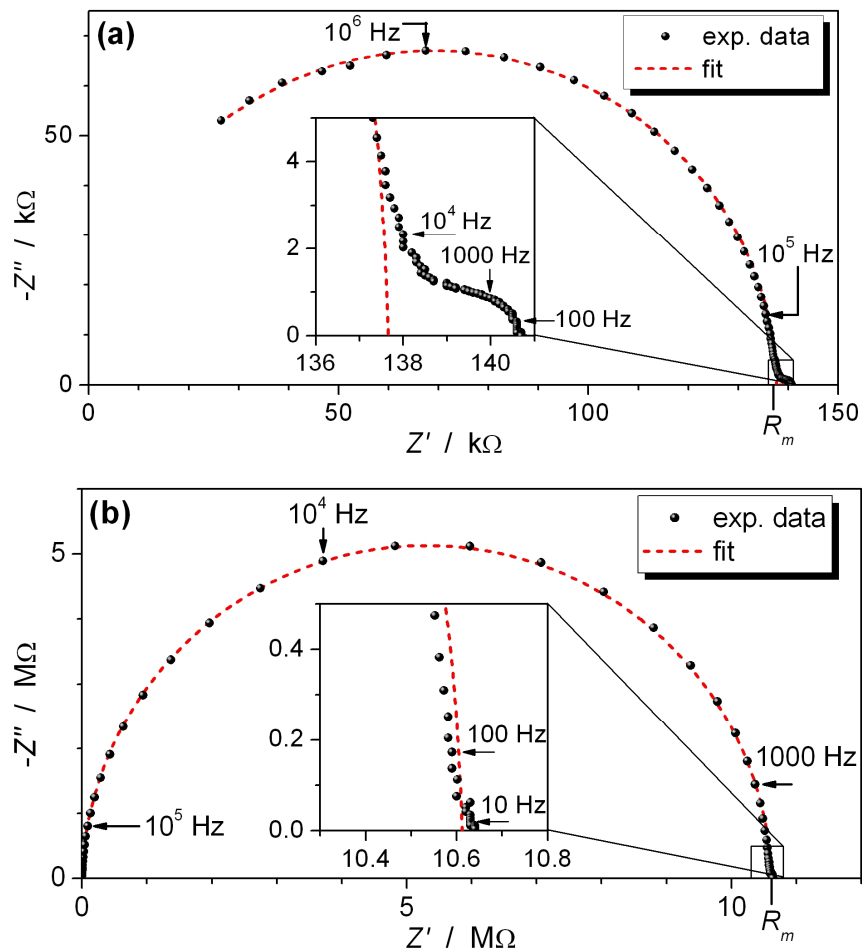


Fig. 35: Typical Impedance Spectra Recorded in this Study

(a) Impedance Spectrum of a 10 mol% Gd Doped CeO_2 Thin Film

The electrode contribution at low frequencies is clearly visible and can easily be separated. For the fit only the data points at high frequencies are considered.

(b) Impedance Spectrum of a Nominally Pure CeO_2 Thin Film

No significant electrode contribution can be observed and all data points are considered for the fit.

For both cases the equivalent circuit in the right panel of Fig. 38 was used as explained below.

5.2.2 Equivalent Circuits

To understand why in most cases only one semicircle is observed let us consider the general equivalent circuit of CeO_2 thin films (Fig. 36). It includes all significant components. For each charge carrier (here oxygen vacancies and electrons) four contributions have to be taken into consideration: the bulk, the perpendicular GBs, the parallel GBs and the electrode. Additionally, there is a contribution from the measurement setup consisting of the stray resistance R_{Stray} and the stray capacitance C_{Stray} .

However, the resistance and capacitance values of the individual contributions vary considerably, often by many orders of magnitude. This makes it possible to strongly simplify the

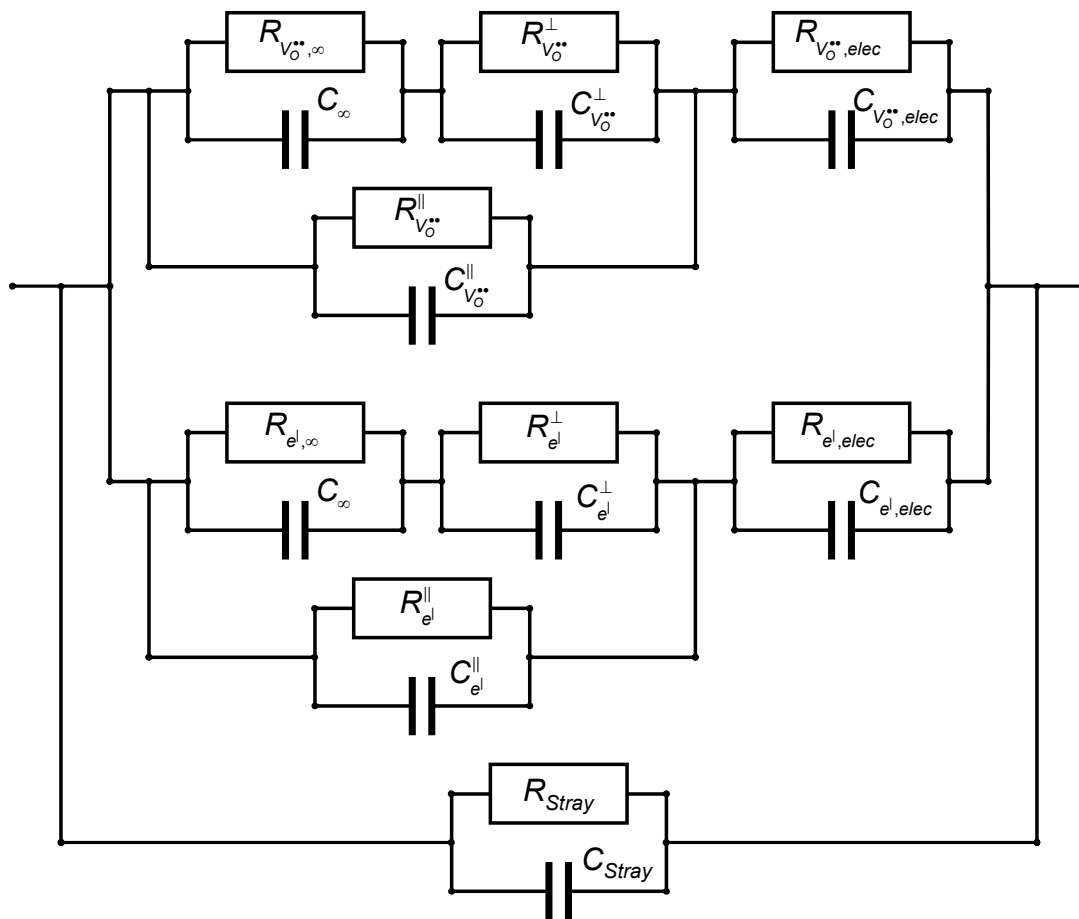


Fig. 36: General Non-Simplified Equivalent Circuit of CeO_2 Thin Films

This equivalent circuit is valid for the in-plane configuration (see Fig. 2 and Fig. 15).^{55, page 81}

C_{∞} : bulk capacitance

$R_{V_{O}^{\bullet\bullet},\infty}$: bulk resistance of the oxygen vacancies, $R_{V_{O}^{\bullet\bullet}}^{\parallel}$ ($C_{V_{O}^{\bullet\bullet}}^{\parallel}$): resistance (capacitance) of the parallel GBs on the oxygen vacancy transport, $R_{V_{O}^{\bullet\bullet}}^{\perp}$ ($C_{V_{O}^{\bullet\bullet}}^{\perp}$): resistance (capacitance) of the perpendicular GBs on the oxygen vacancy transport, $R_{V_{O}^{\bullet\bullet},elec}$ ($C_{V_{O}^{\bullet\bullet},elec}$): resistance (capacitance) of the electrodes on the oxygen vacancy transport

$R_{e^{\bullet},\infty}$, $R_{e^{\bullet}}^{\parallel}$, $C_{e^{\bullet}}^{\parallel}$, $R_{e^{\bullet}}^{\perp}$, $C_{e^{\bullet}}^{\perp}$, $R_{e^{\bullet},elec}$ and $C_{e^{\bullet},elec}$: as above but concerning the electrons instead of the oxygen vacancies

equivalent circuit. Let us firstly focus on the stray resistance and the stray capacitance. As mentioned in section 4.3.5 the measurement cell and the sample holder were optimized in order to increase the stray resistance. The resulting stray resistance values were indeed found to be very large (Fig. 20). Special care, however, has to be taken when extremely thin films of lowly conductive materials (such as nominally pure ceria) are considered. For such samples the thin film's thickness must exceed a certain value to yield reliable conductivity values. For the samples investigated here this evaluation was taken into consideration before preparing the thin films and indeed all samples showed a conductance sufficiently larger than the stray values given in Fig. 20. As a result, the stray resistance can be neglected in the following sections.

Concerning the stray capacitance the situation is very different. For the used measurement cell C_{Stray} was found to be about $2 \cdot 10^{-12}$ F; a value that is rather small in comparison with other measurement cells but still orders of magnitudes larger than the capacitances of the sample. The reason for this is the extremely small thickness of the films in the nano range compared with the macroscopic cell dimensions. As an example the bulk capacitance for a 100 nm thin ceria film can be easily estimated (using $C_{\infty} = \epsilon_r \epsilon_0 L l_2 / l_1$) and is only in the order of 10^{-16} F. The parallel GB capacitances are on the same order of magnitude whereas the perpendicular GB capacitances are merely two orders of magnitude larger: 10^{-14} F.⁵⁴ This implies that it is not possible to distinguish between bulk and GB contributions and that the measured resistance is the sum of these contributions as explained in section 5.2.3.

As expected, the electrode capacitances were found to be much larger than C_{Stray} (about 10^{-10} - 10^{-9} F). Therefore, the resulting impedance spectra are divided into two parts. At high frequencies it is the stray capacitance that dominates the spectrum and at low frequencies – if existing – the electrode contribution (Fig. 37).

The electrode was chosen to be reversible and, hence, to have a minimal resistance. As expected, for dense electrodes prepared using silver paste an electrode contribution was visible while for sputtered, porous, very thin and, hence, reversible Pt electrodes used for the vast majority of the samples investigated here the electrode semicircle did not appear or was only very small (as in Fig. 35a). Only for oxygen vacancy conductors (acceptor doped ceria) the electrode was found to hinder the electric transport and the corresponding second semicircle was observed whereas in electronic conductors (pure and donor doped ceria) the electrodes were observed not to be blocking as expected.

⁵⁴ Given that ϵ_r and the area $L \cdot l_2$ are expected to be constant we can assume $C_1/C_2 = d_2/d_1$, which is specifically $C^{\perp}/C_{\infty} \approx d/l_{SCL}$ here. Thereby, d/l_{SCL} represents the ratio between the grain size and the SCL extent. Since the grain size in the investigated films was observed to be in the order of tens of nm while the SCL extent is expected not to be smaller than a few Å C^{\perp}/C_{∞} is estimated not to be larger than two orders of magnitude.

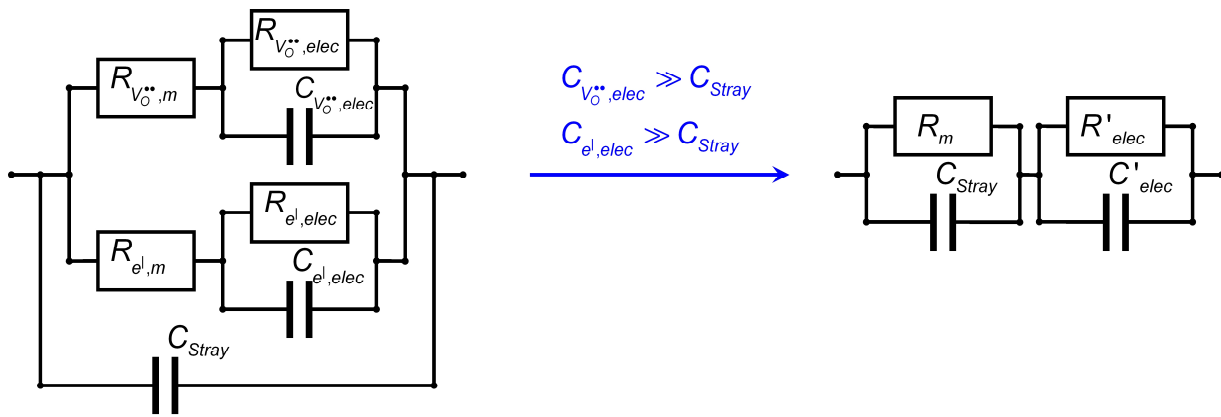


Fig. 37: Simplified Equivalent Circuits of CeO₂ Thin Films with Electrode Resistance Contribution

The equivalent circuit on the left panel bases on the one in Fig. 36 with the simplifications (1) $C_\infty, C_{V_O^{**}}^{\parallel}, C_{V_O^{**}}^{\perp}, C_{e^l}^{\parallel}$ & $C_{e^l}^{\perp} \ll C_{Stray}$ and (2) $R_{V_O^{**},m}$ & $R_{e^l,m} \ll R_{Stray}$. Thereby $R_{V_O^{**},m}$ and $R_{e^l,m}$ are the effective resistances of the oxygen vacancies and electrons, respectively, which comprise bulk and GB contributions: $R_{V_O^{**},m} = ((R_{V_O^{**},\infty} + R_{V_O^{**}}^{\perp})^{-1} + (R_{V_O^{**}}^{\parallel})^{-1})^{-1}$ and $R_{e^l,m} = ((R_{e^l,\infty} + R_{e^l}^{\perp})^{-1} + (R_{e^l}^{\parallel})^{-1})^{-1}$.

Since furthermore $C_{e^l,elec} \gg C_{Stray}$ and $C_{V_O^{**},elec} \gg C_{Stray}$ the equivalent circuit reduces to the one given in the right panel with $R_m = ((R_{V_O^{**},m})^{-1} + (R_{e^l,m})^{-1})^{-1}$. Here R'_{elec} (C'_{elec}) is the effective resistance (capacitance) of the electrodes comprising both the oxygen vacancy and electron transport.

Note that all information relevant for this study (i.e. the bulk and boundary contributions) was given in the total effective resistance R_m (see also below, eq. {137}). Therefore, the spectra in this study were fitted using the equivalent circuits shown in Fig. 38. If necessary, the electrode contribution could easily be separated by considering for the fit the high frequency data points only (Fig. 35a).

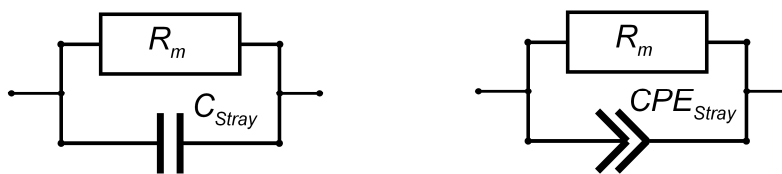


Fig. 38: Two Simplified Equivalent Circuits of CeO₂ Thin Films without Electrode Resistance Contribution

CPE_{Stray} : stray constant phase element

Specifically, the R-CPE circuit in the right panel of Fig. 38 was used. Here the capacitor is replaced by a constant phase element (CPE). CPEs are often applied in solid state ionics. They are used to describe the non-ideal behavior of ionic conductors and base on the assumption that a sample is not only characterized by one relaxation time but by a distribution of relaxation times.^[103, 104] The impedance of the R-CPE circuit is $Z = R \cdot (1 + (i\omega)^\kappa QR)^{-1}$. Here Q is the admittance ($|Z|^{-1}$) of the CPE at $\omega = 1s^{-1}$ and κ describes its degree of ideal behavior. κ is 1 for

an ideal capacitor and in ionic conductors usually values between 0.8 and 1 are observed. In the present study the κ values were found to vary merely slightly from the value of 1 (they were between 0.95 and 1) indicating a nearly ideal behavior of the investigated films.

5.2.3 Total Effective Resistance and Conductivity

In any case the total effective resistance R_m could be determined easily. R_m includes bulk and boundary contributions of both electrons and oxygen vacancies:

$$R_m = \left(\left(R_{V_{O}^{\bullet\bullet},m} \right)^{-1} + \left(R_{e',m} \right)^{-1} \right)^{-1} = \left(\left(R_{V_{O}^{\bullet\bullet},\infty} + R_{V_{O}^{\bullet\bullet}}^{\perp} \right)^{-1} + \left(R_{V_{O}^{\bullet\bullet}}^{\parallel} \right)^{-1} + \left(R_{e',\infty} + R_{e'}^{\perp} \right)^{-1} + \left(R_{e'}^{\parallel} \right)^{-1} \right)^{-1} \quad \{137\}^{55}$$

From the R_m value the total effective conductivity σ_m can be directly determined. σ_m is in general given by eq. {37} and {38}. For the thin film geometry and with regard to eq. {137} it reads specifically:

$$\sigma_m = \frac{l_1}{l_2 L} \frac{1}{R_m} \quad \{138\}^{56}$$

Hereby the individual bulk and boundary resistances correspond to the conductivity contributions introduced in section 2.2.3.2:

$$\sigma_{V_{O}^{\bullet\bullet},\infty} = \frac{J}{R_{V_{O}^{\bullet\bullet},\infty}}, \Delta\sigma_{V_{O}^{\bullet\bullet},m}^{\perp} = \frac{J}{R_{V_{O}^{\bullet\bullet}}^{\perp}}, \Delta\sigma_{V_{O}^{\bullet\bullet},m}^{\parallel} = \frac{J}{R_{V_{O}^{\bullet\bullet}}^{\parallel}}, \sigma_{e',\infty} = \frac{J}{R_{e',\infty}}, \Delta\sigma_{e',m}^{\perp} = \frac{J}{R_{e'}^{\perp}}, \Delta\sigma_{e',m}^{\parallel} = \frac{J}{R_{e'}^{\parallel}} \quad \text{with } J = \frac{l_1}{l_2 L} \quad \{139\}$$

Hence, in general σ_m is given by:

$$\sigma_m = \left(\left(\sigma_{V_{O}^{\bullet\bullet},\infty} \right)^{-1} + \left(\Delta\sigma_{V_{O}^{\bullet\bullet},m}^{\perp} \right)^{-1} \right)^{-1} + \Delta\sigma_{V_{O}^{\bullet\bullet},m}^{\parallel} + \left(\left(\sigma_{e',\infty} \right)^{-1} + \left(\Delta\sigma_{e',m}^{\perp} \right)^{-1} \right)^{-1} + \Delta\sigma_{e',m}^{\parallel} \quad \{140\}^{55}$$

Depending on the sample (doping content, microstructure, etc.) and the measurement conditions most of the contributions in eq. {140} become negligibly small and the relationship falls in several simple cases as explained in detail in section 2.2.3.2. This allowed for the investigation of the boundary effects by comparing the conductivity of two or more samples.

As an example, in an epitaxial, acceptor doped ceria thin film the effective conductivity was found to coincide with the ionic bulk conductivity: $\sigma_m = \sigma_{V_{O}^{\bullet\bullet},\infty}$ (case (i) in section 2.2.3.2). A polycrystalline thin film of the same material additionally included grain boundary

⁵⁵ Not that the here given relationships cover the bulk and GB effects in ceria. In thin films effects at the FSI can add an additional, parallel contribution as discussed in detail in the section 5.3.

⁵⁶ For the definition of the thin film geometry and the geometrical factors l_1 , l_2 and L see Fig. 15.

contributions (case (ii)): $\sigma_m = s_{V_0^{\perp},m}^{\perp} \cdot \sigma_{V_0^{\perp},\infty} = ((\sigma_{V_0^{\perp},\infty})^{-1} + (\Delta\sigma_{V_0^{\perp},m}^{\perp})^{-1})^{-1}$. The comparison of the σ_m values of both films allowed for the separation of the conductivity change at the GBs ($\Delta\sigma_{V_0^{\perp},m}^{\perp}$ and $s_{V_0^{\perp},m}^{\perp} = s_{V_0^{\perp},m}^{\perp}$) and, hence, for the determination of the SCL potential at the GBs (e.g. with Table 7).

Therefore, generally speaking the disadvantage of CeO₂ thin films compared with macroscopic CeO₂ samples (pellets, single crystals) in which the bulk and GB effects can often be distinguished in the impedance spectra is compensated by the easier availability of epitaxial thin films in comparison with macroscopic single crystals.

5.3 Grain Boundary vs. Film Substrate Interface Effects – Cerium Oxide Thin Films on Al₂O₃ <0001> and SiO₂ <0001>

5.3.1 Section Introduction

One of the first experimental studies in the framework of the PhD project was the investigation of film-substrate interface effects in CeO₂ thin films. The general idea behind the study is shown in Fig. 39. In a thought experiment let us firstly assume a series of thin films of the same material but different thicknesses with no effect at the film-substrate interface (FSI). In this case, a plot of the effective conductance values

$$G_m = 1/R_m \quad \{141\}$$

against the film thickness L will result in a straight line going through the plot's origin (black line in Fig. 39). However, if there is a significant conductivity increase (decrease) at the FSI, the data points are expected to be shifted towards higher (lower) values resulting in a positive (negative) intercept of the linear fit on the y-axis.⁵⁷ Therefore, using a conductance vs. thickness plot the bulk conductivity contribution (= slope of the linear fit) and the interface conductivity contribution of the samples (= intercept on the y-axis) can be separated.

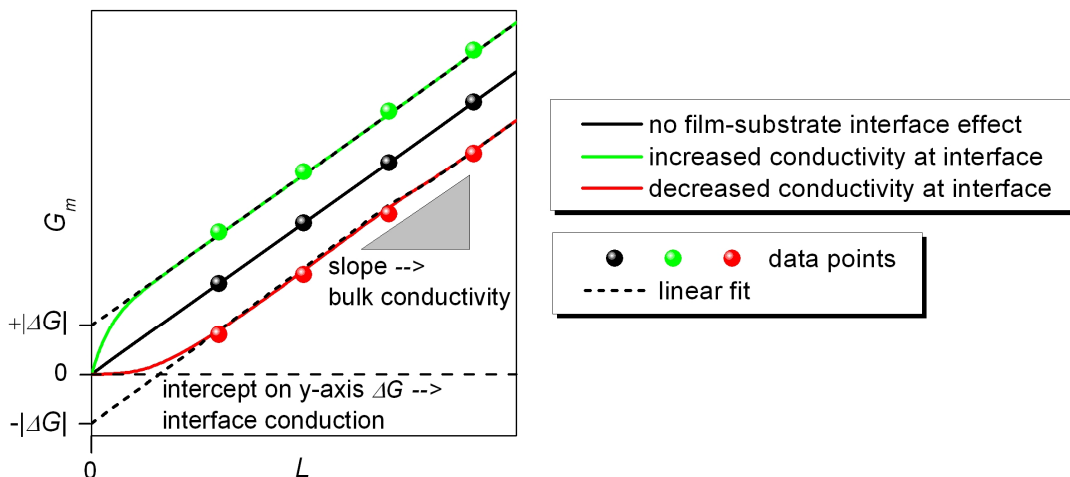


Fig. 39: Idealized Conductance vs. Thickness Plot of Three Series of Thin Films

Reproduced from Göbel et al.^[14] by permission of the PCCP Owner Societies.

⁵⁷ Of course for very small thicknesses the conductance will bend towards the origin of the chart. However, for films with a thickness larger than the extent of the FSI effect this bending is expected not to be perceptible and the linear fit of the data points will have a positive or negative intercept on the y-axis.

Here 4 sets of 4 ceria thin films each were prepared and investigated: Nominally pure and 10 mol% Gd doped samples on two substrates: Al_2O_3 $\langle 0001 \rangle$ and SiO_2 $\langle 100 \rangle$.

5.3.2 Microstructure

The XRD patterns of the films grown on Al_2O_3 $\langle 0001 \rangle$ were found to exhibit strong (111), (222) and (333) CeO_2 reflections (Fig. 40a). Only for very few of these samples weak other orientations were detected. Correspondingly, also the TEM micrographs indicate an epitaxial growth of the films. The epitaxial microstructure of CeO_2 films on Al_2O_3 $\langle 0001 \rangle$ is in agreement with previous studies.^[105, 106] Merely for the thickest films of the series a limited number of wedged shaped grains were found (Fig. 41a) probably due to the relaxation of the structural stress imposed by the lattice mismatch between Al_2O_3 $\langle 0001 \rangle$ and CeO_2 .

For the films on SiO_2 $\langle 0001 \rangle$ the TEM micrographs were observed to show a polycrystalline, columnar growth (Fig. 41b). Correspondingly, the XRD patterns of these samples exhibit a large number of independent reflections due to the multiple oriented grains (Fig. 40b).

Table 9 gives an overview of the results of the TEM and XRD investigations. As expected, the lattice constant of the nominally pure epitaxial films is in agreement with the single crystal value of 5.41 Å^[102] and increases both due to acceptor doping^[107-109] and for the polycrystalline films.^[99, 110-112] Furthermore, an important feature of the two series of films grown on SiO_2 $\langle 0001 \rangle$ is the increasing lateral grain size with increasing film thickness.

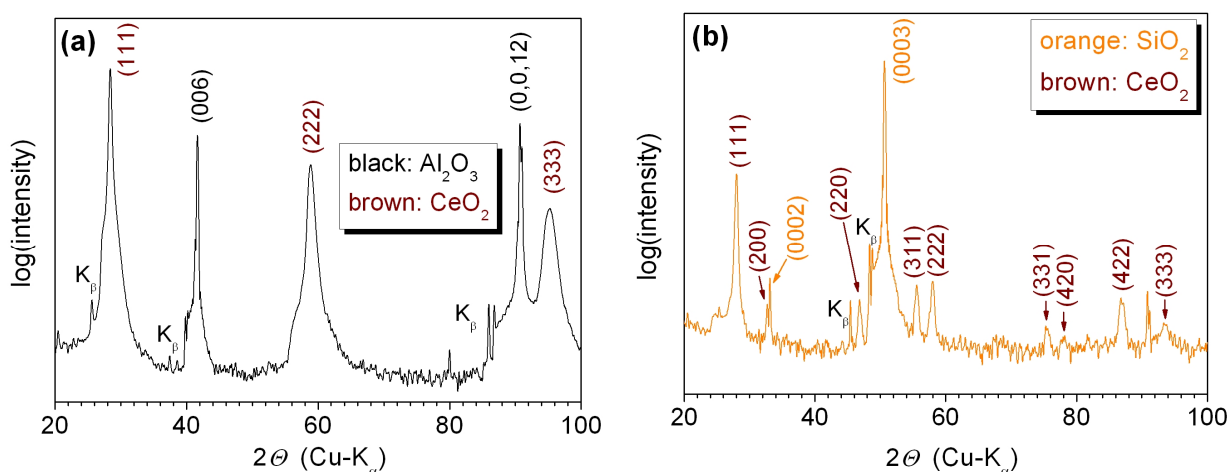


Fig. 40: XRD Patterns of the CeO_2 Thin Films Grown on Al_2O_3 $\langle 0001 \rangle$ and SiO_2 $\langle 0001 \rangle$

(a) Nominally Pure CeO_2 on Al_2O_3 $\langle 0001 \rangle$

(b) 10 mol% Gd-doped CeO_2 on SiO_2 $\langle 0001 \rangle$

The curves have been smoothed for clarity.

θ : Bragg angle, $K\beta$: XRD signals originating from spurious Cu $K\beta$ radiation

Reproduced from Göbel et al.^[14] by permission of the PCCP Owner Societies.

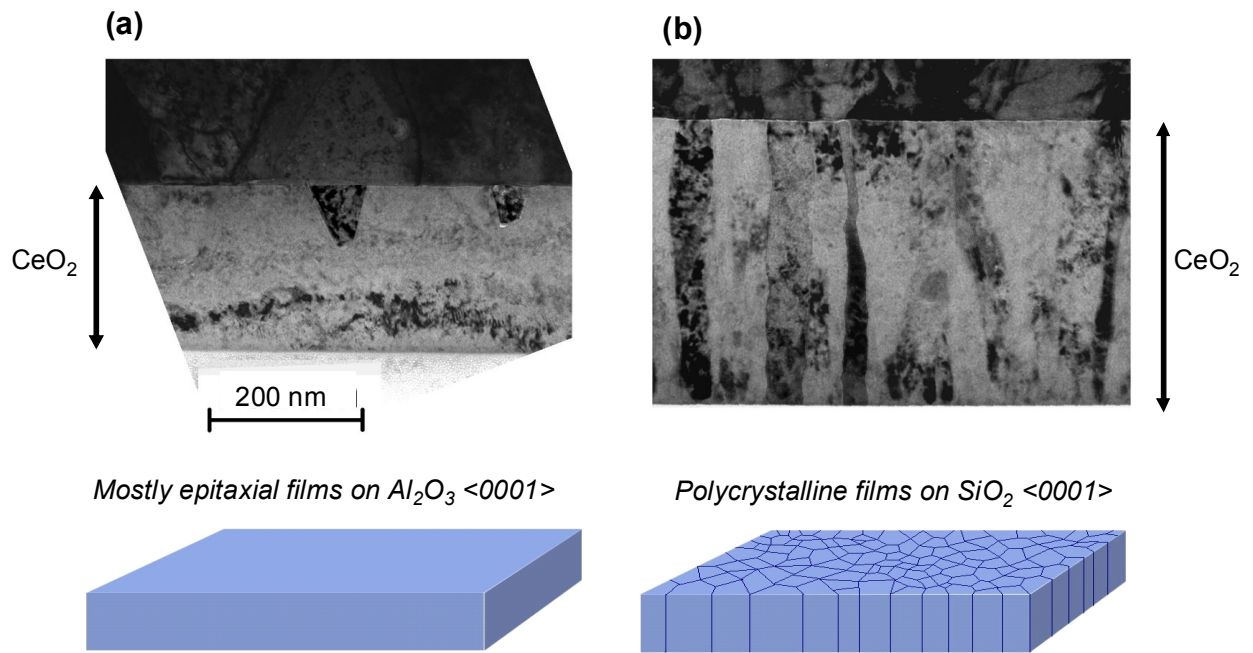


Fig. 41: TEM Micrographs of the CeO₂ Thin Films Grown on Al₂O₃ <0001> and SiO₂ <0001>

(a) Nominally Pure CeO₂ on Al₂O₃ <0001> (Thickness: 214 nm)

(b) 10 mol% Gd Doped CeO₂ on SiO₂ <0001> (Thickness: 347 nm)

From the Top: Pt-Electrode, CeO₂ Thin Film and Substrate

Reproduced from Göbel et al.^[14] by permission of the PCCP Owner Societies.

Substrate	Al ₂ O ₃ <0001>				SiO ₂ <0001>			
	nominally pure		10 mol% Gd		nominally pure		10 mol% Gd	
TEM: Film Thickness <i>L</i> / nm	25	214	45	384	40	197	55	347
XRD: Lattice Constant / Å	5.42	5.41	5.43	5.44	5.46	5.46	5.49	5.51
Microstructure	mostly epitaxial				polycrystalline with columnar grains			
TEM: Lateral Grain Size - Distribution / nm	no grains	*	no grains		7 - 26	19 - 54	6 - 32	18 - 70
TEM: Lateral Grain Size - Statistical Average <i>d</i> / nm	-	-	-	-	16	38	15	39

Table 9: Results of the XRD and TEM Investigation of the CeO₂ Thin Films Grown on Al₂O₃ <0001> and SiO₂ <0001>

* very few wedge-shaped grains at the surface (50 - 100 nm)

Reproduced from Göbel et al.^[14] by permission of the PCCP Owner Societies.

5.3.3 Conductivity Data

5.3.3.1 Acceptor Doped Thin Films

Fig. 42 shows the effective conductivity σ_m as a function of temperature. Let us firstly discuss the Gd doped samples. As expected, for the strongly doped films no pO_2 dependence of the conductivity was found indicating ionic conduction (see defect chemistry regime (I) in Table 1).

5.3.3.1.1 Epitaxial Thin Films on Al_2O_3 <0001>

For the epitaxial films σ_m corresponds to the bulk conductivity ($\sigma_m = \sigma_{V_O^{\bullet\bullet}, \infty}$, case (i) in section 2.2.3.2). As a matter of fact, for the given temperature and doping content the conductivity and activation energy values were found to be typical for the ionic conduction in the bulk of ceria^[40, 74] and in epitaxial films^[113, 114] (see Table 10: 4 S/m at 700°C and 0.7 eV, respectively).

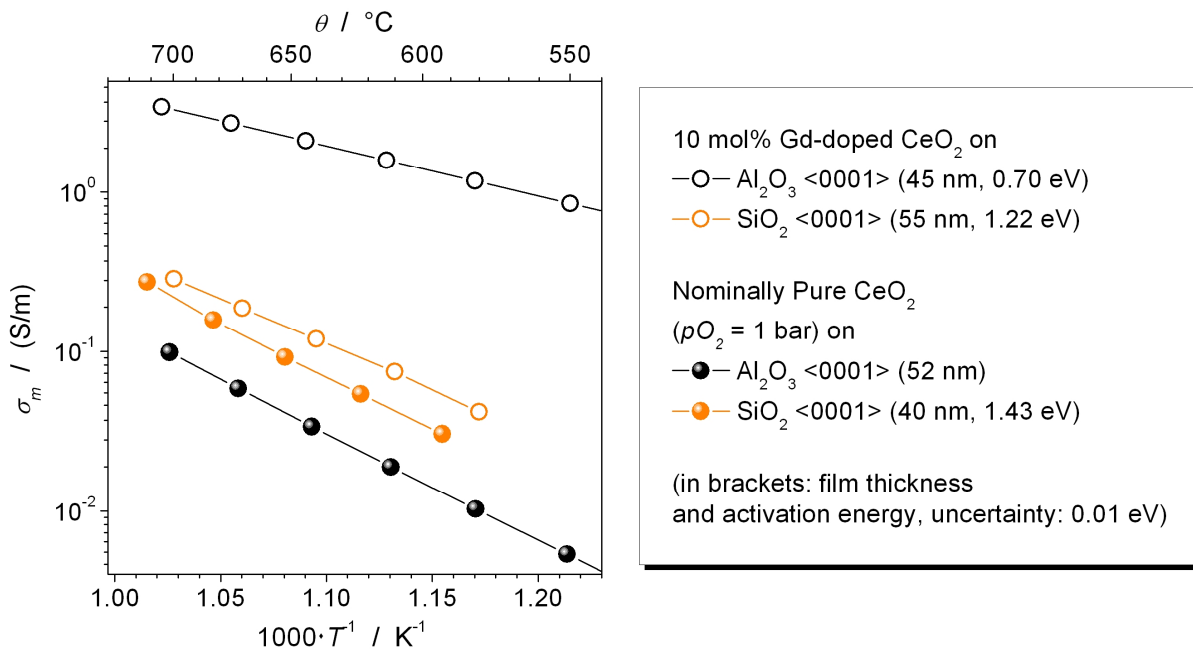


Fig. 42: Temperature Dependence of the Effective Conductivity of Selected CeO_2 Thin Films Grown on Al_2O_3 <0001> and SiO_2 <0001>

Reproduced from Göbel et al.^[14] by permission of the PCCP Owner Societies.

The conductivity and activation energy of the epitaxial films was found to be nearly thickness independent (Fig. 43a-c and Table 10). As a consequence, for these samples the linear fit of the data points in the conductance vs. thickness plot intersects the y-axis at $y=0$ under

consideration of the measurement uncertainty (Fig. 43d). As elucidated in section 5.3.1 this behavior indicates the absence of significant FSI effects on the conductivity.

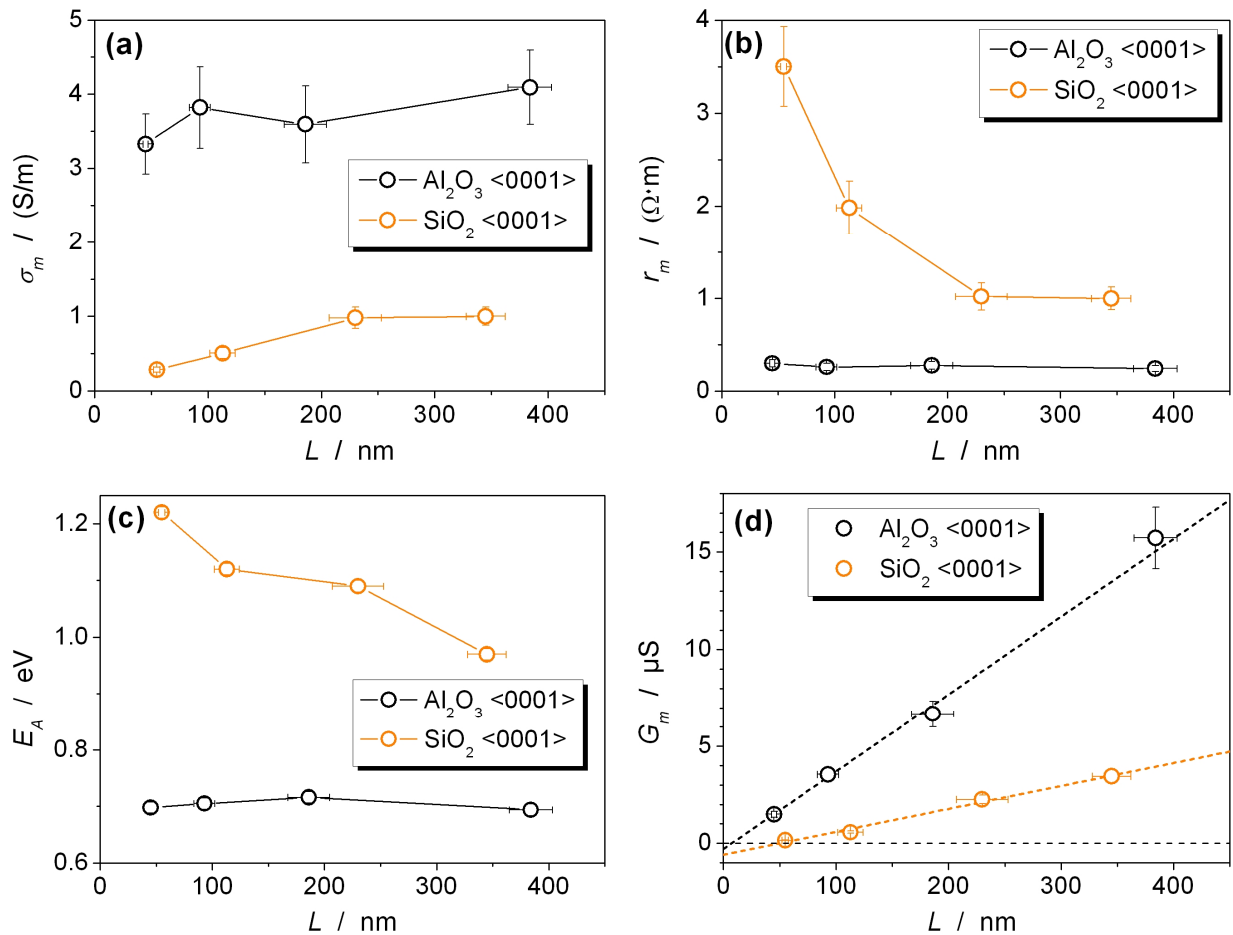


Fig. 43: Thickness Dependence of the Effective Electrical Transport Properties of the 10 mol% Gd-Doped CeO₂ Thin Films Grown on Al₂O₃ <0001> and SiO₂ <0001>

(a) Conductivity vs. Thickness Plot

(b) Resistivity r_m vs. Thickness Plot ($r_m = \sigma_m^{-1}$)

(c) Activation Energy vs. Thickness Plot

(d) Conductance vs. Thickness Plot

Reproduced from Göbel et al.^[14] by permission of the PCCP Owner Societies.

Substrate	Al ₂ O ₃ <0001>				SiO ₂ <0001>				
	Thickness / nm	45	93	186	384	55	113	230	345
Effective Conductivity / (S/m)		3.3	3.8	3.6	4.1	0.29	0.50	0.98	1.0
Activation Energy / eV		0.70	0.71	0.72	0.69	1.22	1.12	1.09	0.97

Table 10: Effective Conductivity at 700 °C and Activation Energy between 700 °C and 550 °C of the 10 mol% Gd-Doped CeO₂ Thin Films Grown on Al₂O₃ <0001> and SiO₂ <0001>

Uncertainties: conductivity ± 10 %, activation energy ± 0.01 eV

Reproduced from Göbel et al.^[14] by permission of the PCCP Owner Societies.

5.3.3.1.2 Polycrystalline Thin Films on SiO₂ <0001>

For the polycrystalline films grown on quartz the situation is very different. Here the electrical conductivity is reduced by roughly one order of magnitude compared with the epitaxial samples (Fig. 42). The origin for the reduced ionic conduction is the well known, positive SCL potential at the perpendicular GBs which is characterized by a depletion of the local oxygen vacancy concentration.^[10, 11, 22] Thus, here case (ii) of section 2.2.3.2 needs to be applied: $\sigma_m = \sigma_{V_{O}^{\bullet\bullet}, m}^{\perp} = ((\sigma_{V_{O}^{\bullet\bullet}, \infty})^{-1} + (\Delta\sigma_{V_{O}^{\bullet\bullet}, m}^{\perp})^{-1})^{-1}$. Under consideration of the conductivity decrease the lateral grains size and other parameters (temperature, dielectric constant, doping level) the value of the corresponding mean SCL potential at the GBs can be calculated using eq. {122} or numerical computations (Chapter 3). For the present samples the calculation results in a potential Φ_0 of (0.32 ± 0.05) V which is in the same range as the values found in other studies for acceptor doped and pure ceria (between 0.20 and 0.34 V).^[10, 16, 17, 98, 99]

In agreement with the strong reduction of the conductivity the activation energy is increased to values between 1.0 and 1.2 eV (Table 10). Such E_a values are typical for polycrystalline acceptor doped ceria.^[6-8, 10-12] Under the assumption of a temperature independent SCL potential for a hypothetical sample which is completely dominated by blocking grain boundaries the activation energy is expected to increase until it reaches a value of $h_{V_{O}^{\bullet\bullet}} + z_{V_{O}^{\bullet\bullet}} e\Phi_0$.^[10] With $h_{V_{O}^{\bullet\bullet}} \approx 0.7$ eV (from the epitaxial films), $z_{V_{O}^{\bullet\bullet}} = 2$ and $\Phi_0 \approx 0.3$ V this leads to maximum activation energy value of 1.3 eV. Hence, the observed activation energies between 1.0 and 1.2 eV indicate the strong yet not entirely dominating influence of the blocking GBs here.

The so far discussed results of both the epitaxial and the polycrystalline films are in accordance with what is expected for these kinds of samples. However, what is stunning about this experiment is the large thickness dependence of the conduction properties of the films on quartz as displayed in Fig. 43. Thus, for decreasing film thickness the resistivity $r_m = \sigma_m^{-1}$ increases by a factor larger than 3 (Fig. 43b). Correspondingly, there is a significant negative intercept of the linear fit on the y-axis in the conductance vs. thickness plot (Fig. 43d) and a strong increase of the activation energy with decreasing thickness (Fig. 43c).

At first glance, as schematically illustrated in Fig. 39 the negative intercept in the G_m vs. L plot is typical for a FSI effect. However, can a SCL at the FSI have such a large impact on the conductivity? Experimentally, we can take the intercept of the linear fit on the x-axis in Fig. 43d as an estimate of the extent of such a hypothetical SCL. It is at about 45 nm. However, for strong doping levels the SCL extent can only be very small; for 10 mol% of Gd doping not more than a few Å (see eq. {33} and Fig. 23). Already this simple argument shows that the negative intercept of the linear fit on the conductance values cannot be the result of a FSI effect.⁵⁸

The origin of this finding is rather the microstructure of the samples. In particular, as shown in Fig. 44 the lateral grain size d is not constant but increases with increasing film thickness L .

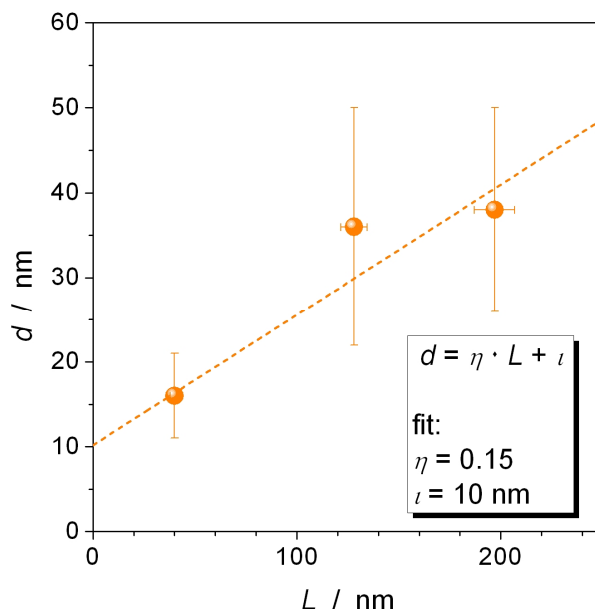


Fig. 44: Thickness Dependence of the Lateral Grain Size d of the Nominally Pure CeO_2 Thin Films Grown on SiO_2 <0001>

Data obtained from the TEM Analysis.

The 10 mol% Gd doped samples exhibit a similar trend with $\eta = 0.08$ and $\iota = 10$ nm.

Reproduced from Göbel et al.^[14] by permission of the PCCP Owner Societies.

This is of major importance for the conductivity as schematically illustrated in Fig. 45. Here the G_m vs. L plot in panel (a) shows the situation of a set of epitaxial films with a (1) unchanged, (2) increased and (3) decreased conductivity at the FSI, as already elucidated before in Fig. 39.

Let us now focus on panel (b). Here line (4) shows the conductance of an epitaxial film with no significant FSI effect and, thus, an intercept on the y-axis at zero. For a polycrystalline film with invariant lateral grain size, line (5), the intercept of the linear fit on the y-axis is at the origin of the plot as well. Nonetheless, due to the blocking GBs, the slope of line (5) is much smaller compared with the epitaxial film, line (4). For the measured samples the lateral grain size increases with thickness. In this case, line (6), the conductance values at small thicknesses are low and comparable with line (5) but then increase more steeply with increasing film thickness. Of course also this bent curve (6) goes through the origin of the plot. However, since

⁵⁸ This does not mean that there is no FSI effect present in the samples. However, such an effect cannot be sufficiently strong to explain the large thickness dependence of the conduction properties.

experimentally only a finite number of data points can be recorded in a certain thickness range these may easily be fitted linearly as illustrated in panel (b). For this situation the result of the linear fit will always give a negative intercept on the y-axis despite the absence of FSI effects.

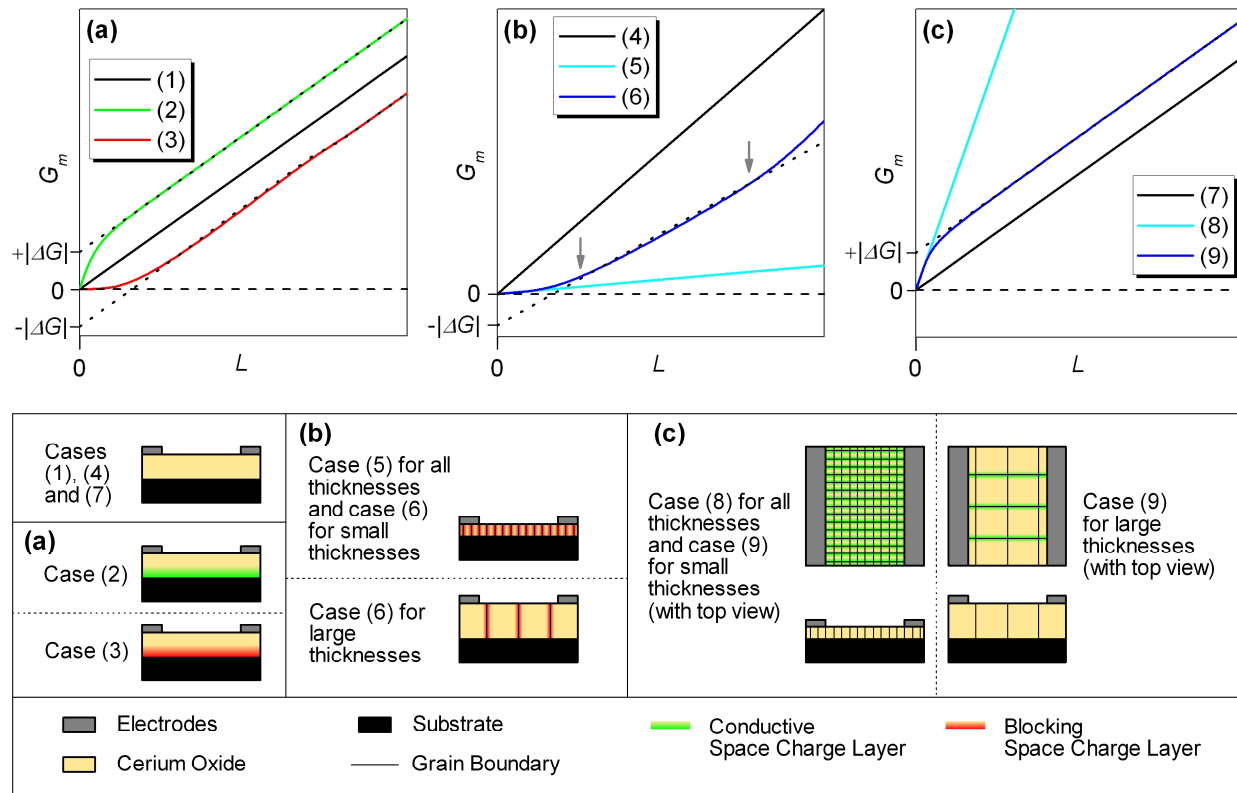


Fig. 45: Schematic Conductance vs. Thickness Diagrams of CeO₂ Thin Films

(a) Influence of FSI Effects on the Effective Conductance

(b) Influence of GB Effects on the Effective Conductance of Strongly Acceptor Doped CeO₂

(c) Influence of GB Effects on the Effective Conductance of Nominally Pure CeO₂

Case (1): epitaxial film (or polycrystalline film with columnar grains of identical shape and lateral size) without FSI effect

Case (2): like case (1) but with a conductive FSI effect

Case (3): like case (1) but with a blocking FSI effect

Cases (4) and (7): epitaxial film (without FSI effect)

Cases (5) and (8): polycrystalline film with columnar grains of the identical, small lateral size (blocking GBs in the case of doped CeO₂ and conductive GBs in the case of nominally pure CeO₂) (without FSI effect)

Cases (6) and (9): polycrystalline film with columnar grains of increasing lateral size with film thickness (without FSI effect)

In the cases (8) and (9) the perpendicular conductive space charge layers have been omitted for clarity.

Reproduced from Göbel et al.^[14] by permission of the PCCP Owner Societies.

More quantitatively we can assume a linear dependence between lateral grain size d and thickness L as in Fig. 44:

$$d = \eta \cdot L + \iota \quad \{142\}$$

According to the TEM analysis η and ι are equal to 0.08 and 10 nm, respectively. It is then helpful to use reduced conductances Y (and reduced resistances W) which are independent of the geometrical factors l_1 and l_2 (l_2 and L) of the sample (see Fig. 15):

$$Y = \frac{l_1}{l_2} \cdot G, \quad W = l_2 \cdot L \cdot R \quad \{143\}$$

The effective reduced conductance of the oxygen vacancies $Y_{V_{O}^{\bullet\bullet},m}$ can be separated in the bulk value $Y_{V_{O}^{\bullet\bullet},\infty}$ and the (normalized) resistance of the perpendicular GBs on the oxygen vacancy transport $R_{V_{O}^{\bullet\bullet}}^{\perp}$ ($W_{V_{O}^{\bullet\bullet}}^{\perp}$).

$$Y_{V_{O}^{\bullet\bullet},m} = \frac{l_1}{l_2} \cdot \left(R_{V_{O}^{\bullet\bullet},\infty} + R_{V_{O}^{\bullet\bullet}}^{\perp} \right)^{-1} \quad \text{with} \quad Y_{V_{O}^{\bullet\bullet},\infty} = \frac{l_1}{l_2} \cdot R_{V_{O}^{\bullet\bullet},\infty}^{-1} = L \cdot \sigma_{V_{O}^{\bullet\bullet},\infty} \quad \{144\}$$

$R_{V_{O}^{\bullet\bullet}}^{\perp}$ ($W_{V_{O}^{\bullet\bullet}}^{\perp}$) can be expressed as the product of the number of perpendicular SCLs $N_{SCL}^{\perp} = l_1 \cdot \Gamma^{\perp}$ (with $\Gamma^{\perp} = 2/d$, eq. {61}) and the (normalized) resistance of a single SCL $R_{V_{O}^{\bullet\bullet},1}^{\perp}$ ($W_{V_{O}^{\bullet\bullet},1}^{\perp}$):

$$W_{V_{O}^{\bullet\bullet}}^{\perp} = l_2 \cdot L \cdot R_{V_{O}^{\bullet\bullet},1}^{\perp} = N_{SCL}^{\perp} \cdot W_{V_{O}^{\bullet\bullet},1}^{\perp} \quad \{145\}$$

Hereby $R_{V_{O}^{\bullet\bullet},1}^{\perp}$ and $W_{V_{O}^{\bullet\bullet},1}^{\perp}$ are correlated with the value of $\Omega_{V_{O}^{\bullet\bullet}}$ introduced in section 2.2.3.4 (see eq. {55} and {56}):

$$W_{V_{O}^{\bullet\bullet},1}^{\perp} = l_2 \cdot L \cdot R_{V_{O}^{\bullet\bullet},1}^{\perp} = \frac{\Omega_{V_{O}^{\bullet\bullet}}}{u_{V_{O}^{\bullet\bullet}}} \quad \{146\}$$

From eq. {142} to {146} it follows that:

$$Y_{V_{O}^{\bullet\bullet},m} = Y_{V_{O}^{\bullet\bullet},\infty} - \frac{2L\sigma_{V_{O}^{\bullet\bullet},\infty}^2 W_{V_{O}^{\bullet\bullet},1}^{\perp}}{\eta \cdot L + \iota + 2\sigma_{V_{O}^{\bullet\bullet},\infty} W_{V_{O}^{\bullet\bullet},1}^{\perp}} \quad \{147\}$$

Eq. {147} corresponds to the bent curve shown in Fig. 45b, line (6). Since $Y_{V_{O}^{\bullet\bullet},m}(L=0) = 0$ and $d^2 Y_{V_{O}^{\bullet\bullet},m} / dL^2 > 0$ each secant through two points on $Y_{V_{O}^{\bullet\bullet},m}$ for $L > 0$ (or each linear fit of data points) will have a negative intercept on the y-axis as experimentally observed. Two further simplifications are possible:

$$\text{for } L \ll \frac{\iota + 2\sigma_{V_{O}^{\bullet\bullet},\infty} W_{V_{O}^{\bullet\bullet},1}^{\perp}}{\eta} \Rightarrow Y_{V_{O}^{\bullet\bullet},m} \approx \left(\frac{\iota}{\iota + 2\sigma_{V_{O}^{\bullet\bullet},\infty} W_{V_{O}^{\bullet\bullet},1}^{\perp}} \right) \cdot Y_{V_{O}^{\bullet\bullet},\infty} \quad \{148\}$$

$$\text{for } L \gg \frac{\iota + 2\sigma_{V_{O}^{\bullet\bullet},\infty} W_{V_{O}^{\bullet\bullet},1}^{\perp}}{\eta} \Rightarrow Y_{V_{O}^{\bullet\bullet},m} \approx Y_{V_{O}^{\bullet\bullet},\infty} - \frac{2\sigma_{V_{O}^{\bullet\bullet},\infty}^2 W_{V_{O}^{\bullet\bullet},1}^{\perp}}{\eta} \quad \{149\}$$

For the given experimental data the term $2\sigma_{V_{O}^{\bullet\bullet},\infty} W_{V_{O}^{\bullet\bullet},1}^{\perp} / \eta$ is about $2 \mu\text{m}^{59}$ and, hence, much larger than L . Therefore, here simplification {148} can be used which predicts a straight line with a much smaller slope compared with the epitaxial film. This agrees with the experimental findings in Fig. 43d. Hence, here the thickness dependence of the conductivity can fully be

understood under consideration of the blocking influence of the GBs. The GB effects again are in good agreement with the SCL model and a Φ_0 value of (0.32 ± 0.05) V as discussed above.

5.3.3.2 Nominally Pure Thin Films

5.3.3.2.1 Oxygen Partial Pressure Dependence

Let us now continue with the nominally pure samples. As expected, they exhibit a pO_2 dependent conductivity with an exponent in the $\log(G_m)$ vs. $\log(pO_2)$ plot of $-1/6$ (Fig. 46). This value shows that the material is in the intrinsic defect chemistry regime (I) (see Table 1) indicating a very low impurity content.

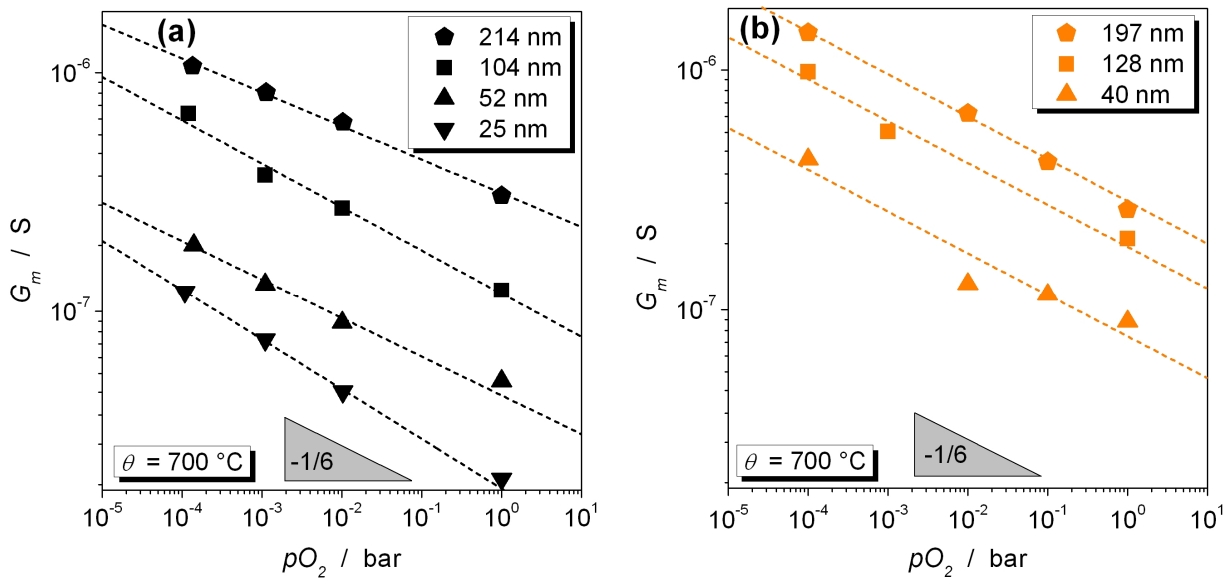


Fig. 46: pO_2 Dependence of the Effective Conductance of the Nominally Pure CeO_2 Thin Films Grown on (a) Al_2O_3 $\langle 0001 \rangle$ and (b) SiO_2 $\langle 0001 \rangle$

Reproduced from Göbel et al.^[14] by permission of the PCCP Owner Societies.

5.3.3.2.2 Epitaxial Thin Films on Al_2O_3 $\langle 0001 \rangle$

Since the nominally pure CeO_2 films on Al_2O_3 $\langle 0001 \rangle$ were found to be epitaxial (only the thickest films showed a very small number of wedged shaped grains, Fig. 41) GB effects can be disregarded here, corresponding to case (vi) in section 2.2.3.2 ($\sigma_m = \sigma_{e',\infty}$).

⁵⁹ This term can be calculated using $2\sigma_{V\delta^{\bullet,\infty}} W_{V\delta^{\bullet,1}}^{\dagger} / \eta = d / \eta \cdot (R_{V\delta^{\bullet}}^{\dagger} / 2R_{V\delta^{\bullet,\infty}} - 1)$ as following from eq. {142} to {146}. Here $R_{V\delta^{\bullet}}^{\dagger}$, $R_{V\delta^{\bullet,\infty}}$, d and η are experimentally available.

It is remarkable to see how the conductivities of the two sets of films on Al_2O_3 and SiO_2 in Fig. 47a diverge for smaller thicknesses. For the samples on Al_2O_3 the conductivity decreases and the activation energy increases with decreasing thickness (Fig. 47a, Fig. 47b and Table 11). As a result, the intercept on the y-axis in linear fit of the G_m vs. L plot is negative (Fig. 47c).

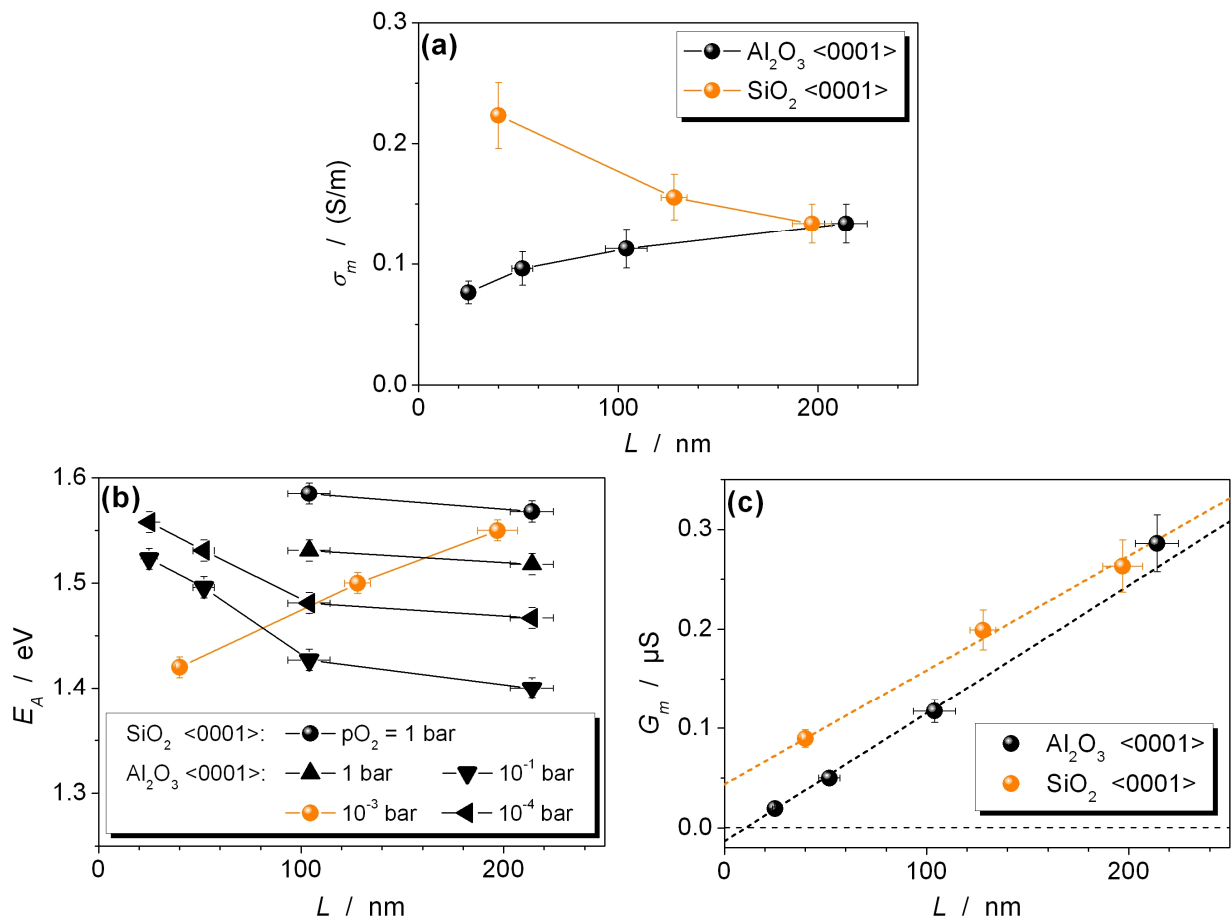


Fig. 47: Thickness Dependence of the Effective Electrical Transport Properties of the Nominally Pure CeO_2 Thin Films Grown on Al_2O_3 $\langle 0001 \rangle$ and SiO_2 $\langle 0001 \rangle$

(a) Conductivity vs. Thickness Plot

(b) Activation Energy vs. Thickness Plot

(c) Conductance vs. Thickness Plot

Reproduced from Göbel et al.^[14] by permission of the PCCP Owner Societies.

A possible explanation for the negative intercept is a SCL at the FSI in which the electrons are depleted. This is expected to coincide with an increase in the oxygen vacancy conductivity which, however, is experimentally unavailable here due to the much lower ionic mobility in comparison with the electronic mobility. In order to check whether the experimental data is in agreement with the SCL theory we can again take the characteristics of the G_m vs. L plot. A SCL with a negative potential would decrease the normalized effective conductance of the electrons $Y_{e,m}$ by a value of $\Delta Y_{e,m}$:^[1, 14]

Substrate		Al ₂ O ₃ <0001>				SiO ₂ <0001>		
		25	52	104	214	40	128	197
Effective Conductivity / (S/m)	pO ₂ = 10 ⁻⁴ bar	0.47	0.35	0.62	0.47	1.07	0.77	0.73
	pO ₂ = 10 ⁻³ bar	0.29	0.24	0.34	0.36	-	-	-
	pO ₂ = 10 ⁻² bar	0.18	0.17	0.25	0.27	-	-	-
	pO ₂ = 1 bar	0.076	0.096	0.11	0.13	0.22	0.16	0.13
Activation Energy / eV	pO ₂ = 10 ⁻⁴ bar	1.52	1.50	1.43	1.40	1.39	1.30	1.46
	pO ₂ = 10 ⁻³ bar	1.56	1.53	1.48	1.47	-	-	-
	pO ₂ = 10 ⁻² bar	-	-	1.53	1.52	-	-	-
	pO ₂ = 1 bar	-	-	1.59	1.57	1.43	1.50	1.55

Table 11: Effective Conductivity at 700 °C and Activation Energy between 700 °C and 550 °C of the Nominally Pure CeO₂ Thin Films Grown on Al₂O₃ <0001> and SiO₂ <0001>

Uncertainties: conductivity ± 10 %, activation energy ± 0.01 eV

Reproduced from Göbel et al.^[74] by permission of the PCCP Owner Societies.

$$\Delta Y_{e'} = -2\lambda \cdot \sigma_{e',\infty} \left(1 - e^{-\frac{e\Phi_0}{2kT}} \right) \quad \{150\}$$

If the depletion of electrons is sufficiently large (if $-\Phi_0$ is sufficiently large) $\Delta Y_{e',m}$ becomes $-2\lambda\sigma_{e',\infty}$. As a result, the linear fit of the conductance on the x-axis should coincide with the effective SCL extent 2λ :

$$Y_{e',m} = Y_{e',\infty} + \Delta Y_{e'} \approx (L - 2\lambda)\sigma_{e',\infty} \quad \text{for } L \gg 2\lambda \quad \{151\}^{60}$$

The value of 2λ can be calculated using eq. {34} if the electron bulk concentration n_∞ is known. Here the mobility data of ref. ^[74] ($U_{e',0} = 390 \text{ cm}^2\text{K}/(\text{Vs})$, $h_{e'} = 0.40 \text{ eV}$) and the experimental conductivity of this study ($\sigma_{e',\infty} = 0.13 \text{ S/m}$ at 700 °C and a pO_2 of 1 bar)⁶¹ are utilized to determine n_∞ with eq. {11} and {17}. The result is $n_\infty = 2 \cdot 10^{18} \text{ cm}^{-3}$ and $2\lambda = 7 \text{ nm}$. Under consideration of the measurement uncertainty this value for 2λ is in agreement with the intercept on the x-axis in the G_m vs. L plot of 10 nm. Hence, a SCL at the FSI could well be the origin of the observed conductivity changes.

Another possibility to explain the FSI effect is structural strain originating from the rather large lattice mismatch between CeO₂ and Al₂O₃ <0001>. The observed wedged shaped grains indicate that the films are able to relax the strain for larger thicknesses as expected. In contrast, the thinner films do not exhibit grains and, hence, are expected to perceive a strong strain which

⁶⁰ $Y_{e',\infty}$: normalized bulk conductance of the electrons ($Y_{e',\infty} = L \cdot \sigma_{e',\infty}$)

⁶¹ slope of the linear fit in Fig. 47c

may result in a change of the conductivity. Also in other materials strain effects are well known to alter the conductivity due to concentration and/or mobility variations.^[23, 27, 29, 115-117]

5.3.3.2.3 Polycrystalline Thin Films on SiO₂ <0001>

The films which were grown on SiO₂ <0001> show an increase of the conductivity and a decrease of the activation energy with decreasing thickness resulting in a positive intercept on the y-axis in the G_m vs. L plot (Fig. 47 and Table 11). Again also in this case an effect at the FSI, such as a SCL or structural strain, could well explain the found thickness dependence of the conductivity.

However, as for the doped, polycrystalline samples on SiO₂ <0001> (section 5.3.3.1.2) the GB effects should be taken into account here too. Consequently, here case (iv) of section 2.2.3.2 ($\sigma_m = \sigma_{e',m}^{\parallel} = \sigma_{e',\infty} + \Delta\sigma_{e',m}^{\parallel}$) applies. As for the Gd doped samples also for the pure films the lateral grain size was observed to increase with thickness (eq. {142} and Fig. 44). Using TEM the η and l parameters were found to be 0.15 and 10 nm, respectively.

As illustrated in Fig. 45c also for pure CeO₂ the GB effects are able to induce a conductivity change which can be misinterpreted as a FSI effect. Here line (7) represents the conductance of an epitaxial film. For a pure, polycrystalline film with constant lateral grain size (line (8)) the slope of the conductance is expected to be larger given that the electrons are well known to be enriched at the GBs.^[3, 4, 7, 8, 10, 22] However, if the lateral grain size increases with increasing thickness the curve will bend to smaller conductance values (line (9)). Here the linear fit of the data points will yield a positive intercept on the y-axis despite the absence of a FSI effects.

In analogy to eq. {143}-{149} we can take $Y_{e',m}$ and separate it in bulk and GB contributions $Y_{e',\infty}$ and $Y_{e'}^{\parallel}$, respectively. The latter one is the product of the number of parallel SCLs $N_{SCL}^{\parallel} = l_2 \cdot l^{\parallel}$ (with $l^{\parallel} = 2/d$, eq. {60}) and the reduced conductance of a single GB $Y_{e',1}^{\parallel}$. Here $Y_{e',1}^{\parallel}$ and $G_{e',1}^{\parallel}$ are connected with the contribution of the electrons on the total SCL charge (see section 2.2.3.4 and eq. {53}, {54} and {56})

$$Y_{e',1}^{\parallel} = \frac{l_1}{L} G_{e',1}^{\parallel} = -u_{e'} \Sigma_{e'} \quad \{152\}^{62}$$

For $Y_{e',m}$ it follows that:

$$Y_{e',m} = \frac{l_1}{l_2} \cdot (G_{e',\infty} + G_{e'}^{\parallel}) = Y_{e',\infty} + \frac{L}{l_2} Y_{e'}^{\parallel} = Y_{e',\infty} + \frac{L}{l_2} N_{SCL}^{\parallel} Y_{e',1}^{\parallel} = Y_{e',\infty} + \frac{2LY_{e',1}^{\parallel}}{\eta L + l} \quad \{153\}$$

⁶² in general, for an arbitrary CC i : $Y_{i,1}^{\parallel} = z_i/|z_i| \cdot u_i \Sigma_i$ (see eq. {53})

$$\text{for } L \ll \frac{l}{\eta} \Rightarrow Y_{e',m} \approx \left(1 + \frac{2Y_{e',1}^{\parallel}}{l\sigma_{e',\infty}} \right) Y_{e',\infty} \quad \{154\}$$

$$\text{for } L \gg \frac{l}{\eta} \Rightarrow Y_{e',m} \approx Y_{e',\infty} + \frac{2Y_{e',1}^{\parallel}}{\eta} \quad \{155\}$$

Since $l/\eta \approx 70$ nm for the most data points in Fig. 47 simplification {155} can be applied. It predicts a straight line with a positive intercept on the y-axis and the slope of the bulk (e.g. the same slope as for the epitaxial films on Al_2O_3 <0001>). This is exactly what was observed experimentally (Fig. 47c). Therefore, also GB effects could be the origin of the found thickness dependence. In contrast to the acceptor doped, polycrystalline samples where FSI effects could be excluded (section 5.3.3.1.2), in the case of the nominally pure, polycrystalline films both FSI and GB effects can explain the experimental data. Therefore, here it is not possible to distinguish between both kinds of boundary effects.

5.3.3.2.4 Reduced Reduction Enthalpy

A further interesting outcome of the above experiment concerns the absolute values of the electronic transport properties. For both the polycrystalline and the epitaxial films the electronic conductivity is about 1 order of magnitude larger compared with the single crystal data,^[74] probably due to the reduced electronic activation energy of only about 1.5 eV compared with 1.96 eV in the single crystal.

Given that in the intrinsic regime the activation energy is $\frac{1}{3}\Delta H_R + h_{e'}$, (see Table 1), with $0.2 \text{ eV} < h_{e'} < 0.6 \text{ eV}$,^[91] a change of only the electron hopping energy (and thus the electron mobility) is unlikely to produce such a large change in E_a . Hence, it is the reduction enthalpy that must be considerably decreased to a value of approximately 3.3 eV (with $h_{e'} \approx 0.4 \text{ eV}$ ^[74, 90]). Experimentally, this is in agreement with a number of other studies (e.g. ref. ^[6, 118, 119]) which also report a reduction of ΔH_R for CeO_2 in the nanoscale.

However, the exact physico-chemical origin of the decrease of E_a remains unclear. Unfortunately, also the dataset presented here could not clarify the situation. On the one hand, GB effects seem not to be the cause since also the epitaxial films show low E_a values. On the other hand, also the thickness of the films in the nanoscale cannot explain the effect. In this case, the activation energy should be reduced further with decreasing film thickness. However, for the epitaxial films the opposite behavior is observed: an increase of E_a with decreasing thickness (Fig. 47b).

5.3.4 Section Conclusions

The experiments discussed in this section show that the substrate is able to strongly influence the conductivity of the grown film. Two major results (1) and (2) can be distinguished:

- (1) *Reduced Electronic Conductivity at the Film-Substrate Interface (FSI) in the Nominally Pure Films on Al_2O_3 <0001>*

As first outcome the nominally pure, epitaxial CeO_2 thin films grown on Al_2O_3 <0001> exhibit a significant conductivity decrease and activation energy increase with decreasing film thickness. Since GB effects can be neglected in this set of samples the change in conductivity and activation energy can be attributed to an effect at the FSI which was found to be in agreement with the SCL theory.

- (2) *Grain Boundary (GB) Effects in the Films on SiO_2 <0001>*

The second result concerns the polycrystalline films grown on SiO_2 <0001>. Here the way the substrate affects the transport properties of the thin films was found to occur rather indirect by controlling the microstructure of the thin films and, hence, the GB effects. Especially, it could be shown that GB effects can result in very similar conductivity changes and might, therefore, be misinterpreted as FSI effects. As for the 10 mol% Gd doped films, the GB effects (and, hence, also the thickness dependence) can fully be explained within the framework of the SCL model and a SCL potential of (0.32 ± 0.05) V.

Finding (2) is of particular significance for a series of other studies which deal with FSI effects or interface effects in multilayer structures such as the ones in ref. [24-26, 28]. These studies include the investigation of polycrystalline multilayer structures of acceptor doped ZrO_2 (a similar material as acceptor doped CeO_2) and a second insulating (or less conductive) material (e.g. Al_2O_3 , Y_2O_3 , Lu_2O_3 and Sc_2O_3). In ref. [24-26, 28] at least some of the thin films show a thickness dependent lateral grain size. Despite this, for the interpretation of the found conductivity changes the GB effects were not considered and the conductivity variations were fully attributed to the interfaces between the individual layers. In contrast to this, our findings show that the GB effects cannot be neglected and that otherwise they can be mistaken for other boundary effects easily.

5.4 Reduced Grain Boundary Effects in Cerium Oxide Thin Films on Al_2O_3 $\langle 1\bar{1}02 \rangle$ and MgO $\langle 100 \rangle$

5.4.1 Section Introduction

In the last chapter it was observed that in the investigated thin films, especially for a high acceptor doping, the FSI effects are only small whereas the GB effects considerably influence the conductivity. Therefore, in the next two studies which are presented in this and the subsequent section 5.5 the GB effects were investigated more in detail.

As shown in section 5.3.3.1.2 acceptor doped CeO_2 thin films grown on SiO_2 $\langle 0001 \rangle$ show pronounced GB effects with rather large SCL potentials resulting in a severely reduced ionic conductivity. Is it possible that nanocrystalline thin films grown on other substrates exhibit less significant conductivity changes? In order to answer this question it is useful to consider the influence of the orientation of adjacent grains. The angle of the GBs is known to affect the strength of the SCL effects significantly.^[20] Since (1) the substrate influences the growth and, hence, the microstructure of the thin films and since (2) the structure of quartz is very different from the one in ceria, it is quite likely that the grains of the thin films grown on SiO_2 $\langle 0001 \rangle$ are oriented more or less randomly with respect to each other (compared with films on substrates with smaller lattice mismatches). Therefore, the angles of the GBs in the films on SiO_2 are probably rather large resulting in strong deviations from the bulk stoichiometry in the GB core and, thus, large core charges and pronounced SCL effects.

Consequently, thin films which are grown on structurally more similar substrates might feature less pronounced SCL effects and, hence, a smaller decrease of the ionic conductivity. In order to verify this hypothesis thin films of 10 mol% Gd doped ceria were prepared on substrates whose lattice mismatch with CeO_2 is as small as possible but still large enough to avoid an epitaxial growth of the films: Al_2O_3 $\langle 1\bar{1}02 \rangle$ and MgO $\langle 100 \rangle$.

5.4.2 Microstructure

For ceria films on MgO $\langle 100 \rangle$ usually SrTiO_3 ^[114] or BaSnO_3 ^[120] buffer layers are used to ensure epitaxial growth. This means that without buffer layer no epitaxial growth is expected. As a matter of fact, for the here prepared thin films on MgO the XRD patterns (Fig. 48b) are characterized by several orientations and the TEM micrographs (Fig. 49b) show a columnar, polycrystalline microstructure. Similarly to the films on SiO_2 (section 5.3.3.1.2) also the samples on MgO show an increase of the lateral grain size with increasing film thickness (Table 12).

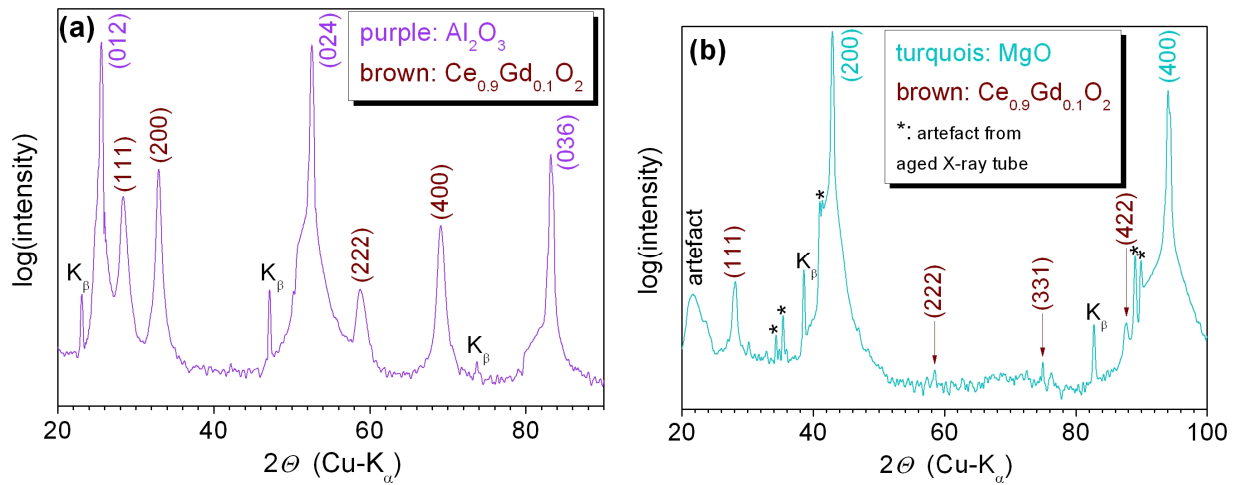


Fig. 48: XRD Patterns of the 10 mol% Gd Doped CeO₂ Thin Films Grown on (a) Al₂O₃ <1 $\bar{1}$ 02> and (b) MgO <100>

The curves have been smoothed for clarity.

Substrate	Al ₂ O ₃ <1 $\bar{1}$ 02>		MgO <100>	
TEM: Film Thickness L / nm	45 ± 2	309 ± 15	39 ± 2	431 ± 22
XRD: Lattice Constant / Å	5.45 ± 0.01	5.43 ± 0.02	5.49 ± 0.05	5.47 ± 0.02
Microstructure	Polycrystalline with columnar grains	Polycrystalline, irregular	Polycrystalline with columnar grains	
TEM: Lateral Grain Size / nm	18 ± 9	-	16 ± 11	59 ± 26

Table 12: Results of the XRD and TEM Investigation of Selected 10 mol% Gd Doped CeO₂ Thin Films Grown on Al₂O₃ <1 $\bar{1}$ 02> and MgO <100>

For nominally pure ceria thin films grown on Al₂O₃ <1 $\bar{1}$ 02> (r-cut Al₂O₃) the literature reports an epitaxial microstructure.^[121-127] Indeed also in the framework of this study nominally pure CeO₂ films on this kind of substrate were fabricated and found to be structured epitaxially. However, the lattice mismatch between ceria (CeO₂ [100]: 5.41 Å)^[102] and the relevant Al₂O₃ [11 $\bar{2}$ 0]-axis is still quite large (Al₂O₃ [11 $\bar{2}$ 0]: 4.76 Å, Al₂O₃ [$\bar{1}$ 101]: 5.21 Å)^[128]. When the lattice constant of CeO₂ increases upon Gd doping^[107-109] the mismatch becomes even larger. For this reason the 10 mol% Gd doped samples were found not to grow epitaxially anymore. The XRD signals of the films on Al₂O₃ <1 $\bar{1}$ 02> indicate the presence of multiple orientations (Fig. 48a) and for the thinnest films (about 45 nm thickness) the TEM micrographs display a polycrystalline, columnar microstructure (Fig. 49a). Interestingly, for the thicker films the grains seem to be grown together at larger distances from the substrate. Hence, in the following conductivity analysis (section 5.4.3) only the thinnest films with a well defined columnar microstructure are considered.

Also HRTEM micrographs were recorded (Fig. 49a, above). At the GBs no segregation of a second phase was found.

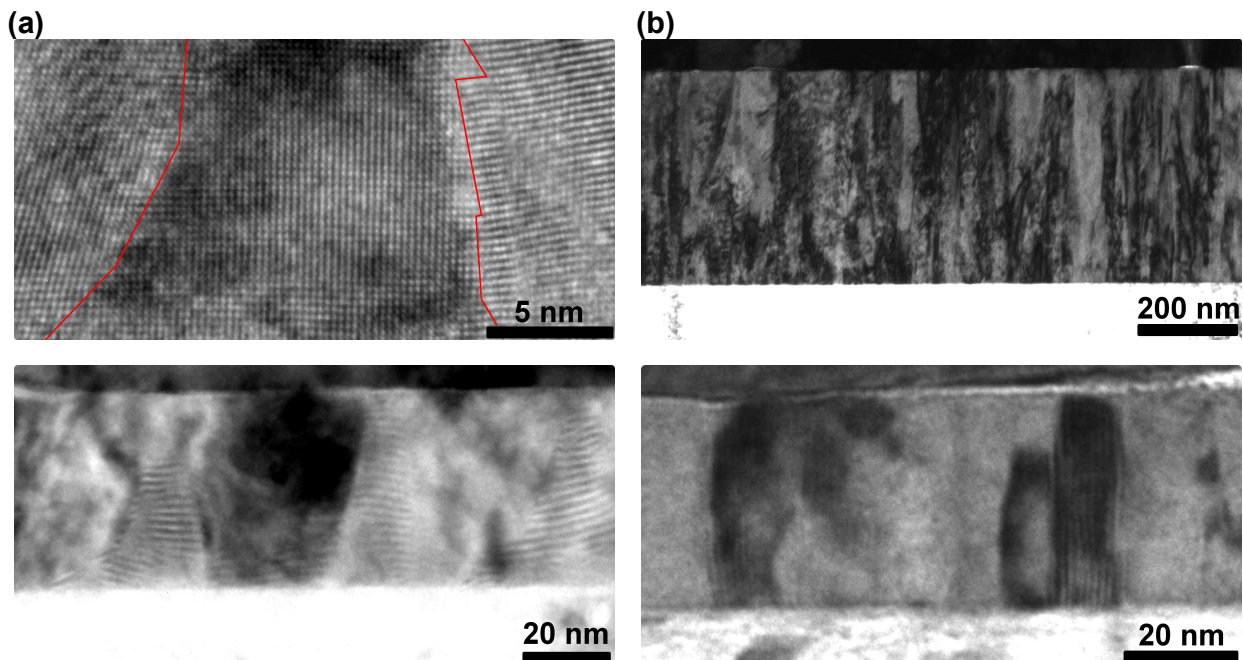


Fig. 49: TEM and HRTEM Micrographs of the 10 mol% Gd Doped CeO₂ Thin Films Grown on (a) Al₂O₃ <1102> and (b) MgO <100>

(a) Thinnest Film Grown on Al₂O₃ <1102> (45 nm):

Above: HRTEM Micrograph, with Red Lines Indicating the GBs

Below: TEM Micrograph

(b) TEM Micrographs of Two Films Grown on MgO <100>:

Above: Thickest Prepared Film (431 nm)

Below: Thinnest Prepared Film (39 nm)

TEM Micrographs - From the Top: Pt-Electrode, CeO₂ Thin Film and Substrate

5.4.3 Conductivity Data

As expected for the strongly acceptor doped samples no pO_2 dependent conductivity was observed between 10^{-5} and 1 bar. The films were observed to exhibit activation energy values in the range from 0.7 to 0.9 eV (Fig. 50 and Table 13) which are, hence, slightly larger than the bulk value of 0.7 eV measured in single crystals^[40, 74] and epitaxial films^[14, 113, 114] (see section 5.3.3.1.1). Such an increase of the E_a in polycrystalline material is expected^[6-8, 10-12] and shows that case (ii) of section 2.2.3.2 ($\sigma_m = \sigma_{V_{O}^{\bullet\bullet}, m}^{\perp} = [[\sigma_{V_{O}^{\bullet\bullet}, \infty}]^{-1} + [\Delta\sigma_{V_{O}^{\bullet\bullet}, m}^{\perp}]^{-1}]^{-1}$) needs to be applied here. However, the activation energies are considerably lower compared with the polycrystalline films on SiO₂ ($E_a \approx 1.0$ to 1.2 eV, see Table 10, page 87).

For the absolute conductivity values a similar trend can be observed. The ionic conductivity of the films on Al₂O₃ <1102> and MgO <100> between 2 and 3 S/m is lower compared with the

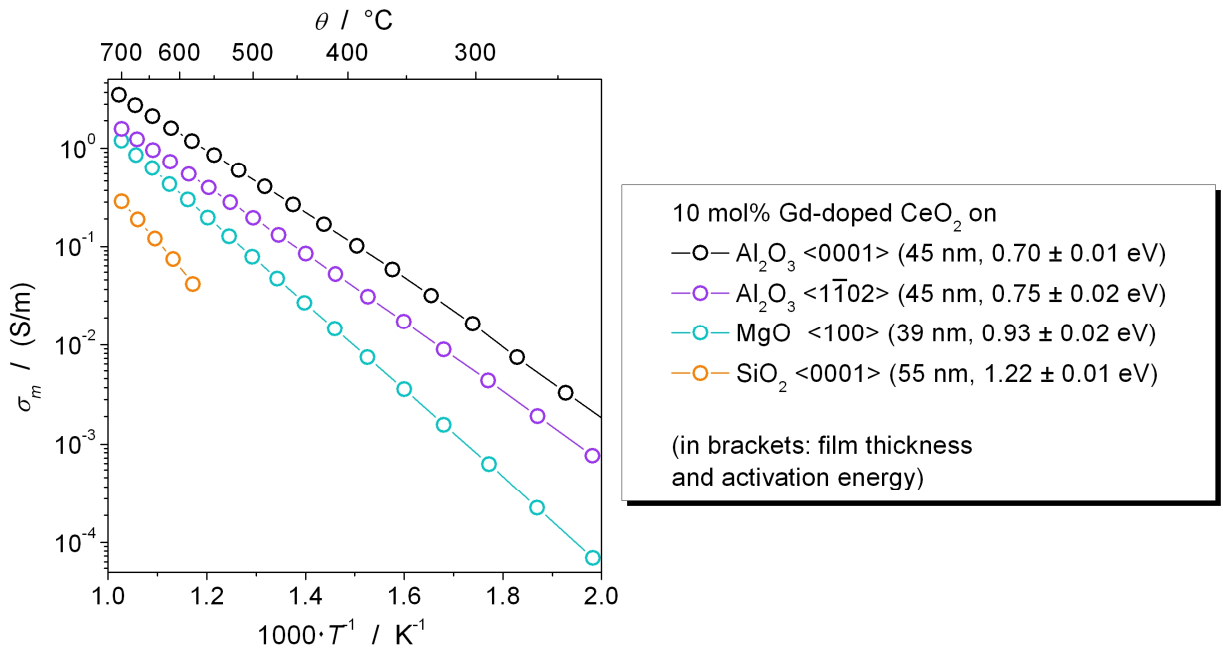


Fig. 50: Temperature Dependence of the Effective Conductivity of the Thinnest Prepared 10 mol% Gd Doped CeO₂ Thin Films Grown on Al₂O₃ <11̄02> and MgO <100>, in Comparison with the Films Grown on Al₂O₃ <0001> and SiO₂ <0001>

Substrate	Al ₂ O ₃ <11̄02>				MgO <100>			
	45	83	158	309	39	95	207	431
Thickness / nm	45	83	158	309	39	95	207	431
Conductivity / (S/m)	1.8	3.1	2.5	3.3	1.9	2.3	2.1	2.4
Activation Energy / eV	0.75	0.72	0.84	0.69	0.93	0.91	0.91	0.87

Table 13: Effective Conductivity at 700 °C and Activation Energy between 700 °C and 550 °C of the 10 mol% Gd-Doped CeO₂ Thin Films Grown on Al₂O₃ <11̄02> and MgO <100>

Uncertainties: Conductivity $\pm 10\%$, Activation Energy ± 0.01 eV

epitaxial films on Al₂O₃ <0001> (about 4 S/m) but much larger than the conductivity of the samples on SiO₂ <0001> (between 0.3 and 1 S/m) (see Table 10 and Table 13).

Remarkably, despite the large differences in conductivity the lateral grain size of the films on all three substrates is similar.⁶³ Therefore, the average SCL potential of the films on Al₂O₃ <11̄02> and MgO <100> must be significantly smaller compared with the films on quartz. For the thinnest films on Al₂O₃ <11̄02> and MgO <100> the conductivity at 700 °C is very similar (about 1.8 S/m, Table 13). Using this value and a lateral grain size of 17 nm the SCL potential is calculated to be 0.19 ± 0.05 V (eq. {122}). This value is not only much smaller than the value for

⁶³ $d \approx 15-20$ nm (see the thinnest films of thicknesses around 50 nm in Table 9 and Table 12)

the samples on $\text{SiO}_2 <0001>$ ($0.32 \pm 0.05 \text{ V}$) but also at the lower limit of the SCL potentials observed in ceria in other studies between 0.20 and 0.34 V.^[10, 14, 16, 17, 98, 99]

For lower temperatures the SCL potential in CeO_2 is known to decrease.^[11] This effect can be observed here too. As an example, we can take the films on $\text{Al}_2\text{O}_3 <1\bar{1}02>$ which show a particularly high conductivity at low temperatures. At 300 °C their conductivity is reduced compared with the epitaxial films on $\text{Al}_2\text{O}_3 <0001>$ by a factor of about three only. This corresponds to a very low potential of merely $0.14 \pm 0.05 \text{ V}$.

In addition to this, also the thickness dependence of the conductivity was investigated (Fig. 51). Here the films on MgO as the films on SiO_2 exhibited a columnar microstructure and an increasing lateral grain size with increasing thickness. Therefore, for the linear fit of the data points in the conductance vs. thickness plot similar characteristics as shown in section 5.3.3.1.2 (eq. {147}) were expected here: a smaller slope compared with the epitaxial films on Al_2O_3

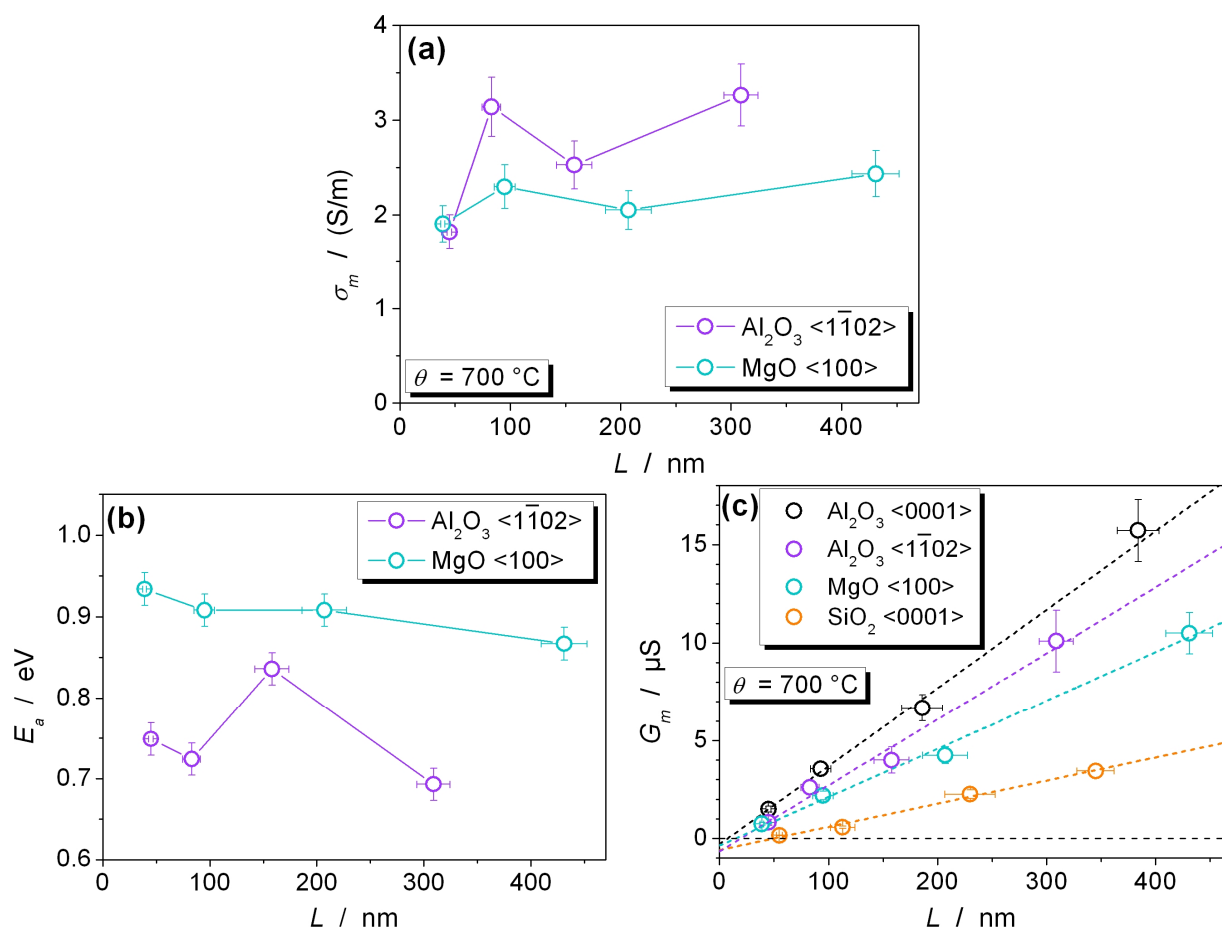


Fig. 51: Thickness Dependence of the Effective Electrical Transport Properties of the 10 mol% Gd Doped CeO_2 Thin Films Grown on $\text{Al}_2\text{O}_3 <1\bar{1}02>$ and $\text{MgO} <100>$

(a) Conductivity vs. Thickness Plot

(b) Activation Energy vs. Thickness Plot

(c) Conductance vs. Thickness Plot

$\langle 0001 \rangle$ and a small negative intercept on the y-axis. The films on MgO were found to show exactly this behavior (Fig. 51c). However, here the effect is less pronounced in comparison with the films on SiO₂ due to the smaller SCL potential.

Also for the films on Al₂O₃ $\langle 1\bar{1}02 \rangle$ a similar trend in the G_m vs. L plot is found. Nevertheless, here the data points scatter considerably probably because of the non-columnar microstructure of the thicker films.

5.4.4 Section Conclusions

In conclusion, the thinnest films on Al₂O₃ $\langle 1\bar{1}02 \rangle$ and MgO $\langle 100 \rangle$, which exhibit a columnar polycrystalline structure, show a rather small decrease of the ionic conductivity at the GBs. The origin of this effect is a strongly reduced SCL potential at the GBs of 0.19 ± 0.05 V at 700 °C.

The origin of the microscopic cause of the low SCL potential is not obvious. However, one could correlate the reduced potential with the rather low lattice mismatch between substrate and thin film. Due to this the angle of the individual grains between each other is most likely in average smaller compared with films grown on substrates characterized by more severe structural differences to ceria (such as SiO₂). As a result, the GB core charge is expected to be reduced resulting in smaller GB effects. Indeed studies on other model oxide materials indicate that the strength of the SCL effects depend strongly on the angle at the GBs (e.g. ref. [20]).

The finding of the reduced SCL potential in the samples discussed here shows that for thin films the GB effects can be adjusted by using different substrates and growth conditions. Specifically, it is not only possible (1) to prepare epitaxial and polycrystalline thin films (no GB effects vs. pronounced GB effects), and (2) to fabricate polycrystalline thin films with different lateral grain sizes and, hence, different GB densities (but comparable properties of the individual GBs, section 5.3). The results of this section indicate that, additionally to this, (3) also samples with different average characteristics of the individual GBs can be prepared.

Notably, the impact of a single GB on the conductivity can either be increased (e.g. by applying appropriate growth conditions, as shown in the next section 5.5) or reduced as elucidated here by choosing suitable substrates. Of course, while for basic research both directions are very interesting for practical applications based on ceria thin films (e.g. μ SOFCs, see section 1.3) it is this reduction of the SCL effects and the corresponding larger ionic conductivity (compared with other nanocrystalline samples) that is of particular significance.

5.5 Strongly Enhanced Electronic Conductivity Domain in Nanocrystalline Cerium Oxide Thin Films

5.5.1 Section Introduction

In the previous section it was demonstrated that a modification of the GBs can result in a reduction of the SCL conductivity effects. This raises the question whether also the opposite can be achieved, namely an increase of the GB effects in ceria. The experiments discussed in this section deal with this problem. In particular, here it is addressed how strongly the effective electrical transport properties in CeO₂ are changed in an extreme situation, i.e. in a sample characterized by a very larger density of GBs.

In order to fabricate such thin films with ultra small grains the deposition temperature during the PLD process was decreased to room temperature. At such low temperatures the ion diffusion is expected to be reduced resulting in a diminished grain growth. In the following this sample shall be designated as *rt-nano* film (deposition temperature: room temperature, microstructure: nanocrystalline). The *rt-nano* film was then compared with two other samples, (1) a nanocrystalline thin film prepared also on SiO₂ <0001> but at higher temperatures (720 °C): *ht-nano*, and (2) an epitaxial thin film fabricated at 720 °C on Al₂O₃ (<0001> or <1 $\bar{1}$ 02> orientation): *ht-epitaxial*. In particular, the comparison with the *ht-epitaxial* sample allows for the separation of bulk and GB contributions.

Table 14 gives an overview of the properties of the three thin films. This set of samples was prepared for different doping contents. Let us here firstly focus on the 10 mol% Gd doped films.

Sample Name	<i>ht-epitaxial</i>	<i>ht-nano</i>	<i>rt-nano</i>
Thickness	≈ 400 nm	≈ 400 nm	≈ 400 nm
Substrate	Al ₂ O ₃ <0001> or Al ₂ O ₃ <1 $\bar{1}$ 02>	SiO ₂ <0001>	SiO ₂ <0001>
Deposition Temperature	720 °C	720 °C	room temperature
Microstructure	epitaxial	polycrystalline with columnar grains	polycrystalline with columnar grains
TEM: Lateral Grain Size / nm	-	≈ 40 nm	≈ 10 nm

Table 14: General Characteristics of the *ht-epitaxial*, *ht-nano*, and *rt-nano* Thin Films

5.5.2 Microstructure

The microstructures of the samples prepared at 720 °C have already been discussed in detail in section 5.3.2 (*ht-epitaxial* sample: Fig. 40a and Fig. 41a, *ht-nano* sample: Fig. 40b and Fig. 41b, see also the thickest films in Table 9). Let us, therefore, here focus on the *rt-nano* thin film.

The *rt-nano* sample exhibited XRD signals very similar to the *ht-nano* thin film (Fig. 52) indicating a nanocrystalline microstructure. The finding of a crystalline structure indicates that during the deposition the kinetic energy of the ions when they hit the substrate was high enough to allow for crystallization despite the low temperature. Further independent techniques, namely electron diffraction, TEM and HRTEM, clearly confirm that the *rt-nano* sample is crystalline (Fig. 53).

The observation that the positions of the XRD signals of both films, *rt-nano* and *ht-nano*, are matching implies an unchanged fluorite structure also in the *rt-nano* film and identical lattice parameters. In addition, from the electron diffraction pattern (Fig. 53) the lattice constant was determined to be 5.42 Å, a typical value for Gd doped CeO₂.^[107]

Already the broadening of the XRD signals in Fig. 52 indicates a smaller average grain size for the *rt-nano* sample as expected. This was further confirmed by the TEM micrographs which showed lateral grain sizes of about 10 nm on average (in comparison with \approx 40 nm for the *ht-nano* film, Table 9). Interestingly, the columnar microstructure of the *rt-nano* film was slightly distorted. Here the small grains were still considerably elongated; however, not in every case they spanned over the full film thickness from the substrate to the film surface.

An analysis of selected GBs with HRTEM did not show segregation of a second phase (Fig. 53).

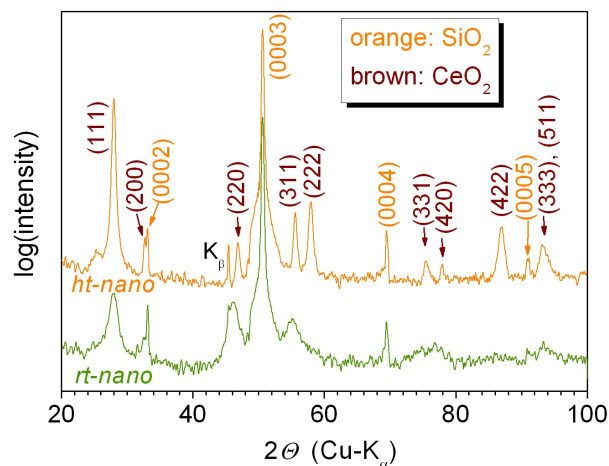


Fig. 52: XRD Patterns of the 10 mol% Gd doped *ht-nano* and *rt-nano* CeO₂ thin films

The curves have been smoothed for clarity.

Reproduced from Göbel et al.^[16] by permission of the PCCP Owner Societies.

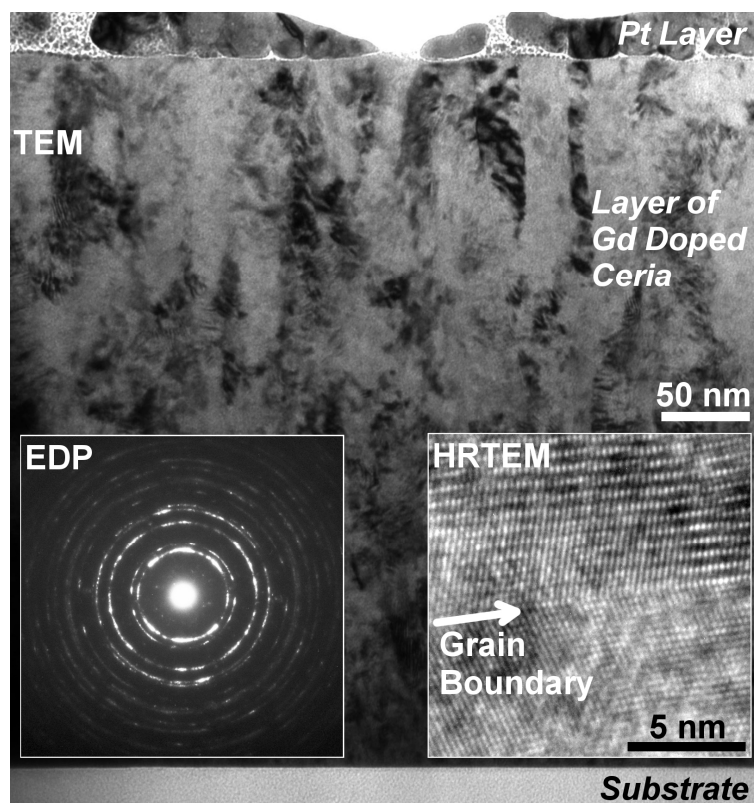


Fig. 53: TEM and HRTEM Micrographs and Electron Diffraction Pattern (EDP) of the 10 mol% Gd Doped *rt-nano* CeO₂ Thin Film

TEM Micrograph - From the top: Pt-Electrode, Ceria Thin Film and SiO₂ Substrate

Reproduced from Göbel et al.^[16] by permission of the PCCP Owner Societies.

5.5.3 Conductivity Data

5.5.3.1 Preliminary Considerations

5.5.3.1.1 Thermal Stability of the *rt-nano* Thin Film

Before discussing in detail the measured conductivity let us firstly make two preliminary considerations on (1) the thermal stability of the *rt-nano* sample and (2) the expected electrical transport properties of ceria thin films at similar conditions in the literature.

Fig. 54 displays the conductivity of the *rt-nano* and *ht-nano* thin films upon heating to 700 °C and subsequent cooling down. At low temperatures (before heating to 700 °C) the ionic conductivity of the *rt-nano* sample is reduced with respect to the *ht-nano* sample. Clearly, during heating the conductivity of the *rt-nano* film increases more steeply compared with the *ht-nano* film as a result of the irreversible grain growth occurring at higher temperatures. Hence, in the subsequent cooling down phase the conductivity of the *rt-nano* film decreases much more slowly. It is remarkable to see that now its conductivity is basically identical with the one of the

ht-nano thin film which was already exposed to temperatures around 700 °C during its preparation.

Therefore, in order to study the unique properties of the *rt-nano* sample due to its very small grains the sample had to be kept at temperatures below 400 °C in order to prevent an irreversible increase of the grain size.

All measurements presented in the below sections were performed at such low temperatures. As a matter of fact, the here shown data in Fig. 54 was measured in the very last step after performing all other experiments discussed below.

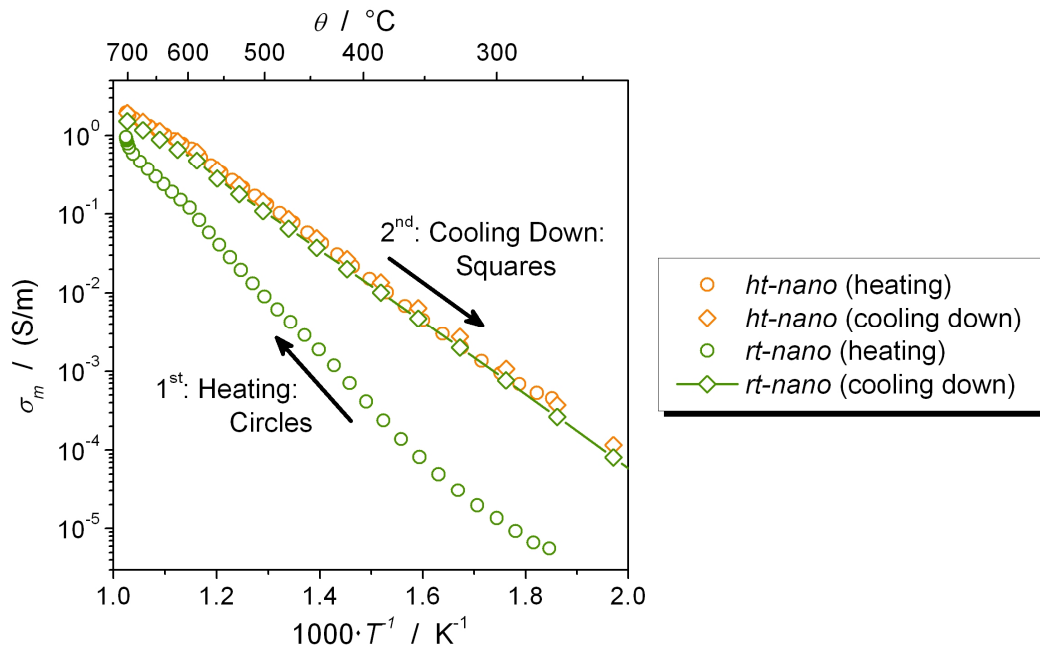


Fig. 54: Effective Conductivity of the 10 mol% Gd Doped *rt-nano* and *ht-nano* CeO₂ Thin Films Upon Heating to 700 °C and Subsequent Cooling Down

The *rt-nano* sample exhibits an irreversible grain growth upon heating to temperatures above 400 °C.

Reproduced from Gregori, Göbel and Maier^[17] with permission from ECS Transactions, The Electrochemical Society (Copyright 2012).

5.5.3.1.2 Expected Conductivity Properties

It is instructive to consider what electric transport properties can be expected for the *rt-nano* sample at temperatures below 400 °C. In particular, the expected electrolytic domain boundary values in both the bulk of ceria, $pO_{2,\infty}^{EDB}$, and in nanocrystalline material, $pO_{2,m}^{EDB}$, shall be regarded here. As introduced in sections 2.1.4 and 2.2.3.3 the EDB strongly shifts if (even only small) SCL effects are present. This makes the EDB value an ideal fingerprint for detecting SCL effects.

5.5.3.1.2.1 Expected Bulk Properties

Concerning the bulk of CeO₂ the single crystal data of Tuller and Nowick can be applied.^[74, 92] Also a series of studies^[129-131] dealing with pellets sintered at very high temperatures can be regarded since due to the resulting large grains sizes in the μm range these samples are expected to be dominated by bulk and not by GB effects (Table 15).

Unfortunately, while the investigation of the *rt-nano* sample is restricted to temperatures below 400 °C, in the literature CeO₂ is measured at higher temperatures (probably because of (1) the lower resistances there and (2) the importance of ceria as an electrolyte in SOFCs which usually operate above 400 °C). Thus, the lowest given temperature in ref. ^[74, 92, 129-131] is 635 °C making it necessary to extrapolate the data. In defect chemistry regimes (II-a) and (II-b) (see Table 1) the pO_2 dependence of the electron concentration is $-1/4$. This and eq. {4}, {11}, {16} and {17} yield the following dependence of $pO_{2,\infty}^{EDB}$:

$$pO_{2,\infty}^{EDB} \propto (|z_A|c_A)^{-6} \cdot e^{-\frac{4}{k_B T} \left(\frac{\Delta H_R}{2} + h_{e'} - h_{V_O^{**}} \right)} \quad \{156\}$$

Ref.	Samples	$pO_{2,\infty}^{EDB}$ / bar	θ / °C	c_A / mol% (Dopant)	ΔH_R / eV	$h_{e'}$ / eV	$h_{V_O^{**}}$ / eV	$pO_{2,\infty}^{EDB}$ / bar (extra- polated)
[74, 92]	Single Crystal	10 ⁻²⁰	635	5 (Y)	4.67	0.40	0.76	10 ⁻⁵⁰
[129]	Two Sintered Pellets**	1.3·10 ⁻¹⁷	700	10 (Gd)	$\Delta H_R/2 + h_{e'} - h_{V_O^{**}} = 1.22$			10 ⁻³⁶
		1.2·10 ⁻¹⁹		20 (Gd)	$\Delta H_R/2 + h_{e'} - h_{V_O^{**}} = 1.50$			10 ⁻⁴¹
[131]	Sintered Pellet ($d = 3.5 \mu\text{m}$)*	7·10 ⁻²¹	700	20 (Gd)	$\Delta H_R/2 + h_{e'} - h_{V_O^{**}} = 1.29$			10 ⁻³⁹
[130]	Sintered Pellet ($d = 0.8 \mu\text{m}$)*	10 ⁻¹⁶	800	10 (Gd)	4.03	0.60	0.70	10 ⁻⁵⁰

Table 15: Literature Data of the Electrolytic Domain Boundary in the Bulk of CeO₂

In the right, grey shaded column the $pO_{2,\infty}^{EDB}$ values which are extrapolated to the measurement conditions used here are given. The data are extrapolated to $\theta = 280$ °C and $|z_A|c_A = 10$ mol% Gd using eq. {156}.

Ref. ^[74, 92]: Tuller and Nowick, ref. ^[129]: Kudo and Obayashi, ref. ^[131]: Rupp, Infortuna and Gauckler, ref. ^[130]: Park and Yoo

* The sintered pellets have large grains in the μm range. Therefore, they are expected to exhibit mainly bulk properties.

** No grain size is given in ref. ^[129]. Since it is stated that the pellets were sintered at 1800 °C the grains are expected to be in the μm range here too.

Using eq. {156} the literature data of Table 15 was extrapolated to an acceptor doping content $|z_A|c_A$ of 10 mol% and a temperature of 280 °C (i.e. the conditions at which most of the measurements on the *rt-nano* film were performed). The results are listed in the grey shaded column in Table 15.

Probably due to the different preparation and measurement techniques the extrapolated $pO_{2,\infty}^{EDB}$ values deviate to some extent. Nonetheless, what is important to note here is that in the bulk of ceria at 280 °C the EDB is expected to be at extremely low oxygen partial pressures between 10^{-50} and 10^{-36} bar.

5.5.3.1.2.2 Expected Properties of Nanocrystalline Material

As explained in section 2.2.3.3 in nanocrystalline samples (such as the *ht-nano* and *rt-nano* films) the EDB is expected to occur at larger pO_2 values compared with the bulk (i.e. $pO_{2,m}^{EDB} > pO_{2,\infty}^{EDB}$). For this reason, data collected from previous studies on nanocrystalline ceria is summarized in Table 16. In order (1) to consider as many influences as possible and (2) to get an overview as broad as possible the studies, ref. [10, 119, 131], have been chosen because they deal with different sample geometries (pellets vs. thin films), different preparation techniques (PLD vs. spray pyrolysis) and different doping contents. Additionally, they originate from different research groups.

The data in Table 16 was not taken at low temperatures too making it necessary to extrapolate. In ref. [10] it was found that the SCL potential does not significantly change with the pO_2 and as a matter of fact all studies in Table 16 report on M_{pO_2} values of the electronic conductivity around $-1/4$ as in the bulk. Hence, for the nanocrystalline samples a similar approach as in eq. {156} can be used. However, for these samples which are dominated by GB effects eq. {156} which refers to the bulk properties needs to be modified. Firstly, the activation energies can be affected by the GB effects. This makes it necessary to use effective ionic and electronic activation energies $E_{a,e'}$ and $E_{a,V_O^{\bullet\bullet}}$ as they are given in the relevant publications:

$$E_{a,V_O^{\bullet\bullet}} = -k_B \frac{d \ln(\sigma_{V_O^{\bullet\bullet},m} T)}{d(T^{-1})}, \quad E_{a,e'} = -k_B \frac{d \ln(\sigma_{e',m} T)}{d(T^{-1})} \quad \{157\}$$

As second modification the results can be extrapolated with regard to the grain size too. Since for 10 mol% acceptor doped samples the extent of the SCL is only in the Å range (Fig. 23a) and, hence, much smaller than the grain size the SCLs do not overlap. Furthermore, for the nanocrystalline samples in Table 16 the conductivity is expected to be controlled by the GBs. Therefore, the relations $\sigma_{V_O^{\bullet\bullet},m} \propto d$ and $\sigma_{e',m} \propto 1/d$ are approximately valid (compare with eq. {56} to {59}). With the electronic pO_2 dependence of $-1/4$ this gives a dependence of $pO_{2,m}^{EDB}$ on d^{-8} .⁶⁴ As a result, the following relation was used to extrapolate the data of the

nanocrystalline samples to 280 °C, an acceptor doping content of 10 mol% and a grain size of 10 nm as in *rt-nano* thin film:

$$pO_{2,m}^{EDB} \propto d^{-8} \cdot (|z_A|c_A)^{-6} \cdot e^{-\frac{4}{k_B T}(E_{a,e'} - E_{a,V_O^{**}})} \quad \{158\}$$

The resulting $pO_{2,m}^{EDB}$ values (grey shaded column in Table 16) lie in the range between 10^{-34} and 10^{-25} bar. This is significantly larger than in the bulk (10^{-50} to 10^{-36} bar) and shows that, as expected, the EDB is shifted towards higher oxygen partial pressures due to the GB effects.

Ref.	Samples	$pO_{2,m}^{EDB}$ / bar	θ / °C	c_A / mol% (Dopant)	d / nm	$E_{a,e'}$ / eV	$E_{a,V_O^{**}}$ / eV	$pO_{2,m}^{EDB}$ / bar (extra- polated)
[10]	Nanocrystalline Pellet	10^{-3}	491	≈ 0.0015	30	1.9	1.1	10^{-30}
		10^{-18}			11	2.48	1.13	10^{-34}
		10^{-19}			15	2.52	1.19	10^{-34}
	Seven	10^{-17}		20 (Gd)	20	2.53	1.25	10^{-30}
[119]	Nanocrystalline Thin Films (PLD)	10^{-16}	600		36	2.48	1.33	10^{-25}
		10^{-15}			15	2.38	1.28	10^{-27}
		10^{-17}		10 (Gd)	30	2.59	1.34	10^{-30}
		10^{-16}			58	2.54	1.36	10^{-26}
	Nanocrystalline Thin Film (PLD)	$2 \cdot 10^{-17}$			65	$E_{a,e'} - E_{a,V_O^{**}} = 1.28$		10^{-29}
[131]	Nanocrystalline Thin Film (Spray Pyrolysis)	$4 \cdot 10^{-16}$	700	20 (Gd)	78	$E_{a,e'} - E_{a,V_O^{**}} = 1.28$		10^{-27}

Table 16: Literature Data of the Electrolytic Domain Boundary in Nanocrystalline CeO₂

In the right, grey shaded column the $pO_{2,m}^{EDB}$ values which are extrapolated to the measurement conditions used here are given. The data are extrapolated to $\theta = 280$ °C, $|z_A|c_A = 10$ mol% Gd and $d = 10$ nm using eq. {158}.

Ref. [10]: Kim and Maier, ref. [119]: Suzuki, Kosacki and Anderson, ref. [131]: Rupp, Infortuna and Gauckler

⁶⁴ In defect chemistry regimes (II-a) and (II-b) the pO_2 dependencies of the electronic and ionic conductivity contributions are $M_{pO_2} = -1/4$ and $M_{pO_2} = 0$, respectively (left panel of Fig. 4). Therefore, for the ratio $\sigma_{e',m}/\sigma_{V_O^{**},m}$ the relationship $\sigma_{e',m}/\sigma_{V_O^{**},m} \propto pO_2^{-1/4}$ and, hence, $pO_2 \propto (\sigma_{e',m}/\sigma_{V_O^{**},m})^{-4}$ is valid.

Therefore, if the pO_2 is decreased the ratio $\sigma_{e',m}/\sigma_{V_O^{**},m}$ will be increased. For this reason, the pO_2 at which $\sigma_{e',m} = \sigma_{V_O^{**},m}$ (i.e. the $pO_{2,m}^{EDB}$ value) will be shifted towards higher values if $\sigma_{e',m}/\sigma_{V_O^{**},m}$ (and, thus, $s_{e',m}/s_{V_O^{**},m}$) increases as given in eq. {52}: $pO_{2,m}^{EDB} = (s_{e',m}/s_{V_O^{**},m})^4 \cdot pO_{2,\infty}^{EDB}$.

Hence, an increase of *only* $s_{e',m}$ by one order of magnitude (or a decrease of *only* $s_{V_O^{**},m}$) corresponds to an increase of the $pO_{2,m}^{EDB}$ value by four orders of magnitude. If d decreases *both* $s_{e',m}$ and $s_{V_O^{**},m}$ change ($s_{e',m}$ increases and $s_{V_O^{**},m}$ decreases). As a consequence, if d is decreased by one order of magnitude the $pO_{2,m}^{EDB}$ value will be increased by eight orders of magnitude (see also eq. {52}).

However, the absolute $pO_{2,m}^{EDB}$ values between 10^{-34} and 10^{-25} bar are still exceptionally low compared with the pO_2 range considered in this study between 10^{-5} and 1 bar. Consequently, for the *rt-nano* sample under the given conditions ($\theta=280^\circ\text{C}$, $pO_2 \geq 10^{-5}$ bar) the electronic conductivity contribution is expected to be negligibly small and, therefore, the effective conductivity to be purely ionic (pO_2 independent).

5.5.3.2 Temperature Dependence

After the preliminary considerations let us now focus on the measured conductivity data of the three samples as shown in Fig. 55. The *ht-epitaxial* thin film exhibited the largest conductivity and an activation energy of 0.73 eV that is typical for the bulk and epitaxial films of acceptor doped ceria.^[14, 40, 92, 113, 114, 130] The activation energy increased for the *ht-nano* sample by 0.2 eV indicating that, as expected, the perpendicular GBs block the ionic transport.^[11, 14, 22, 50, 119, 131] For the *rt-nano* film E_a increased even stronger, up to a value of 1.14 eV.

The changes in the activation energy correspond to a decrease in the conductivity values. Thus, with respect to the *ht-epitaxial* film the *ht-nano* sample showed a conductivity decrease by one order of magnitude and, remarkably, the *rt-nano* thin film by 3 orders of magnitude.

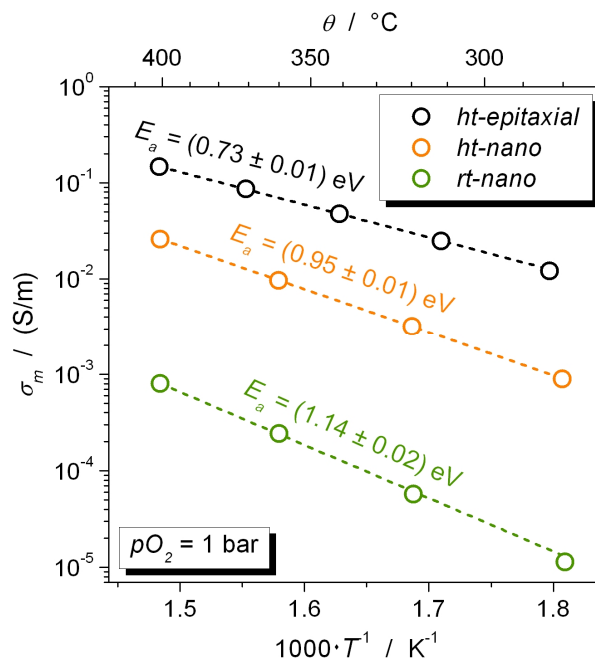


Fig. 55: Temperature Dependence of the Effective Conductivity of the 10 mol% Gd Doped *ht-epitaxial*, *ht-nano* and *rt-nano* CeO_2 Thin Films

Reproduced from Göbel et al.^[16] by permission of the PCCP Owner Societies.

Hence, while the *ht-epitaxial* film is dominated by bulk properties (case (i) in section 2.2.3.2, $\sigma_m = \sigma_{V_0^{\bullet\bullet}, \infty}$), the nanocrystalline samples are controlled by the GBs. For the *ht-nano* film case (ii) of section 2.2.3.2 ($\sigma_m = \sigma_{V_0^{\bullet\bullet}, m}^{\perp} = [[\sigma_{V_0^{\bullet\bullet}, \infty}]^{-1} + [\Delta\sigma_{V_0^{\bullet\bullet}, m}^{\perp}]^{-1}]^{-1}$) applies.

Clearly, this large conductivity reduction of the *rt-nano* sample is qualitatively connected with its particularly small grains. Interestingly, however, the different grain size of the two nanocrystalline films is not sufficient to quantitatively give an explanation. While the conductivity difference between *ht-nano* and *rt-nano* sample is a factor of about 100 the grain size differs only by a factor of 4 (40 nm vs. 10 nm). As a consequence, the average properties of the individual GBs in both films must be different.

Two different mechanisms can explain the conductivity data:

(A) *Higher SCL Potential in the rt-nano Sample*

Using eq. {122} the SCL potentials can be calculated under the assumption of a Mott-Schottky type profile (i.e. a flat dopant profile). For the *ht-nano* thin film this yields a value of 0.22 ± 0.05 V whereas the *rt-nano* sample exhibits a higher value of 0.30 ± 0.05 V. A different potential value is well possible given that both samples exhibit slightly different microstructures. In particular, the orientations of the GBs are well known to influence the SCL potential.^[20] Also in another study an increase in the SCL potential in ceria with decreasing grain size was found.^[132]

While both values are in agreement with other studies^[10, 14, 98, 99] in which potential values between 0.20 and 0.34 V are found still the value of the *rt-nano* sample is remarkably high under the given conditions. In ref. ^[11] it was found that the SCL potential in acceptor doped ceria decreases with decreasing temperature. Here we can observe the same behavior. The nearly identical nanocrystalline films (compared with the *ht-nano* sample) presented in section 5.3.3.1.2 show a potential value of 0.32 ± 0.05 V at 700 °C which then obviously decreases to a value of only 0.22 ± 0.05 V at around 300 °C. The *rt-nano* film instead exhibits a potential of 0.30 ± 0.05 V despite the low temperature. Since not only the potential Φ_0 but the whole term $e\Phi_0/k_B T$ exponentially influences the conductivity (see e.g. eq. {98} or {122}) for a given potential the conductivity changes at reduced temperatures are much more severe.⁶⁵

(B) *SCLs Characterized by a Partial Enrichment of the Acceptor Dopant in the ht-nano Sample*

It is, however, not entirely clear whether for both samples the MS assumption is strictly valid. On the one hand, for the *rt-nano* film this is most likely since this sample never

⁶⁵ As an example the conductivity change due to a potential of 0.3 V at 300 °C is expected to be about as large as for a potential of 0.5 V at 700 °C.

perceived temperatures sufficiently high to mobilize the cations. On the other hand, for the *ht-nano* sample the cations may have been sufficiently mobile to be enriched in the SCLs during the deposition at 720 °C. Since an enrichment of the cations partially shields the positive GB core charge higher SCL potentials are needed to result in the same conductivity changes as for a flat dopant profile. In the extreme situation of a pure Gouy-Chapman case (e.g. very large cation enrichment) a potential of 0.27 V⁶⁶ is necessary to explain the conductivity drop of the *ht-nano* sample shown in Fig. 55. This is already very close to the value of 0.30 ± 0.05 V calculated for the *rt-nano* film. Note, however, that (1) the actual degree of dopant enrichment at the GBs in the *ht-nano* film is not obvious and that (2) at temperatures below 400 °C the supposedly non-flat cation concentration profile becomes frozen, complicating the situation considerably.

5.5.3.3 Oxygen Partial Pressure Dependence

The conductivity of the 10 mol% Gd doped *rt-nano* film being reduced by 3 orders of magnitude shows that this sample indeed fulfils the original goal of this study, namely to obtain a sample with extremely pronounced GB effects. Nevertheless, even more striking are the following properties of the *rt-nano* sample concerning its pO_2 dependence.

Let us firstly concentrate on the *ht-epitaxial* and *ht-nano* films. As entirely expected both films do not exhibit a pO_2 dependent conductivity in the available pO_2 range between 10^{-5} and 1 bar. For the *ht-nano* sample this result is important since it confirms the finding of ref. [22] that the SCL potential is pO_2 independent in acceptor doped ceria.

Given the conductivity data in the literature (section 5.5.3.1.2) also for the *rt-nano* film no pO_2 dependent conductivity is expected. However, surprisingly in this sample the conductivity was observed to considerably change upon a pO_2 variation (Fig. 56). This effect was found to be quantitatively reversible and reproducible.

Since, as explained above a change of the SCL potential with pO_2 can be excluded here the pO_2 dependent contribution of the conductivity must be electronic. In particular, for the *rt-nano* sample the measured conductivity has to be described by case (iii) of section 2.2.3.2, which predicts a constant ionic conductivity contribution and a pO_2 dependent electronic conductivity contribution: $\sigma_m = \sigma_{V\dot{O}^{\bullet\bullet},m}^{\perp} + \sigma_{e^{\bullet},m,0}^{\parallel} \cdot (pO_2/pO_{2,0})^{-1/4}$. Indeed, the data points in Fig. 56b can nicely be fitted with eq. {159}:

⁶⁶ calculated using the numerical approach (Chapter 3)

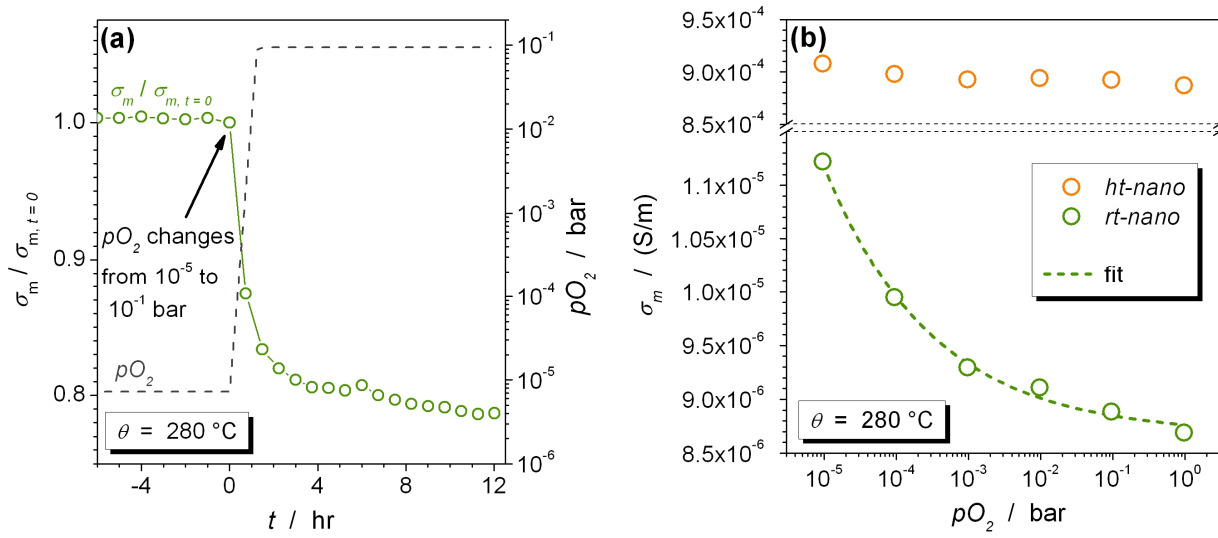


Fig. 56: pO_2 Dependence of the Effective Conductivity of the 10 mol% Gd Doped *ht-nano* and *rt-nano* CeO_2 Thin Films

(a) Relative, Effective Conductivity vs. Time upon an Abrupt pO_2 Increase:

Upon a sudden increase in pO_2 the effective conductivity of the *rt-nano* sample decreased significantly.

t : time, $\sigma_{m,t=0}$: effective conductivity at the onset of the pO_2 jump

(b) Effective Conductivity vs. pO_2 (Linear Plot):

The pO_2 dependence of the conductivity can be well fitted with eq. {159} that describes a pO_2 independent ionic conductivity contribution and a pO_2 dependent electronic conductivity contribution. Notice the break across the y-axis.

Panel (a): Reproduced from Gregori, Göbel and Maier^[17] with permission from ECS Transactions, The Electrochemical Society (Copyright 2012).

Panel (b): Reproduced from Göbel et al.^[16] by permission of the PCCP Owner Societies.

$$\sigma_m = \sigma_{V_O^{\bullet\bullet},m}^{\perp} + \sigma_{e',m,0}^{\parallel} \cdot \left(\frac{pO_2}{pO_{2,0}} \right)^{m_{pO_2}} \quad \{159\}^{67}$$

With an exponent M_{pO_2} of $-1/3.5$ that is close to the expected value of $-1/4$ the fit confirms the finding of a perceptible electronic conductivity contribution.

It is now possible to independently verify the consistency of the SCL theory for this sample by checking whether the increase of the electronic conductivity can be explained with the same SCL potential already determined from the decrease of the ionic conductivity of 0.30 ± 0.05 V. However, to accomplish this the electronic bulk conductivity must be known (see eq. {39}, {57} and {121}) which in the 10 mol% Gd doped *rt-nano* sample itself is not experimentally accessible. For this purpose, we can use the data of the *ht-epitaxial* nominally pure film in Fig. 65a (page 125). Under consideration of the electron mobility data of Tuller^[74] (eq. {17}, $U_{e',0} = 390 \text{ cm}^2 \text{ K}/(\text{Vs})$, $h_{e'} = 0.40 \text{ eV}$) and the reduction equilibrium (eq. {4})⁶⁸ the calculation

⁶⁷ $pO_{2,0}$: reference oxygen partial pressure, $\sigma_{e',m,0}^{\parallel}$: $\sigma_{e',m}^{\parallel}$ at $pO_{2,0}$

⁶⁸ For further details on the calculation see Göbel et al.^[16] and the supplementary information therein.

yields that the electronic conductivity increase in the 10 mol% Gd doped *rt-nano* sample corresponds to a SCL potential of 0.29 ± 0.07 V, which is in good agreement with the value found from the decrease of the ionic conductivity (0.30 ± 0.05 V).

5.5.3.4 Further Considerations on the Activation Energy

SCL effects are well known to strongly change the conductivity properties in nanocrystalline materials. As an example we can take SrTiO₃. Here in a previous study of nanocrystalline pellets (grain size: 30 nm) the electron hole conductivity was found to be decreased by 3 orders of magnitude while the electron conductivity was increased by the same ratio.^[21] These conductivity changes were observed to result in a shift of the pO_2 of the transition point between *p*- and *n*-type conductivity of 12 orders of magnitude.^[21] This extreme example shows that in some cases SCL effects can result in extraordinarily large shifts of the transition oxygen partial pressure.

A comparable transition oxygen partial pressure in CeO₂ is the pO_2 at the electrolytic domain boundary. The fit in Fig. 56b yields that for a pO_2 of 10^{-5} bar the electronic conductivity contribution reaches 25 % of the total effective conductivity (i.e. $\sigma_{e,m}/\sigma_{V_0^{**},m} = 1/3$). Hence, with $pO_2 \propto (\sigma_{e,m}/\sigma_{V_0^{**},m})^{-4}$ ^{64, page 110} the electrolytic domain boundary (where $\sigma_{e,m}/\sigma_{V_0^{**},m} = 1$) is determined to be at a $pO_{2,m}^{EDB}$ value of 10^{-7} bar.

Let us now compare this value with the literature data on CeO₂. Since at such low temperatures comparable systems have not been investigated in previous studies we have no other possibility but to take the next best data available. These are the values in Table 15 and Table 16 which are extrapolated from the high temperature literature data. In comparison with the extrapolated data, the $pO_{2,m}^{EDB}$ value of 10^{-7} bar measured in this study is larger by at least 29 orders of magnitude (compared with the bulk, Table 15) or 18 orders of magnitude (compared with other nanocrystalline samples, Table 16). What is the exact physico-chemical origin of this stunning result (e.g. a change in the activation energy) and how well the high and low temperature properties of ceria can be compared will be discussed below and in the following sections.

In the bulk of acceptor doped ceria the electron concentration is temperature dependent in contrast to the oxygen vacancy concentration which is constant. Therefore, the electronic activation energy ($\Delta H_R/2 + h_{e'}$) is much larger than the ionic one ($h_{V_0^{**}}$). As a consequence, at low temperatures the conductivity is mainly ionic and at high temperatures it is mainly electronic (Fig. 57a).

In the presence of grain boundaries, however, the activation energies change. Since the oxygen vacancies are depleted and the electrons are enriched at the GBs the ionic activation energy

increases and the electronic activation energy decreases. This effect is well known in the literature which even reports on samples exhibiting reduced $E_{a,e'}$ values of down to 0.7 eV.^[6, 133] Consistently, also in this study an increase of $E_{a,V_O^{\bullet\bullet}}$ above 1 eV (Fig. 55) and a decrease of $E_{a,e'}$ below 0.8 eV (Fig. 65a) were observed.

Nevertheless, what remained unknown so far is what happens in an extreme situation. As the values above suggest it might be possible that the electronic activation energy becomes even larger than the ionic one. Such a switch over would correspond to drastic consequences for the sample since now at low temperatures the conductivity would be expected to be mainly electronic and at high temperatures mainly ionic (Fig. 57b).

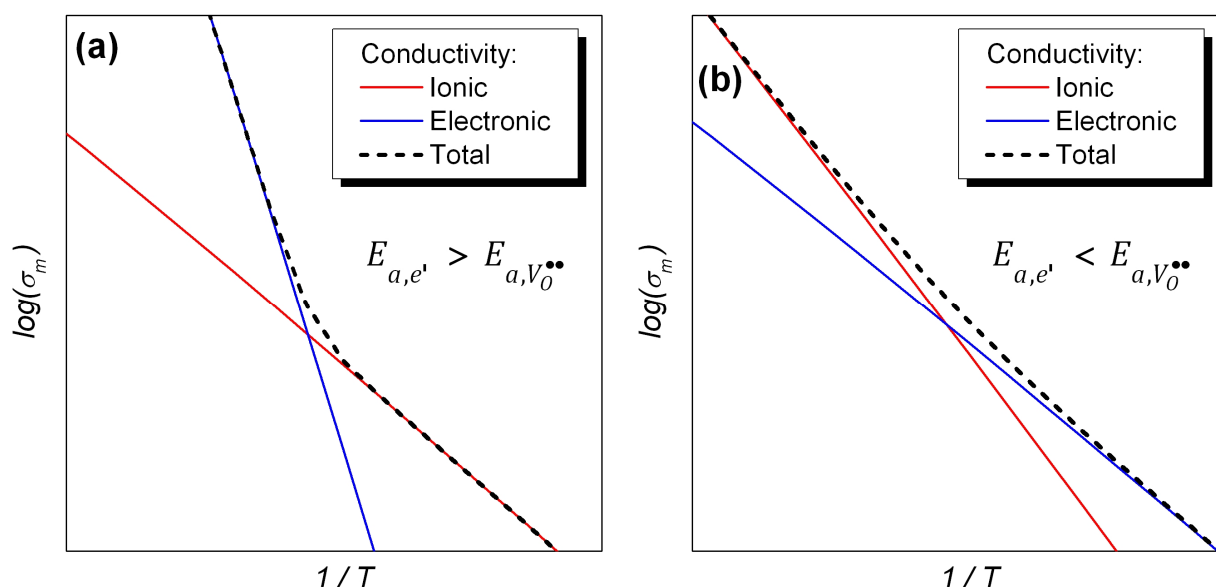


Fig. 57: (a) Usually Observed and (b) Reversed Ranking of the Activation Energies in Acceptor Doped Ceria

(a) For $E_{a,e'} > E_{a,V_O^{\bullet\bullet}}$, as in the bulk of CeO_2 , at low temperatures oxygen vacancies dominate the total conductivity and at high temperatures electrons.

(b) In a (hypothetical) sample exhibiting $E_{a,e'} < E_{a,V_O^{\bullet\bullet}}$ the temperature regimes are switched over. Here the conductivity is expected to be mainly electronic at low temperatures and mainly ionic at high temperatures.

In order to answer the question whether the 10 mol% Gd doped *rt-nano* sample indeed shows such a reversed order of the activation energies the experiment already shown in Fig. 56a, i.e. a sudden increase of pO_2 , was carried out at several temperatures (Fig. 58a). Due to the abrupt change in pO_2 the electronic conductivity contribution decreased while the ionic one stayed constant. As shown in Fig. 58a the relative drop of conductivity upon pO_2 increase was found to be larger for lower temperatures. This means that also the electronic conductivity contribution was larger at lower temperatures and that indeed the sample behaves as qualitatively indicated in Fig. 57b. For this sample the electronic activation energy must be smaller than the ionic one.

Quantitatively, the results shown in Fig. 58a can be used to separate the ionic and electronic contributions. This yields effective ionic and electronic activation energies of 1.2 eV and 0.9 eV, respectively. Hence, the intermediate total activation energy value of 1.1 eV previously given in Fig. 55 is a combination of both contributions.

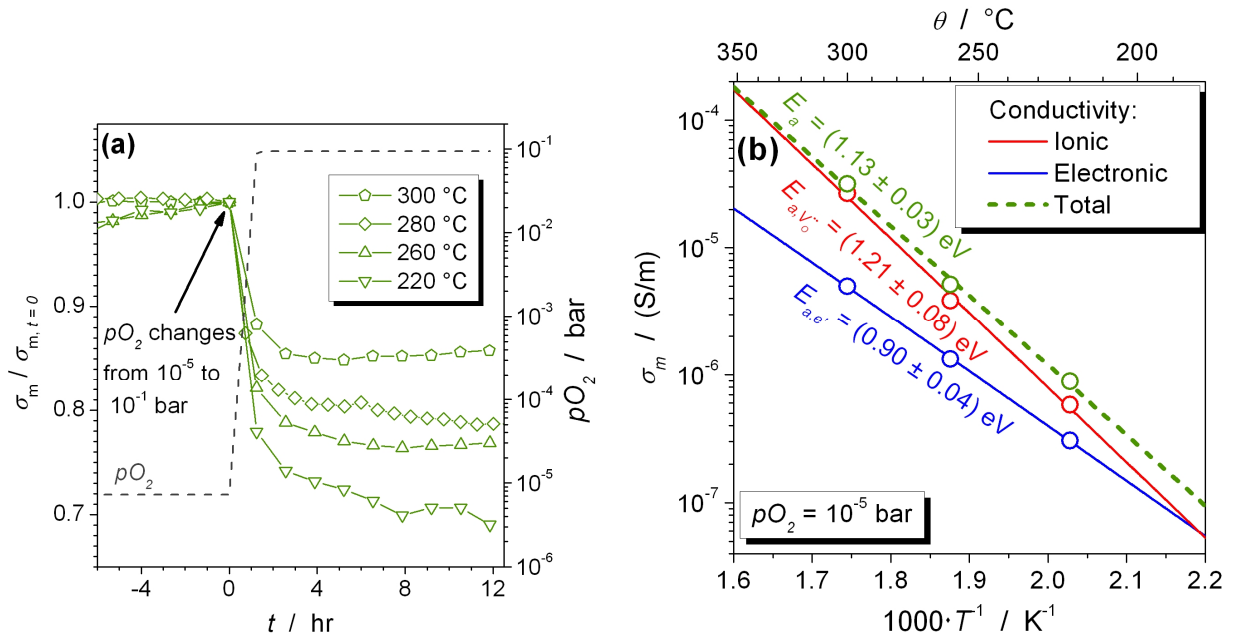


Fig. 58: Separation of the Ionic and Electronic Conductivity Contributions of the 10 mol% Gd Doped *rt-nano* Thin Film at Various Temperatures

(a) Relative Conductivity vs. Time upon an Abrupt pO_2 increase:

Due to the electronic conductivity contribution the overall conductivity decreased upon an increase in pO_2 while the ionic contribution was pO_2 independent. Clearly, the relative conductivity reduction (and, hence, the relative electronic conductivity contribution) was larger at lower temperatures (i.e. $E_{a,e'} < E_{a,V_0^{**}}$)

(b) Temperature Dependence of the Ionic and Electronic Conductivity Contributions:

A quantitative analysis of the data in plot (a) allowed for the determination of the ionic and electronic activation energies $E_{a,V_0^{**}}$ and $E_{a,e'}$. There were found to be 1.21 ± 0.08 eV and 0.90 ± 0.04 eV, respectively.

Due to the switch over of the activation energies the nature of the *rt-nano* film may be considered to be completely different compared with regular ceria samples (e.g. the ones in Table 15 and Table 16). Usually, i.e. for $E_{a,e'} > E_{a,V_0^{**}}$, the EDB shifts towards smaller pO_2 values upon temperature decrease since $pO_{2,m}^{EDB} \propto \exp(-4/(kBT) \cdot (E_{a,e'} - E_{a,V_0^{**}}))$.⁶⁹ Indeed, all studies listed in Table 15 and Table 16 report on samples with this kind of behavior. However, for the here presented *rt-nano* sample $E_{a,e'} < E_{a,V_0^{**}}$ and, therefore, the $pO_{2,\infty}^{EDB}$ and $pO_{2,m}^{EDB}$ values increase with decreasing temperatures. Hence, the lower the temperature the larger the

⁶⁹ see eq. {158}

difference in $pO_{2,m}^{EDB}$ is expected to be between both kinds of samples. This explains the astonishingly large $pO_{2,m}^{EDB}$ value of the *rt-nano* film compared with the literature data given in Table 15 and Table 16.

This reasoning also clarifies why in none of the abundant studies on nanocrystalline ceria so far an effect was found that is equivalent with the drastic increase of the $pO_{2,m}^{EDB}$ value observed in the *rt-nano* sample. For such a particular sample and at high pO_2 it is possible to observe the large electronic conductivity at low temperatures only. However, nearly all studies in the literature focus on temperatures considerably higher than 300 °C where this effect is simply inaccessible. As an example, if we take the $pO_{2,m}^{EDB}$ value of the *rt-nano* film of 10^{-7} bar at 280 °C and extrapolate it with eq. {158} to 700 °C (by ignoring the grain growth for a moment) the resulting value of 10^{-12} bar is very similar with the ones found in other studies at 700 °C.⁷⁰

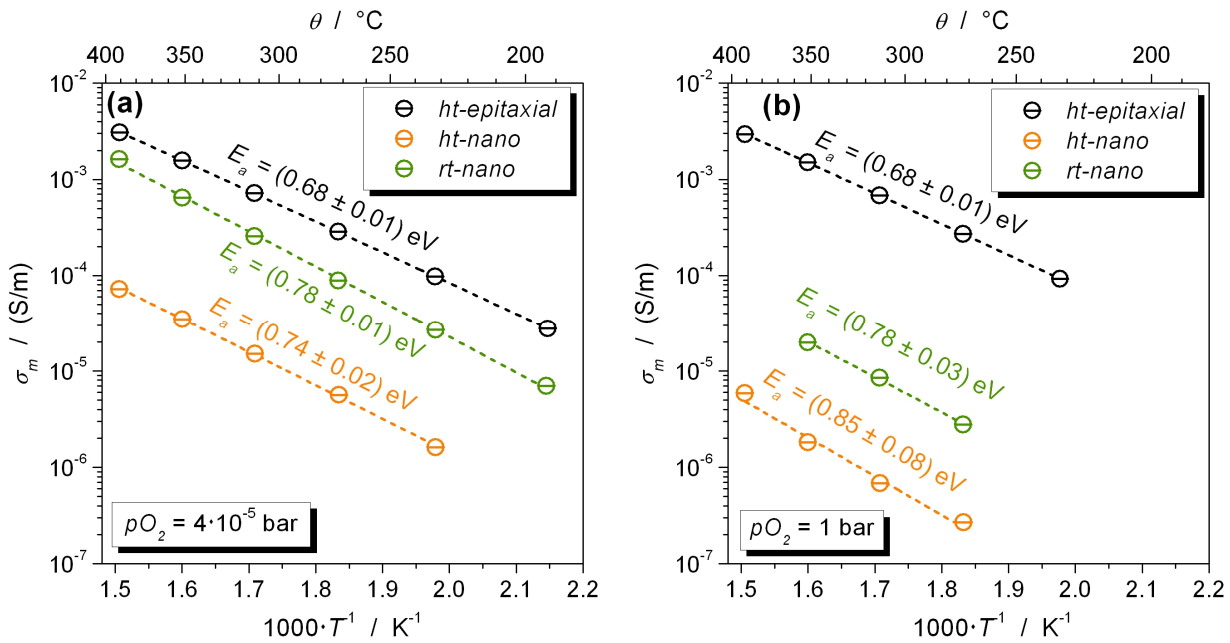


Fig. 59: Temperature Dependence of the Effective Conductivity of the 1 mol% Gd Doped *ht-epitaxial*, *ht-nano* and *rt-nano* CeO₂ Thin Films

(a) $pO_2 = 4 \cdot 10^{-5}$ bar

(b) $pO_2 = 1$ bar

See section 5.5.3.5.

At both pO_2 the *ht-epitaxial* sample is a mainly ionic conductor (i.e. $E_a \approx E_{a,V_O^{\bullet\bullet}}$) while the *ht-nano* and *rt-nano* films exhibit *n*-type conductivity (i.e. $E_a \approx E_{a,e^-}$) (see also Fig. 60).

⁷⁰ As an example, the 20 mol% Gd doped, nanocrystalline PLD film with a grain size of 65 nm studied in ref. [131] showed a $pO_{2,m}^{EDB}$ of $2 \cdot 10^{-17}$ bar at 700 °C (see Table 16). Extrapolated using eq. {158} to a doping content of 10 mol% Gd and a grain size of 10 nm, as in the *rt-nano* film, for this sample a $pO_{2,m}^{EDB}$ value of $4 \cdot 10^{-9}$ bar is expected at 700 °C. This value is even larger than the hypothetical $pO_{2,m}^{EDB}$ value of the *rt-nano* sample at 700 °C (of 10^{-12} bar) which, hence, at these temperatures would not have been unexpectedly large at all.

Therefore, only because the measurements were restricted to low temperatures in our study we had the chance to discover this surprising effect.

5.5.3.5 Enhanced Electronic Bulk Conductivity

On the one hand, as stated above the conductivity effects in the *rt-nano* sample are in agreement with the SCL theory. On the other hand, the shift of $pO_{2,m}^{EDB}$ is unexpectedly large compared with the literature values. This suggests that also the bulk properties, and specifically the $pO_{2,\infty}^{EDB}$ values, are changed in the CeO₂ thin films investigated here.

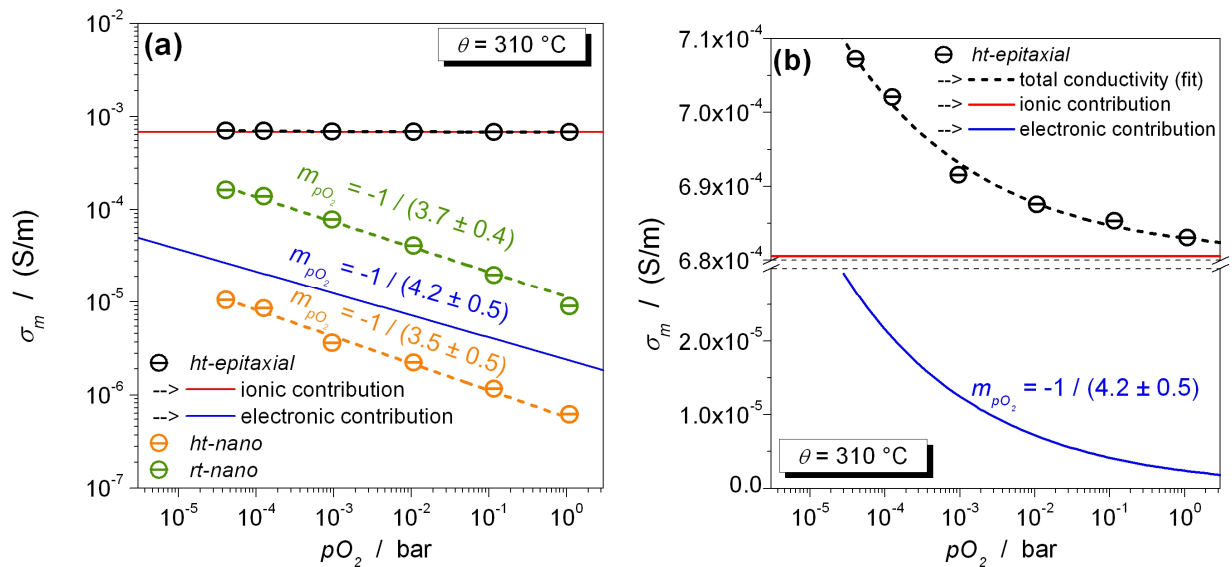


Fig. 60: pO_2 Dependence of the Effective Conductivity of the 1 mol% Gd Doped *ht-epitaxial*, *ht-nano* and *rt-nano* CeO₂ Thin Films

(a) Logarithmic Plot

See main text below.

The *ht-nano* and *rt-nano* samples showed pO_2 dependencies close to $-1/4$, typical for n -type conductivity. Notably, the effective conductivity of the *ht-epitaxial* sample was found to be also very slightly pO_2 dependent (see linear plot (b)). The fit using eq. {159} yields a large, predominant ionic contribution and a small electronic contribution. Notice the break across the y-axis in plot (b).

The ionic conductivity contribution of the *ht-nano* sample is too small to be separated from the large electronic contribution. Hence, under consideration of the data at $pO_2 = 1$ bar in panel (a) it must be smaller than about 3.5 orders of magnitude compared with the ionic contribution of the *ht-epitaxial* film. Using the relationships in Table 7 (or the numerical approach) at 310 °C this was found to correspond to a SCL potential of at least 0.33 ± 0.05 V in this sample.

(b) Linear Plot (only *ht-epitaxial*)

In the 10 mol% Gd doped *rt-nano* sample (with the experimentally found SCL potential of about 0.3 V) the ionic conductivity was decreased by 3 orders of magnitude (eq. {122}) and the electronic one increased by 1 order of magnitude (eq. {121}). This corresponds to a difference

between the $pO_{2,m}^{EDB}$ and $pO_{2,\infty}^{EDB}$ values of roughly $(3+1) \cdot 4 = 16$ orders of magnitude (eq. {52}) which shows that as in the above mentioned case of nanocrystalline $SrTiO_3$ [21] (shift of the transition pO_2 by 12 orders of magnitude) also in nanocrystalline ceria SCL effects dominate the conductivity properties. Due to the shift of 16 orders of magnitude on account of the GB effects in the *rt-nano* sample the $pO_{2,\infty}^{EDB}$ value is expected to be at around $10^{-(7+16)} = 10^{-23}$ bar. This value, however, is more than 13 orders of magnitude larger than what is expected from the literature data ($pO_{2,\infty}^{EDB}$ values in the range between 10^{-50} and 10^{-36} bar, Table 15).

In order to experimentally verify, whether the bulk electron conductivity is enhanced in the thin films, two series of films with a smaller doping content of 1 and 0.15 mol% Gd were fabricated.

Also in this case it is convenient to consider first what is expected for these doping contents in the literature. By extrapolating the bulk data of Table 15 down to 310 °C $pO_{2,\infty}^{EDB}$ values between 10^{-40} and 10^{-28} bar are expected for 1 mol%, and between 10^{-35} and 10^{-23} bar for 0.15 mol% acceptor doping (eq. {156}).

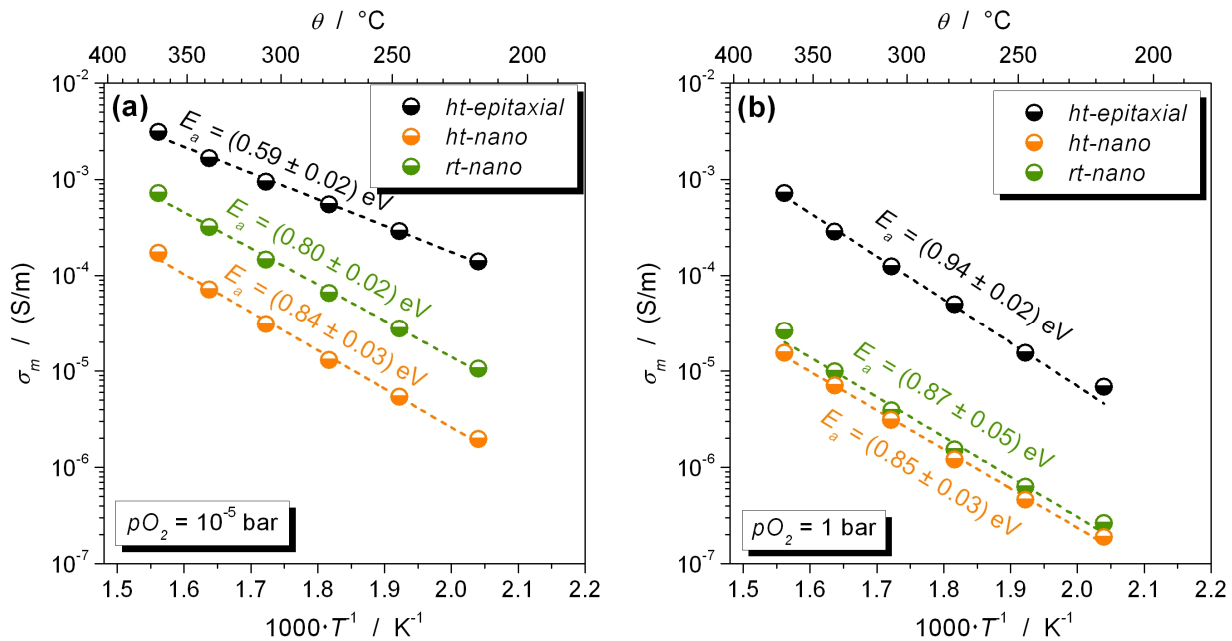


Fig. 61: Temperature Dependence of the Effective Conductivity of the 0.15 mol% Gd Doped *ht-epitaxial*, *ht-nano* and *rt-nano* CeO₂ Thin Films

(a) $pO_2 = 10^{-5}$ bar

(b) $pO_2 = 1$ bar

At 10^{-5} bar the *ht-epitaxial* sample is a mainly electronic conductor (i.e. $E_a \approx E_{a,e}$) whereas at 1 bar the electronic and ionic contributions are comparably large (see Fig. 62). Both the *ht-nano* and *rt-nano* thin films are electronic conductors with $E_a \approx E_{a,e}$.

As for the experimental data, the 1 mol% doped *ht-epitaxial* sample showed an activation energy around 0.7 eV typical for bulk ionic conductivity (Fig. 59).[14, 40, 92, 113, 114, 130] Nevertheless,

a careful analysis of the pO_2 dependence of this film (Fig. 60b) revealed a small electronic conductivity contribution with $M_{pO_2} = -1/4.2 \pm 0.5$ (case (v) in section 2.2.3.2, $\sigma_m = \sigma_{V_0^{**},\infty} + \sigma_{e',\infty}$). The recorded electronic contribution corresponds to a $pO_{2,\infty}^{EDB}$ value of 10^{-10} bar⁷¹ at 310 °C which is more than 18 orders of magnitude larger than expected from the literature.

Also the 0.15 mol% doped *ht-epitaxial* sample exhibited significant ionic and electronic conductivity contributions as shown in Fig. 62.⁷² Due to the lower doping content the $pO_{2,\infty}^{EDB}$ value is here higher than for the 1 mol% doped film. It is 1 bar (see Fig. 62) and, hence, more than 23 orders of magnitude larger than expected from the literature values.

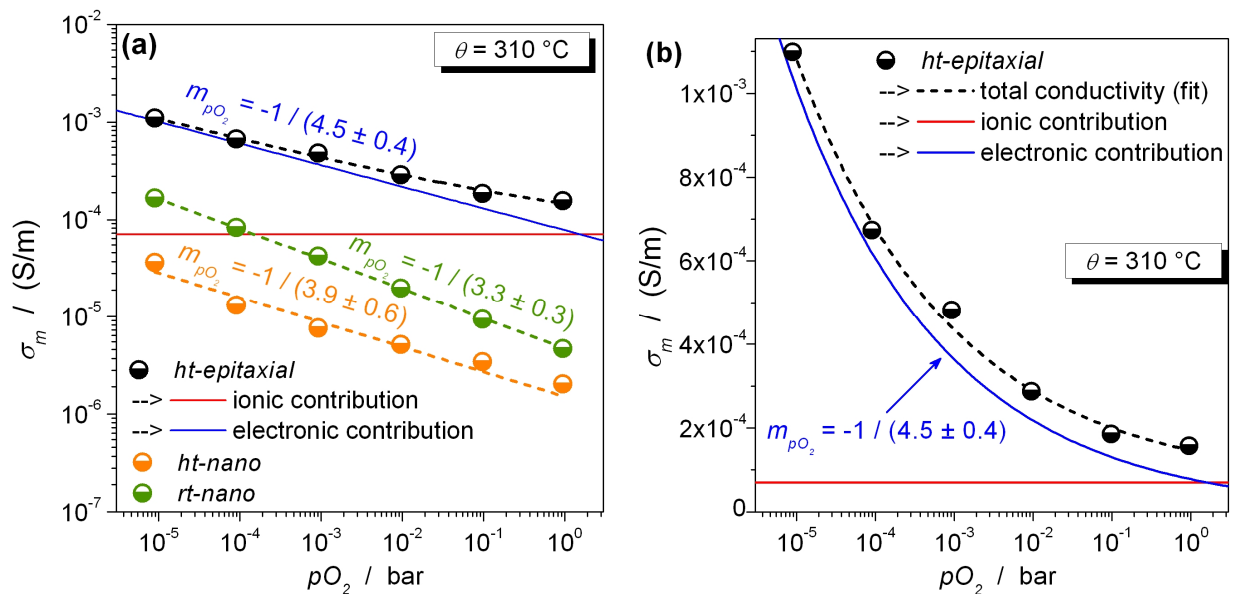


Fig. 62: pO_2 Dependence of the Effective Conductivity of the 0.15 mol% Gd Doped *ht-epitaxial*, *ht-nano* and *rt-nano* CeO_2 Thin Films

(a) Logarithmic Plot

(b) Linear Plot (only *ht-epitaxial*)

As for the 1 mol Gd doped films also here the *ht-nano* and *rt-nano* samples were observed to be electronic conductors ($M_{pO_2} \approx -1/4$) while the *ht-epitaxial* film exhibited an additional ionic contribution. The lower dopant level shifts the ratio of both contributions in the *ht-epitaxial* film towards a more electronically dominated conductivity compared with Fig. 60.

The ionic conductivity contribution of the *ht-nano* sample (which cannot be separated from the electronic one) is least 2 orders of magnitude smaller compared the *ht-epitaxial* film. This yields a minimum value for the SCL potential in the *ht-nano* film of 0.21 ± 0.05 V using the relationships in Table 7 or the numerical approach.

⁷¹ The $pO_{2,\infty}^{EDB}$ value of 10^{-10} bar was determined by extrapolating the electronic conductivity contribution observed between 10^{-5} and 1 bar in Fig. 60 to a value for $\sigma_{e',m}/\sigma_{V_0^{**},m}$ of 1 with $pO_2 \propto (\sigma_{e',m}/\sigma_{V_0^{**},m})^{-4}$ (see also footnote ⁶⁴, page 110).

⁷² The applicable case in section 2.2.3.2 is, thus, again case (v) with $\sigma_m = \sigma_{V_0^{**},\infty} + \sigma_{e',\infty}$.

Hence, the experiments on the 0.15 and 1 mol% doped samples confirm that the $pO_{2,\infty}^{EDB}$ values are strongly increased compared with the literature. This fascinating outcome shows that the exceptionally large shift of the EDB towards high pO_2 which was observed in all films investigated here, with the 10 mol% Gd doped *rt-nano* film being the most prominent example, bases on two origins: (1) for all films a very high bulk electron conductivity (and hence a large $pO_{2,\infty}^{EDB}$ value) and (2) additionally for the nanocrystalline samples strong SCL effects characterized by a drastic decrease in the ionic conductivity and a further, strong increase in the electron conductivity (leading to a large value of $s_{e',m}/s_{V_O^{\bullet\bullet},m}$ and, hence, an enormously large value of $pO_{2,m}^{EDB}$, eq. {52}).

5.5.3.6 Change in the Electronic Activation Energy at 500 °C

The enhanced bulk electron conductivity corresponds to a very small electronic activation energy (Fig. 59, Fig. 61 and Fig. 65a). A previous study (section 5.3.3.2.4, page 96) showed that the electronic activation energies of nominally pure thin films between 550 and 700 °C are surprisingly low (Table 11) corresponding to a reduction enthalpy of merely 3.3 eV (compared with 4.67 eV in the singly crystal^[74]). Clearly, the lower reduction enthalpy results in a large electron conductivity increase particularly at low temperatures.

In addition to this, a measurement performed on an epitaxial, nominally pure film (case (vi) in section 2.2.3.2, $\sigma_m = \sigma_{e',\infty}$) over a broad temperature range between 250 and 700 °C showed a significant further reduction of E_a from 1.4 eV at higher temperatures to 1.0 eV at temperatures below 500 °C (Fig. 63).

The fact that the variation in E_a is around 0.4 eV suggests that not only the electron mobility is changed (since $h_{e'} \approx 0.4$ eV)^[74] but that a significant contribution must originate from a further decrease of the reduction enthalpy.

The change of E_a can be incorporated in the schemes previously shown in Fig. 57 as illustrated in Fig. 64. As elucidated in section 5.5.3.4 for the *rt-nano* sample at low temperatures $E_{a,e'}$ was found to be smaller than $E_{a,V_O^{\bullet\bullet}}$. The data in Fig. 63 suggests that for higher temperatures $E_{a,e'}$ increases to values around 1.4 eV⁷³ which are significantly larger than $E_{a,V_O^{\bullet\bullet}}$ (that in nanocrystalline samples is typically between 1.0 and 1.2 eV, e.g. see Table 10 and Fig. 58). Hence, qualitatively three temperature regimes can be distinguished. The conductivity is

⁷³ 1.4 eV were observed in the nominally pure sample. However, the change of the reduction enthalpy is expected to result in a strongly increased $E_{a,e'}$ value in the acceptor doped samples too.

predominantly (1) electronic at low temperatures, (2) ionic at intermediate temperatures and (3) at high temperatures electronic again (Fig. 64).

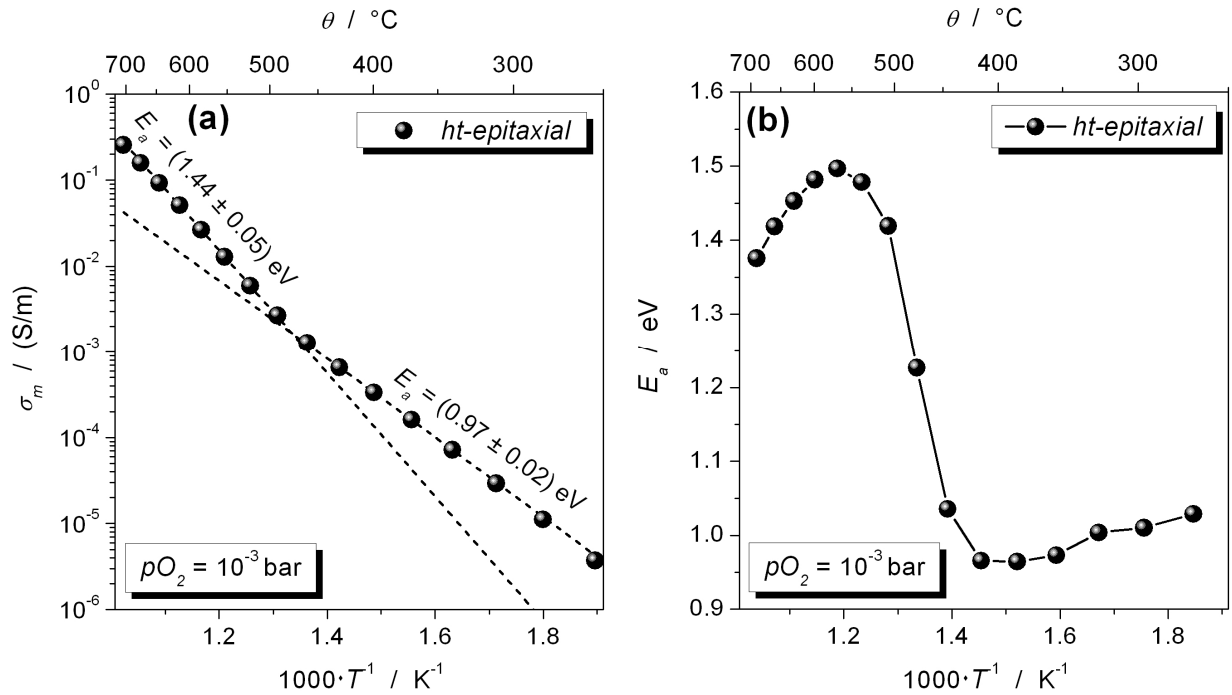


Fig. 63: Temperature Dependence of the Effective Conductivity of a Nominally Pure, *ht-epitaxial* CeO₂ Thin Film over a Broad Temperature Range between 250 and 700 °C

(a) Effective Conductivity as a Function of Temperature

(b) Activation Energy Calculated between Two Adjacent Data Points in Plot (a) as a Function of Temperature

The electronic activation energy was found to change at around 500 °C by about 0.4 eV. Note that the lower activation energy at reduced temperatures is not a cause of a slow kinetics. Also at low temperatures the thin film was observed to be in thermodynamic equilibrium with the surrounding atmosphere.

This explains why in the literature, in which the data was recorded around or above 500 °C, for decreasing temperatures a shift of the EDB towards lower pO_2 values (i.e. $E_{a,e'} > E_{a,V_o^{\bullet\bullet}}$) was observed (Table 15 and Table 16) whereas in this study, performed at temperatures below 400 °C the exact opposite (i.e. $E_{a,e'} < E_{a,V_o^{\bullet\bullet}}$) was found.

5.5.3.7 Grain Boundary Effects in the 1 and 0.15 mol% Gd Doped and Nominally Pure Thin Films

As shown above the 1 and 0.15 mol% Gd doped *ht-epitaxial* films exhibited a mixed ionic and electronic conductivity (Fig. 60 and Fig. 62). Due to the positive SCL potential at the GBs the ionic conductivity contribution vanishes in the respective *ht-nano* and *rt-nano* films which exhibit pO_2 dependencies typical for *n*-type conduction ($\sigma_m = \sigma_{e',m}^{\parallel} = \sigma_{e',\infty} + \Delta\sigma_{e',m}^{\parallel}$, case (iv) in

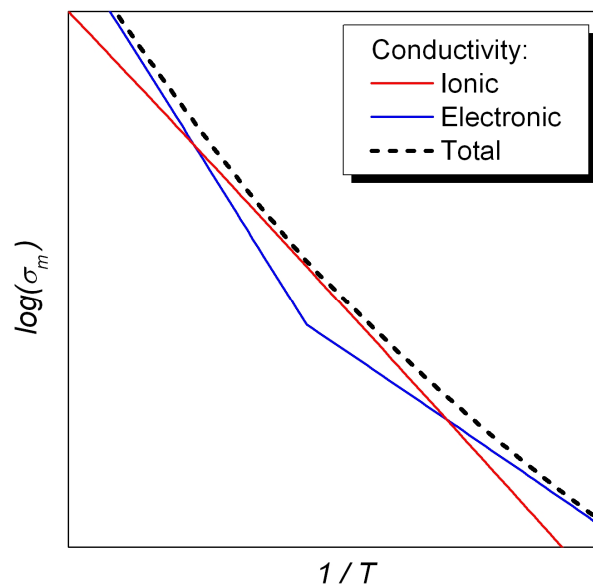


Fig. 64: Proposed Activation Energies in Acceptor Doped Ceria

As shown in Fig. 63 the electronic activation energy changes around 500 °C. For acceptor doped samples qualitatively this corresponds to a separation in three temperature regimes. (1) At low temperatures the total conductivity is expected to be mainly electronic, (2) at intermediate temperatures predominantly ionic and (3) at high temperature once more electronic.

section 2.2.3.2). However, the electronic conductivity of the *ht-nano* samples is surprisingly reduced compared with the *ht-epitaxial* films (Fig. 59 to Fig. 62). The same effect was also observed in nominally pure films (Fig. 65).

While the SCL theory predicts an increase of the electronic conductivity instead the finding is in agreement with a recent investigation of GB effects in ceria where a similar reduction of the electronic conductivity was observed.^[132] This also fits well to what was found for donor doped CeO₂ thin films in the framework of this PhD study (section 5.6). Here the GBs were observed to block the electron transport too.

The fact that the ionic conductivity is reduced in the *ht-nano* film shows that SCL effects are significant in these samples as expected. Therefore, the most likely explanation of the reduced electron conductivity is a second superimposed conductivity effect at the GBs. This might well be a reduced electron mobility as explained in detail in section 5.6.3.2 or a grain size dependence of the reduction enthalpy.

In any case for the *rt-nano* samples the electron conductivity was detected to be increased again for all three doping contents compared with the respective *ht-nano* samples (Fig. 59 to Fig. 62 and Fig. 65). Here it is useful to consider that the 10 mol% doped *rt-nano* sample exhibited particularly strong SCL effects (see paragraphs (A) and (B) in section 5.5.3.2). Probably also the

less doped and nominally pure *rt-nano* films are characterized by similarly pronounced SCLs effects which overcompensate the reduction of the electron conductivity.

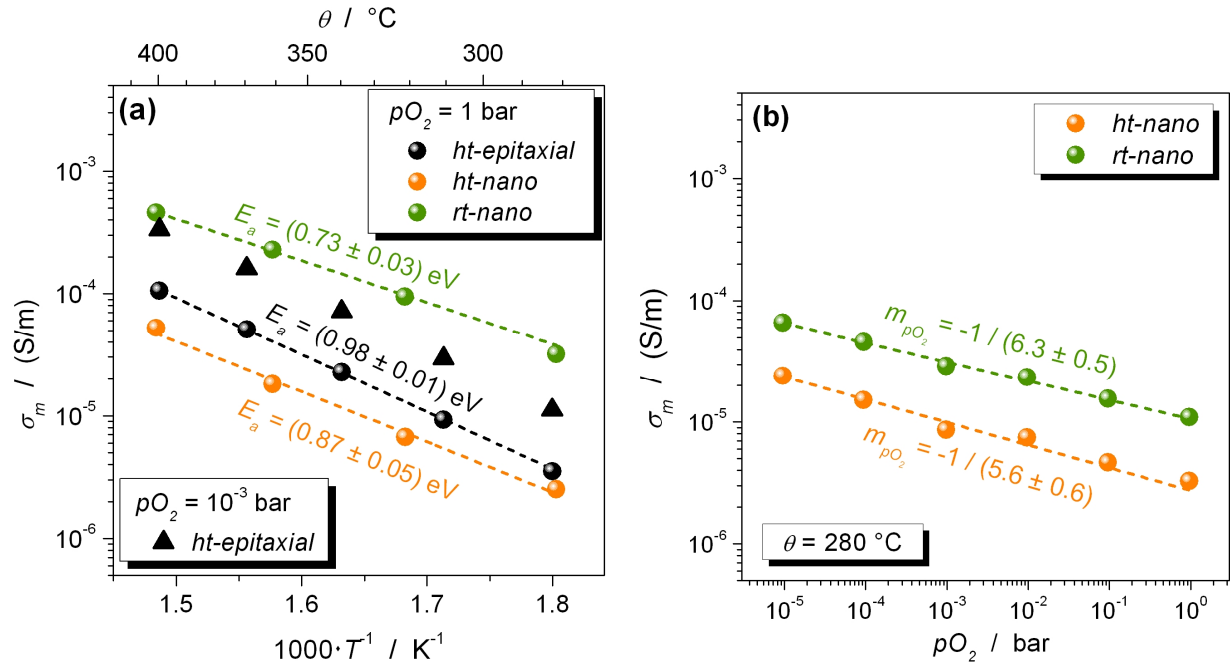


Fig. 65: (a) Temperature and (b) $p\text{O}_2$ Dependence of the Effective Conductivity of the Nominally Pure *ht-epitaxial*, *ht-nano* and *rt-nano* CeO_2 Thin Films

For plot (a) the *ht-nano* and *rt-nano* samples were recorded at a $p\text{O}_2$ of 1 bar. The *ht-epitaxial* sample was measured in the framework of a different study (the one shown in section 5.3) at a different $p\text{O}_2$ of 10^{-3} bar (triangles). In order to compare all three films the data of the *ht-epitaxial* sample was extrapolated to a $p\text{O}_2$ of 1 bar using the measured $p\text{O}_2$ dependence of $-1/6$, see plot (b). This $M_{p\text{O}_2}$ value is also expected for pure ceria (Table 1).

5.5.4 Section Conclusions

In summary, nanocrystalline ceria thin films prepared at low temperatures and characterized by very small grains were investigated and compared with nanocrystalline samples prepared at high temperatures and with epitaxial films. In order to prevent grain growth the samples needed to be measured at temperatures below 400 $^{\circ}\text{C}$. At these conditions the thin films exhibit conductivity features which are markedly different compared with the properties extrapolated from the literature data.

For the most prominent example, the 10 mol% Gd doped *rt-nano* film, the ionic conductivity was observed to be decreased by 3 orders of magnitude while the electronic conductivity was found to be strongly increased. In this sample the $p\text{O}_2$ of the electrolytic domain boundary $p\text{O}_{2,m}^{\text{EDB}}$ was measured to be at a value of 10^{-7} bar. Since no literature data for the low temperature properties of CeO_2 were available this result could be compared only with the literature data recorded at

high temperatures which for this purpose has been extrapolated to low temperatures. Compared with these extrapolated values the measured $pO_{2,m}^{EDB}$ value was found to be strongly increased. Further measurements have been carried out in order to examine (a) what is the cause of this drastic effect and (b) how well the high and low temperature properties of ceria are comparable. It could also be shown why the data here recorded varies strongly from other studies performed at high temperatures. The electronic activation energy decreases considerably for temperatures below 500 °C.

Furthermore, the effective electronic activation energy was found to be smaller than the ionic activation energy leading to the very unusual effect of an increase of the electronic transference number for decreasing temperatures.

These remarkable conductivity features were observed to originate from two causes. (1) Due to the very pronounced SCL effects the ratio between electronic and ionic conductivity contributions is enhanced. This was found to result in a large increase of the $pO_{2,m}^{EDB}$ value by 16 orders of magnitude that is comparable with recent results on nanocrystalline SrTiO₃ indicating a large shift of the transition pO_2 between *p*- and *n*-type conduction of 12 orders of magnitude. (2) Compared to what is expected from measurements at high temperatures, at low temperatures the bulk electron conductivity is strongly increased (leading to an increase of $pO_{2,\infty}^{EDB}$ by further at least 13 orders of magnitude). The conductivity data indicates that the cause of this conductivity increase is most probably a decreased reduction enthalpy. Hence, altogether compared with the literature bulk data extrapolated to low temperatures the pO_2 of the EDB was found to be shifted by at least $16 + 13 = 29$ orders of magnitude.

A number of *ht-nano* samples showed a decrease of the electronic conductivity at the GBs. This was attributed to a second GB conductivity effect which superimposes the SCL effects. This effect is probably due to structural reasons (a change in mobility and/or reduction enthalpy).

5.6 Electronically Blocking Grain Boundaries in Donor Doped Cerium Oxide

5.6.1 Section Introduction

In the last section it could be shown that not only the ionic but also the electronic conductivity can be drastically changed at the GBs in ceria. Therefore, in order to get a further understanding on the electronic GB effects the next experiment was performed on a pure *n*-type conductor that is so far only barely investigated: donor doped CeO₂. While in the literature only very few data is available on the defect chemistry of this material (e.g. ref. [73, 83-89]), the conductivity variations at the GBs have not been examined at all. This makes a study of these effects particularly interesting.

As discussed in section 5.5.3.7 the electronic conductivities in the measured nominally pure and acceptor doped *ht-nano* films were decreased despite the presence of a positive SCL potential at the GBs. This indicates the existence of additional GB effects on the electronic conductivity which are, however, difficult to analyze in these samples since they are superimposed by strong SCL effects. For donor doped cerium oxide the situation is different. Let us here regard again Fig. 34 (page 73) which shows the expected SCL effects in ceria under consideration of the SCL charge. As explained in section 5.1.5.3 for positive SCL potentials, as they are found in ceria, the SCL effects strongly affect the ionic conductivity for acceptor doping as indicated by arrow A in Fig. 34a. However, due to the limiting influence of the SCL charge a positive SCL potential in donor doped ceria is not expected to result in a considerable change of the electron conductivity (see arrow C in Fig. 34b). This indicates that the further GB effects on the electronic conductivity shown in section 5.5.3.7 should become nearly unperturbed in donor doped ceria (under the assumption of a positive SCL potential there too). Also due to this the investigation of donor doped CeO₂ is of high relevance.

Specifically, as above an *ht-epitaxial* (here grown on an Al₂O₃ <1102> substrate), an *ht-nano* and an *rt-nano* film were prepared and investigated. The doping content of the samples was 2 mol% of Nb.

5.6.2 Microstructure

The XRD, TEM and EDP experiments confirmed the epitaxial microstructure of the *ht-epitaxial* thin film. (1) Only the (100) and related orientations were recorded in the XRD pattern, (2) the

TEM and HRTEM micrographs did not show grain boundaries and (3) the EDP featured the regular array of a single crystalline phase (Fig. 66 and Fig. 67).

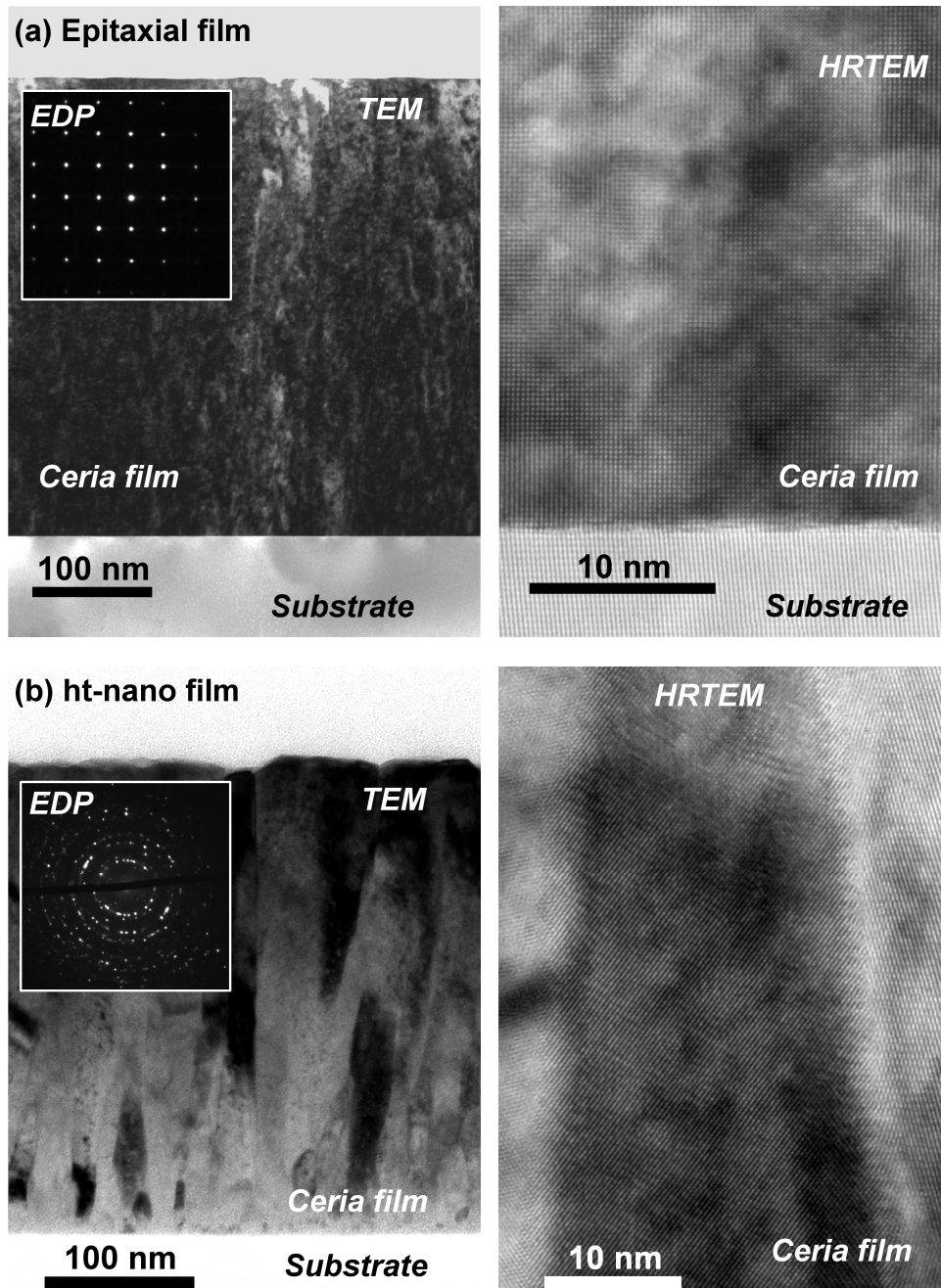


Fig. 66: TEM and HRTEM Micrographs and Electron Diffraction Patterns (EDP) of the 2 mol% Nb Doped CeO₂ Thin Films

(a) *ht-epitaxial*

(b) *ht-nano*

From the Top: CeO₂ Thin Film and Substrate

Reprinted from Göbel et al.^[15] (Copyright 2012) with permission from Elsevier.

The *ht-nano* and *rt-nano* samples exhibited a polycrystalline, columnar microstructure. Here (1) many orientations were found in the XRD experiment, (2) the TEM and HRTEM micrographs featured a columnar microstructure and (3) the EDP was typical for a polycrystalline sample.

Notably, also the *rt-nano* film showed all expected XRD signals indicating a crystalline structure of this sample. The broadening of the peaks can be attributed to the decrease in lateral grain size compared with the *ht-nano* film. Interestingly, for this particular donor doped *rt-nano* sample the XRD signals were slightly shifted.

The GBs observed with HRTEM were found to be clean. No second phase was detected.

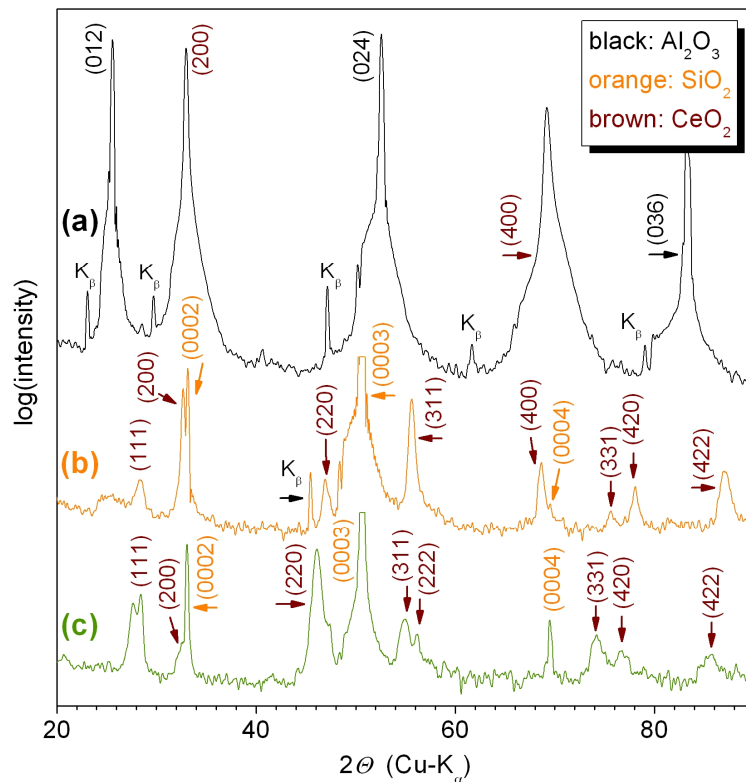


Fig. 67: XRD Patterns of the 2 mol% Nb Doped CeO₂ Thin Films

(a) *ht-epitaxial*

(b) *ht-nano*

(c) *rt-nano*

For clarity the curves have been smoothed. The very intense SiO₂ (0003) signals have been cut.

Reprinted from Göbel et al.^[15] (Copyright 2012) with permission from Elsevier.

5.6.3 Conductivity Data

5.6.3.1 Defect Chemistry

The conductivity of the donor doped films exhibited a pO_2 dependence between $-1/4$ and $-1/2$ (see Fig. 68) with no significant difference between the M_{pO_2} values of the three samples (under

consideration of the measurement uncertainty). As shown in section 2.1 this indicates not only *n*-type conductivity dominated by the presence of oxygen interstitial defects but also that a considerable fraction of the oxygen interstitials is only singly charged. Hence, in the considered pO_2 range between 10^{-5} and 1 bar the samples are at the border between defect chemistry regimes (IV) and (V) (see Table 1 and Fig. 4, right panel). This finding is in good agreement with ref. [73, 88] in which for donor and uranium doped CeO_2 under similar conditions pO_2 dependencies between $-1/4$ and $-1/2$ were found.

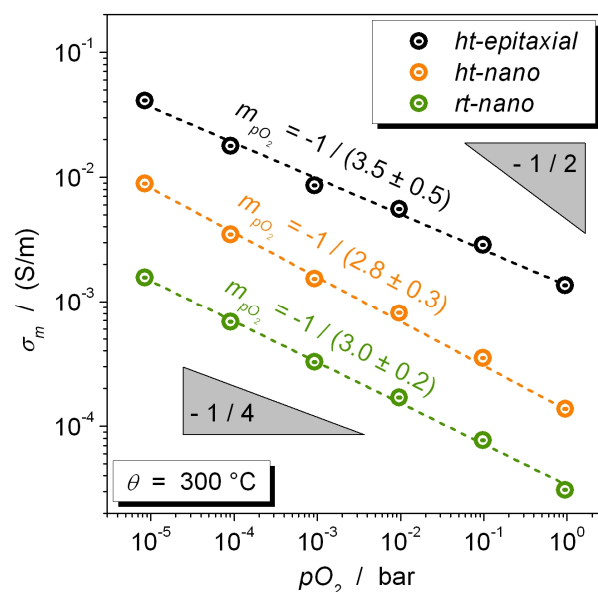


Fig. 68: pO_2 Dependence of the Effective Conductivity of the 2 mol% Nb Doped CeO_2 Thin Films

Reprinted from Göbel et al.^[15] (Copyright 2012) with permission from Elsevier.

A previous study on U doped ceria, a comparable material, indicates that the oxygen insertion reaction is exothermic (enthalpy of -0.76 ± 0.5 eV).^[73] Due to this the border between defect chemistry regimes (III) and (IV) is expected to shift towards higher pO_2 values for increasing temperatures resulting in a less steeper pO_2 dependence in the given constant pO_2 range. As a matter of fact, at 700 °C the M_{pO_2} values were found to decrease to -0.12 ± 0.02 .

More quantitatively it is possible to calculate the oxygen insertion enthalpy from the temperature dependence of the conductivity (Fig. 69a). Here we can take the data of the *ht-epitaxial* film in which (1) no GB effects are present (i.e. case (vi) in section 2.2.3.2 and $\sigma_m = \sigma_{e',\infty}$ can be applied) and (2) the charge neutrality condition of defect chemistry regime (IV), $|z_D|c_D = 2c_{O''}$, is fulfilled best compared with the two other films (since $M_{pO_2} = -1/3.5 \pm 0.5 \approx -1/4$). Under the assumption that Tuller's electron mobility data^[74, 90] is also valid in donor doped ceria the enthalpy of the oxygen insertion ΔH_I is determined to be -0.35 ± 0.1 eV (Fig. 69b). If the fairly large measurement uncertainty is considered this is in

reasonable agreement with the value found in ref. [73] of -0.76 ± 0.5 eV. Note, however, that both studies base on differently doped samples (2 mol% Nb vs. 1 mol% U) with different microstructures (epitaxial thin film vs. polycrystalline pellet).

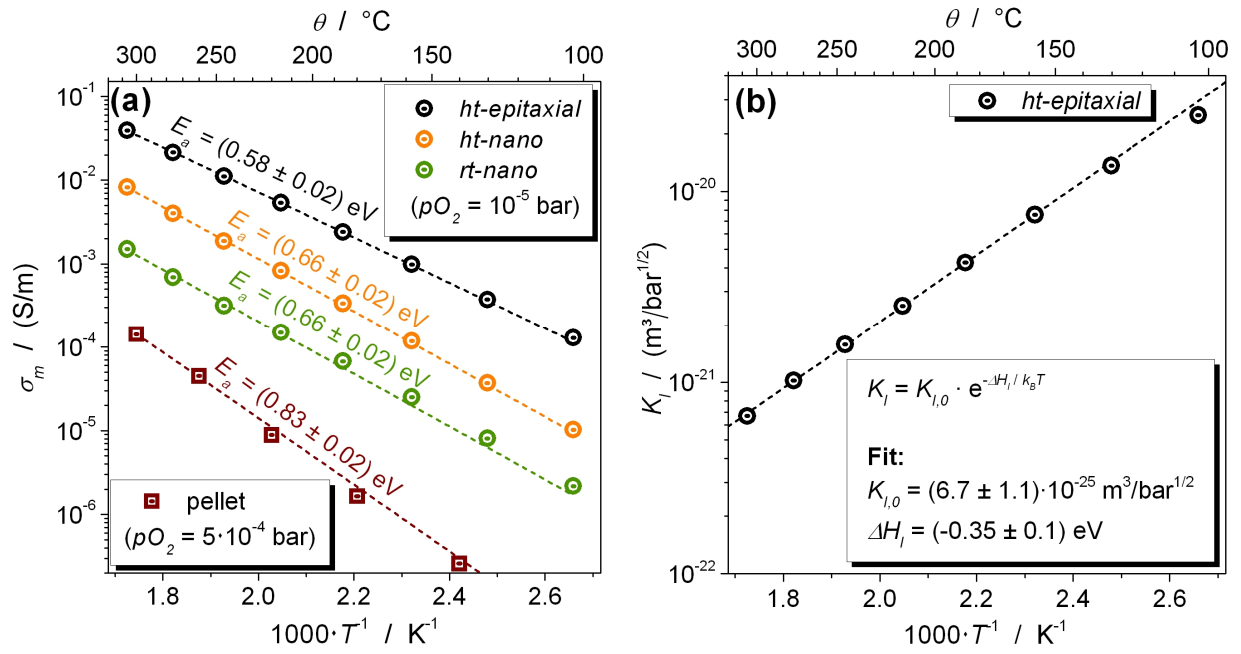


Fig. 69: Temperature Dependence of the (a) Effective Conductivity and (b) Oxygen Insertion Equilibrium of the 2 mol% Nb Doped CeO₂ Thin Films

$K_{I,0}$: pre exponential factor of the oxygen insertion equilibrium constant (see reaction {7} and eq. {16})

Reprinted from Göbel et al. [15] (Copyright 2012) with permission from Elsevier.

5.6.3.2 Grain Boundary Effects

Notably, the *n*-type conductivity of the *ht-nano* sample was observed to be reduced with respect to the *ht-epitaxial* film by one and for the *rt-nano* film by even up to two orders of magnitude (Fig. 68 and Fig. 69a). In addition, the activation energies of the nanocrystalline films were increased by about 0.1 eV (Fig. 69a). Both findings indicate that the GBs in donor doped cerium oxide block the electronic conduction in accordance with case (vii) of section 2.2.3.2 and, hence,

$$\sigma_m = \sigma_{e',m}^\perp = ((\sigma_{e',\infty})^{-1} + (\Delta\sigma_{e',m}^\perp)^{-1})^{-1}.^{74}$$

⁷⁴ Also a pellet of 2 mol% Nb doped ceria was prepared and measured. The resulting impedance spectra (Fig. 70) showed only one semicircle which, however, could clearly be assigned to the GB resistance for two reasons. In comparison with the bulk values (1) its capacitance was 5 times larger and (2) its resistance and activation energy values were strongly increased (Fig. 69). Probably here the bulk semicircle (which is expected to have an extremely small resistance) is out of the frequency range of the measurement. As a matter of fact, the $p\text{O}_2$ dependence of the pellet which is about $-1/5.4$ also at low temperatures indicates that the pellet is at the border of the defect chemistry regimes (III) and (IV) while ... footnote continued on next page

Given that in the literature pure and acceptor doped ceria are well known to exhibit an enhanced electronic conductivity at the GBs,^[3, 4, 6-8, 10, 12, 16, 17, 22] this is quite a remarkable finding. For the origin of this effect three possibilities can be considered:⁷⁵

(A) *Segregation at the GBs*

The segregation of a second phase at the GBs could induce an additional resistance. However, not only is CeO₂ found to tolerate even larger donor dopant concentrations than 2 mol% (about 4 mol%)^[86] but also the HRTEM micrographs (Fig. 66) showed clean GBs with no second phase. Hence, segregations can be ruled out to be the origin of the blocking GBs.

(B) *Negative SCL Potential*

A negative electric potential at the GBs, leading to a depletion of the electrons in the SCLs, could in principle explain the reduced *n*-type conductivity. Nevertheless, the positive SCL potential in pure and acceptor doped ceria originates from a positive GB core charge which again has fundamental structural origins such as a lower local occupancy of oxide ions in the GB core (as experimentally confirmed in related materials, see ref. ^[93]). The reason why the GB core should be structurally different in donor doped ceria (e.g. due to an increase of excess electrons or other negatively charged defects in the core) is not

for similar conditions the thin films are between defect chemistry regimes (IV) and (V). This can explain the higher bulk conductivity in the pellet compared with the *ht-epitaxial* film (compare with Fig. 4, right panel); however, the origin of the shifted defect chemistry regimes is unclear.

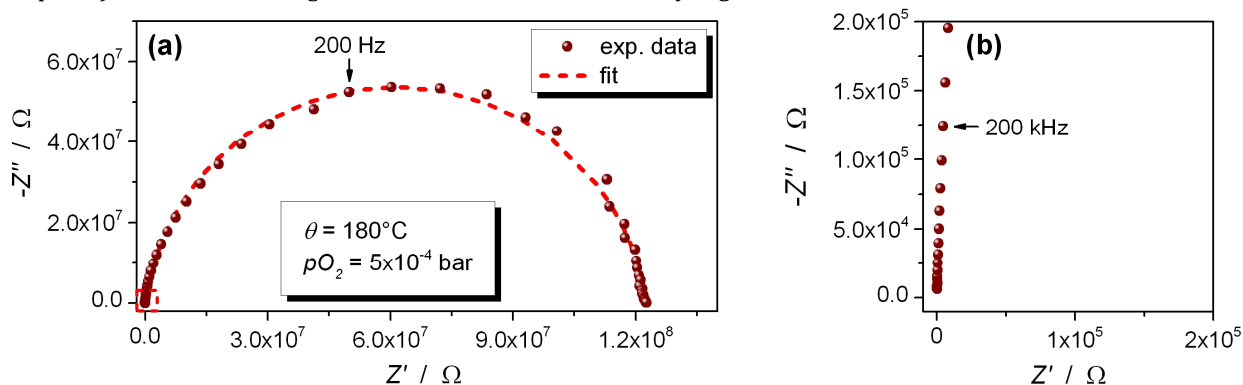


Fig. 70: Impedance Spectrum of a 2 mol% Nb Doped Ceria Pellet

- (a) The impedance spectrum features one semicircle.
 (b) Also at high frequencies no additional semicircle is observed.

Reprinted from Göbel et al.^[15] (Copyright 2012) with permission from Elsevier.

⁷⁵ For the *rt-nano* film also a fourth cause is possible. For this particular donor doped sample a small shift in the XRD signals was detected (Fig. 67). The corresponding slight structural change could result in conductivity changes. However, this does not affect the general finding of the electronically blocking nature of the GBs given that in comparison with the *ht-epitaxial* sample the conductivity is already strongly diminished in the *ht-nano* film which does not show a change in the positions of the XRD reflections.

obvious. However, for other materials such as TiO_2 ^[134, 135] and SrTiO_3 ^[136] a very similar switch-over of the sign of Φ_0 upon changing from acceptor to donor doping was found. Hence, also for donor doped CeO_2 a negative SCL potential is in principle conceivable.

In this case, Φ_0 can be determined using the relationships in Table 7 or the numerical approach (Chapter 3). The calculation yields a value of -0.32 ± 0.05 V. Interestingly, while the sign is different the absolute value of Φ_0 is comparable with what is found in pure and donor doped ceria (0.20 to 0.34 V).^[10, 14, 16, 17, 98, 99] It is not clear whether this similarity originates from a fundamental physico-chemical origin or is merely coincidental.

(C) *Positive SCL Potential and Mobility Changes*

As elucidated in the section introduction 5.6.1 in donor doped ceria the SCL effects on the effective conductivity are expected to be minor if Φ_0 remains positive as in pure and acceptor doped ceria. Therefore other boundary effects on the conductivity can become perceivable which in acceptor doped and pure ceria are superimposed by the strong SCL effects.

A possible additional effect might be a change of the electron mobility, maybe due to local strain at the GBs. In the literature many studies confirm that strain effects locally affect the conductivity (e.g. ref. ^[23, 27, 29, 115, 116]). In addition, it is known that depending on the reduction level the activation energy of the electron mobility h_e , varies from about 0.2 eV to 0.6 eV.^[90, 91] In acceptor doped cerium oxide even a change of the electron mobility at the GBs is reported.^[119] Here already a change of h_e from 0.4 to 0.5 eV would result in a conductivity drop by more than one order of magnitude at 200 °C if the preexponential factor is assumed to stay constant (eq. {17}). Hence, mobility changes could explain the observed conductivity decrease.

It is not obvious which of the last two scenarios occurs in the donor doped films investigated here. However, the finding discussed in section 5.5.3.7 indicates that also in pure and acceptor doped CeO_2 other boundary effects on the electron conductivity, e.g. mobility changes, are present. Therefore, scenario (C) appears to be more likely than scenario (B).

5.6.4 Section Conclusions

Thin films of 2 mol% Nb doped cerium oxide were investigated. At the given temperatures and pO_2 range the defect chemistry of the samples was found to be dominated by oxygen interstitials. At temperatures around and below 300 °C the thin films appeared to be at the border between defect chemistry regimes (IV) and (V), whereas for higher temperatures the pO_2 dependence decreased indicating a shift to the region between defect chemistry regimes (III)

and (IV) (see Table 1 and Fig. 4, right panel). The oxygen insertion enthalpy was observed to be -0.35 ± 0.1 eV in acceptable agreement with previous studies.^[73]

Remarkably, the GBs in the donor doped films were found to block the electron transport in contrast to acceptor doped ceria where they are well known to induce an increase of the electron conductivity^[3, 4, 6-8, 10, 12, 16, 17, 22] (with the exception of the results discussed in section 5.5.3.7). The conductivity drop can be explained with three possibilities. Here the first one, segregation of a second phase, can be excluded due to the HRTEM investigations. The results of the previous section indicate that a decrease in the electron mobility is the most likely explanation. However, also a negative SCL potential is conceivable.

Chapter 6

Main Conclusions

Boundary effects were found to crucially affect the ionic and electronic conductivity in cerium oxide thin films. Here two different kinds of boundaries can be distinguished: the film substrate interface (FSI) and grain boundaries (GBs).

(A) *FSI Effects on the Ionic Conductivity*⁷⁶

Only strongly acceptor doped ceria is a predominantly ionic conductor. However, due to the high doping content the size of a space charge layer (SCL) at the FSI is expected to be negligibly small resulting in only insignificant conductivity changes. The results of this study confirm this expectation. Thus, epitaxial, acceptor doped ceria films grown on Al_2O_3 $\langle 0001 \rangle$ were found not to exhibit a thickness dependent ionic conductivity.

(B) *FSI Effects on the Electronic Conductivity*⁷⁷

The studied epitaxial, nominally pure ceria films grown on Al_2O_3 $\langle 0001 \rangle$ which were characterized by a predominantly electronic conductivity showed a conductivity drop and an increase of the activation energy with decreasing film thickness. Since GB effects can be excluded in this case the effect can be attributed to the FSI. Qualitatively and quantitatively the conductivity decrease is in agreement with the SCL theory.

(C) *GB Effects on the Ionic Conductivity*

(C.1) *Nanocrystalline Films Grown on SiO_2* ⁷⁸

In the most of the investigated samples the GBs were found to control the conductivity even more significantly than effects at the FSI. As an example in nanocrystalline, acceptor doped ceria films grown on SiO_2 $\langle 0001 \rangle$ the effective conductivity was observed to be decreased by one order of magnitude in

⁷⁶ See section 5.3 and in particular 5.3.3.1.1.

⁷⁷ See section 5.3 and in particular 5.3.3.2.2.

⁷⁸ See section 5.3 and in particular 5.3.3.1.2.

comparison with the bulk value. This corresponds with a SCL potential at the GBs of 0.32 ± 0.05 V at 700 °C.

(C.2) *Thickness Dependent Conductivity due to GB Effects*⁷⁸

Interestingly, due to a dependence of the grain size on the film thickness in this last mentioned set of samples the conductivity was observed to follow a very similar trend compared with what is expected for FSI effects. This indicates that in polycrystalline thin films GB effects can be misinterpreted as FSI effects easily. That is of significance not only for future investigations of boundary effects in CeO₂ and related materials but also for a number of recent studies (e.g. ref. [24-26, 28]).

(C.3) *Reduced SCL Effects*⁷⁹

The diminished ionic conductivity at the GBs considerably limits the usability of cerium oxide in applications. This made it particularly promising to investigate whether the SCL potential can be reduced in polycrystalline ceria samples. For nanocrystalline, acceptor doped CeO₂ thin films grown on Al₂O₃ and MgO <100> substrates a strong decrease of the SCL potential to a value of 0.19 ± 0.05 V at 700 °C was observed. This corresponds to a much larger ionic conductivity in comparison with the nanocrystalline films on SiO₂ <0001> and is most likely the result of the lower lattice mismatch between the substrate material and CeO₂. Here the lattice mismatch is (1) still large enough to result in the growth of polycrystalline films but (2) small enough to yield only small misorientations of adjacent grains. This again results in low GB core charges and, therefore, diminished SCL effects.

(C.4) *Enhanced SCL Effects*⁸⁰

The strongest boundary effects were detected in strongly acceptor doped films prepared at room temperature. In these nanocrystalline films with very small grains (≈ 10 nm) the ionic conductivity was measured to be decreased by three orders of magnitude corresponding with an increased SCL potential of 0.30 ± 0.05 V at 300 °C (in comparison with films prepared at 720 °C with 0.22 ± 0.05 V at 300 °C). Additionally, here the assumption of a flat dopant concentration profile (Mott-Schottky case) is expected to be fulfilled better resulting in less steep SCL profiles and, hence, more pronounced conductivity effects.

⁷⁹ See section 5.4.

⁸⁰ See section 5.5 and in particular 5.5.3.2.

(D) *GB Effects on the Electronic Conductivity*

(D.1) *Strong Shift of the Electrolytic Domain Boundary*⁸¹

The samples prepared at room temperature were found to exhibit unique properties of the electronic conductivity as well. Here the electrolytic domain boundary was observed to be considerably shifted to higher pO_2 values compared to what is expected in the literature for the bulk of ceria (extrapolated to the given measurement conditions): by 29 orders of magnitude. This remarkable shift was found to be the result of a superposition of two effects.

Firstly, the pronounced SCL effects at the GBs severely block and shortcut the ionic and electronic transport, respectively, and contribute to 16 orders of magnitude of the pO_2 shift. Hence, as in nanocrystalline $SrTiO_3$ where a comparable shift of the pO_2 at the transition point between n - and p -type conduction by 12 orders of magnitude was observed^[21] also in nanocrystalline CeO_2 the SCL effects can result in very strong displacements of the conductivity domains (ionic, n - or p -type) concerning the pO_2 .

Secondly, at low temperatures the electronic bulk conductivity was found to be unexpectedly large accounting for a shift of the electrolytic domain boundary by 13 orders of magnitude (see bullet point (E)). Both effects were found to add to the observed total shift by $16 + 13 = 29$ orders of magnitude.

(D.2) *Electronically Blocking GBs in Acceptor Doped and Nominally Pure Cerium Oxide*⁸²

Interestingly, while the electronic conductivity was found to be increased in the nanocrystalline samples prepared at room temperature, in the films grown at 720 °C it was observed to be decreased despite the presence of a positive SCL potential at the GBs. This indicates the existence of additional boundary effects on the electronic conductivity in cerium oxide thin films such as mobility variations and/or a change of the reduction enthalpy.

(D.3) *Electronically Blocking GBs in Donor Doped Cerium Oxide*⁸³

In order to get a better insight in how the GBs affect the electronic conductivity also thin films of a material only barely investigated so far were studied: donor doped CeO_2 . Here the measurements could confirm the observations on the defect chemistry of this material made in earlier studies, namely the presence of oxygen

⁸¹ See section 5.5 and in particular 5.5.3.3.

⁸² See section 5.5 and in particular 5.5.3.7.

⁸³ See section 5.6.

interstitial defects. Notably, the GBs in donor doped ceria were found to significantly block the electron transport. Two mechanism for this effect remain possible: (1) a negative SCL potential at the GBs and (2) a change of the electron mobility.

(E) *Bulk Effects on the Electronic Conductivity*⁸⁴

The electronic activation energy of the investigated nominally pure and acceptor doped thin films was observed to be reduced in comparison with the single crystal data,^[74] probably due to a diminished reduction enthalpy. Moreover, at low temperatures the electronic activation energy was found to be decreased further resulting in a particularly large electronic conductivity at such conditions. Since in the above mentioned nanocrystalline samples prepared at room temperature strong SCL effects were present here the electronic activation energy was decreased even more while the ionic value was increased. Remarkably, this change of the activation energies was found to result in a reduction of the electronic value even below the ionic one. Therefore, contrary to the usual observation made in ceria in these samples an increase of the electronic transference number with decreasing temperature was detected.

(F) *Numerical Analysis of the SCL Effects in Cerium Oxide*⁸⁵

Additionally to the experimental investigations the SCL effects in ceria were also analyzed by numerically calculating the expected SCL profiles. This allowed for a careful analysis of the complex relationships between (1) the material parameters (doping, equilibrium constants, etc.), (2) the profile characteristics (SCL potential, SCL charge, SCL extent, SCL steepness, etc.) and (3) the strength of the resulting conductivity effects. In contrast to the analytical solutions for non-overlapping SCLs in the literature the numerical approach was found to very precisely determine both SCL profiles and conductivity effects without the use of further assumptions, even for asymmetric and mixed cases.

(G) *Improvement of the SCL Analysis*⁸⁶

Beyond the applicability to CeO₂ the numerical approach allowed for a test of the assumptions made in the widely used analytical solutions which could show that their preciseness varies significantly depending on the actual case (Gouy-Chapman, Mott-Schottky or mixed). Remarkably, the test resulted in the formulation of new, improved relationships. These generally applicable formulae were found to reliably yield very precise outcomes even for complicated situations, such as low potentials and mixed cases.

⁸⁴ See sections 5.3 and 5.5 and in particular 5.3.3.2.4 and 5.5.3.4 to 5.5.3.6.

⁸⁵ See section 5.1 and in particular 5.1.3 and 5.1.5.

⁸⁶ See section 5.1 and in particular 5.1.4.

Acknowledgements

First and foremost I would like to express my deep gratitude to Prof. Dr. Joachim Maier who not only gave me the possibility to perform my PhD project in his excellent group but also always had time and constructive suggestions for me despite his tight schedule.

I acknowledge Prof. Dr. Joachim Bill and Prof. Dr. Joris van Slageren from *Stuttgart University* for investing a significant amount of their time in being on my examination committee.

Particular tribute goes to my direct supervisor Dr. Giuliano Gregori with whom I had the pleasure to work nearly every day of the PhD project. Clearly, his competent advices concerning the (1) experimental strategy, (2) the experimental setup, (3) the data interpretation and (4) the presentation/publication of the results were a great support for me.

I acknowledge Dr. Dominik Samuelis for helpful scientific discussion.

I would like to thank my external supervisor Dr. Hagen Klauk for his supportive advices.

Georg Christiani and Benjamin Stuhlhofer from the *Technology Group* are acknowledged (1) for preparing the first of the investigated thin films with PLD, (2) for teaching me how to operate the PLD machine on my own and (3) for their support in maintaining the PLD machine.

I gratefully thank Gabi Götz for performing the XRD experiments. Bernhard Fenk is acknowledged for preparing the lamellae for TEM with FIB and SEM. I express thanks to Kersten Hahn, Peter Kopold, Dr. Behnaz Rahmati and Ute Salzberger from the *Stuttgart Center for Electron Microscopy (StEM) at the Max-Planck-Institute for Intelligent Systems*, Stuttgart, for performing the TEM, HRTEM and electron diffraction experiments.

Prof. Dr. Xiangxin Guo from the *Shanghai Institute of Ceramics of the Chinese Academy of Science* is acknowledged for helpful scientific discussion of the experimental study described in section 5.2. I particularly express gratitude for helpful scientific discussion to Prof. Dr. Harry Tuller, (from the *Massachusetts Institute of Technology*, Cambridge, USA), Prof. Dr. Sean Bishop (from the *International Institute for Carbon Neutral Energy Research (I2CNER)*, *Kyushu University*, Japan), Dr. Roger De Souza (from *RWTH Aachen*, Germany), Prof. Dr. Enrico Traversa,

II Acknowledgements

Dr. Emiliana Fabbri, Dr. Daniele Pergolesi (all three from the *National Institute for Materials Science (NIMS)*, Tsukuba, Japan).

Annette Fuchs is thanked for preparing the donor doped cerium oxide powder. I am grateful to Udo Klock, Ewald Schmitt and Peter Senk for their helpful technical advices concerning the measurement setup. Uwe Traub is acknowledged for his support concerning the IT infrastructure. I thank Sofia Weiglein for her competent administrative support.

The glassblower workshop and the mechanical workshop of our institute are acknowledged for manufacturing in excellent quality the quartz measurement cell and the PLD target holders, respectively.

I am grateful to my further (former) colleagues of the Maier department for helpful scientific discussion; i.e. especially Kiran Adepalli, Federico Baiutti, Dr. Seniz Beyazyildirim, Evgeny Blokhin, Dr. Carla Cavalca de Araujo, Dr. Olga Delmer, Dr. Lijun Fu, Dr. Lida Ghassemzadeh, Oliver Gerbig, Elisa Gilardi, Dr. Denis Gryaznov, Katharina Höfer, Dr. Jong Hoon Joo, Dr. Nitin Kaskhedikar, Dr. Eugene Kotomin, Dr. Klaus-Dieter Kreuer, Dr. Chilin Li, Dr. Piero Lupetin, Piero Mazzolini, Dr. Rotraut Merkle, Dr. Jelena Popović, Daniel Pöttsch, Dr. Jiyong Shin, Dr. Mona Shirpour, Dr. Kun Tang, Dr. Ahmed Telfah, Dr. Linas Vilciauskas, Dr. Lei Wang, Anja Wedig, Dr. Katja Weichert, Dr. Yan Yu and Changbao Zhu.

In particular Chia-Chin Chen, Michael Marino, Jan Melchior, Nils Ohmer, Christian Pfaffenhuber, Sebastian Stämmler, Michael Weissmayer and Andreas Wohlfarth are thanked not only for helpful scientific discussion but also for our frequent table soccer matches which allowed me to relief stress and gather new concentration for my work.

Christian Pfaffenhuber is additionally acknowledged for his collaboration in our extra project of developing a software to simulate soggy sand electrolytes.

Very special tributes go to my fiancé Mariya Rasshchupkyna for her support in all fields of life, particularly in the hectic time of writing this thesis.

Last but not least, appreciation goes to my parents Konstanze Göbel and Wilfried Henning for inspiring my curiosity during my childhood which later resulted in me becoming a scientist. Also my former chemistry teachers Frau Drechsel and Frau Rieck and also Prof. Dr. Joachim Sieler from *Leipzig University* (who already supported me before my study) are gratefully acknowledged for arousing my interest in the topic of chemistry.

Finally, I would like to thank you, the reader of this thesis, for your interest in my work.

List of Abbreviations

CC	charge carrier
ceria	cerium oxide, CeO ₂
CPE	constant phase element
depl.....	depletion
EDB.....	electrolytic domain boundary
EDP.....	electron diffraction pattern
eq.....	equation
erf.....	error function: $\text{erf}(x) = 2/\pi \int_0^x e^{-t^2} dt$
erfi.....	imaginary error function: $\text{erfi}(x) = -i \cdot \text{erf}(i \cdot x)$ with i as the imaginary unit
exp.	experimental
FC.....	flow controller
FIB.....	focused ion beam
Fig.	figure
FSI	film-substrate interface
GB.....	grain boundary
GC case.....	Gouy-Chapman case
HRTEM	high-resolution transmission electron microscopy
<i>ht-epitaxial</i>	CeO ₂ thin films prepared on Al ₂ O ₃ substrates (<0001> or <1 $\bar{1}$ 02> orientation) at 720 °C deposition temperature which feature an epitaxial microstructure
<i>ht-nano</i>	CeO ₂ thin films prepared on SiO ₂ <0001> substrates at 720 °C deposition temperature which feature a polycrystalline, columnar microstructure with a lateral grain size of about 40 nm
MIEC.....	mixed ionic electronic conductor
MS case.....	Mott-Schottky case
nil.....	nothing
<i>n</i> -type.....	conductivity dominated by electron (e ⁻) defects

IV List of Abbreviations

- PC.....personal computer
- PLD.....pulsed laser deposition
- RC element.....one resistor and one capacitor connected in parallel
- RSOFC.....reversible solid oxide fuel cell
- rt-nano*CeO₂ thin films prepared on SiO₂ <0001> substrates at room temperature which feature a polycrystalline, columnar microstructure with a lateral grain size of about 10 nm
- sccm.....standard cubic centimeters per minute
- SCL.....space charge layer
- SEM.....scanning electron microscopy
- sgn.....signum function: $\text{sgn}(x)$ is -1 for $x < 0$, 0 for $x = 0$ and +1 for $x > 0$
- SOFC.....solid oxide fuel cell
- TEM.....transmission electron microscopy
- XRD.....X-ray diffraction
- YSZ.....yttria stabilized zirconia

μ SOFC.....micro solid oxide fuel cell

List of Symbols

Defects

A'_{Ce}	singly charged acceptor dopant on cerium site
Ce'_{Ce}	Ce^{III} cation on cerium site
D^{\bullet}_{Ce}	singly charged donor dopant on cerium site
e'	excess electrons ($e' = \text{Ce}'_{\text{Ce}}, \text{Ce}^{\text{III}}$ cation on cerium site)
h^{\bullet}	electron holes
O_0^x	oxide ions on oxygen sublattice sites
O_i'	oxygen interstitials (singly charged)
O_i''	oxygen interstitials (doubly charged)
V_i^x	unoccupied interstitial positions
$V_0^{\bullet\bullet}$	oxygen vacancies

Quantities

a_i	activity of an arbitrary CC i (see eq. {20})
A	abbreviation for the term $e^{-z_{maj}e\Phi_0/2k_B T}$ in the GC case
$A_{\Delta\Sigma}$	abbreviation for the erfi terms in eq. {133}
$A_{\Delta\Omega}$	abbreviation for the erfi terms in eq. {135}
b'	relative decrease in the SCL potential for each step of the numerical calculation of a SCL profile (see eq. {76})
c	(local) concentration
c_{∞}	bulk concentration
$c_{1,\infty}$	bulk concentration of CC 1
$c_{2,\infty}$	bulk concentration of CC 2
c_A	bulk concentration of the acceptor dopant

c_{Ce}	concentration of the cerium cations in pure CeO ₂ ($c_{Ce} = 2.526 \cdot 10^{22} \text{ cm}^{-3}$)
c_D	bulk concentration of the donor dopant
$c_{depl,\infty}$	bulk concentration of an arbitrary depleted CC
c_{Dop}	bulk concentration of the (either acceptor or donor) dopant ($z_{Dop}c_{Dop} \equiv z_Ac_A + z_Dc_D$)
$c_{e',\infty}$	bulk concentration of electrons ($n_\infty \equiv c_{e',\infty}$)
c_{End}	desired final concentration in the last step of the numerical calculation of a SCL profile (see eq. {75})
$c_{enr,\infty}$	bulk concentration of an arbitrary enriched CC
c_h	local concentration of an arbitrary CC h
$c_{h,\infty}$	bulk concentration of an arbitrary CC h
$c_{h^\bullet,\infty}$	bulk concentration of electron holes
c_i	local concentration of an arbitrary CC i (see eq. {22})
$c_{i,0}$	local concentration of an arbitrary CC i at the interface (see eq. {22})
$c_{i,\infty}$	bulk concentration of an arbitrary CC i
c_{i,x_B}	local concentration of an arbitrary CC i at the coordinate x_B , where the electric field becomes zero (for overlapping SCLs)
c_{i,x_k}	local concentration of an arbitrary CC i at calculation step k
$c_{IM,j}$	bulk concentration of an arbitrary immobile CC j
$c_{maj,\infty}$	bulk concentration of the enriched majority CC in the GC case
$c_{maj,max}$	maximal, physically possible concentration of the enriched majority CC in the GC or mixed case
c_{max}	maximal, local concentration of the enriched CC in the GC case (see eq. {36})
$c_{O_i',\infty}$	bulk concentration of singly charged oxygen interstitials
$c_{O_i'',\infty}$	bulk concentration of doubly charged oxygen interstitials
$c_{V_O^\bullet}$	local concentration of oxygen vacancies
$c_{V_O^{\bullet\bullet},0}$	local concentration of oxygen vacancies at the interface
$c_{V_O^{\bullet\bullet},\infty}$	bulk concentration of oxygen vacancies
C	capacitance
C_∞	bulk capacitance
C_e^{\parallel}	capacitance of the parallel GBs on the electron transport
C_e^\perp	capacitance of the perpendicular GBs on the electron transport
$C_{e',elec}$	capacitance of the electrodes on the electron transport

C'_{elec}	effective capacitance of the electrodes comprising both the oxygen vacancy and electron transport
C_{Stray}	stray capacitance
$C_{V_o}^{ }$	capacitance of the parallel GBs on the oxygen vacancy transport
$C_{V_o}^{\perp}$	capacitance of the perpendicular GBs on the oxygen vacancy transport
$C_{V_o}^{\bullet\bullet,elec}$	capacitance of the electrodes on the oxygen vacancy transport
CPE_{Stray}	stray constant phase element
d	grain size (for polycrystalline, columnar thin films: lateral grain size)
d_{ML}	thickness of an individual multilayer
e	electron charge, $1.602 \cdot 10^{-19}$ C
E	electric field
E_0	electric field at the interface (see eq. {28})
E_a	effective activation energy (slope of the data points in the $\ln(\sigma_m T)$ vs. $1/T$ plot, see eq. {13})
$E_{a,e'}$	effective activation energy of the electrons (see eq. {157})
$E_{a,V_o^{\bullet\bullet}}$	effective activation energy of the oxygen vacancies (see eq. {157})
E_E	electric field where the charge density of the enriched majority CC in the mixed case reaches the value of the immobile CCs
E_{x_k}	electric field at coordinate x_k (see eq. {27})
f	frequency
G	conductance
$G_{e',\infty}$	bulk conductance of the electrons
$G_{e'}^{ }$	conductance of all perpendicular GBs on the electron transport
$G_{e',1}^{ }$	conductance of a single parallel GB on the electron transport
G_m	effective conductance
ΔG	intercept on the y-axis in the G_m vs. L plot (see Fig. 39)
h	as subscript: describes an arbitrary mobile charge carrier (CC)
h_e	electron hopping energy
h_i	activation energy of the mobility of an arbitrary CC i (see eq. {17})
$h_{V_o^{\bullet\bullet}}$	activation energy of the oxygen vacancy mobility
ΔH	reaction enthalpy (see eq. {16})
ΔH_F	enthalpy of the anti-Frenkel pair formation (reaction {1})
ΔH_H	enthalpy of the electron-hole formation (reaction {5})
ΔH_I	enthalpy of the oxygen insertion (reaction {7})

- ΔH_R enthalpy of the reduction under oxygen excorporation (reaction {3})
- ΔH_S enthalpy of the formation of singly charged oxygen interstitials (reaction {9})
- i first meaning as a subscript: describes an arbitrary mobile charge carrier (CC)
 second meaning, only in Table 7 and section 5.2: imaginary unit
- Int integral in the solution of an arbitrary parabolic potential profile, see footnote ⁵²
- j as subscript: describes an arbitrary immobile charge carrier (CC)
- J geometrical factor depending on the sample dimensions (for the thin films $J = l_1/(l_2 \cdot L)$, see Fig. 15)
- k as subscript: describes a single calculation step in the numerical approach
- k_B Boltzmann constant, $1.381 \cdot 10^{-23}$ J/K
- K equilibrium constant (see eq. {16})
- K_0 pre exponential factor (equilibrium constant for $T \rightarrow \infty$, see eq. {16})
- K_F equilibrium constant of the anti-Frenkel pair formation (reaction {1})
- K_H equilibrium constant of the electron-hole formation (reaction {5})
- K_I equilibrium constant of the oxygen insertion (reaction {7})
- $K_{OI'}$ equilibrium constant of the formation of singly charged oxygen interstitials (reaction {9})
- K_R equilibrium constant of the reduction under oxygen excorporation (reaction {3})
- K_S pre exponential factor of the oxygen insertion equilibrium constant (see reaction {7} and eq. {16})
- K_β XRD signals originating from spurious Cu K_β radiation
- l_1 distance between the electrodes (here 1 mm, see Fig. 15)
- l_2 edge length of the square substrate (here 10 mm, see Fig. 15)
- l_{SCL} SCL extent (calculated using the numerical approach, see eq. {79} and {80})
- L thickness of the thin film (see Fig. 15)
- M_A acceptor dopant dependence (slope of the data points in the $\log(\sigma_m)$ vs. $\log(|z_A|c_A)$ plot, see eq. {15})
- M_D donor dopant dependence (slope of the data points in the $\log(\sigma_m)$ vs. $\log(|z_D|c_D)$ plot, see eq. {15})
- M_{pO_2} pO_2 dependence (slope of the data points in the $\log(\sigma_m)$ vs. $\log(pO_2)$ plot, see eq. {14})
- n local electron concentration
- n_0 local electron concentration at the interface
- n_∞ bulk concentration of electrons

$N_{Immobile}$	number of immobile defects
N_{Mobile}	number of mobile defects
N_{SCL}^{\parallel}	number of parallel SCLs ($N_{GB}^{\parallel} = 2l_2/d$)
N_{SCL}^{\perp}	number of perpendicular SCLs ($N_{GB}^{\perp} = 2l_1/d$)
N_{Steps}	number of calculation steps in the numerical approach
pO_2	oxygen partial pressure
$pO_{2,0}$	reference oxygen partial pressure (see eq. {159})
pO_2^{EDB}	pO_2 at the electrolytic domain boundary (i.e. pO_2 at the boundary between defect chemistry regimes (II-a) and (II-b) where $\sigma_{e',m} = \sigma_{V_o^{\bullet\bullet},m}$, see Table 1)
q	criterion used to define the SCL extent l_{SCL} in the numerical approach, with $0 < q < 1$ (see eq. {79} and {80}). Between the interface ($x=0$) and $x=l_{SCL}$ a contribution on Σ_i and Ω_i of at least $q \cdot \Sigma_i$ and $q \cdot \Omega_i$, respectively is reached for each mobile CC i . In section 5.1 a q value of 0.99 is used.
Q	admittance ($ Z ^{-1}$) of a constant phase element at $\omega = 1s^{-1}$
r_m	effective resistivity ($r_m = \sigma_m^{-1}$)
R	resistance
$R_{e',\infty}$	bulk resistance of the electrons
$R_{e'}^{\parallel}$	resistance of the parallel GBs on the electron transport
$R_{e'}^{\perp}$	resistance of the perpendicular GBs on the electron transport
$R_{e',elec}$	resistance of the electrodes on the electron transport
$R_{e',m}$	effective resistance of the electrons comprising bulk and GB contributions, $R_{e',m} = (R_{e',\infty} + R_{e'}^{\perp})^{-1} + (R_{e'}^{\parallel})^{-1}$
R'_{elec}	effective resistance of the electrodes comprising both the oxygen vacancy and electron transport
R_m	effective resistance (see eq. {137})
R_{Stray}	stray resistance
$R_{V_o^{\bullet\bullet},\infty}$	bulk resistance of the oxygen vacancies
$R_{V_o^{\bullet\bullet}}^{\parallel}$	resistance of the parallel GBs on the oxygen vacancy transport
$R_{V_o^{\bullet\bullet}}^{\perp}$	resistance of the perpendicular GBs on the oxygen vacancy transport
$R_{V_o^{\bullet\bullet},1}^{\perp}$	resistance of a single perpendicular GB on the oxygen vacancy transport
$R_{V_o^{\bullet\bullet},elec}$	resistance of the electrodes on the oxygen vacancy transport
$R_{V_o^{\bullet\bullet},m}$	effective resistance of the oxygen vacancies comprising bulk and GB contributions, $R_{V_o^{\bullet\bullet},m} = (R_{V_o^{\bullet\bullet},\infty} + R_{V_o^{\bullet\bullet}}^{\perp})^{-1} + (R_{V_o^{\bullet\bullet}}^{\parallel})^{-1}$
s	conductivity normalized with regard to the bulk conductivity ($s = \sigma/\sigma_{\infty}$)
$s_{e',m}$	effective conductivity contribution of the electrons, normalized with regard to the bulk conductivity (see Table 7)

- $s_{i,m}$ contribution of an arbitrary CC i to the total effective conductivity σ_m , normalized with regard to the bulk conductivity (see eq. {39} and {83})
- $s_{i,m}^{Approx}$ $s_{i,m}$ value calculated using the analytical approximations
- $s_{i,m}^{Num}$ $s_{i,m}$ value calculated using the numerical approach
- $s_{i,m}^{\parallel}$ effective conductivity of an arbitrary CC i comprising its bulk conductivity and the conductivity change at the parallel GBs, normalized with regard to the bulk conductivity (see eq. {42})
- $s_{i,m}^{\perp}$ effective conductivity of an arbitrary CC i comprising its bulk conductivity and the conductivity change at the perpendicular GBs, normalized with regard to the bulk conductivity (see eq. {43})
- $s_{V_o^{\bullet\bullet},m}$ effective conductivity contribution of the oxygen vacancies, normalized with regard to the bulk conductivity (see Table 7)
- Δs change in the conductivity, normalized with regard to the bulk conductivity
- $\Delta s_{i,m}^{\parallel}$ effective conductivity change of an arbitrary CC i at the parallel GBs, normalized with regard to the bulk conductivity (see eq. {42} and Table 2)
- $\Delta s_{i,m}^{\perp}$ effective conductivity change of an arbitrary CC i at the perpendicular GBs, normalized with regard to the bulk conductivity (see eq. {43} and Table 2)
- t time
- T temperature in K
- T_{Oven} temperature in K of the thermocouple at the heater coil of the oven
- $T_{Sample,1}$ temperature in K of thermocouple 1 in Fig. 16
- $T_{Sample,2}$ temperature in K of thermocouple 2 in Fig. 16
- $u_{e'}$ electron mobility
- u_i mobility of an arbitrary CC i (see eq. {17})
- $u_{V_o^{\bullet\bullet}}$ oxygen vacancy mobility
- $U_{e',0}$ pre exponential factor of the electron mobility (see eq. {17})
- $U_{i,0}$ pre exponential factor of the mobility of an arbitrary CC i (see eq. {17})
- W resistance normalized with regard to the geometrical factor (see eq. {143})
- $W_{V_o^{\bullet\bullet}}^{\perp}$ normalized resistance of all perpendicular GBs on the oxygen vacancy transport
- $W_{V_o^{\bullet\bullet},1}^{\perp}$ normalized resistance of a single perpendicular GB on the oxygen vacancy transport
- x distance to the interface
- x_B coordinate where the electric field becomes zero (for overlapping SCLs)
- x_E coordinate where the charge density of the enriched majority CC in the mixed case reaches the value of the immobile CCs
- x_k in Chapter 2: arbitrary x coordinate
in Chapter 3: x coordinate at calculation step k

x_{MS}	coordinate of the minimum of the electric potential for the parabola profile of eq. {108}
x_ρ	charge balance point of the SCL (see eq. {81})
Δx	interval along the x-axis between two subsequent calculation steps
Δx_k	interval along the x-axis between the next calculation step $k + 1$ and the current one k ($\Delta x_k = x_{k+1} - x_k$, see eq. {74} and {78})
Y	conductance normalized with regard to the geometrical factor (see eq. {143})
$Y_{e',\infty}$	normalized bulk conductance of the electrons ($Y_{e',\infty} = L \cdot \sigma_{e',\infty}$)
$Y_{e',m}$	normalized, effective conductance of the electrons
$Y_{e'}^{\parallel}$	normalized conductance of all perpendicular GBs on the electron transport
$Y_{e',1}^{\parallel}$	normalized conductance of a single parallel GB on the electron transport
$Y_{V_O^{\bullet\bullet},\infty}$	normalized bulk conductance of the oxygen vacancies ($Y_{V_O^{\bullet\bullet},\infty} = L \cdot \sigma_{V_O^{\bullet\bullet},\infty}$)
$Y_{V_O^{\bullet\bullet},m}$	normalized, effective conductance of the oxygen vacancies
$\Delta Y_{e'}$	intercept on the y-axis in the $Y_{e',m}$ vs. L plot
z	charge number
z_1	charge number CC 1
z_2	charge number CC 2
z_A	charge number of the acceptor dopant
z_D	charge number of the donor dopant
z_{depl}	charge number of an arbitrary depleted CC
z_{Dop}	charge number of the (either acceptor or donor) dopant ($z_{Dop}c_{Dop} \equiv z_Ac_A + z_Dc_D$)
$z_{e'}$	charge number of the electrons ($z_{e'} = -1$)
z_{enr}	charge number of an arbitrary enriched CC
z_h	charge number of an arbitrary CC h
z_i	charge number of an arbitrary CC i
$z_{IM,j}$	charge number of an arbitrary immobile CC j
z_{maj}	charge number of the enriched majority CC in the GC case
z_{max}	$ z_{max} $: largest absolute charge number of all mobile CCs (i.e. largest of all $ z_i $) charge number of the oxygen vacancies ($z_{V_O^{\bullet\bullet}} = 2$)
Z	impedance (Z' = real part, Z'' = imaginary part)

α	steepness of the SCL (see eq. {82})
β_L^{\parallel}	fraction of the parallelly aligned SCLs on all SCLs (in the brick layer model $\beta_L^{\parallel} = 2/3$, see eq. {70})
β_L^{\perp}	fraction of the perpendicularly aligned SCLs on all SCLs (in the brick layer model $\beta_L^{\perp} = 1/3$, see eq. {70})
$\gamma_1, \gamma_2, \gamma_3$	coefficients used in the solution of an arbitrary, parabolic potential profile, see footnote 52
Γ^{\parallel}	one-dimensional density of the parallel SCLs (see Table 2)
Γ^{\perp}	one-dimensional density of the perpendicular SCLs (see Table 2)
δ_e	deviation between the two effective conductivity values of the electrons using the numerical approach and the analytical approximations
δ_i	deviation between the two effective conductivity values of an arbitrary CC i calculated using the numerical approach and the analytical approximations
$\delta_{V_o^{\bullet\bullet}}$	deviation between the two effective conductivity values of the oxygen vacancies calculated using the numerical approach and the analytical approximations
ε_0	vacuum permittivity, $8.854 \cdot 10^{-12}$ F/m
ε_r	relative permittivity
η	slope of the linear fit of the data points in the d vs. L plot (see eq. {142})
ϑ_i	degree of influence of an arbitrary CC i (symmetrical GC case) (see eq. {35})
θ	temperature in °C
θ_{Oven}	temperature in °C of the thermocouple at the heater coil of the oven
$\theta_{Sample,1}$	temperature in °C of thermocouple 1 in Fig. 16
$\theta_{Sample,2}$	temperature in °C of thermocouple 2 in Fig. 16
Θ	Bragg angle
ι	intercept on the y-axis of the linear fit of the data points in the d vs. L plot (see eq. {142})
κ	exponent in the CPE (For an ideal capacitor κ is 1. In ionic conductors usually κ values between 0.8 and 1 are observed.)
λ	Debye length (see eq. {34})
λ_e	Debye length with regard to the electrons (see eq. {100} and footnote 44)
$\lambda_{V_o^{\bullet\bullet}}$	Debye length with regard to the oxygen vacancies (see eq. {100} and footnote 44)
λ^*	screening length in the MS case (see eq. {33})
μ_i	chemical potential of an arbitrary CC i (see eq. {20})
μ_i^0	chemical potential of an arbitrary CC i at standard conditions (see eq. {20})
$\bar{\mu}_i$	electrochemical potential of an arbitrary CC i (see eq. {20})

ξ_1, ξ_2, ξ_3	coefficients used in the solution of an arbitrary, parabolic potential profile, see footnote ⁵²
π	pi
ρ	local charge density (see eq. {25})
ρ_0	local charge density at the interface
ρ_E	local charge density where the charge density of the enriched majority CC in the mixed case reaches the value of the immobile CCs
ρ_{IM}	accumulated charge density of all immobile defects (see eq. {25})
ρ_M	accumulated charge density of all mobile defects (see eq. {25})
ρ_{x_k}	charge density at calculation step k
$\Delta\rho_{x_{k-1}}$	difference in charge density between the current calculation step k and the previous one $k - 1$ (see eq. {73})
σ	conductivity
$\sigma_{e',\infty}$	bulk conductivity of the electrons
$\sigma_{e',m}$	contribution of the electrons on the total effective conductivity σ_m (for the usually observed case in ceria of non-overlapping SCLs with a positive potential $\sigma_{e',m} \approx \sigma_{e',m}^{\parallel}$, see eq. {40})
$\sigma_{e',m}^{\parallel}$	effective conductivity of the electrons comprising their bulk conductivity and the conductivity change at the parallel GBs, $\sigma_{e',m}^{\parallel} = \Delta\sigma_{e',m}^{\parallel} + \sigma_{e',\infty}$
$\sigma_{e',m,0}^{\parallel}$	$\sigma_{e',m}^{\parallel}$ at the reference oxygen partial pressure $pO_{2,0}$
$\bar{\sigma}_{e'}^{\parallel}$	local mean electron conductivity in the SCLs at the parallel GBs (excluding the bulk contribution, see eq. {70}))
$\sigma_{e',m}^{\perp}$	effective conductivity of the electrons comprising their bulk conductivity and the conductivity change at the perpendicular GBs, $(\sigma_{e',m}^{\perp})^{-1} = (\Delta\sigma_{e',m}^{\perp})^{-1} + \sigma_{e',\infty}^{-1}$
$\sigma_{i,\infty}$	bulk conductivity of an arbitrary CC i (see eq. {11})
$\sigma_{i,m}$	contribution of an arbitrary CC i to the total effective conductivity σ_m (see eq. {38}, {40} and {41})
$\sigma_{i,m}^{\parallel}$	effective conductivity of an arbitrary CC i comprising its bulk conductivity and the conductivity change at the parallel GBs (see eq. {42})
$\sigma_{i,m}^{\perp}$	effective conductivity of an arbitrary CC i comprising its bulk conductivity and the conductivity change at the perpendicular GBs (see eq. {43})
$\bar{\sigma}_i^{\parallel}$	local mean conductivity in the SCLs at the parallel GBs (excluding the bulk contribution, see eq. {70}))
$\bar{\sigma}_i^{\perp}$	local mean conductivity in the SCLs at the perpendicular GBs (excluding the bulk contribution, see eq. {70}))
σ_m	total effective conductivity, i.e. sum of all contributions $\sigma_{i,m}$ (see eq. {37}, {38} and {138})
$\sigma_{m,t=0}$	effective conductivity at the onset of the pO_2 jump

$\sigma_{V_o^{\bullet\bullet},\infty}$bulk conductivity of the oxygen vacancies
$\sigma_{V_o^{\bullet\bullet},m}$contribution of the oxygen vacancies on the total effective conductivity σ_m (for the usually observed case in ceria of non-overlapping SCLs with a positive potential $\sigma_{V_o^{\bullet\bullet},m} \approx \sigma_{V_o^{\bullet\bullet},m}^{\perp}$, see eq. {41})
$\sigma_{V_o^{\bullet\bullet},m}^{\perp}$effective conductivity of the oxygen vacancies comprising their bulk conductivity and the conductivity change at the parallel GBs, $(\sigma_{V_o^{\bullet\bullet},m}^{\perp})^{-1} = (\Delta\sigma_{V_o^{\bullet\bullet},m}^{\perp})^{-1} + \sigma_{V_o^{\bullet\bullet},\infty}^{-1}$
$\bar{\sigma}_{V_o^{\bullet\bullet}}^{\perp}$local mean oxygen vacancy conductivity in the SCLs at the perpendicular GBs (excluding the bulk contribution, see eq. {43})
$\Delta\sigma$conductivity change
$\Delta\sigma_{e',m}^{\parallel}$effective conductivity change of the electrons at the parallel GBs
$\Delta\sigma_{e',m}^{\perp}$effective conductivity change of the electrons at the perpendicular GBs
$\Delta\sigma_{i,m}^{\parallel}$effective conductivity change of an arbitrary CC i at the parallel GBs (see eq. {42} and {56} and Table 2)
$\Delta\sigma_{i,m}^{\perp}$effective conductivity change of an arbitrary CC i at the perpendicular GBs (see eq. {43} and {56} and Table 2)
$\Delta\sigma_{V_o^{\bullet\bullet},m}^{\parallel}$effective conductivity change of the oxygen vacancies at the parallel GBs
$\Delta\sigma_{V_o^{\bullet\bullet},m}^{\perp}$effective conductivity change of the oxygen vacancies at the perpendicular GBs
Σ_{Core}charge of the GB core
$\Sigma_{e'}$contribution of the electrons on the total SCL charge Σ_{SCL} (see eq. {53} and {152})
Σ_{enr}contribution of an arbitrary enriched CC on the total SCL charge Σ_{SCL}
Σ'_{enr}preliminary (non-corrected) Σ_{enr} value
Σ_icontribution of an arbitrary CC i on the total SCL charge Σ_{SCL} (see eq. {53})
Σ'_i	preliminary (non-corrected) Σ_i value
Σ'_{i,Φ_0} Σ'_i value with Φ_0 being inserted as SCL potential in the respective relationships of the GC case in Table 7
Σ'_{i,Φ_T} Σ'_i value with Φ_T being inserted as SCL potential in the respective relationships of the GC case in Table 7
Σ_{maj}contribution of the enriched majority CC in the GC case on the total SCL charge Σ_{SCL}
Σ'_{maj}preliminary (non-corrected) Σ_{maj} value
Σ_{SCL}total, accumulated charge of the SCL (see eq. {18}, {19}, {28} and {54})
Σ'_{SCL}preliminary (non-corrected) Σ_{SCL} value
Σ_{SCL,Φ_0} Σ_{SCL} value with Φ_0 being inserted as SCL potential in the respective relationships of the GC case in Table 7
Σ_{SCL,Φ_T} Σ_{SCL} value with Φ_T being inserted as SCL potential in the respective relationships of the GC case in Table 7

$\Sigma_{V_0^{**}}$	contribution of the oxygen vacancies on the total SCL charge Σ_{SCL} (see eq. {53})
$\Delta\Sigma_{i,E}$	contribution of the part of the SCL profile where $ \Phi_0 > \Phi > \Phi_E $ on Σ_i
$\Delta\Sigma_{i,GC}$	contribution of the GC like part of the SCL profile on Σ_i in the mixed case
$\Delta\Sigma'_{i,GC}$	preliminary (non-corrected) $\Delta\Sigma_{i,GC}$ value
$\Delta\Sigma_{i,MS}$	contribution of the MS like part of the SCL profile on Σ_i in the mixed case
$\Delta\Sigma_{maj,E}$	contribution of the part of the SCL profile where $ \Phi_0 > \Phi > \Phi_E $ on Σ_{maj}
$\Delta\Sigma_{SCL,GC}$	contribution of the GC like part of the SCL profile on Σ_{SCL} in the mixed case
$\Delta\Sigma'_{SCL,GC}$	preliminary (non-corrected) $\Delta\Sigma_{SCL,GC}$ value
$\Delta\Sigma_{Step}$	accumulated charge in the SCL between x and $x + \Delta x$ (see eq. {74})
τ	relaxation time
ν	coefficient used in the solution of an arbitrary, parabolic potential profile, see footnote ⁵² (usually $\nu = -z_i e / k_B T$)
φ_L	volume fraction of all SCLs (see eq. {70})
Φ	electric potential
Φ_0	SCL potential (electric potential at the interface)
Φ_∞	electric potential in the bulk (here defined as zero)
Φ_{End}	desired final potential in the last step of the numerical calculation of a SCL profile (see eq. {75})
Φ_T	electric potential where the charge density of the enriched majority CC in the mixed case reaches the value of the immobile CCs
Φ_E	electric potential where the enriched majority CC reaches its maximum concentration
Φ_{x_B}	electric potential at the coordinate x_B , where the electric field becomes zero (for overlapping SCLs)
Φ_{x_k}	electric potential at coordinate x_k (see eq. {72} and {77})
ψ	coefficient used in the solution of an arbitrary, parabolic potential profile to distinguish between the determination of Σ_i and Ω_i , see footnote ⁵² ($\psi \in \{1, -1\}$, to determine Σ_i : $\psi = 1$, to determine Ω_i : $\psi = -1$)
ω	angular frequency
Ω_{depl}	resistance of a single perpendicular SCL on the conduction of an arbitrary depleted CC, normalized with regard to the mobility and sample geometry
Ω'_{depl}	preliminary (non-corrected) Ω_{depl} value
Ω_i	resistance of a single perpendicular SCL on the conduction of an arbitrary CC i , normalized with regard to the mobility and sample geometry (see eq. {55})
Ω'_i	preliminary (non-corrected) Ω_i value

- Ω'_{i,Φ_0} Ω'_i value with Φ_0 being inserted as SCL potential in the respective relationships of the GC case in Table 7
- Ω'_{i,Φ_T} Ω'_i value with Φ_T being inserted as SCL potential in the respective relationships of the GC case in Table 7
- $\Omega_{V_0}^{\bullet\bullet}$ resistance of a single perpendicular SCL on the oxygen vacancy conduction, normalized with regard to the mobility and sample geometry (see eq. {55} and {146})
- $\Delta\Omega_{i,E}$ contribution of the part of the SCL profile where $|\Phi_0| > |\Phi| > |\Phi_E|$ on Ω_i
- $\Delta\Omega_{i,GC}$ contribution of the GC like part of the SCL profile on Ω_i in the mixed case
- $\Delta\Omega'_{i,GC}$ preliminary (non-corrected) $\Delta\Omega_{i,GC}$ value
- $\Delta\Omega_{i,MS}$ contribution of the MS like part of the SCL profile on Ω_i in the mixed case

Index of Equations

{1}.....5	{31}.....16	{61}.....23	{91}.....55	{121}.....64	{151}.....94
{2}.....5	{32}.....16	{62}.....23	{92}.....55	{122}.....64	{152}.....95
{3}.....5	{33}.....16	{63}.....23	{93}.....55	{123}.....65	{153}.....95
{4}.....5	{34}.....17	{64}.....23	{94}.....55	{124}.....65	{154}.....96
{5}.....6	{35}.....17	{65}.....23	{95}.....55	{125}.....65	{155}.....96
{6}.....6	{36}.....18	{66}.....23	{96}.....55	{126}.....68	{156}.....108
{7}.....6	{37}.....18	{67}.....23	{97}.....55	{127}.....69	{157}.....109
{8}.....6	{38}.....18	{68}.....23	{98}.....55	{128}.....69	{158}.....110
{9}.....6	{39}.....18	{69}.....23	{99}.....55	{129}.....69	{159}.....114
{10}.....6	{40}.....19	{70}.....23	{100}.....55	{130}.....69	
{11}.....7	{41}.....19	{71}.....25	{101}.....57	{131}.....69	
{12}.....7	{42}.....19	{72}.....25	{102}.....57	{132}.....69	
{13}.....12	{43}.....19	{73}.....25	{103}.....62	{133}.....69	
{14}.....12	{44}.....19	{74}.....26	{104}.....62	{134}.....69	
{15}.....12	{45}.....19	{75}.....26	{105}.....62	{135}.....69	
{16}.....12	{46}.....20	{76}.....26	{106}.....62	{136}.....69	
{17}.....12	{47}.....20	{77}.....26	{107}.....62	{137}.....81	
{18}.....13	{48}.....21	{78}.....26	{108}.....62	{138}.....81	
{19}.....13	{49}.....21	{79}.....28	{109}.....63	{139}.....81	
{20}.....13	{50}.....21	{80}.....28	{110}.....63	{140}.....81	
{21}.....14	{51}.....21	{81}.....28	{111}.....63	{141}.....83	
{22}.....14	{52}.....21	{82}.....28	{112}.....64	{142}.....91	
{23}.....14	{53}.....22	{83}.....28	{113}.....64	{143}.....91	
{24}.....15	{54}.....22	{84}.....30	{114}.....64	{144}.....91	
{25}.....15	{55}.....22	{85}.....31	{115}.....64	{145}.....91	
{26}.....15	{56}.....22	{86}.....44	{116}.....64	{146}.....91	
{27}.....15	{57}.....22	{87}.....44	{117}.....64	{147}.....91	
{28}.....15	{58}.....23	{88}.....55	{118}.....64	{148}.....91	
{29}.....16	{59}.....23	{89}.....55	{119}.....64	{149}.....91	
{30}.....16	{60}.....23	{90}.....55	{120}.....64	{150}.....94	

Index of Figures

Fig. 1: Ionic Conductivities of Selected SOFC Electrolytes.....	3
Fig. 2: Idealized Geometries of Epitaxial and Polycrystalline Thin Films.....	4
Fig. 3: Dopant Dependence Kröger-Vink Diagrams of Acceptor Doped (Left Panel) and Donor Doped CeO ₂ (Right Panel)	9
Fig. 4: pO_2 Dependence Kröger-Vink Diagrams of Acceptor Doped (Left Panel) and Donor Doped CeO ₂ (Right Panel)	10
Fig. 5: Temperature Dependence Kröger-Vink Diagrams of Acceptor Doped (Left Panel) and Donor Doped CeO ₂ (Right Panel)	11
Fig. 6: Basic Characteristics of a Space Charge Layer at a Grain Boundary: the GB Core Charge Σ_{Core} , the SCL Charge Σ_{SCL} and the SCL Potential Φ_0	14
Fig. 7: Example SCL Concentration Profiles Calculated Using the Analytical Approach	17
Fig. 8: Idealized Conductivity Maps of Polycrystalline, Acceptor Doped CeO ₂	20
Fig. 9: Example SCL Concentration Profiles Calculated using the Numerical Approach	27
Fig. 10: Illustration of the SCL Extent l_{SCL} , Charge Balance Point x_p and Steepness α for Three Example Profiles	29
Fig. 11: Example Concentration Profiles of Overlapping SCLs, Calculated using the Numerical Approach.....	30
Fig. 12: Pulsed Laser Deposition	32
Fig. 13: Design of the PLD Target Holder.....	34
Fig. 14: Typically Measured Impedance Spectrum of a Thin Film Characterized by One RC Element in the Equivalent Circuit.....	36
Fig. 15: Geometry of the Investigated Thin Films with Pt Electrodes	37
Fig. 16: Design of the Measurement Cell for Simultaneous Measurement of 4 Samples	38
Fig. 17: Calibration of the Mass Flow Controller System	39
Fig. 18: Temperature Calibration of the Measurement Cell	40
Fig. 19: Comparison between the Old and Newly Designed Sample Holders	41
Fig. 20: Spurious Conductances of the Sample Holder and Various Substrates	42

Fig. 21: Expected Bulk Concentrations in CeO₂ at 700 °C and $pO_2 = 10^{-10}$ bar for Different Doping Contents 46

Fig. 22: (a) Charge Contribution of the Oxygen Vacancies and (b) SCL Steepness as a Function of Dopant Concentration and SCL Potential..... 48

Fig. 23: (a) SCL Extent and (b) Charge Balance Point as a Function of Dopant Concentration and SCL Potential 50

Fig. 24: Normalized Effective Conductivity of the (a) Oxygen Vacancies and (b) Electrons as a Function of Dopant Concentration and SCL Potential, Calculated Using the Numerical Approach 51

Fig. 25: SCL Characteristics as a Function of Dopant Concentration and SCL Potential, Calculated under the Assumption of a Sufficiently Mobile Dopant Using the Numerical Approach 53

Fig. 26: (a) Areas of the Different Analytical Approximation Cases and (b) Screening Lengths 2λ and λ^* as a Function of Dopant Concentration and SCL Potential 54

Fig. 27: Normalized Effective Conductivity of the (a) Oxygen Vacancies and (b) Electrons as a Function of Dopant Concentration and SCL Potential, Calculated Using the Analytical Solutions in ref. [22] (Table 6) 57

Fig. 28: Normalized Effective Conductivity of the (a) Oxygen Vacancies and (b) Electrons as a Function of Dopant Concentration and SCL Potential, Calculated Using the Analytical Solutions in ref. [22] (Table 6) under Consideration of the Bulk Conductivity Contribution 58

Fig. 29: Deviance δ_i between the Analytical^[22] (Table 6, under Consideration of the Bulk Conductivity) and the Numerical Approach as a Function of Dopant Concentration and SCL Potential 59

Fig. 30: Example SCL Potential Profiles of the MS Case..... 63

Fig. 31: Normalized Effective Conductivity of the (a) Oxygen Vacancies and (b) Electrons as a Function of Dopant Concentration and SCL Potential, Calculated Using the Improved Analytical Solutions in Table 7..... 66

Fig. 32: Deviance δ_i between the Improved Analytical (Table 7) and the Numerical Approach as a Function of Dopant Concentration and SCL Potential..... 67

Fig. 33: Relationship between the SCL Potential and the SCL Charge as a Function of Dopant Concentration, Calculated Using the Numerical Approach 72

Fig. 34: Normalized Effective Conductivity of the (a) Oxygen Vacancies and (b) Electrons as a Function of Dopant Concentration and SCL Charge, Calculated Using the Numerical Approach 73

Fig. 35: Typical Impedance Spectra Recorded in this Study..... 77

Fig. 36: General Non-Simplified Equivalent Circuit of CeO₂ Thin Films 78

Fig. 37: Simplified Equivalent Circuits of CeO₂ Thin Films with Electrode Resistance Contribution 80

Fig. 38: Two Simplified Equivalent Circuits of CeO₂ Thin Films without Electrode Resistance Contribution 80

Fig. 39: Idealized Conductance vs. Thickness Plot of Three Series of Thin Films 83

Fig. 40: XRD Patterns of the CeO ₂ Thin Films Grown on Al ₂ O ₃ <0001> and SiO ₂ <0001>	84
Fig. 41: TEM Micrographs of the CeO ₂ Thin Films Grown on Al ₂ O ₃ <0001> and SiO ₂ <0001>	85
Fig. 42: Temperature Dependence of the Effective Conductivity of Selected CeO ₂ Thin Films Grown on Al ₂ O ₃ <0001> and SiO ₂ <0001>	86
Fig. 43: Thickness Dependence of the Effective Electrical Transport Properties of the 10 mol% Gd-Doped CeO ₂ Thin Films Grown on Al ₂ O ₃ <0001> and SiO ₂ <0001>	87
Fig. 44: Thickness Dependence of the Lateral Grain Size <i>d</i> of the Nominally Pure CeO ₂ Thin Films Grown on SiO ₂ <0001>	89
Fig. 45: Schematic Conductance vs. Thickness Diagrams of CeO ₂ Thin Films	90
Fig. 46: <i>pO</i> ₂ Dependence of the Effective Conductance of the Nominally Pure CeO ₂ Thin Films Grown on (a) Al ₂ O ₃ <0001> and (b) SiO ₂ <0001>	92
Fig. 47: Thickness Dependence of the Effective Electrical Transport Properties of the Nominally Pure CeO ₂ Thin Films Grown on Al ₂ O ₃ <0001> and SiO ₂ <0001>	93
Fig. 48: XRD Patterns of the 10 mol% Gd Doped CeO ₂ Thin Films Grown on (a) Al ₂ O ₃ <1 $\bar{1}$ 02> and (b) MgO <100>	99
Fig. 49: TEM and HRTEM Micrographs of the 10 mol% Gd Doped CeO ₂ Thin Films Grown on (a) Al ₂ O ₃ <1 $\bar{1}$ 02> and (b) MgO <100>	100
Fig. 50: Temperature Dependence of the Effective Conductivity of the Thinnest Prepared 10 mol% Gd Doped CeO ₂ Thin Films Grown on Al ₂ O ₃ <1 $\bar{1}$ 02> and MgO <100>, in Comparison with the Films Grown on Al ₂ O ₃ <0001> and SiO ₂ <0001>	101
Fig. 51: Thickness Dependence of the Effective Electrical Transport Properties of the 10 mol% Gd Doped CeO ₂ Thin Films Grown on Al ₂ O ₃ <1 $\bar{1}$ 02> and MgO <100>	102
Fig. 52: XRD Patterns of the 10 mol% Gd doped <i>ht-nano</i> and <i>rt-nano</i> CeO ₂ thin films	105
Fig. 53: TEM and HRTEM Micrographs and Electron Diffraction Pattern (EDP) of the 10 mol% Gd Doped <i>rt-nano</i> CeO ₂ Thin Film	106
Fig. 54: Effective Conductivity of the 10 mol% Gd Doped <i>rt-nano</i> and <i>ht-nano</i> CeO ₂ Thin Films Upon Heating to 700 °C and Subsequent Cooling Down	107
Fig. 55: Temperature Dependence of the Effective Conductivity of the 10 mol% Gd Doped <i>ht-epitaxial</i> , <i>ht-nano</i> and <i>rt-nano</i> CeO ₂ Thin Films	111
Fig. 56: <i>pO</i> ₂ Dependence of the Effective Conductivity of the 10 mol% Gd Doped <i>ht-nano</i> and <i>rt-nano</i> CeO ₂ Thin Films	114
Fig. 57: (a) Usually Observed and (b) Reversed Ranking of the Activation Energies in Acceptor Doped Ceria	116
Fig. 58: Separation of the Ionic and Electronic Conductivity Contributions of the 10 mol% Gd Doped <i>rt-nano</i> Thin Film at Various Temperatures	117
Fig. 59: Temperature Dependence of the Effective Conductivity of the 1 mol% Gd Doped <i>ht-epitaxial</i> , <i>ht-nano</i> and <i>rt-nano</i> CeO ₂ Thin Films	118
Fig. 60: <i>pO</i> ₂ Dependence of the Effective Conductivity of the 1 mol% Gd Doped <i>ht-epitaxial</i> , <i>ht-nano</i> and <i>rt-nano</i> CeO ₂ Thin Films	119

Fig. 61: Temperature Dependence of the Effective Conductivity of the 0.15 mol% Gd Doped <i>ht-epitaxial</i> , <i>ht-nano</i> and <i>rt-nano</i> CeO ₂ Thin Films.....	120
Fig. 62: <i>pO</i> ₂ Dependence of the Effective Conductivity of the 0.15 mol% Gd Doped <i>ht-epitaxial</i> , <i>ht-nano</i> and <i>rt-nano</i> CeO ₂ Thin Films.....	121
Fig. 63: Temperature Dependence of the Effective Conductivity of a Nominally Pure, <i>ht-epitaxial</i> CeO ₂ Thin Film over a Broad Temperature Range between 250 and 700 °C.....	123
Fig. 64: Proposed Activation Energies in Acceptor Doped Ceria.....	124
Fig. 65: (a) Temperature and (b) <i>pO</i> ₂ Dependence of the Effective Conductivity of the Nominally Pure <i>ht-epitaxial</i> , <i>ht-nano</i> and <i>rt-nano</i> CeO ₂ Thin Films.....	125
Fig. 66: XRD Patterns of the 2 mol% Nb Doped CeO ₂ Thin Films.....	129
Fig. 67: TEM and HRTEM Micrographs and Electron Diffraction Patterns (EDP) of the 2 mol% Nb Doped CeO ₂ Thin Films.....	128
Fig. 68: <i>pO</i> ₂ Dependence of the Effective Conductivity of the 2 mol% Nb Doped CeO ₂ Thin Films.....	130
Fig. 69: Temperature Dependence of the (a) Effective Conductivity and (b) Oxygen Insertion Equilibrium of the 2 mol% Nb Doped CeO ₂ Thin Films.....	131
Fig. 70: Impedance Spectrum of a 2 mol% Nb Doped Ceria Pellet.....	132

Index of Tables

Table 1: Defect Chemistry Regimes in CeO ₂	8
Table 2: The Brick Layer Model Applied to Several Sample Geometries.....	23
Table 3: Used PLD Parameters.....	33
Table 4: Typically Used Parameters for Impedance Spectroscopy.....	37
Table 5: Expected SCL Concentration Profiles in CeO ₂ Calculated for Constant Potential Values of 0.3 V and -0.3 V Using the Numerical Approach	47
Table 6: Analytical Approximations of Non-Overlapping SCL Conductivity Effects in CeO ₂ taken from ref. [22]	55
Table 7: Improved Analytical Approximations of Non-Overlapping SCL Conductivity Effects...	65
Table 8: Expected SCL Concentration Profiles in CeO ₂ Calculated for Constant SCL Charge Values of -0.3 C/m ² and 0.3 C/m ² Using the Numerical Approach.....	75
Table 9: Results of the XRD and TEM Investigation of the CeO ₂ Thin Films Grown on Al ₂ O ₃ <0001> and SiO ₂ <0001>.....	85
Table 10: Effective Conductivity at 700 °C and Activation Energy between 700 °C and 550 °C of the 10 mol% Gd-Doped CeO ₂ Thin Films Grown on Al ₂ O ₃ <0001> and SiO ₂ <0001>	87
Table 11: Effective Conductivity at 700 °C and Activation Energy between 700 °C and 550 °C of the Nominally Pure CeO ₂ Thin Films Grown on Al ₂ O ₃ <0001> and SiO ₂ <0001>	94
Table 12: Results of the XRD and TEM Investigation of Selected 10 mol% Gd Doped CeO ₂ Thin Films Grown on Al ₂ O ₃ <1 $\bar{1}$ 02> and MgO <100>	99
Table 13: Effective Conductivity at 700 °C and Activation Energy between 700 °C and 550 °C of the 10 mol% Gd-Doped CeO ₂ Thin Films Grown on Al ₂ O ₃ <1 $\bar{1}$ 02> and MgO <100>	101
Table 14: General Characteristics of the <i>ht-epitaxial</i> , <i>ht-nano</i> , and <i>rt-nano</i> Thin Films.....	104
Table 15: Literature Data of the Electrolytic Domain Boundary in the Bulk of CeO ₂	108
Table 16: Literature Data of the Electrolytic Domain Boundary in Nanocrystalline CeO ₂	110

References

- [1] J. Maier, "IONIC CONDUCTION IN SPACE CHARGE REGIONS," *Progress in Solid State Chemistry* **23**, no. 3, 171–263, (1995).
- [2] J. Maier, "ON THE CONDUCTIVITY OF POLYCRYSTALLINE MATERIALS," *Berichte der Bunsengesellschaft für physikalische Chemie* **90**, no. 1, 26–33, (1986).
- [3] Y. M. Chiang, E. B. Lavik, I. Kosacki, H. L. Tuller, and J. Y. Ying, "DEFECT AND TRANSPORT PROPERTIES OF NANOCRYSTALLINE CeO_{2-x} ," *Applied Physics Letters* **69**, 185–187, (1996).
- [4] Y. M. Chiang, E. B. Lavik, I. Kosacki, H. L. Tuller, and J. Y. Ying, "NONSTOICHIOMETRY AND ELECTRICAL CONDUCTIVITY OF NANOCRYSTALLINE CeO_{2-x} ," *Journal of Electroceramics* **1**, 7–14, (1997).
- [5] Y. M. Chiang, E. Lavik, and D. Blom, "DEFECT THERMODYNAMICS AND ELECTRICAL PROPERTIES OF NANOCRYSTALLINE OXIDES: PURE AND DOPED CeO_2 ," *Nanostructured materials* **9**, no. 1–8, 633–642, (1997).
- [6] A. Tschöpe and R. Birringer, "GRAIN SIZE DEPENDENCE OF ELECTRICAL CONDUCTIVITY IN POLYCRYSTALLINE CERIUM OXIDE," *Journal of Electroceramics* **7**, no. 3, 169–177, (2001).
- [7] A. Tschöpe, "GRAIN SIZE-DEPENDENT ELECTRICAL CONDUCTIVITY OF POLYCRYSTALLINE CERIUM OXIDE II: SPACE CHARGE MODEL," *Solid State Ionics* **139**, no. 3–4, 267–280, (2001).
- [8] A. Tschöpe, E. Sommer, and R. Birringer, "GRAIN SIZE-DEPENDENT ELECTRICAL CONDUCTIVITY OF POLYCRYSTALLINE CERIUM OXIDE: I. EXPERIMENTS," *Solid State Ionics* **139**, no. 3–4, 255–265, (2001).
- [9] X. Guo and J. Maier, "GRAIN BOUNDARY BLOCKING EFFECT IN ZIRCONIA: A SCHOTTKY BARRIER ANALYSIS," *Journal of The Electrochemical Society* **148**, no. 3, E121–E126, (2001).
- [10] S. Kim and J. Maier, "ON THE CONDUCTIVITY MECHANISM OF NANOCRYSTALLINE CERIA," *Journal of The Electrochemical Society* **149**, no. 10, J73, (2002).
- [11] X. Guo, W. Sigle, and J. Maier, "BLOCKING GRAIN BOUNDARIES IN YTTRIA-DOPED AND UNDOPED CERIA CERAMICS OF HIGH PURITY," *Journal of the American Ceramic Society* **86**, no. 1, 77–87, (2003).
- [12] A. Tschöpe, S. Kilassonia, and R. Birringer, "THE GRAIN BOUNDARY EFFECT IN HEAVILY DOPED CERIUM OXIDE," *Solid State Ionics* **173**, no. 1–4, 57–61, (2004).
- [13] X. Guo and R. Waser, "ELECTRICAL PROPERTIES OF THE GRAIN BOUNDARIES OF OXYGEN ION CONDUCTORS: ACCEPTOR-DOPED ZIRCONIA AND CERIA," *Progress in Materials Science* **51**, no. 2, 151–210, (2006).

- [14] M. C. Göbel, G. Gregori, X. X. Guo, and J. Maier, "BOUNDARY EFFECTS ON THE ELECTRICAL CONDUCTIVITY OF PURE AND DOPED CERIUM OXIDE THIN FILMS," *Physical Chemistry Chemical Physics* **12**, 14351–14361, (2010).
- [15] M. C. Göbel, G. Gregori, and J. Maier, "ELECTRONICALLY BLOCKING GRAIN BOUNDARIES IN DONOR DOPED CERIUM DIOXIDE," *Solid State Ionics* **215**, 45–51, (2012).
- [16] M. C. Göbel, G. Gregori, and J. Maier, "MIXED CONDUCTIVITY IN NANOCRYSTALLINE HIGHLY ACCEPTOR DOPED CERIUM OXIDE THIN FILMS UNDER OXIDIZING CONDITIONS," *Physical Chemistry Chemical Physics* **13**, 10940–10945, (2011).
- [17] G. Gregori, M. C. Göbel, and J. Maier, "ELECTRONIC CONDUCTIVITY IN NANOCRYSTALLINE $\text{Ce}_{0.9}\text{Gd}_{0.1}\text{O}_{1.95}$ THIN FILMS AT HIGH OXYGEN PARTIAL PRESSURES," *ECS Transactions* **45**, no. 1, 181–187, (2012).
- [18] J. Maier, "NANOIONICS: IONIC CHARGE CARRIERS IN SMALL SYSTEMS," *Phys. Chem. Chem. Phys.* **11**, no. 17, 3011–3022, (2009).
- [19] N. Sata, K. Eberman, K. Eberl, and J. Maier, "MESOSCOPIC FAST ION CONDUCTION IN NANOMETRE-SCALE PLANAR HETEROSTRUCTURES," *Nature* **408**, no. 6815, 946–949, (2000).
- [20] R. A. De Souza, "THE FORMATION OF EQUILIBRIUM SPACE-CHARGE ZONES AT GRAIN BOUNDARIES IN THE PEROVSKITE OXIDE SrTiO_3 ," *Phys. Chem. Chem. Phys.* **11**, no. 43, 9939–9969, (2009).
- [21] P. Lupetin, G. Gregori, and J. Maier, "MESOSCOPIC CHARGE CARRIERS CHEMISTRY IN NANOCRYSTALLINE SrTiO_3 ," *Angewandte Chemie International Edition* **49**, no. 52, 10123–10126, (2010).
- [22] S. Kim, J. Fleig, and J. Maier, "SPACE CHARGE CONDUCTION: SIMPLE ANALYTICAL SOLUTIONS FOR IONIC AND MIXED CONDUCTORS AND APPLICATION TO NANOCRYSTALLINE CERIA," *Physical Chemistry Chemical Physics* **5**, 2268–2273, (2003).
- [23] S. Azad, O. A. Marina, C. M. Wang, L. Saraf, V. Shutthanandan, D. E. McCready, A. El-Azab, J. E. Jaffe, M. H. Engelhard, C. H. F. Peden, and S. Thevuthasan, "NANOSCALE EFFECTS ON ION CONDUCTANCE OF LAYER-BY-LAYER STRUCTURES OF GADOLINIA-DOPED CERIA AND ZIRCONIA," *Applied Physics Letters* **86**, (2005).
- [24] A. Peters, C. Korte, D. Hesse, N. Zakharov, and J. Janek, "IONIC CONDUCTIVITY AND ACTIVATION ENERGY FOR OXYGEN ION TRANSPORT IN SUPERLATTICES - THE MULTILAYER SYSTEM $\text{CSZ} (\text{ZrO}_2 + \text{CaO}) / \text{Al}_2\text{O}_3$," *Solid State Ionics* **178**, no. 1–2, 67–76, (2007).
- [25] C. Korte, A. Peters, J. Janek, D. Hesse, and N. Zakharov, "IONIC CONDUCTIVITY AND ACTIVATION ENERGY FOR OXYGEN ION TRANSPORT IN SUPERLATTICES—THE SEMICOHERENT MULTILAYER SYSTEM $\text{YSZ} (\text{ZrO}_2 + 9.5 \text{ MOL\% } \text{Y}_2\text{O}_3) / \text{Y}_2\text{O}_3$," *Phys. Chem. Chem. Phys.* **10**, no. 31, 4623–4635, (2008).
- [26] N. Schichtel, C. Korte, D. Hesse, and J. Janek, "ELASTIC STRAIN AT INTERFACES AND ITS INFLUENCE ON IONIC CONDUCTIVITY IN NANOSCALED SOLID ELECTROLYTE THIN FILMS—THEORETICAL CONSIDERATIONS AND EXPERIMENTAL STUDIES," *Phys. Chem. Chem. Phys.* **11**, no. 17, 3043–3048, (2009).
- [27] K. M. Kant, V. Esposito, and N. Pryds, "ENHANCED CONDUCTIVITY IN PULSED LASER DEPOSITED $\text{Ce}_{0.9}\text{Gd}_{0.1}\text{O}_{2-\delta} / \text{SrTiO}_3$ HETEROSTRUCTURES," *Applied Physics Letters* **97**, no. 14, 143110–143110–3, (2010).
- [28] N. Schichtel, C. Korte, D. Hesse, N. Zakharov, B. Butz, D. Gerthsen, and J. Janek, "ON THE INFLUENCE OF STRAIN ON ION TRANSPORT: MICROSTRUCTURE AND IONIC CONDUCTIVITY OF NANOSCALE $\text{YSZ} - \text{Sc}_2\text{O}_3$ MULTILAYERS," *Physical Chemistry Chemical Physics* **12**, 14596–14608, (2010).

- [29] M. Sillassen, P. Eklund, N. Pryds, E. Johnson, U. Helmersson, and J. Bøttiger, "LOW-TEMPERATURE SUPERIONIC CONDUCTIVITY IN STRAINED YTTRIA-STABILIZED ZIRCONIA," *Advanced Functional Materials* **20**, no. 13, 2071–2076, (2010).
- [30] N. Q. Minh, "CERAMIC FUEL-CELLS," *Journal of the American Ceramic Society* **76**, 563–588, (1993).
- [31] B. C. H. Steele and A. Heinzl, "MATERIALS FOR FUEL-CELL TECHNOLOGIES," *Nature* **414**, 345–352, (2001).
- [32] A. J. Jacobson, "MATERIALS FOR SOLID OXIDE FUEL CELLS," *Chem. Mater.* **22**, no. 3, 660–674, (2009).
- [33] S. D. Park, J. M. Vohs, and R. J. Gorte, "DIRECT OXIDATION OF HYDROCARBONS IN A SOLID-OXIDE FUEL CELL," *Nature* **404**, 265–267, (2000).
- [34] S. McIntosh and R. J. Gorte, "DIRECT HYDROCARBON SOLID OXIDE FUEL CELLS," *Chemical Reviews* **104**, 4845–4865, (2004).
- [35] E. D. Wachsman, C. A. Marlowe, and K. T. Lee, "ROLE OF SOLID OXIDE FUEL CELLS IN A BALANCED ENERGY STRATEGY," *Energy & Environmental Science* **5**, no. 2, 5498, (2012).
- [36] R. Doshi, V. L. Richards, J. D. Carter, X. P. Wang, and M. Krumpelt, "DEVELOPMENT OF SOLID-OXIDE FUEL CELLS THAT OPERATE AT 500 DEGREES C," *Journal of the Electrochemical Society* **146**, 1273–1278, (1999).
- [37] T. Hibino, A. Hashimoto, T. Inoue, J. Tokuno, S. Yoshida, and M. Sano, "A LOW-OPERATING-TEMPERATURE SOLID OXIDE FUEL CELL IN HYDROCARBON-AIR MIXTURES," *Science* **288**, 2031–2033, (2000).
- [38] B. C. H. Steele, "MATERIALS FOR IT-SOFC STACKS 35 YEARS R&D: THE INEVITABILITY OF GRADUALNESS?," *Solid State Ionics* **134**, 3–20, (2000).
- [39] E. D. Wachsman and K. T. Lee, "LOWERING THE TEMPERATURE OF SOLID OXIDE FUEL CELLS," *Science* **334**, no. 6058, 935–939, (2011).
- [40] B. C. H. Steele, "APPRAISAL OF $\text{Ce}_{1-y}\text{Gd}_y\text{O}_{2-y/2}$ ELECTROLYTES FOR IT-SOFC OPERATION AT 500 °C," *Solid State Ionics* **129**, 95–110, (2000).
- [41] H. Inaba and H. Tagawa, "CERIA-BASED SOLID ELECTROLYTES," *Solid State Ionics* **83**, no. 1–2, 1–16, (1996).
- [42] A. Trovarelli, "CATALYTIC PROPERTIES OF CERIA AND CeO_2 -CONTAINING MATERIALS," *Catalysis Reviews-Science and Engineering* **38**, 439–520, (1996).
- [43] J. Kašpar, P. Fornasiero, and M. Graziani, "USE OF CeO_2 -BASED OXIDES IN THE THREE-WAY CATALYSIS," *Catalysis Today* **50**, no. 2, 285–298, (1999).
- [44] A. Trovarelli, C. de Leitenburg, M. Boaro, and G. Dolcetti, "THE UTILIZATION OF CERIA IN INDUSTRIAL CATALYSIS," *Catalysis Today* **50**, no. 2, 353–367, (1999).
- [45] V. V. Kharton, A. V. Kovalevsky, A. P. Viskup, F. M. Figueiredo, A. A. Yaremchenko, E. N. Naumovich, and F. M. B. Marques, "OXYGEN PERMEABILITY OF $\text{Ce}_{0.8}\text{Gd}_{0.2}\text{O}_{2-d}$ - $\text{La}_{0.7}\text{Sr}_{0.3}\text{MnO}_{3-d}$ COMPOSITE MEMBRANES," *Journal of the Electrochemical Society* **147**, 2814–2821, (2000).
- [46] V. V. Kharton, A. V. Kovalevsky, A. P. Viskup, A. L. Shaula, F. M. Figueiredo, E. N. Naumovich, and F. M. B. Marques, "OXYGEN TRANSPORT IN $\text{Ce}_{0.8}\text{Gd}_{0.2}\text{O}_{2-d}$ -BASED COMPOSITE MEMBRANES," *Solid State Ionics* **160**, no. 3–4, 247–258, (2003).

- [47] D. P. Fagg, A. L. Shaula, V. V. Kharton, and J. R. Frade, "HIGH OXYGEN PERMEABILITY IN FLUORITE-TYPE $\text{Ce}_{0.8}\text{Pr}_{0.2}\text{O}_{2-\delta}$ VIA THE USE OF SINTERING AIDS," *Journal of Membrane Science* **299**, no. 1–2, 1–7, (2007).
- [48] X. Zhu and W. Yang, "COMPOSITE MEMBRANE BASED ON IONIC CONDUCTOR AND MIXED CONDUCTOR FOR OXYGEN PERMEATION," *AIChE Journal* **54**, no. 3, 665–672, (2008).
- [49] A. Leo, S. Liu, and J. C. D. da Costa, "DEVELOPMENT OF MIXED CONDUCTING MEMBRANES FOR CLEAN COAL ENERGY DELIVERY," *International Journal of Greenhouse Gas Control* **3**, no. 4, 357–367, (2009).
- [50] H. J. Avila-Paredes and S. Kim, "THE EFFECT OF SEGREGATED TRANSITION METAL IONS ON THE GRAIN BOUNDARY RESISTIVITY OF GADOLINIUM DOPED CERIA: ALTERATION OF THE SPACE CHARGE POTENTIAL," *Solid state ionics* **177**, no. 35, 3075–3080, (2006).
- [51] P. Lupetin, F. Giannici, G. Gregori, A. Martorana, and J. Maier, "EFFECTS OF GRAIN BOUNDARY DECORATION ON THE ELECTRICAL CONDUCTION OF NANOCRYSTALLINE CeO_2 ," *Journal of The Electrochemical Society* **159**, B417, (2012).
- [52] G. Gregori, B. Rahmati, W. Sigle, P. A. Van Aken, and J. Maier, "ELECTRIC CONDUCTION PROPERTIES OF BORON-DOPED CERIA," *Solid State Ionics* **192**, no. 1, 65–69, (2011).
- [53] S. J. Litzelman, R. A. Souza, B. Butz, H. L. Tuller, M. Martin, and D. Gerthsen, "HETEROGENEOUSLY DOPED NANOCRYSTALLINE CERIA FILMS BY GRAIN BOUNDARY DIFFUSION: IMPACT ON TRANSPORT PROPERTIES," *Journal of Electroceramics* **22**, no. 4, 405–415, (2008).
- [54] D. Beckel, A. Bieberle-Hutter, A. Harvey, A. Infortuna, U. P. Muecke, M. Prestat, J. L. M. Rupp, and L. J. Gauckler, "THIN FILMS FOR MICRO SOLID OXIDE FUEL CELLS," *Journal of Power Sources* **173**, 325–345, (2007).
- [55] A. Bieberle-Hütter, D. Beckel, A. Infortuna, U. P. Muecke, J. L. M. Rupp, L. J. Gauckler, S. Rey-Mermet, P. Muralt, N. R. Bieri, N. Hotz, M. J. Stutz, D. Poulikakos, P. Heeb, P. Müller, A. Bernard, R. Gmür, and T. Hocker, "A MICRO-SOLID OXIDE FUEL CELL SYSTEM AS BATTERY REPLACEMENT," *Journal of Power Sources* **177**, no. 1, 123–130, (2008).
- [56] A. Evans, A. Bieberle-Hutter, H. Galinski, J. L. M. Rupp, T. Ryll, B. Scherrer, R. Tolke, and L. J. Gauckler, "MICRO-SOLID OXIDE FUEL CELLS: STATUS, CHALLENGES, AND CHANCES," *Monatshefte Fur Chemie* **140**, 975–983, (2009).
- [57] P.-C. Su and F. B. Prinz, "NANOSCALE MEMBRANE ELECTROLYTE ARRAY FOR SOLID OXIDE FUEL CELLS," *Electrochemistry Communications* **16**, no. 1, 77–79, (2012).
- [58] H. Huang, M. Nakamura, P. Su, R. Fasching, Y. Saito, and F. B. Prinz, "HIGH-PERFORMANCE ULTRATHIN SOLID OXIDE FUEL CELLS FOR LOW-TEMPERATURE OPERATION," *Journal of The Electrochemical Society* **154**, no. 1, B20–B24, (2007).
- [59] A. C. Johnson, A. Baclig, D. V. Harburg, B.-K. Lai, and S. Ramanathan, "FABRICATION AND ELECTROCHEMICAL PERFORMANCE OF THIN-FILM SOLID OXIDE FUEL CELLS WITH LARGE AREA NANOSTRUCTURED MEMBRANES," *Journal of Power Sources* **195**, no. 4, 1149–1155, (2010).
- [60] P.-C. Su and F. B. Prinz, "SILICON-BASED THIN FILM SOLID OXIDE FUEL CELL ARRAY," *Proceedings of SPIE* **7649**, no. 1, 764907–764907–6, (2010).
- [61] Y. Takagi, B.-K. Lai, K. Kerman, and S. Ramanathan, "LOW TEMPERATURE THIN FILM SOLID OXIDE FUEL CELLS WITH NANOPOROUS RUTHENIUM ANODES FOR DIRECT METHANE OPERATION," *Energy & Environmental Science* **4**, no. 9, 3473, (2011).

- [62] K. Kerman, B.-K. Lai, and S. Ramanathan, "PT/Y_{0.16}ZR_{0.84}O_{1.92}/PT THIN FILM SOLID OXIDE FUEL CELLS: ELECTRODE MICROSTRUCTURE AND STABILITY CONSIDERATIONS," *Journal of Power Sources* **196**, no. 5, 2608–2614, (2011).
- [63] B.-K. Lai, A. C. Johnson, M. Tsuchiya, and S. Ramanathan, "TOWARD WAFER-SCALE FABRICATION AND 3D INTEGRATION OF MICRO-SOLID OXIDE FUEL CELLS FOR PORTABLE ENERGY," *Proceedings of SPIE* **7679**, no. 1, 767916–767916–6, (2010).
- [64] B.-K. Lai, H. Xiong, M. Tsuchiya, A. C. Johnson, and S. Ramanathan, "MICROSTRUCTURE AND MICROFABRICATION CONSIDERATIONS FOR SELF-SUPPORTED ON-CHIP ULTRA-THIN MICRO-SOLID OXIDE FUEL CELL MEMBRANES," *Fuel Cells* **9**, no. 5, 699–710, (2009).
- [65] A. C. Johnson, B.-K. Lai, H. Xiong, and S. Ramanathan, "AN EXPERIMENTAL INVESTIGATION INTO MICRO-FABRICATED SOLID OXIDE FUEL CELLS WITH ULTRA-THIN LA_{0.6}SR_{0.4}CO_{0.8}FE_{0.2}O₃ CATHODES AND YTTRIA-DOPED ZIRCONIA ELECTROLYTE FILMS," *Journal of Power Sources* **186**, no. 2, 252–260, (2009).
- [66] Y. Yan, S. C. Sandu, J. Conde, and P. Murali, "EXPERIMENTAL STUDY OF SINGLE TRIPLE-PHASE-BOUNDARY AND PLATINUM–YTTRIA STABILIZED ZIRCONIA COMPOSITE AS CATHODES FOR MICRO-SOLID OXIDE FUEL CELLS," *Journal of Power Sources* **206**, no. 0, 84–90, (2012).
- [67] B.-K. Lai, K. Kerman, and S. Ramanathan, "ON THE ROLE OF ULTRA-THIN OXIDE CATHODE SYNTHESIS ON THE FUNCTIONALITY OF MICRO-SOLID OXIDE FUEL CELLS: STRUCTURE, STRESS ENGINEERING AND IN SITU OBSERVATION OF FUEL CELL MEMBRANES DURING OPERATION," *Journal of Power Sources* **195**, no. 16, 5185–5196, (2010).
- [68] C. Sun and H.-C. Ou, "NUMERICAL CHARACTERIZATION OF A MICROSCALE SOLID-OXIDE FUEL CELL," *Journal of Power Sources* **185**, no. 1, 363–373, (2008).
- [69] M. Kuhn, T. Napporn, M. Meunier, D. Therriault, and S. Vengallatore, "FABRICATION AND TESTING OF COPLANAR SINGLE-CHAMBER MICRO SOLID OXIDE FUEL CELLS WITH GEOMETRICALLY COMPLEX ELECTRODES," *Journal of Power Sources* **177**, no. 1, 148–153, (2008).
- [70] P. Jasinski, "MICRO SOLID OXIDE FUEL CELLS AND THEIR FABRICATION METHODS," *Microelectronics International* **25**, no. 2, 42–48, (2008).
- [71] P. Sarkar, L. Yamarte, H. Rho, and L. Johanson, "ANODE-SUPPORTED TUBULAR MICRO-SOLID OXIDE FUEL CELL," *International Journal of Applied Ceramic Technology* **4**, no. 2, 103–108, (2007).
- [72] M. Mogensen, N. M. Sammes, and G. A. Tompsett, "PHYSICAL, CHEMICAL AND ELECTROCHEMICAL PROPERTIES OF PURE AND DOPED CERIA," *Solid State Ionics* **129**, 63–94, (2000).
- [73] T. G. Stratton and H. L. Tuller, "THERMODYNAMIC AND TRANSPORT STUDIES OF MIXED OXIDES - THE CeO₂-UO₂ SYSTEM," *Journal of the Chemical Society-Faraday Transactions II* **83**, 1143–1156, (1987).
- [74] H. L. Tuller and A. S. Nowick, "DEFECT STRUCTURE AND ELECTRICAL-PROPERTIES OF NONSTOICHIOMETRIC CeO₂ SINGLE-CRYSTALS," *Journal of the Electrochemical Society* **126**, 209–217, (1979).
- [75] D. A. Andersson, S. I. Simak, B. Johansson, I. A. Abrikosov, and N. V. Skorodumova, "MODELING OF CeO₂, Ce₂O₃, AND CeO_{2-x} IN THE LDA+U FORMALISM," *Physical Review B* **75**, no. 3, 035109, (2007).
- [76] E. Wuilloud, B. Delley, W.-D. Schneider, and Y. Baer, "SPECTROSCOPIC EVIDENCE FOR LOCALIZED AND EXTENDED F-SYMMETRY STATES IN CeO₂," *Physical Review Letters* **53**, no. 2, 202–205, (1984).

- [77] D. D. Koelling, A. M. Boring, and J. H. Wood, "THE ELECTRONIC STRUCTURE OF CeO_2 AND PrO_2 ," *Solid State Communications* **47**, no. 4, 227–232, (1983).
- [78] B. T. M. Willis, "POSITIONS OF THE OXYGEN ATOMS IN $\text{UO}_{2.13}$," *Nature* **197**, no. 4869, 755–756, (1963).
- [79] B. T. M. Willis, "STRUCTURES OF UO_2 , UO_{2+x} AND U_4O_9 BY NEUTRON DIFFRACTION," *Journal de Physique* **25**, no. 5, 431–439, (1964).
- [80] B. T. M. Willis, "THE DEFECT STRUCTURE OF HYPER-STOICHIOMETRIC URANIUM DIOXIDE," *Acta Crystallographica Section A* **34**, no. 1, 88–90, (1978).
- [81] K. Govers, S. Lemehov, M. Hou, and M. Verwerft, "COMPARISON OF INTERATOMIC POTENTIALS FOR UO_2 . PART I: STATIC CALCULATIONS," *Journal of Nuclear Materials* **366**, no. 1–2, 161–177, (2007).
- [82] D. A. Andersson, J. Lezama, B. P. Uberuaga, C. Deo, and S. D. Conradson, "COOPERATIVITY AMONG DEFECT SITES IN AO_{2+x} AND A_4O_9 (A=U,NP,PU): DENSITY FUNCTIONAL CALCULATIONS," *Physical Review B* **79**, no. 2, 024110, (2009).
- [83] H. L. Tuller, J. A. Kilner, A. E. McHale, and B. C. H. Steele, "OXYGEN DIFFUSION IN OXYGEN EXCESS CeO_2 - UO_2 SOLID SOLUTIONS," *Reactivity of Solids*, ed. P. Barrett and L.-C. Dufour (Elsevier, Amsterdam) 315–319, (1985).
- [84] I. K. Naik and T. Y. Tien, "ELECTRICAL-CONDUCTION IN Nb_2O_5 -DOPED CERIUM DIOXIDE," *Journal of the Electrochemical Society* **126**, 562–566, (1979).
- [85] M. R. Deguire, M. J. Shingler, and E. Dincer, "POINT-DEFECT ANALYSIS AND MICROSTRUCTURAL EFFECTS IN PURE AND DONOR-DOPED CERIA," *Solid State Ionics* **52**, 155–163, (1992).
- [86] P. V. Ananthapadmanabhan, S. B. Menon, D. S. Patil, N. Venkatramani, and V. K. Rohatgi, "ELECTRICAL-CONDUCTIVITY OF CERIUM DIOXIDE DOPED WITH TANTALUM PENTOXIDE," *Journal of Materials Science Letters* **11**, 501–503, (1992).
- [87] C. Ftikos, M. Nauer, and B. C. H. Steele, "ELECTRICAL-CONDUCTIVITY AND THERMAL-EXPANSION OF CERIA-DOPED WITH PR, NB AND SN," *Journal of the European Ceramic Society* **12**, 267–270, (1993).
- [88] E. Lucchini, C. Schmid, I. Barbariol, and S. Roitti, "THERMOGRAVIMETRIC AND ELECTRICAL CHARACTERISATION OF A TANTALUM PENTOXIDE DOPED CERIA-ZIRKONIA SOLID SOLUTION," *Key Engineering Materials* **132–136**, 1353–1356, (1997).
- [89] K. Yashiro, I. Suzuki, A. Kaimai, H. Matsumoto, Y. Nigara, T. Kawada, J. Mizusaki, J. Sfeir, and J. Van Herle, "ELECTRICAL PROPERTIES AND DEFECT STRUCTURE OF NIOBIA-DOPED CERIA," *Solid State Ionics* **175**, 341–344, (2004).
- [90] H. L. Tuller and A. S. Nowick, "SMALL POLARON ELECTRON TRANSPORT IN REDUCED CeO_2 SINGLE CRYSTALS," *Journal of Physics and Chemistry of Solids* **38**, no. 8, 859–867, (1977).
- [91] I. K. Naik and T. Y. Tien, "SMALL-POLARON MOBILITY IN NONSTOICHIOMETRIC CERIUM DIOXIDE," *Journal of Physics and Chemistry of Solids* **39**, 311–315, (1978).
- [92] H. L. Tuller and A. S. Nowick, "DOPED CERIA AS A SOLID OXIDE ELECTROLYTE," *Journal of The Electrochemical Society* **122**, no. 2, 255–259, (1975).
- [93] C. L. Jia and K. Urban, "ATOMIC-RESOLUTION MEASUREMENT OF OXYGEN CONCENTRATION IN OXIDE MATERIALS," *Science* **303**, no. 5666, 2001–2004, (2004).
- [94] J. Maier, "PHYSICAL CHEMISTRY OF IONIC MATERIALS: IONS AND ELECTRONS IN SOLIDS." John Wiley & Sons, (2004).

- [95] R. Paul, "HALBLEITERPHYSIK." Dr. Alfred Hüthig Verlag, (1983).
- [96] M. C. Göbel, G. Gregori, and J. Maier, "NUMERICAL CALCULATIONS OF ONE-DIMENSIONAL SPACE CHARGE LAYER PROFILES AND CONDUCTIVITY EFFECTS IN NANOCRYSTALLINE CERIUM OXIDE", in preparation.
- [97] A. Tschöpe, "NUMERICAL ANALYSIS OF SPACE CHARGE LAYERS AND ELECTRICAL CONDUCTIVITY IN MESOSCOPIC CERIUM OXIDE CRYSTALS," *Journal of Applied Physics* **95**, no. 3, 1203, (2004).
- [98] S. J. Litzelman and H. L. Tuller, "MEASUREMENT OF MIXED CONDUCTIVITY IN THIN FILMS WITH MICROSTRUCTURED HEBB-WAGNER BLOCKING ELECTRODES," *Solid State Ionics* **180**, no. 20–22, 1190–1197, (2009).
- [99] A. Kossov, Y. Feldman, E. Wachtel, K. Gartsman, I. Lubomirsky, J. Fleig, and J. Maier, "ON THE ORIGIN OF THE LATTICE CONSTANT ANOMALY IN NANOCRYSTALLINE CERIA," *Phys. Chem. Chem. Phys.* **8**, no. 9, 1111–1115, (2006).
- [100] M. C. Göbel, G. Gregori, and J. Maier, "LOW SPACE CHARGE LAYER POTENTIAL IN NANOCRYSTALLINE CERIUM OXIDE THIN FILMS", in preparation.
- [101] F. Maglia, F. Farina, M. Dapiaggi, I. G. Tredici, and U. Anselmi-Tamburini, "TRANSPORT PROPERTIES IN BULK NANOCRYSTALLINE SM-DOPED CERIA WITH DOPING CONTENT BETWEEN 2 AND 30 AT.%, " *Solid State Ionics*(2012).
- [102] "ICPDS – INTERNATIONAL COMMITTEE FOR DIFFRACTION DATA, CARD #34-0394." .
- [103] F. Dion and A. Lasia, "THE USE OF REGULARIZATION METHODS IN THE DECONVOLUTION OF UNDERLYING DISTRIBUTIONS IN ELECTROCHEMICAL PROCESSES," *Journal of Electroanalytical Chemistry* **475**, no. 1, 28–37, (1999).
- [104] K. S. Cole and R. H. Cole, "DISPERSION AND ABSORPTION IN DIELECTRICS I. ALTERNATING CURRENT CHARACTERISTICS," *The Journal of Chemical Physics* **9**, no. 4, 341–351, (1941).
- [105] Z. Q. Yu, S. V. N. T. Kuchibhatla, M. H. Engelhard, V. Shutthanandan, C. M. Wang, P. Nachimuthu, O. A. Marina, L. V. Saraf, S. Thevuthasan, and S. Seal, "GROWTH AND STRUCTURE OF EPITAXIAL $\text{Ce}_{0.8}\text{Sm}_{0.2}\text{O}_{1.9}$ BY OXYGEN-PLASMA-ASSISTED MOLECULAR BEAM EPITAXY," *Journal of Crystal Growth* **310**, no. 10, 2450–2456, (2008).
- [106] S. V. N. T. Kuchibhatla, P. Nachimuthu, F. Gao, W. Jiang, V. Shutthanandan, M. H. Engelhard, S. Seal, and S. Thevuthasan, "GROWTH-RATE INDUCED EPITAXIAL ORIENTATION OF CeO_2 ON Al_2O_3 (0001)," *Applied Physics Letters* **94**, no. 20, 204101, (2009).
- [107] "ICPDS – INTERNATIONAL COMMITTEE FOR DIFFRACTION DATA, CARD #75-0161." .
- [108] "ICPDS – INTERNATIONAL COMMITTEE FOR DIFFRACTION DATA, CARD #75-0162." .
- [109] "ICPDS – INTERNATIONAL COMMITTEE FOR DIFFRACTION DATA, CARD #75-0163." .
- [110] L. Wu, H. J. Wiesmann, A. R. Moodenbaugh, R. F. Klie, Y. Zhu, D. O. Welch, and M. Suenaga, "OXIDATION STATE AND LATTICE EXPANSION OF CeO_{2-x} NANOPARTICLES AS A FUNCTION OF PARTICLE SIZE," *Physical Review B* **69**, no. 12, 125415, (2004).
- [111] S. Tsunekawa, S. Ito, and Y. Kawazoe, "SURFACE STRUCTURES OF CERIUM OXIDE NANOCRYSTALLINE PARTICLES FROM THE SIZE DEPENDENCE OF THE LATTICE PARAMETERS," *Applied Physics Letters* **85**, no. 17, 3845–3847, (2004).
- [112] R. K. Hailstone, A. G. DiFrancesco, J. G. Leong, T. D. Allston, and K. J. Reed, "A STUDY OF LATTICE EXPANSION IN CeO_2 NANOPARTICLES BY TRANSMISSION ELECTRON MICROSCOPY," *J. Phys. Chem. C* **113**, no. 34, 15155–15159, (2009).

- [113] L. Chen, C. L. Chen, D. X. Huang, Y. Lin, X. Chen, and A. J. Jacobson, "HIGH TEMPERATURE ELECTRICAL CONDUCTIVITY OF EPITAXIAL GD-DOPED CeO_2 THIN FILMS," *Solid State Ionics* **175**, no. 1–4, 103–106, (2004).
- [114] S. Sanna, V. Esposito, D. Pergolesi, A. Orsini, A. Tebano, S. Licocchia, G. Balestrino, and E. Traversa, "FABRICATION AND ELECTROCHEMICAL PROPERTIES OF EPITAXIAL SAMARIUM-DOPED CERIA FILMS ON SrTiO_3 -BUFFERED MGO SUBSTRATES," *Advanced Functional Materials* **19**, no. 11, 1713–1719, (2009).
- [115] N. I. Karageorgakis, A. Heel, J. L. M. Rupp, M. H. Aguirre, T. Graule, and L. J. Gauckler, "PROPERTIES OF FLAME SPRAYED $\text{Ce}_{0.8}\text{Gd}_{0.2}\text{O}_{1.9-\delta}$ ELECTROLYTE THIN FILMS," *Advanced Functional Materials* **21**, no. 3, 532–539, (2011).
- [116] E. Fabbri, D. Pergolesi, and E. Traversa, "IONIC CONDUCTIVITY IN OXIDE HETEROSTRUCTURES: THE ROLE OF INTERFACES," *Science and Technology of Advanced Materials* **11**, 054503, (2010).
- [117] A. Karthikeyan and S. Ramanathan, "TEMPERATURE-DEPENDENT INTERFACIAL CARRIER TRANSPORT IN LOW-DIMENSIONAL OXIDES USING IONIC CONDUCTOR-INSULATOR (YDZ-SiO_2) SUPERLATTICES," *Journal of Applied Physics* **104**, no. 12, 124314, (2008).
- [118] I. Kosacki, T. Suzuki, V. Petrovsky, and H. U. Anderson, "ELECTRICAL CONDUCTIVITY OF NANOCRYSTALLINE CERIA AND ZIRCONIA THIN FILMS," *Solid State Ionics* **136**, 1225–1233, (2000).
- [119] T. Suzuki, I. Kosacki, and H. U. Anderson, "DEFECT AND MIXED CONDUCTIVITY IN NANOCRYSTALLINE DOPED CERIUM OXIDE," *Journal of the American Ceramic Society* **85**, no. 6, 1492–1498, (2002).
- [120] M. Mukaida, M. Miura, A. Ichinose, K. Matsumoto, Y. Yoshida, S. Horii, A. Saito, F. Hirose, Y. Takahashi, and S. Ohshima, "HETERO-EPITAXIAL GROWTH OF CeO_2 FILMS ON MGO SUBSTRATES," *Japanese Journal of Applied Physics* **44**, no. No. 10, L318–L321, (2005).
- [121] M. Maul, B. Schulte, P. Haussler, G. Frank, T. Steinborn, H. Fuess, and H. Adrian, "EPITAXIAL CeO_2 BUFFER LAYERS FOR $\text{YBa}_2\text{Cu}_3\text{O}_{7-\delta}$ FILMS ON SAPPHIRE," *Journal of applied physics* **74**, no. 4, 2942–2944, (1993).
- [122] F. Wang and R. Wördenweber, "LARGE-AREA EPITAXIAL CeO_2 BUFFER LAYERS ON SAPPHIRE SUBSTRATES FOR THE GROWTH OF HIGH QUALITY $\text{YBa}_2\text{Cu}_3\text{O}_7$ FILMS," *Thin Solid Films* **227**, no. 2, 200–204, (1993).
- [123] M. Maul, B. Schulte, P. Häussler, and H. Adrian, " $\text{YBa}_2\text{Cu}_3\text{O}_{7-\delta}$ -THIN FILMS ON SAPPHIRE WITH BUFFER LAYERS OF CeO_2 ," *Physica B: Condensed Matter* **194–196, Part 2**, no. 0, 2285–2286, (1994).
- [124] K. Fröhlich, J. Šouc, D. Machajdík, M. Jergel, J. Snauwaert, and L. Hellemans, "SURFACE QUALITY OF EPITAXIAL CeO_2 THIN FILMS GROWN ON SAPPHIRE BY AEROSOL MOCVD," *Chemical Vapor Deposition* **4**, no. 6, 216–220, (1998).
- [125] K. Fröhlich, D. Machajdík, L. Hellemans, and J. Snauwaert, "GROWTH OF HIGH CRYSTALLINE QUALITY THIN EPITAXIAL CeO_2 FILMS ON (1102) SAPPHIRE," *Le Journal de Physique IV* **09**, no. PR8, Pr8–341–Pr8–347, (1999).
- [126] J. Kurian and M. Naito, "GROWTH OF EPITAXIAL CeO_2 THIN FILMS ON R-CUT SAPPHIRE BY MOLECULAR BEAM EPITAXY," *Physica C: Superconductivity* **402**, no. 1–2, 31–37, (2004).
- [127] G. Linker, R. Smithey, J. Geerk, F. Ratzel, R. Schneider, and A. Zaitsev, "THE GROWTH OF ULTRA-THIN EPITAXIAL CeO_2 FILMS ON R-PLANE SAPPHIRE," *Thin solid films* **471**, no. 1–2, 320–327, (2005).

- [128] J. C. Nie, H. Yamasaki, Y. Nakagawa, K. Develos-Bagarinao, M. Murugesan, H. Obara, and Y. Mawatari, "EPITAXIAL CeO_2 BUFFER LAYER ON DELIBERATELY MISCUT SAPPHIRE FOR MICROCRACK-FREE THICK $\text{YBa}_2\text{Cu}_3\text{O}_{7-\delta}$ FILMS," *Journal of Crystal Growth* **284**, no. 3–4, 417–424, (2005).
- [129] T. Kudo, "MIXED ELECTRICAL CONDUCTION IN THE FLUORITE-TYPE $\text{Ce}_{1-x}\text{Gd}_x\text{O}_{2-x/2}$," *Journal of The Electrochemical Society* **123**, no. 3, 415, (1976).
- [130] S.-H. Park and H.-I. Yoo, "THERMOELECTRIC BEHAVIOR OF A MIXED IONIC ELECTRONIC CONDUCTOR, $\text{Ce}_{1-x}\text{Gd}_x\text{O}_{2-x/2-\delta}$," *Physical Chemistry Chemical Physics* **11**, no. 2, 391, (2009).
- [131] J. L. M. Rupp, A. Infortuna, and L. J. Gauckler, "THERMODYNAMIC STABILITY OF GADOLINIA-DOPED CERIA THIN FILM ELECTROLYTES FOR MICRO-SOLID OXIDE FUEL CELLS," *Journal of the American Ceramic Society* **90**, no. 6, 1792–1797, (2007).
- [132] E. C. C. Souza, W. C. Chueh, W. Jung, E. N. S. Muccillo, and S. M. Haile, "IONIC AND ELECTRONIC CONDUCTIVITY OF NANOSTRUCTURED, SAMARIA-DOPED CERIA," *Journal of The Electrochemical Society* **159**, K127, (2012).
- [133] A. Tschöpe, J. Y. Ying, and H. L. Tuller, "CATALYTIC REDOX ACTIVITY AND ELECTRICAL CONDUCTIVITY OF NANOCRYSTALLINE NON-STOICHIOMETRIC CERIUM OXIDE," *Sensors and Actuators B: Chemical* **31**, no. 1–2, 111–114, (1996).
- [134] J. A. S. Ikeda and Y. Chiang, "SPACE CHARGE SEGREGATION AT GRAIN BOUNDARIES IN TITANIUM DIOXIDE: I, RELATIONSHIP BETWEEN LATTICE DEFECT CHEMISTRY AND SPACE CHARGE POTENTIAL," *Journal of the American Ceramic Society* **76**, no. 10, 2437–2446, (1993).
- [135] J. A. S. Ikeda, Y. Chiang, A. J. Garratt-Reed, and J. B. V. Sande, "SPACE CHARGE SEGREGATION AT GRAIN BOUNDARIES IN TITANIUM DIOXIDE: II, MODEL EXPERIMENTS," *Journal of the American Ceramic Society* **76**, no. 10, 2447–2459, (1993).
- [136] R. Meyer and R. Waser, "RESISTIVE DONOR-DOPED SrTiO_3 SENSORS: I, BASIC MODEL FOR A FAST SENSOR RESPONSE," *Sensors and Actuators B: Chemical* **101**, no. 3, 335–345, (2004).

Curriculum Vitae

Personal Information

Name: Marcus C. Göbel
Nationality: German
Date of Birth: July 21, 1983
Place of Birth: Halle (Saale), Germany
Contact: mail@marcus-goebel.de

Education

Since Oct. 2008 **PhD in Chemistry**
Max Planck Institute for Solid State Research, Stuttgart (Germany),
Supervisor: Prof. Dr. Maier, Thesis: „Boundary Effects on the
Electrical Conductivity of Cerium Oxide Thin Films“

Sept. 2006 – Sept. 2008 **MPhil in Chemistry**
Cardiff University (UK), Supervisor: Dr. Murphy, Thesis: „An EPR
and ENDOR Investigation of Paramagnetic Chiral Metal Complexes“

Oct. 2003 – Aug. 2006 **BSc in Chemistry**
Leipzig University (Germany), Supervisor: Prof. Dr. Morgner,
Thesis: „Investigation of Micelles in Polar Liquids with Molecular
Dynamics Simulations “
Further activities during study:
✦ Member of the student council of the Faculty of Chemistry and
Mineralogy
✦ Tutor of the seminar “Physical Chemistry – Thermodynamics”
✦ Traineeship at the Max Planck Institute for Solid State Research,
Stuttgart (Germany), Department: Prof. Dr. Simon

May 2003 – Sept. 2003 **Traineeship**
Institute for Non-classical Chemistry (Leipzig University)

July 2002 – April 2003

Alternative Civilian Service

University Hospital Leipzig

Sept. 1994 – June 2002

Academic Upper Secondary School

Gymnasium Humboldt-Schule Leipzig

- ✦ Special scientific project in the subject chemistry: „X-ray Crystallography of Two Organic Compounds“, Supervisor: Prof. Dr. Sieler (Leipzig University)

Publications

- ✦ M.C. Göbel, G. Gregori, J. Maier, „Electronically Blocking Grain Boundaries in Donor Doped Cerium Dioxide“, *Solid State Ionics* **215**, 45 (2012).
- ✦ G. Gregori, M.C. Göbel, J. Maier, „Electronic Conductivity in Nanocrystalline Ce_{0.9}Gd_{0.1}O_{1.95} Thin Films at High Oxygen Partial Pressures“, *ECS Transactions* **45**, 181 (2012).
- ✦ M.C. Göbel, G. Gregori, J. Maier, „Mixed Conductivity in Nanocrystalline Highly Acceptor Doped Cerium Oxide Thin Films Under Oxidizing Conditions“, *Phys. Chem. Chem. Phys.* **13**, 10940 (2011).
- ✦ C. Pfaffenhuber, S. Sörgel, K. Weichert, M. Bele, T. Mundinger, M.C. Göbel, J. Maier, „In Situ Recording of Particle Network Formation in Liquids by Ion Conductivity Measurements“, *J. Am. Chem. Soc.* **133**, 14514 (2011).
- ✦ D.M. Murphy, I. Caretti, E. Carter, I.A. Fallis, M.C. Göbel, J. Landon, S. Van Doorslaer, D.J. Willock, „Visualizing Diastereomeric Interactions of Chiral Amine – Chiral Copper Salen Adducts by EPR Spectroscopy and DFT“, *Inorg. Chem.* **50**, 6944 (2011).
- ✦ M.C. Göbel, G. Gregori, X.X. Guo, J. Maier, „Boundary Effects on the Electrical Conductivity of Pure and Doped Cerium Oxide Thin Films“, *Phys. Chem. Chem. Phys.* **12**, 14351 (2010).
- ✦ In Preparation:
 - „Numerical Calculations of Space Charge Layer Effects in Nanocrystalline Cerium Oxide“
 - „Low Space Charge Layer Potentials in Polycrystalline Cerium Oxide Thin Films“
 - „Switch-Over from Ionic to Electronic Conductivity in Nanocrystalline CeO₂ Thin Films“
 - „Structure – Conductivity Relationships in Soggy Sand Electrolytes Determined with Kinetic Monte Carlo Simulations and FEM Calculations“